



Doctoral Thesis

Linear-Rotary Bearingless Actuators

Author(s):

Miric, Spasoje

Publication Date:

2021

Permanent Link:

<https://doi.org/10.3929/ethz-b-000509755> →

Rights / License:

[In Copyright - Non-Commercial Use Permitted](#) →

This page was generated automatically upon download from the [ETH Zurich Research Collection](#). For more information please consult the [Terms of use](#).

Diss. ETH No. 27421

Linear-Rotary Bearingless Actuators

A thesis submitted to attain the degree of

DOCTOR OF SCIENCES of ETH ZURICH
(Dr. sc. ETH Zurich)

presented by

SPASOJE MIRIĆ

PhD in Electrical Engineering,
University of Belgrade

born on 29.09.1989
citizen of Serbia

accepted on the recommendation of

Prof. Dr. Johann W. Kolar, examiner
Prof. Dr. Emil Levi, co-examiner

2021

ETH Zurich
Power Electronic Systems Laboratory
Physikstrasse 3 | ETL H23
8092 Zurich | Switzerland

<https://www.pes.ee.ethz.ch>

© 2021, Spasoje Mirić

Acknowledgments

FIRST and foremost I would like to thank Prof. Dr. Johann W. Kolar for giving me the opportunity to be part of his team at ETH Zurich. It is an enormous pleasure and honor to work under his supervision. His knowledge, full-scale commitment and passion for science has motivated my dedication to work. I greatly appreciate his guidance and support through my PhD that resulted in many new ideas and novel motor concepts. Finally, I thank him indelibly for his care and motivation to engage in greater depth with Power Electronics, to which I will dedicate during my further academic career.

I also thank Prof. Dr. Emil Levi for reading and reviewing my thesis and for being my co-examiner. I am very much honored to receive feedback from such an expert in the field of electric machines.

I would like to express my gratitude to ETH Foundation for financially supporting a part of this project.

For the smooth start at PES I thank my supervisor, office colleague and friend Dr. Arda Tüysüz, who very patiently taught me so much about electric machines. He was always there when I had questions or needed help.

During the time I designed my first inverter, I got great help from Dr. Marcel Alexander-Schuck and I thank him for his time and support.

I would like to thank Dr. Dominik Bortis for his great help during the design of my second actuator and inverter. Also, I thank him very much for the opportunity to be part of his electrical machine lecture team.

Many thanks to my colleague Rosario Giuffrida for the help with laboratory measurements and numerous lunch and coffee break discussions.

I thank all master and semester students that I supervised. Special mention goes to those whose work directly contributed to this thesis: Pascal Küttel, Fabian Dietschi, Stefan Nehls, Gwendolin Rohner and Andreas Horat. Also, many thanks to Varsha Behrunani, for developing the USB based interface for our digital control board.

Thanks a lot to the PES administrative team, Monica Kohn, Prisca Maurantonio, Roswitha Coccia and Yvonne Schnyder. Thanks to Florian Krismer for the help with the Windows file system. Many thanks to Peter Seitz for the great help with soldering. Manufactured hardware prototypes would not be possible without the help of the D-ITET workshop staff, whom I greatly thank for the support. Special mention goes to Martin Vogt and Daniel Wegmann. Many thanks to Claudia Stucki and Marina Eisenstat for their IT support.

I thank very much my old office colleagues Dr. Mario Mauerer, Dr. Michael Flankl for the great atmosphere and spirit in the office that made work joyful. Special thanks to Dr. Mario Mauerer for the significant assistance with the ZYNQ board.

Many thanks to my past office colleague, electrical machine lecture team-mate and good friend Emanuel Hubmann, from whom I learned so much through technical and non-technical discussions and got so many supportive and motivating advises and spent a lot of great time outside PES.

Many thanks to all the colleagues for the tips and wonderful time at PES. Among them, I would like to mention from the older generation Dr. Christoph Gammeter - thanks for many discussions about electrical machines, Dr. Oliver Knecht, Dr. Roman Bosshard, Dr. Jonas Huber, Dr. Tobias Wellerdieck, Dr. Lukas Franz Schrittwieser, Dr. Pascal Püntener and Dr. Thomas Holenstein. Thanks to the recent generation of PhD students for an unforgettable time and life changing experiences, in particular: Dr. Mattia Guacci, Dr. Thomas Guillod, Dr. Daniel Rothmund - USA road trip team; Dr. Jon Azurza - thanks for FCC discussions, Michael Haider - thanks for showing me TCM operation, Panteleimon Papamanolis - thanks for the inductor optimization script, Dr. Michael Antivachis, Dr. Dominik Neumayr, Morris Heller, David Menzi, Pascal Niklaus, Dr. Jannik Schäfer, Gustavo Carlos Knabben, Piotr Czyz, Julian Böhler and Pedro Bezerra. Many thanks to Davide Cittanti for inspiring discussions on motor control. Also, I would like to mention and thank the younger generation who brought so much energy and desire for research and knowledge to PES: Yunni Li, Daifei Zhang, Neha Nain, Ivana Bargaric, Marc Röthlisberger; Gwendolin Rohner and Reto Bonetti - my current office colleagues.

A very special mention in this acknowledgment deserve two people who played an extremely important role in my education and life. The person to whom I am indelibly thankful is Prof. Dr. Predrag Pejović, who took me as a PhD student at the University of Belgrade and in the last year of my first PhD studies recommended me for the second one. Therefore, he very much caused my current situation - me writing a second PhD thesis. The person, who unfortunately since 2018 is not anymore with us, who was my teacher and supervisor, who was always there when I needed an advice, the person who opened my eyes for many things in life. Thank you endlessly Prof. Gradimir Božilović, I had a crazy luck in my life to get to know you.

I thank Prof. Dr. Marija Hribšek for lending me the money for my first month in Zurich, June 2016.

I thank my family for their care and everything that I am and everything that I have.

Last but important, I thank my beloved girlfriend Anastassia, for her understanding, support and love.

Dr. Spasoje Mirić
Zurich, December 2020

There is nothing invisible, there are only poor eyes.

(Nema nevidljivog, ima samo nemoćnih očiju.)

MIROSLAV MIKA ANTIĆ (1932-1986, Serbia)

Abstract

LINEAR and linear-rotary machines (motors or actuators) are used in many applications that require controlled linear or combined linear and rotary motion. In particular, those are pick-and-place robots used in packaging lines for very precise component mounting on printed circuit boards or die placing into integrated circuit cases, surgery robots, active suspension of vehicles, wave electric power generation or linear compressors, to mention a few. These machines have been built for years and always improved and adjusted to application requirements. The most simple linear-rotary actuator (LiRA) is built by mechanically connecting individual linear and rotary actuators, which results in the linear and rotary degrees of freedom of an end effector. Such actuator is bulky and renders limited dynamics. In order to suffice higher dynamics and extreme compactness, a wave of research has been initiated and many new LiRA topologies with linear and rotary feature integrated into a single machine volume have been proposed in literature.

In this thesis, a step further in the actuator area is taken by proposing a LiRA with integrated magnetic bearings (MBs). Typically, MBs are added as two independent standalone machines at each axial end of the actuator, which would increase the length of the actuator. Therefore, in this thesis, MBs are integrated into the existing actuator volume, resulting in a so called *bearingless* actuator. Such actuator in certain applications has superior properties compared to a LiRA with conventional bearings. For example, tilting control of the rotor/mover would be only possible in a LiRA with MBs, which allows pick-and-place robots to place smaller and more brittle electronic components, i.e. allowing further size reduction of PCB components. In particular, two actuators with MBs are proposed in this thesis: (1) a *magnetically levitated tubular actuator* (MALTA) and (2) a *double stator linear-rotary actuator* (DS LiRA).

Both of the proposed actuators, the MALTA and the DS LiRA, are optimized using FEM simulations and built in hardware. In order for MBs to function, it is necessary to “close the loop” between the position measurement, control system and an amplifier. Therefore, for the MALTA and the DS LiRA, a dedicated position sensor and an inverter are built and a control system is developed. Their operation is verified with measurements taken on the hardware prototypes.

Even though LiRAs with MBs would have great advantages over the ones with conventional bearings, they have not been extensively analyzed in literature. Consequently, the models that provide understanding of their operation and give basis for the control system implementation are not entirely covered.

Therefore, in this thesis an enhanced complex space vector based model of the LiRA with MBs is derived and expressions for the torque, thrust force and MB force are given. The LiRA complex space vector of the voltage, current or flux linkage, is defined using the proposed transformation with two complex frames, one related to the rotation and the MBs and another to the linear motion. This results in complex space vectors having components in two complex frames, where each of them is defined with a dedicated complex unit.

For the control system design, a full nonlinear dynamic mechanical model of the LiRAs rotor/mover is derived and afterwards linearized. The functioning of two kinds of control systems is presented, a MIMO one based on the LQR tuning method and structure, and a SISO one based on the decentralized control system strategy.

The performed experiments verify the tilting control capability of the MALTA and, therefore, confirm its applicability in high-precision applications. The MALTA control system is implemented as MIMO and SISO system, and the operation of both approaches is verified with measurements. The DS LiRA controller is implemented as SISO system and its operation is verified with measurements.

Kurzfassung

LINEARE und linear-rotatorische Motoren/Aktuatoren werden in Anwendungen eingesetzt, die kontrollierte lineare bzw. translatorische, rotatorische oder kombiniert linear-rotatorische Bewegungen erfordern. Dies sind insbesondere Pick-and-Place-Roboter, die in Verpackungslinien zur hochpräzisen Bestückung von Leiterplatten oder zum Einlegen von Chips in die Gehäuse integrierter Schaltungen eingesetzt werden, Operationsroboter, die aktive Federung von Fahrzeugen, Linearkompressoren oder die Stromerzeugung in Wellenkraftwerken. Der einfachste Aufbau eines linear-rotatorischen Aktuators (LiRA) ist das mechanische Verbinden separierter Linear- und Rotationsaktuatoren, wodurch sich die linearen und rotatorischen Freiheitsgrade eines Endeffektors ergeben. Ein solcher Aktuator ist jedoch sperrig und weist eine begrenzte Dynamik auf. Gegenwärtige Forschungen zielen daher auf höhere Dynamik und extreme Kompaktheit und in der Literatur werden neue LiRA-Konzepte vorgeschlagen bei welchen die Erzeugung der Linear- und Rotationsbewegung in einem einzigen Aktivteil integriert wird. Ziel der vorliegenden Dissertation ist es, einen nächsten massgeblichen Verbesserungsschritt zu setzen und ein LiRA-Konzept mit integrierten Magnetlagern (MBs) incl. Sensorik und Regelung zu konzipieren und experimentell zu verifizieren.

Typischerweise werden MBs als eigenständige Einheiten an den Enden der Achse des Aktuators hinzugefügt, was die Baulänge erhöht. Demgegenüber werden in dieser Arbeit MBs in das vorhandene Aktuatorvolumen integriert, wodurch ein sogenannter lagerloser Aktuator entsteht und Vorteile bzgl. Baugrösse resultieren. Ein Aktuator mit integrierten MBs ist einem LiRA mit herkömmlichen Lagern in zahlreichen Anwendungen überlegen. Beispielsweise ist für MB-LiRA eine Neigesteuerung des Rotors/Movers möglich, die es Pick-and-Place-Robotern erlaubt kleinere spröde elektronische Bauteile exakt platzieren und somit letztlich eine weitere Grössenreduktion elektronischer Komponenten unterstützt. In dieser Arbeit werden zwei neue Aktuatorkonzepte mit integrierten MBs vorgeschlagen: (1) ein magnetgelagerter röhrenförmiger Aktuator (MALTA) und (2) ein Doppel-Stator-Lineardrehantrieb (DS LiRA).

Sowohl MALTA als auch DS LiRA werden mittels FEM-Simulationen optimiert und nachfolgend praktisch realisiert. Dies schliesst auch die Positionssensorik und eine Inverterstufe samt Ansteuerelektronik ein. Die Funktion beider Aktuatoren wird durch Messungen an Hardware-Prototypen überprüft.

Obwohl MB-LiRA massgebliche Vorteile gegenüber Lösungen mit konventionellen Lagern aufweisen, fehlt bisher eine ausführliche Analyse. Daher

werden in der Arbeit Modelle, welche das Verständnis ihrer Funktionsweise unterstützen und die Grundlage für die Implementierung des Regelsystems bilden entwickelt. Insbesondere wird ein neues raumzeigerbasiertes Modell vorgeschlagen welches die Basis für die Ableitung mathematischer Ausdrücke für das Drehmoment, die Schubkraft und die MB-Kraft bildet. Der komplexe LiRA-Raumzeiger der Spannungs-, Strom- oder Flussverkettung wird unter Verwendung der vorgeschlagenen Transformation in zwei komplexen Koordinatensystemen definiert, von denen sich eines auf die Rotation und die Magnetlager und das andere auf die Linearbewegung bezieht. Dies führt zu komplexen Raumzeigern mit Komponenten in zwei Koordinatensystemen, wobei jedem Koordinatensystem einer dedizierte komplexe Einheit zugeordnet ist. Für das Design des Regelsystems wird ein vollständiges nichtlineares dynamisches Modell des LiRA-Rotors/Movers abgeleitet und anschließend linearisiert. Weiters werden zwei Regelkonzepte, ein MIMO-System basierend auf der LQR-Tuning-Methode und Struktur und ein SISO-System basierend auf einer dezentralen Regelsystemstrategie analysiert. Die Funktion beider Ansätze wird durch Messungen überprüft. Der DS LiRA Controller ist als SISO-System implementiert und auch seine Funktion wird durch Messungen verifiziert.

Abschliessende Experimente verifizieren die Neigungssteuerungsfähigkeit des MALTA und bestätigen dessen Potential zum Einsatz in hochpräzisen Anwendungen.

Abbreviations

2D	Two-Dimensional
3D	Three-Dimensional
AC	Alternating Current
AMB	Active Magnetic Bearings
Cu/cu	Copper
COG	Center of Gravity
DC	Direct Current
DS	Double Stator
FEM	Finite Element Method
Fe/fe	Iron
FPGA	Field Programmable Gate Array
GaN	Gallium Nitride
L	Linear
LA	Linear Actuator
LiRA	Linear-Rotary Actuator
LQR	Linear-Quadratic Regulator
MALTA	Magnetically Levitated Tubular Actuator
MB	Magnetic Bearing
MIMO	Multiple-Input Multiple-Output
P	Proportional
PCB	Printed Circuit Board
PI	Proportional-Integral
PID	Proportional-Integral-Derivative
PM	Permanent Magnet
PWM	Pulse-Width Modulation
R	Rotary
RA	Rotary Actuator
RMS	Root-Mean-Square
SISO	Single-Input Single-Output
SMD	Surface Mount Device
SP	Sensor Plane
TLA	Tubular Linear Actuator

Contents

Acknowledgments	iii
Abstract	ix
Kurzfassung	xi
Abbreviations	xiii
1 Introduction	1
1.1 Motivation and Applications	1
1.2 Challenges	5
1.3 Scientific Contributions of the Thesis	6
1.4 Outline of the Thesis	8
1.5 Publications	10
2 Linear-Rotary Machine Realizations and Scaling Laws	13
2.1 Introduction	13
2.2 Actuator Topology Concepts	14
2.3 Interior Rotor Scaling Laws	18
2.4 Exterior Rotor Scaling Laws	25
2.5 Scaling Law Constants	28
2.6 Design Example Discussion	30
2.7 Summary	33
3 Generic Complex Space Vector Modeling	35
3.1 Introduction	35
3.2 Complex Space Vector Model	36
3.3 Rotary Machine: Torque	37
3.4 Rotary Machine: Bearing Force	41
3.5 Linear Machine: Thrust Force	45
3.6 Linear Machine: Bearing Force	46
3.7 Linear-Rotary Machine: Torque + Thrust Force	47
3.8 Linear-Rotary Machine: Bearing Force	51
3.9 Linear Machine: Thrust Force + Bearing Force	52
3.10 Summary	55

4	Design of the Linear Machine with Integrated Magnetic Bearings	57
4.1	Introduction	57
4.2	Derivation of the MALTA Winding	59
4.3	MALTA Winding Realizations	66
4.4	Comparison of the MALTA Winding Realizations	72
4.5	Machine Design	73
4.6	MALTA Prototype	79
4.7	Machine Constant Measurement Results	83
4.8	Summary	93
5	Linear Machine Inverter Supply and Position Sensor	95
5.1	Introduction	95
5.2	MALTA Inverter Supply	95
5.3	MALTA Position Sensor	98
5.4	Summary	102
6	Dynamic Model and Controller Design of the Linear Machine	103
6.1	Introduction	103
6.2	MALTA System Model	105
6.3	Mechanical Model	107
6.4	Position Sensor Model	112
6.5	Electrical Model	113
6.6	MALTA Mechanical Model Linearization	121
6.7	Position Controller Design	127
6.8	Current Controller	133
6.9	Summary	134
7	Experimental Analysis of the Linear Machine	135
7.1	Introduction	135
7.2	Axial Reference Tracking	136
7.3	Steady-State Positioning Performance	139
7.4	Mover Tilting Capability	140
7.5	Summary	142
8	Design of the Double Stator Machine	143
8.1	Introduction	143
8.2	Machine Topology	144
8.3	Optimization and Design Space	147
8.4	Pareto Plots and Selection of the Optimum Design	158

8.5	Winding Design	162
8.6	Prototype Manufacturing	166
9	Inverter Supply and Position Sensor of the Double Stator Machine	179
9.1	Inverter Design Considerations	179
9.2	Position Sensor Design	186
9.3	Radial Position Sensor	186
9.4	Circumferential Position Sensor	193
9.5	Linear Position Sensor	193
9.6	Summary	195
10	Controller Design of the Double Stator Machine	197
10.1	Overview of the DS LiRA Winding Systems	197
10.2	Current Controller of the Rotary Stator	199
10.3	Current Controller of the Linear Stator	200
10.4	Position Controller	203
10.5	Summary	205
11	Experimental Analysis of the Double Stator Machine	207
11.1	Introduction	207
11.2	Current Control	207
11.3	Linear Position Controller	210
11.4	Rotation and Magnetic Bearing Controller	213
11.5	Summary	217
12	Conclusion and Outlook	219
12.1	Summary	219
12.2	Outlook	223
	Appendices	227
A	MALTA SISO Position Controller	229
A.1	MALTA Control Algorithm	229
A.2	Measurements and Results	234
A.3	Soft Start-Up	234
A.4	Linear Motor Operation	237
A.5	Summary	239

B	Double Stator Machine with a Single Set of PMs	241
B.1	Introduction	241
B.2	Proposed Double Stator Actuator	243
B.3	Basic Characteristics of the Conventional and Proposed Double Stator Actuators	246
B.4	Manufacturing of the Proposed Double Stator Actuator	250
B.5	Simplified Planar Hardware Setup	257
B.6	Summary	261
	Bibliography	263
	Curriculum Vitae	277

Introduction

1.1 Motivation and Applications

Linear-Rotary Actuator (LiRA)

Linear-rotary machines/motors/actuators¹ (LiRAs) are used in many industrial areas where combined linear and rotary motion is necessary to allow and automatize manufacturing and packaging of different products. Those industries are: food industry, automotive industry (assembling of parts), semiconductor and electronics industries, medical and pharmaceutical industries, to mention a few. Even though, coupled linear and rotary motion addresses many needs in industry, still the motion systems are built from separate linear and rotary motors/actuators [1–12]. More often they are realized by parallel mechanical coupling, where e.g. the linear actuator moves the whole rotary actuator (its stator and rotor), as shown in **Fig. 1.1(a)**. The drawbacks of this coupling option are limited dynamics (as the linear actuator moves the mass of the whole rotary actuator), moving cables of the rotary actuator and increased size of the overall LiRA. Less often, the LiRA with series mechanical coupling of the linear and rotary actuators can be found in industry [13], cf. **Fig. 1.1(b)**. Such realization allows higher dynamics due to smaller moving mass compared to the parallel mechanical coupling, but, the overall LiRA may have increased length as the linear and the rotary stators are axially displaced. Therefore, in applications where the LiRA length is limited, the stators could be displaced radially instead of axially, which results in a so called double stator (DS) LiRA [14], [15], cf. **Fig. 1.1(c)**. The challenge in realizing such

¹The terms *machine*, *motor* and *actuator* are used equally in this thesis. Typically, in motion control systems where a motor is operated from a certain fixed position reference to another one it is called an actuator.

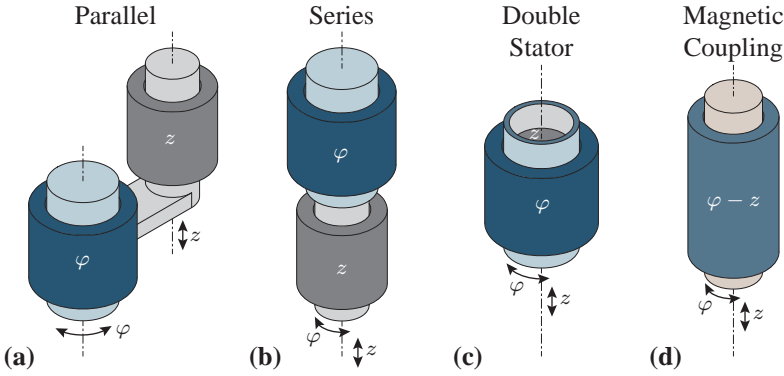


Fig. 1.1: Linear-rotary actuator (LiRA) realization options: (a) parallel mechanical coupling, (b) series mechanical coupling, (c) double stator (DS) LiRA with the stators displaced radially, in particular with the inner linear and outer rotary stator and (d) LiRA with a single stator that can realize linear and rotary motion.

actuator is increased effort in manufacturing due to mechanical support of the inner stator. The LiRA that can realize linear and rotary motion with a single stator is typically realized as so called *checkerboard* actuator [16], [17], cf. **Fig. 1.1(d)**. This actuator may achieve the highest compactness, reliability, robustness and simplified motor assembly into the final product due to fewer mechanical parts. But, in the stator the linear and the rotary motions are magnetically coupled. Consequently, the magnetically coupled LiRA has a higher number of phases (than e.g. the actuators with parallel or series coupling that may be realized with three-phase stators) and requires a more complex current control [18], [19].

Magnetic Bearing (MB)

A magnetic bearing (MB) is an electrical machine which, unlike rotary or linear machines that generate torque or linear force, generates radial force on the rotor² with the goal to magnetically support it such that it hovers without touching the stator. Therefore, MBs have the same role as any other conventional bearings (mechanical or air bearings), to support the rotor with respect to the stator of an electric machine. Of course, as the MBs require

²The rotating part in rotary machines is called *rotor*, while in linear machines the moving part is called *mover*. Since in the thesis linear-rotary machines are analyzed, both terms are used interchangeably and equally.

radial position sensors, amplifiers and controllers, the realization effort and the price are usually higher. But, due to advantageous properties that MBs offer, in certain applications MBs may result in a cheaper overall system, e.g. in case of pipeline turbo compressors [20] or flywheels [21]. Some of the properties of the MBs that open new application areas and/or enhance the existing ones, cf. [22], are:

- ▶ No mechanical contact, therefore, no need for lubrication and no contaminating wear. Desirable for vacuum systems, clean and sterile rooms and high temperatures.
- ▶ Load capacity (bearing stiffness) may be actively controlled during the operation. Therefore, *dynamics* of the hovering rotor may be controlled.
- ▶ Tilting control of the rotor.
- ▶ Precision in the range of micrometers (depends on the installed position sensor).
- ▶ Low maintenance costs and high lifetime.
- ▶ Important functional element of a *smart machine* - based on the MB states, the operation of the whole machine may be optimized.

Linear-Rotary Actuator with Magnetic Bearings

Even though MBs could bring many advantages, to the author's best knowledge, the LiRA with MBs is not used in industry neither is analyzed in literature. Having in mind the LiRA application areas and the MB properties, the LiRA with MBs would be beneficial in the following applications:

- ▶ *Pick-and-place* robot in electronics and semiconductor manufacturing industries. Typically in such machines, a LiRA is moved in horizontal x - and y -directions by a robot arm (parallel kinematics) or a gantry system, where the rotary and the linear orientation of the placed components are performed by a LiRA. Integrating MBs into a LiRA, the following advantageous properties over a conventional solution would be achieved:
 - Handling *smaller components* since a mover *tilting control* would be possible. As PCB track distances are getting smaller, the footprints of the components are reduced as well. Additionally, the

components are becoming more fragile as a result of the size reduction. Consequently, high accuracy (several micrometers) as well as the capability of mover tilting control are required in order to handle the smaller components, which may only be complied with MBs.

- Decoupling from *thermal expansions* by the mover *radial position control*. The temperature change in the LiRAs parallel kinematics or a gantry system will cause thermal expansions of the parts, which consequently would compromise the precision of the pick-and-place machine. Some of the state-of-the-art industry solutions include water cooling of the parallel kinematics, such that the temperature oscillations are minimized. By integrating MBs into the LiRA, this issue can be avoided as any position disturbance in x - and y -directions would be compensated by MBs. Like this, the precision is absolutely decoupled from any thermal expansions and only determined by the precision of the LiRAs radial position sensor.
- *Contamination and wear free* for clean rooms in semiconductor manufacturing. The mover of the LiRA with MBs would not touch at any point the stator and its position would be solely controlled by the magnetic forces. Therefore, its operation would not generate any contaminating particles that might compromise the air purity in clean rooms.
- *High-pressure wash-downs* of LiRAs in food/pharmaceutical industry. In some parts of food and pharmaceutical industries, the used LiRAs require daily washing with highly pressurized water. This requires the mechanical bearings to be detached and attached again after the washing (*wash-downs*). The LiRA with MBs can have the stator and the mover sealed in stainless steel as two separate pieces, where any detaching/attaching of the bearings would not be required to perform the washing. This would result in much shorter and fully automatized wash-downs.

In all cases, the MBs would increase the LiRAs lifetime and reduce maintenance costs, which are mainly driven by mechanical bearing failures.

From the above mentioned advantages, there is a clear motivation to develop a LiRA with integrated MBs, which due to its properties would have a superior performance compared to the conventional solutions in many application areas.

1.2 Challenges

In previous **Section 1.1**, an integration of MBs into a LiRA is motivated by the benefits it would bring to the performance of the LiRA system. The challenges that this integration poses are considered in this section.

- ▶ **Actuator realization:** As it can be seen in **Fig. 1.1**, there are many options for the LiRA realization. The mechanical coupling of the two actuators may result in a large and bulky LiRA (parallel mechanical coupling) or in a compact magnetically coupled LiRA. Integration of the MBs into the LiRA would in this sense represent an addition of a “third” actuator (that actuates in radial direction). To make things worse, the LiRA requires at least two MBs, such that tilting control of the mover is possible. Therefore, it is a challenge to find a realization of the LiRA with MBs that best suits to a specific application. Typical compromises here are between the dynamics (mover’s rotary and linear accelerations) and the maximum torque and the linear force, as the actuator with a larger volume would have higher torque/force, but limited dynamics due to increased moving mass.
- ▶ **Number of actuator phases:** To control the linear and the rotary motion of a LiRA, separately and independently, two power supplies for each motion mode are needed. If the individual actuators are three-phase and magnetically decoupled, the supply inverter should have at least six phases. If the LiRA is magnetically coupled (cf. checkerboard stator in **Fig. 2.3**), the required number of phases in the inverter supply is nine. If now on top of this, two MB machines should be integrated into the LiRA, the number of required phases of the supply inverter would further increase. This aspect should be carefully considered in the design, as it increases the cost and complexity of the overall actuator system.
- ▶ **Position sensors:** The LiRA with MBs should have rotary and linear position sensors, as well as two radial position sensors. Ultimately, the position sensor should not compromise the compactness of the overall LiRA. This becomes a challenge, since a typical size of a LiRA is, e.g. ~ 15 cm in length and ~ 10 cm in width. Typically, in lower cost applications, Hall-effect sensors are used as rotary and linear position sensors, which sense the PM field from the mover and estimate its position. It becomes challenging to estimate the position of the mover when it can move radially, since this would also change the detected

PM field and disturb the desired rotary and linear position estimation. Another challenge is the usage of encoders for the linear and rotary positions, which are required for high precision applications (below μm). Namely, encoders have very narrow radial tolerance, i.e. the distance between the encoder head and the sensing grid should not vary more than $100\ \mu\text{m}$ typically, and this value may be easily exceeded when the LiRA's mover is tilted.

- ▶ **Control system:** It should be kept in mind that the mover of a LiRA with MBs is entirely supported by magnetic forces that are controlled with a position controller. The design of such position controller is challenging since it cannot be generalized, as its requirements depend on the specific LiRA's geometry and application in which it is used.
- ▶ **Cost:** In order to find its way to an application in industry, the investment into the LiRA with MBs must pay off. Therefore, a careful cost analysis of the LiRA is necessary, which was not conducted in this thesis due to lack and confidentiality of price information. But, it should be mentioned that savings compared to conventional solutions would be possible. For example, in a pick-and-place high-precision robot application, the water cooling of parallel kinematics may be removed if a LiRA with MBs is used. Another example would be applications with wash-downs, where cost savings would be achieved with shorter and simpler wash-down procedures that would be possible if a LiRA with MBs is used.

1.3 Scientific Contributions of the Thesis

The main contributions presented in the thesis are summarized below:

- ▶ An overview of possible realization concepts of linear-rotary actuators suitable to implement magnetic bearings is given. Moreover, fundamental scaling laws concerning achievable axial forces and torques of linear and rotary actuators are derived, which enable a qualitative comparison that helps to figure out the most suitable actuator concept.
- ▶ A generic complex space vector modeling of linear-rotary machines (actuators) is introduced. The linear-rotary machine complex space vector is formed by a proposed transformation with two complex frames, where one frame is used for the rotation and MBs and the other for

the linear motion. These two complex reference frames require two different complex units (e.g. i and j), which results in a complex space vector having four components (two real and two complex).

- ▶ A novel linear self-bearing actuator, also called magnetically levitated tubular actuator (MALTA) is proposed. This actuator is capable of generating the drive force and the bearing force on the mover with a single set of stator windings, i.e. the same windings are used for generating both forces. With this approach, the utility of the used materials (copper, iron and PMs) is minimized and compactness of the actuator is preserved when MBs are integrated, compared to the conventional tubular linear actuator without MBs.
- ▶ A decoupling transformation for the MALTA, which is necessary due to magnetic coupling of the linear motion and magnetic bearings, is proposed.
- ▶ A hardware implementation of the MALTA prototype is performed, that in addition required the design and manufacturing of an 18 phase inverter, linear and radial position sensor design and manufacturing, test bench design and manufacturing, position and current control system design and implementation.
- ▶ Taken measurement results prove the new linear actuator concept (MALTA). In addition, mover tilting control measurement results are taken that show MALTA's superior advantage compared to any conventional linear actuator for pick-and-place robot application.
- ▶ Magnetic bearings (MBs) are integrated into the double stator (DS) linear-rotary actuator (LiRA), cf. **Fig. 1.1(c)**.
- ▶ Hardware realization of a DS LiRA with MBs that includes FEM optimizations of the DS LiRA coupled with an analytic thermal model; design, optimization and manufacturing of an 18 phase inverter; design and manufacturing of a linear and radial position sensor; design and manufacturing of an advanced test bench and implementation of the control system.
- ▶ Evaluation of the DS LiRA hardware prototype with measurements that validate the proposed actuator concept.

Chapters 4,5,6,7



MALTA

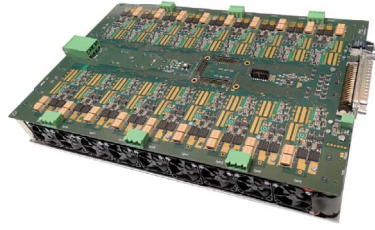


MALTA Inverter

Chapters 8,9,10,11



DS LiRA



DS LiRA Inverter

Fig. 1.2: Overview of the chapters dedicated to the novel linear self-bearing actuator (MALTA): **Chapters 4-7**; double stator (DS) linear-rotary actuator (LiRA): **Chapters 8-11**.

1.4 Outline of the Thesis

The goal of this thesis is the exploration, analysis, optimization and experimental verification of novel tubular actuator topologies with magnetic bearings. Such actuators are not thoroughly analyzed in literature, therefore, this thesis deals with their various aspects such as viable topology and realizations, minimization of the required number of phases, enhancing current decoupling and complex space vector modeling techniques. Following the motivation and the discussion of application areas of LiRAs, challenges and scientific contributions are outlined in **Chapter 1**.

Chapter 2 and **Chapter 3** are dedicated to the general analysis and modeling of LiRAs. In particular, **Chapter 2** identifies possible realization concepts of LiRAs suitable to implement MBs. Moreover, fundamental scaling

laws concerning the achievable force of linear and torque of rotary machines are derived, enabling a qualitative comparison in order to figure out the most suitable actuator concept for given application requirements.

Chapter 3 proposes an enhanced complex space vector based model of the LiRA with MBs, and derives expressions for the torque, linear (thrust) force and the bearing force. A transformation that captures rotary and linear stator quantities by using two complex frames is proposed, which allows for the newly defined complex space vector of voltage, current or flux linkage to capture the information about the torque, MB force and the linear force.

Further chapters are dedicated to the analysis of the MALTA and the DS LiRA, as shown in **Fig. 1.2**.

In **Chapter 4** design and FEM optimization details of the newly proposed MALTA are shown. Moreover, an extensive consideration on the MALTA winding realization is conducted. The designs are verified by measurements of the drive and bearing machine constants in a test bench with force sensors.

Chapter 5 shows the MALTA inverter and the position sensor design details. The resolution of the position sensor and the best signal to noise ratio are given based on measurements on the sensor prototype.

In **Chapter 6** a dynamic electromechanical model of the MALTA is derived. The model is constituted from three sub-models: the nonlinear mechanical model of the mover, the linear model of the position sensor and the linear electric model of the stator. This model allows to develop and design a full state feedback controller, as done and described in the chapter.

Chapter 7 shows the measurement results taken during the MALTA experimental analysis. The MALTA is tested for axial reference tracking and its steady-state positioning performance is given. Moreover, a pick-and-place application scenario is studied, where the tilting control of the mover is demonstrated.

Chapter 8 introduces a DS LiRA with MBs and clarifies the challenges in its design, such as axial heat flow in the inner stator. An automatized optimization procedure, based on coupled FEM magnetic models and analytic thermal models is explained. Supported by Pareto plots, a design of the DS LiRA is chosen and a hardware prototype is manufactured.

In **Chapter 9** the design and prototypes of the DS LiRA inverter and position sensors are shown. The inductor design of the inverter's output LC filter and the heat-sink design are explained. The operation principle of the radial eddy-current sensor is explained and its geometry is optimized.

Chapter 10 shows the concept and the structure of the current and the position controllers of the DS LiRA. The realization of the current controller

is challenging due to many phases that need to be controlled and as well the output filter that requires, besides the DS LiRA current, control of the output capacitor voltage and the inductor current in the filter, resulting in a current controller with three cascaded loops.

In **Chapter 11** the measurement results taken on the DS LiRA prototype are given. In the performed measurements the inverter current control is tested and verified. The operation of the linear and the rotary stators is conducted separately, where the successful operation of the linear and rotary position controllers is shown, as the successful operation of MBs.

Chapter 12 concludes the thesis by summarizing the outcomes of each chapter and gives an outlook for future work in the area.

1.5 Publications

The most relevant publications created as part of this thesis, or in the scope of related projects, are listed in this section in chronological order.

1.5.1 Journal Papers

The papers shown below are published in international journals and are a basis for the creation of this document.

- [J1] **S. Mirić**, P. Küttel, A. Tüysüz, and J. W. Kolar, “Design and Experimental Analysis of a New Magnetically Levitated Tubular Linear Actuator,” *IEEE Transactions on Industrial Electronics*, 2019.
- [J2] **S. Mirić**, R. V. Giuffrida, D. Bortis, and J. W. Kolar, “Enhanced Complex Space Vector Modeling and Control System Design of Multiphase Magnetically Levitated Rotary–Linear Machines,” *IEEE Journal of Emerging and Selected Topics in Power Electronics*, 2019.
- [J3] **S. Mirić**, R. V. Giuffrida, D. Bortis, and J. W. Kolar, “Dynamic Electromechanical Model and Position Controller Design of a New High-Precision Self-Bearing Linear Actuator,” *IEEE Transactions on Industrial Electronics*, 2020.

Furthermore, in the course of the PhD research I also had the opportunity to contribute to the following journal papers:

- [J4] J. A. Anderson, G. Zulauf, P. Papamanolis, S. Hobi, **S. Mirić**, and J. W. Kolar, “Three Levels Are Not Enough: Scaling Laws for Multi-Level Converters in AC/DC Applications,” *IEEE Transactions on Power Electronics*, 2020.
- [J5] M. Haider, J. A. Anderson, **S. Mirić**, N. Nain, G. Zulauf, J. W. Kolar, D. M. Xu and G. Deboy, “Novel ZVS S-TCM Modulation of Three-Phase AC/DC Converters,” *IEEE Open Journal of Power Electronics*, 2020.
- [J6] D. Cittanti, M. Guacci, **S. Mirić**, R. Bojoi, J. W. Kolar, “Analysis and Performance Evaluation of a Three-Phase Sparse Neutral Point Clamped Converter for Industrial Variable Speed Drives,” *Electrical Engineering*, 2021, *Springer*.

1.5.2 Conference Papers

Other core achievements related to this project have been published in the proceedings of international conferences and are partially used for the documentation of this thesis:

- [C1] **S. Mirić**, A. Tüysüz, and J. W. Kolar, “Comparative Evaluation of Linear-Rotary Actuator Topologies for Highly Dynamic Applications,” *Proc. of the IEEE International Electric Machines and Drives Conference (IEMDC)*, Miami, FL, USA, 2017.
- [C2] **S. Mirić**, M. Schuck, A. Tüysüz, and J. W. Kolar, “Double Stator Linear-Rotary Actuator with a Single Set of Mover Magnets,” *Proc. of IEEE Energy Conversion Congress and Exposition (ECCE)*, Portland, OR, USA, 2018.
- [C3] **S. Mirić**, D. Bortis, and J. W. Kolar, “Design and Comparison of Permanent Magnet Self-Bearing Linear-Rotary Actuators,” *Proc. of the 12th International IEEE Symposium on Linear Drives for Industry Applications (LDIA)*, Neuchâtel, Switzerland, 2019.

Additionally, for work on topics that are not in the core area of my PhD research, but I helped in the preliminary studies of the topic and in the writing of the manuscript. I have been recognized as a co-author of:

- [C4] D. Cittanti, **S. Mirić**, M. Guacci, and J. W. Kolar, “Comparative Evaluation of 800 V Three-Phase Three-Level Inverter Concepts,” *Proc. of the International IEEE Conference on Electrical Machines and Systems (ICEMS)*, Hamamatsu, Japan, 2020.

- [C5] R. Giuffrida, **S. Mirić**, D. Bortis, and J. W. Kolar, ““Looking Through Walls” – Actuator Position Measurement Through a Conductive Wall,” *Proc. of the International IEEE Conference on Electrical Machines and Systems (ICEMS)*, Hamamatsu, Japan, 2020.
- [C6] J. W. Kolar, J. Azurza, **S. Mirić**, M. Haider, M. Guacci, M. Antivachis, G. Zulauf, D. Menzi, P. Niklaus, J. Miniböck, P. Papamanolis, G. Rohner, N. Nain, D. Cittanti, D. Bortis, “Application of WBG Power Devices in Future 3-Phase Variable Speed Drive Inverter Systems “How to Handle a Double-Edged Sword”,” *Proc. of the IEEE 66th International Electron Devices Meeting (IEDM)*, San Francisco, USA, 2020.
- [C7] G. Rohner, **S. Mirić**, D. Bortis, J. W. Kolar, M. Schweizer, “Comparative Evaluation of Overload Capability and Rated Power Efficiency of 200V Si/GaN 7-Level FC 3-Phase Variable Speed Drive Inverter Systems,” *Proc. of the IEEE Applied Power Electronics Conference and Exposition (APEC)*, Phoenix, AZ, USA, 2021.

1.5.3 Patents

The most innovative and original outcomes of my PhD research in collaboration with others, which could offer a competitive advantage if commercially exploited, have led to the filing of national and international patent applications. Despite the same title of [P2] and [P3], different actuators are discussed in these patents: [P2] describes the DS LiRA (cf. **Chapter 8**), where [P3] describes the MALTA (cf. **Chapter 4**).

- [P1] **S. Mirić**, A. Tüysüz and J. W. Kolar, “Electrical DC-AC Power Converter,” Swiss patent application, 2017.
- [P2] **S. Mirić**, A. Tüysüz and J. W. Kolar, “Electromechanical Actuator,” EU patent application, 2017.
- [P3] **S. Mirić**, A. Tüysüz, D. Bortis and J. W. Kolar, “Electromechanical Actuator,” EU patent application, 2017.
- [P4] **S. Mirić**, M. Schuck, A. Tüysüz and J. W. Kolar, “Linear-rotatorischer elektromechanischer Aktuator,” Swiss patent application, 2018.
- [P5] J. A. Anderson, M. Haider, **S. Mirić** and J. W. Kolar, “Power Conversion Method and Power Converter,” EU patent application, 2020.

2

Linear-Rotary Machine Realizations and Scaling Laws

To realize a linear-rotary machine that best suits the needs of an application, an overview of possible realizations and their comparison is needed, which is given in this chapter. The material presented in this chapter is further described in [23].

2.1 Introduction

Linear-rotary actuators (LiRAs) are used in many different industries and application areas, for example, in electronics and semiconductor manufacturing industries in pick-and-place robots [24, 25], or in industries such as aerospace or automotive [26–28], food or pharmaceutical. Since LiRAs are used in so many different application areas, they have to meet different torque and/or force requirements, while also a given axial stroke has to be achieved. Consequently, choosing the most suitable actuator for given application specifications is not an easy task. Therefore, in this chapter, torque and force scaling laws that give a quick and clear performance overview of different actuator arrangements are derived and verified with finite element method (FEM) simulations. Compared to scaling law derivations already done in literature [29], also thermal aspects are considered, which show to have a significant influence onto the optimal actuator geometry.

This chapter focuses on permanent magnet (PM) LiRAs, as in general they have the highest power densities [30], but the derived scaling laws can also be applied to reluctance, flux switching or induction machines [25]. Besides the machine type, LiRAs can be realized in many different combinations

of individual actuators, whereby also the coupling of the machines can be versatile, e.g. a parallel or series mechanical coupling, a magnetic coupling (e.g. checkerboard actuator [31]) or a double stator configuration [15,32] can be used. However, as the LiRA with parallel mechanical coupling has a mechanical connection of the linear and rotary actuators [30], with independent rotors (also called 'movers' or 'sliders'), it is not further considered in this work, since it would result in a bulkier and less robust design with lower acceleration performances due to higher moving mass and moment of inertia.

Another important aspect in LiRAs are the bearings. Most of the LiRAs use mechanical bearings, either ball or slider bearings. Besides their high stiffness and simplicity, both of those feature drawbacks, such as the need for lubrication and the particle generation. This is mainly a problem in applications where a high purity is required, e.g. in clean room applications. As an alternative, air bearings could be used, but they require a pressurized air supply and the operation in low pressure environments is prohibited. Accordingly, the mentioned issues can only be solved by magnetic bearings (MBs), which are gaining more and more attention in tubular linear and linear-rotary actuators [33–35].

This chapter first summarizes possible options to realize a LiRA with MBs, and afterwards provides initial design considerations in terms of general scaling laws of electric machines that would help a potential designer to choose a topology suitable to the desired application. In contrast to the existing literature, the derived scaling laws also consider the machine-internal heat flow and the heat transfer to the ambient. Furthermore, the general scaling laws are applicable to any kind of electric machine and are also verified by FEM simulations.

2.2 Actuator Topology Concepts

Depending on the application specifications, the LiRA with magnetic bearings (MB) can be built with different combinations of linear (L) and rotary (R) machines, as shown in **Fig. 2.1**. The considered actuators are divided into two groups, the first that features only an axial stator displacement of the different machines (i.e. linear, rotary or magnetic bearing) with either all interior rotor (cf. **Fig. 2.2(a)**) or all exterior rotor arrangements (cf. **Fig. 2.2(b)**), and the second group featuring a combined stator arrangement, i.e. a double stator LiRA (cf. **Fig. 2.2(c)**).

As can be noticed, for all possible LiRA arrangements always two independent magnetic bearings (MB) on each axial end are required, such that rotor

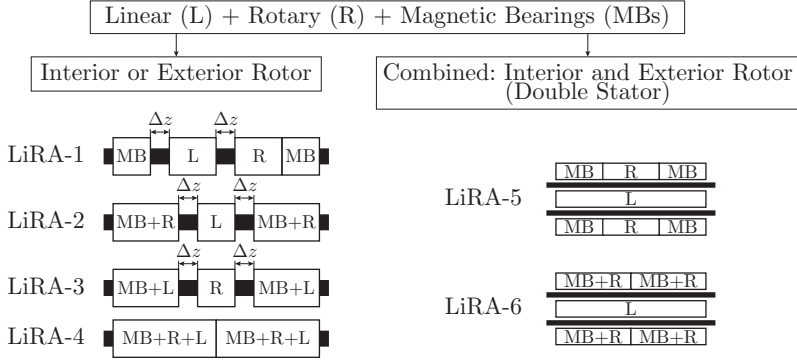


Fig. 2.1: Possible axial combinations of linear machines (L), rotary machines (R) and magnetic bearings (MB) to realize a self-bearing linear-rotary actuator. The possible combinations can be divided into two groups, where the first group uses either only an interior or an exterior rotor, while the second group is using a combined rotor, i.e. a double stator machine.

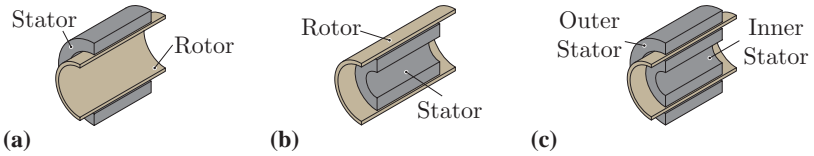


Fig. 2.2: Radial actuator arrangements: **(a)** interior rotor, **(b)** exterior rotor and **(c)** combined rotor featuring two radially displaced stators, also known in literature as double stator motor (cf. [14]).

tilting can be controlled. Furthermore, depending on the degree of integration, the magnetic bearing can be either realized as an independent machine with separate stator (cf. LiRA-1 in **Fig. 2.1**) or can be integrated either into the rotary machine, i.e. a self-bearing rotary machine (MB+R) [36], or into the linear (L) machine (cf. LiRA-2 and LiRA-3 in **Fig. 2.1**), while a full integration of all three machines into a single machine is also possible (cf. LiRA-4 in **Fig. 2.1**). The realization options of these machines are shown in **Fig. 2.3**, where in the first row the different rotor's permanent magnet arrangements and in the second row the corresponding stator's winding configurations are given. As can be noticed, a rotary machine realized with a R-Rotor and R-Stator can also perform self-bearing (MB+R), while a linear machine (L) with L-Rotor and L-Stator doesn't feature magnetic levitation. Hence, the integration of the magnetic bearing into a rotary machine (MB+R) is easier to realize compared to the integration of the MB into a linear machine (MB+L). In order to achieve self-bearing and linear movement in one machine, the L-Rotor must be combined with a CB-Rotor ('Checkerboard-Rotor', cf. [31]), as done in [35]. A further option to realize either a self-bearing rotary machine (MB+R) or a linear machine (L), is to use a S-Rotor ('Square-Magnet-Rotor', cf. [15]) with either a R-Stator or a L-Stator. Finally, to fully integrate all features into a single machine (MB+R+L), a CB-Rotor with the CB-Stator is needed. It should be noted that the same integration concepts (except the full integration) can also be applied to the double stator LiRA (cf. LiRA-5 and LiRA-6 in **Fig. 2.1**) and that the functionalities of the inner and outer stator can also be exchanged, i.e. the linear machine (L) would then be the outer actuator and the magnetic bearing (MB) together with the rotary machine (R) would be the inner actuator.

Another aspect in LiRAs is the maximum axial stroke z_{stroke} that can be achieved with the selected machine arrangement. First of all, it has to be considered that the rotor or mover should be longer than the total stator length for at least z_{stroke} , such that a constant interaction between the stator and the rotor is obtained. Furthermore, it has to be considered that depending on the selected stator and rotor arrangement, a certain distance Δz between the different stators is needed, which in case of an independent linear (L) or rotary (R) machine would have to be $\Delta z = z_{\text{stroke}}$ (cf. LiRA-1 to LiRA-3 in **Fig. 2.1**), while for a fully integrated checkerboard machine or a double stator machine no distance between the stators is needed, i.e. $\Delta z = 0$ (cf. LiRA-4 to LiRA-6 in **Fig. 2.1**). Indeed, LiRAs with an S- or CB-Rotor can be realized with $\Delta z = 0$, however, as will be shown in the following section, they also feature lower torque and force densities due to the inherently lower flux linkage of

	R-Rotor	L-Rotor	S-Rotor	CB-Rotor
Rotor				
	R-Stator	L-Stator	R-Stator or L-Stator	CB-Stator
Stator				
	MB+R	L	MB+R or L	MB+R+L

Fig. 2.3: Viable rotor and stator realization options that can be used for the LiRA design, i.e. R-Rotor and R-Stator to realize a rotary machine which also can perform self-bearing, L-Rotor and L-Stator for the linear machine, S-Rotor ('Square-Magnet-Rotor', cf. [15]) with either R-Stator or L-Stator to realize either a self-bearing rotary machine or a linear machine, and CB-Rotor ('Checkerboard-Rotor', cf. [31]) with CB-Stator to realize a fully integrated machine featuring the linear and rotary movement as well as the magnetic bearing. Furthermore, the L-Rotor can also be in combination with the CB-Stator in order to realize a self-bearing linear machine [35]. These realization concepts are only shown for the interior rotor actuator, but the same winding configuration and permanent magnet arrangement can also be applied for the exterior rotor actuator.

the S-Rotor [15] or the larger end windings of the CB-Stator [16], and therefore finally result in a larger machine volume to achieve the same force and torque performances. For sake of completeness, the LiRA assemblies from **Fig. 2.1** are listed in **Tab. 2.1** for the different rotor and stator realizations given in **Fig. 2.3** and it is shown whether a distance Δz between the stators is needed or not.

In the following section, the scaling laws for the achievable torque and the thrust force of the *Interior Rotor* and *Exterior Rotor* actuator arrangements are derived. In contrast to other literature [29], the current density amplitude \hat{j} is calculated from the thermal (cooling) considerations, which have a significant influence on the achievable torques and forces. The scaling laws are verified with FEM simulations for the stator and rotor realizations shown in **Fig. 2.3**. The considered parameters are given in **Tab. 2.2**.

Furthermore, it is assumed that the thickness of the rotor, the stator back iron, the permanent magnet, and the air gap are identical for all machines

Tab. 2.1: Overview of the LiRA assemblies.

Rotor	Stator	Δz
LiRA-1: (MB, L, R, MB)		
(R, L, R, R)	(R, L, R, R)	z_{stroke}
(S, S, S, S)	(R, L, R, R)	0
LiRA-2: (MB+R, L, MB+R)		
(R, L, R)	(R, L, R)	z_{stroke}
(S, S, S)	(R, L, R)	0
LiRA-3: (MB+L, R, MB+L)		
(L, R, L)	(CB, R, CB)	z_{stroke}
(S, S, S)	(CB, R, CB)	0
LiRA-4: (MB+R+L, MB+R+L)		
(CB, CB)	(CB,CB)	0
LiRA-5: (MB, R, MB / L)		
(R, R, R / L)	(R, R, R / L)	0
(S, S, S / S)	(R, R, R / L)	0
LiRA-6: (MB+R, MB+R / L)		
(R, R / L)	(R, R / L)	0
(S, S / S)	(R, R / L)	0

and much smaller than the outer dimensions (r , R and L). Moreover, also the air gap flux density B_{ag} is fixed to a constant value for all machines.

In [29], the current density amplitude \hat{J} is assumed to be constant. This work extends the approach and \hat{J} is calculated from the thermal (cooling) considerations, which, as shown later, significantly influence the achievable torque and force.

2.3 Interior Rotor Scaling Laws

2.3.1 Torque Scaling Law

According to the fundamental expression for 3-phase permanent magnet electric machines, the torque magnitude T_{int} is proportional to the product of the flux linkage $\hat{\Psi}$ and the current amplitude \hat{I}_{int} of the symmetric 3-phase winding system, i.e. $T_{\text{int}} \sim \hat{\Psi} \hat{I}_{\text{int}}$. The flux linkage $\hat{\Psi}$ is the total flux linked with the N turns of the stator winding. Therefore, the flux $\hat{\Phi}$ that penetrates the stator from the air gap is N times smaller, i.e. $\hat{\Psi} = N\hat{\Phi}$, and consequently the torque is proportional to $T_{\text{int}} \sim \hat{\Phi} \cdot N\hat{I}_{\text{int}}$. Furthermore, $\hat{\Phi}$ is proportional to the flux density in the air gap B_{ag} and the air gap area A_{ag} , while $N\hat{I}_{\text{int}}$ represents the magnetomotive force, which can be written as the product of

the current density amplitude \hat{j}_{int} and the winding area A_w , i.e. $N\hat{I}_{\text{int}} = \hat{j}_{\text{int}}A_w$. Finally, the torque is proportional to $T_{\text{int}} \sim A_{\text{ag}}A_wB_{\text{ag}}\hat{j}_{\text{int}}$.

The air gap and winding areas, A_{ag} and A_w , can be further expressed by the geometrical parameters R and r (the outer and inner radii of the winding volume) shown in **Fig. 2.4(a)**. For the air gap area the expression $A_{\text{ag}} \sim rL$ is applied, where L equals the assumed stator length, and for the winding area the expression $A_w \sim (R^2 - r^2)$ is used. Since in the conducted analysis, the air gap flux density B_{ag} is assumed to be constant, the torque can be scaled as $T_{\text{int}} \sim r(R^2 - r^2)L \cdot \hat{j}_{\text{int}}$ which corresponds with the scaling law deduced in [29]. If a relative parameter $x_r = r/R$ is introduced, the torque is obtained as

$$T_{\text{int}} = K_T \cdot R^3 L \cdot x_r (1 - x_r^2) \cdot \hat{j}_{\text{int}}, \quad (2.1)$$

Tab. 2.2: Parameters used in FEM simulations.

Parameter Name	Value/Expression
Geometrical	
Length (L)	100 mm
Outer Radius (R)	100 mm
Rotor Back Iron Thickness	2 mm
Stator Back Iron Thickness	2 mm
PM Thickness	2 mm
Number of Rotor Poles for Rotation	16(8)*
Number of Rotor Poles for Linear Motion	16(8)*
Number of Stator Teeth for Rotation	6
Number of Stator Teeth for Linear Motion	12
Total LiRA Volume (V)	$\pi R^2 L$
Stator Volume (V_{stator})	$\pi(R^2 - r^2)L$
Relative Winding Radial Size (x_r)	r/R
Magnetic / Electrical	
PM Remanent Flux Density	1.3 T
Rotor/Stator Core Relative Permeability	10 000
Copper Specific Electric Resistance at T_w (ρ_{cu})	$2.36 \times 10^{-8} \Omega \text{ m}$
Relative Copper Volume ($k_{\text{cu}} = V_{\text{cu}}/V_{\text{stator}}$)	0.36
Current Density Constant (K_j)	$2\sqrt{\Delta T/(\rho_{\text{cu}}k_{\text{cu}})}$
Thermal	
Winding Temperature (T_w)	120 °C
Ambient Temperature (T_{amb})	40 °C
Temperature Difference (ΔT)	$T_w - T_{\text{amb}}$
Heat Transfer Coefficient (h)	10 W/(K m ²)
Winding Thermal Conductivity (λ_w)**	2 W/(K m)
Iron Core Thermal Conductivity (λ_{fe})	22 W/(K m)

*Pole number values for S-{Rotor} are in brackets.

**Measured value, see [37].

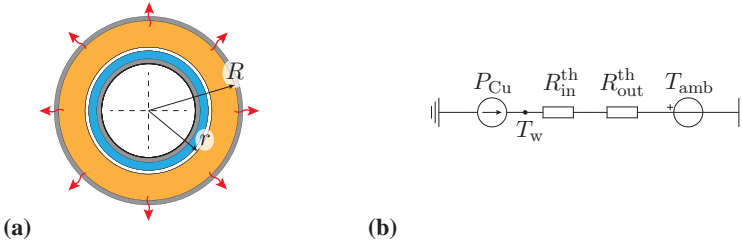


Fig. 2.4: (a) Cross section of the *Interior Rotor* actuator with outer and inner radii, R and r , of the actuator stator winding volume, and (b) the assumed lumped-parameter steady-state thermal model of the actuator with interior rotor.

where K_T is an absolute torque constant that is given in **Tab. 2.3** for the analyzed LiRAs.

As already mentioned, in contrast to the constant current density amplitude \hat{j}_{int} assumed in [29], in the following a loss-dependent current density $\hat{j}_{int} = \hat{j}_{int}(P_{cu})$ is considered, which is given by the maximum allowed copper losses P_{cu} in the stator windings. Based on the $P_{cu} = 1/2 R_{cu} \hat{j}_{int}^2$, the current density can be expressed as $\hat{j}_{int} = \sqrt{(2P_{cu})/(\rho_{cu} V_{cu})}$, where ρ_{cu} is the specific resistance of copper and V_{cu} the copper volume of the stator, which is given as $V_{cu} = k_{cu} V_{stator}$ (cf. **Tab. 2.2**).

The allowed copper losses P_{cu} are deduced from the actuator's thermal properties, whereby the two heat transfer modes are considered: (1) radial heat flow through the windings by thermal conduction, modelled by the thermal resistance R_{in}^{th} and (2) radial heat convection on the outer surface of the actuator to the environment, modelled by the thermal resistance R_{out}^{th} , which assumes a certain loss per surface area. The two thermal resistances can be obtained as

$$R_{in}^{th} = \frac{1}{\lambda_w} \frac{\ln(R/r)}{2\pi L}, \quad R_{out}^{th} = \frac{1}{h} \frac{1}{2\pi RL}, \quad (2.2)$$

where λ_w is the specific thermal conductivity of the winding and h is the heat transfer coefficient from the actuator's outer surface to the environment (cf. **Tab. 2.2**). The assumed thermal model is shown in **Fig. 2.4(b)**. The allowed copper losses are obtained as $P_{cu} = \Delta T / (R_{in}^{th} + R_{out}^{th})$.

The copper volume can be calculated as $V_{cu} = k_{cu} \cdot \pi(R^2 - r^2)L$, where k_{cu} is considering the amount of copper volume relative to the total stator volume. Assuming a winding fill factor equal to 0.6 and winding volume

to stator volume ratio of 0.6, i.e. 60% while 40% is iron), k_{cu} is calculated as $k_{\text{cu}} = 0.6 \cdot 0.6 = 0.36$ (cf. **Tab. 2.2**).

Accordingly, the current density amplitude is calculated as

$$\hat{J}_{\text{int}} = K_J \cdot \frac{1}{R} \frac{1}{\sqrt{1-x_r^2}} \frac{1}{\sqrt{\frac{\ln(1/x_r)}{\lambda_w} + \frac{1}{hR}}}, \quad (2.3)$$

where K_J is given in **Tab. 2.2**.

The loss- and geometry-dependent current density \hat{J}_{int} can now be used in (2.3), in order to obtain the expression for the loss- and geometry-dependent torque T_{int} of the interior rotor actuator. Another important quantity is the torque density $t_{\text{int}} = T_{\text{int}}/V$, which equals the torque T_{int} divided by the total rotary actuator volume V (cf. **Tab. 2.2**) and results in the following expression

$$t_{\text{int}} = \frac{K_T K_J}{\pi} \cdot x_r \sqrt{1-x_r^2} \cdot \frac{1}{\sqrt{\frac{\ln(1/x_r)}{\lambda_w} + \frac{1}{hR}}}. \quad (2.4)$$

The first factor is constant, while the second term only depends on the relative quantity x_r . The last factor, which comes from the thermal considerations, depends on both, the relative parameter x_r and the absolute parameter R . Additionally, the last factor depends on the thermal parameters λ_w and h . In order to examine the influence of these two thermal parameters, the extreme cases when $\lambda_w \rightarrow \infty$ or $h \rightarrow \infty$ are analyzed. Both cases can be physically interpreted and are shown in **Fig. 2.5(a)**.

If $\lambda_w \rightarrow \infty$, then $R_{\text{in}}^{\text{th}} \rightarrow 0$, which means that the temperature drop inside the windings can be neglected. This can be related to the scenario in which the heat transfer coefficient h is low (e.g. natural air cooling), i.e. heat transfer to the ambient is so low such that the temperature drop inside the winding becomes negligible. In this scenario, the torque density t_{int} depends on the absolute value of the outer radius as $t_{\text{int}} \sim \sqrt{R}$ and its maximum is achieved for $x_r = 0.707$ (maximum of the function $x_r \sqrt{1-x_r^2}$, cf. red curve in **Fig. 2.5(a)**).

If $h \rightarrow \infty$, then $R_{\text{out}}^{\text{th}} \rightarrow 0$, which means the case temperature of the actuator is fixed. This corresponds to the scenario where the heat transfer coefficient h would be very high (e.g. water cooling), such that the main temperature drop occurs inside the machine. This is represented with the green curve in **Fig. 2.5(a)**, which is a monotonically increasing function, since in case the windings get thinner (increasing x_r), the thermal resistance $R_{\text{in}}^{\text{th}}$ of the winding in radial direction is decreasing. Consequently, more copper losses can be dissipated and a higher torque can be generated.

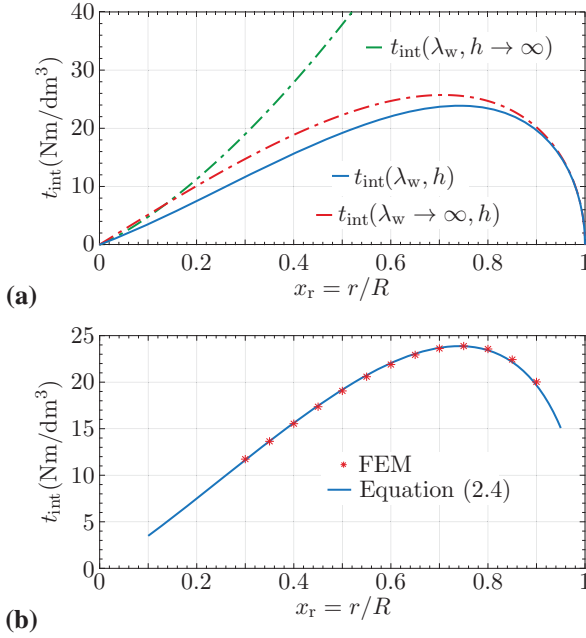


Fig. 2.5: Scaling law of the achievable torque density for the *Interior Rotor* actuator. **(a)** Overall torque density t_{int} (blue), and for the cases where either $\lambda_w \rightarrow \infty$ (red) or $h \rightarrow \infty$ (green). **(b)** Verification of the analytically derived torque density t_{int} with FEM simulations. The parameters used in the simulation are given in **Tab. 2.2**.

The curve that considers both, inner and outer thermal resistances, is always below the curves of the discussed scenarios (cf. **Fig. 2.5(a)**), as it is limited by both thermal resistances. This curve is also verified with FEM simulations as shown in **Fig. 2.5(b)**.

2.3.2 Thrust Force Scaling Law

Similar to the torque, the thrust (axial or drive) force F_{int} is proportional to the flux linkage and the 3-phase current amplitude, $F_{\text{int}} \sim \hat{\Psi} \hat{I}_{\text{int}}$ and therefore is proportional to $F_{\text{int}} \sim A_{\text{ag}} A_{\text{w}} B_{\text{ag}} \hat{J}_{\text{int}}$. The air gap and winding areas, A_{ag} and A_{w} , can be deduced by using the geometrical parameters R and r from **Fig. 2.4(a)**. Similar to the derivation from **Section 2.3.1**, $A_{\text{ag}} \sim rL$, while the winding area is $A_{\text{w}} \sim (R - r)L$. Assuming the air gap flux density B_{ag} to be constant, the force is proportional to $F_{\text{int}} \sim r(R - r)L^2 \cdot \hat{J}_{\text{int}}$, and by using the same relative parameter x_r , can be written as

$$F_{\text{int}} = K_F \cdot R^2 L^2 \cdot x_r (1 - x_r) \cdot \hat{J}_{\text{int}}, \quad (2.5)$$

where K_F is an absolute axial force constant that is given in **Tab. 2.3** for the analyzed LiRAs.

The cooling properties are assumed to be the same as in the case of the rotary actuator, thus the current density \hat{J}_{int} is also given with (2.3) and can be inserted into (2.5). Similar to the torque density, the force density f_{int} can be derived by dividing the force F_{int} by the total linear actuator volume V (cf. **Tab. 2.2**), which results in

$$f_{\text{int}} = \frac{K_F K_J}{\pi} \cdot \frac{L}{R} \cdot x_r \sqrt{\frac{1 - x_r}{1 + x_r}} \cdot \frac{1}{\sqrt{\frac{\ln(1/x_r)}{\lambda_w} + \frac{1}{hR}}}. \quad (2.6)$$

Compared to the torque density in (2.4), the force density has a factor L/R , which means that the force density is increasing with a decreasing actuator's outer radius. Hence, linear actuators (motors) are typically built with rather high length over radius (L/R) ratios.

The last factor in (2.6), which considers the thermal properties of the machine, is the same as the one in (2.4), therefore a discussion similar to **Section 2.3.1** is conducted here.

If $\lambda_w \rightarrow \infty$, the force density depends on the absolute outer radius and length as $f_{\text{int}} \sim L/\sqrt{R}$. The influence of the relative parameter x_r is reduced to $f_{\text{int}} \sim x_r \sqrt{(1 - x_r)/(1 + x_r)}$, which is shown in **Fig. 2.6(a)** with the red curve

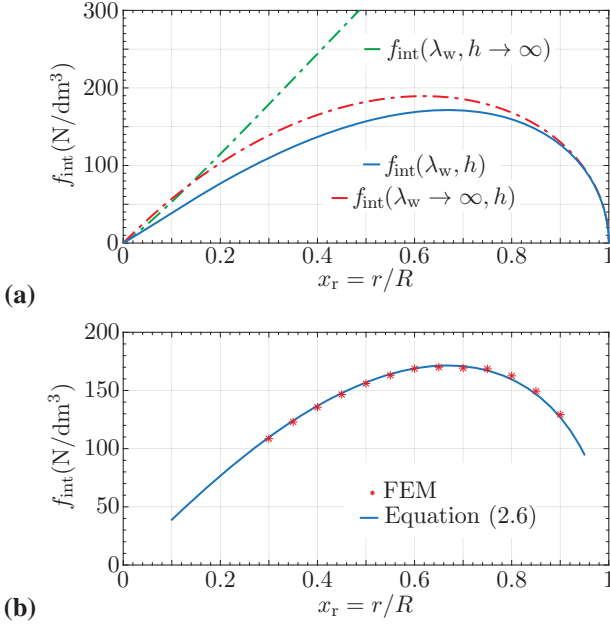


Fig. 2.6: Scaling law of the achievable force density for the *Interior Rotor* actuator. **(a)** Overall force density f_{int} (blue), and for the cases where either $\lambda_w \rightarrow \infty$ (red) or $h \rightarrow \infty$ (green). **(b)** Verification of the analytically derived force density f_{int} with FEM simulations. The parameters used in the simulation are given in **Tab. 2.2**.

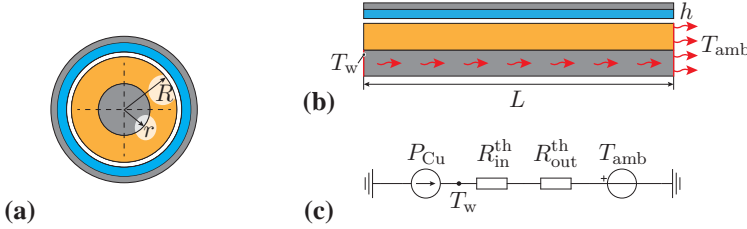


Fig. 2.7: Tubular linear-rotary actuator with *Exterior Rotor* with (a) radial and (b) axial cross sections. Based on the axial mounting of the interior stator, only axial heat flow is assumed and denoted with the red arrows. (c) Corresponding lumped parameter steady-state thermal model.

$f_{int}(\lambda \rightarrow \infty, h)$. In this scenario, the maximum force density is achieved for $x_r = 0.618$.

If $h \rightarrow \infty$, the force density depends on the absolute outer radius and length as $f_{int} \sim L/R$, and in addition is again monotonically increasing with the relative parameter x_r . Again, the curve that considers both heat transfer coefficients λ_w and h is always smaller than the curves where only one of these parameters is considered. The verification with FEM simulations is shown in Fig. 2.6(b).

2.4 Exterior Rotor Scaling Laws

2.4.1 Torque Scaling Law

In analogy to the actuator with interior rotor, the torque T_{ext} of the actuator with exterior rotor is proportional to $T_{ext} \sim A_{ag} A_w B_{ag} \hat{j}_{ext}$. Based on the geometric dimensions given in Fig. 2.7, the air gap area can be expressed by $A_{ag} \sim RL$, and the winding area by $A_w \sim (R^2 - r^2)$. Moreover, with a constant air gap flux density B_{ag} , the torque is calculated as $T_{ext} \sim R(R^2 - r^2)L \cdot \hat{j}_{ext}$. Finally, using the relative parameter $x_r = r/R$, the torque becomes

$$T_{ext} = K_T \cdot R^3 L \cdot (1 - x_r^2) \cdot \hat{j}_{ext}, \quad (2.7)$$

where K_T is again the absolute torque constant given in Tab. 2.3.

For the exterior rotor actuator, i.e. interior stator actuator, the stator can only be mechanically fixed at one of the axial ends, therefore leading to an axial heat flow in the actuator (cf. Fig. 2.7(b)). The end with the mechanical fixation

is assumed to have a heatsink with an area equal to πR^2 and a heat transfer coefficient h , which results in an outer thermal resistance $R_{\text{out}}^{\text{th}}$ (cf. **Fig. 2.7(c)**). Accordingly, due to the axial heat flow, the hot spot temperature is on the opposite axial end, with the temperature T_w (cf. **Fig. 2.7(b)**). It is assumed that the axial heat flow occurs only in the stator back iron (cylinder with the radius r), while it is neglected through the winding volume, since the thermal conductivity in the winding is mainly inhibited by the poor conductance of the wire isolation and potting material ($\lambda_{\text{fe}}/\lambda_w \sim 10$). Furthermore, as the copper losses P_{cu} are distributed in the winding volume, the heat generation is also spatially distributed along the stator, resulting in an inner thermal resistance $R_{\text{in}}^{\text{th}}$ to be half of the total back iron's thermal resistance $R_{\text{fe}}^{\text{th}}$, i.e. $R_{\text{in}}^{\text{th}} = R_{\text{fe}}^{\text{th}}/2$. Accordingly, the thermal resistances for the tubular actuator with the exterior rotor can be calculated as

$$R_{\text{in}}^{\text{th}} = \frac{1}{2\lambda_{\text{fe}}} \frac{L}{\pi r^2}, \quad R_{\text{out}}^{\text{th}} = \frac{1}{h} \frac{1}{\pi R^2}, \quad (2.8)$$

where λ_{fe} is the thermal conductivity of iron given in **Tab. 2.2**. Applying the same considerations as in **Section 2.3.1**, the allowed current density is obtained as

$$\hat{J}_{\text{ext}} = K_J \cdot \frac{1}{\sqrt{L}} \cdot \frac{1}{\sqrt{1-x_r^2}} \cdot \frac{1}{\sqrt{\frac{1}{\lambda_{\text{fe}}} \frac{L}{x_r^2} + \frac{2}{h}}}, \quad (2.9)$$

where K_J is given in **Tab. 2.2**. Inserting this equation into (2.7) and dividing it by the rotary actuator volume V (cf. **Tab. 2.2**), the following expression is obtained for the torque density

$$t_{\text{ext}} = \frac{K_T K_J}{\pi} \cdot \frac{R}{\sqrt{L}} \cdot \sqrt{1-x_r^2} \cdot \frac{1}{\sqrt{\frac{1}{\lambda_{\text{fe}}} \frac{L}{x_r^2} + \frac{2}{h}}}. \quad (2.10)$$

As can be noticed, the torque density t_{ext} depends on the ratio of the absolute outer dimensions R and L , which means that making the actuator longer, reduces the torque density due to the worse axial heat flow. Similarly to **Section 2.3.1**, the two extreme scenarios $h \rightarrow \infty$ or $\lambda_{\text{fe}} \rightarrow \infty$ can be analyzed (cf. **Fig. 2.8(a)**).

Again, the scaling law considering both thermal parameters is verified with FEM simulations as shown in **Fig. 2.8(b)**.

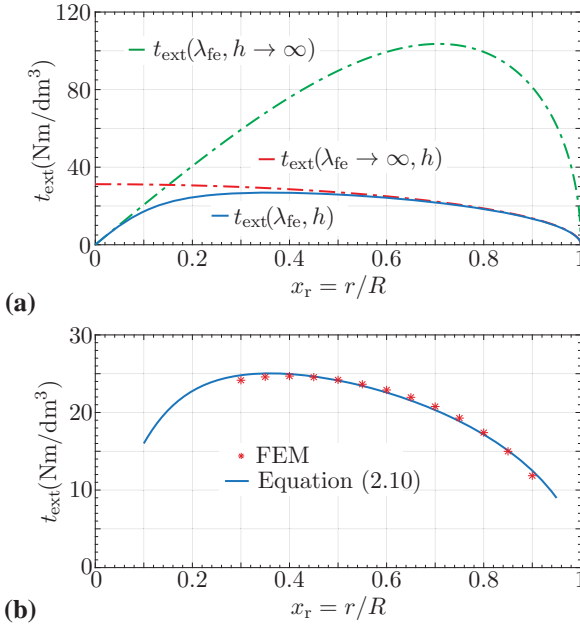


Fig. 2.8: Scaling law of the achievable torque for the *Exterior Rotor* actuator. **(a)** Overall torque density t_{ext} (blue), and influence of the thermal parameters λ_{fe} (red) and h (green) onto the torque density t_{ext} . **(b)** Torque density t_{ext} verified with FEM simulation with parameters given in **Tab. 2.2**.

Tab. 2.3: Scaling law constants determined by FEM simulations.

Rotor	Stator	K_T (N/(A m ³))	K_F (N/(A m ²))
Interior Rotor			
R	R	0.83	-
S	R	0.35	-
L	L	-	0.93
S	L	-	0.48
Exterior Rotor			
R	R	0.71	-
L	L	-	0.99

2.4.2 Thrust Force Scaling Law

In analogy to the derivation done for the interior rotor, the thrust force F_{ext} is given as $F_{\text{ext}} \sim A_{\text{ag}} A_w B_{\text{ag}} \hat{J}_{\text{ext}}$. The air gap and the winding areas are again proportional to $A_{\text{ag}} \sim RL$ and $A_w \sim (R - r)L$ and with the assumption of a constant air gap flux density B_{ag} , the force is proportional to $F_{\text{ext}} \sim R(R - r)L^2 \cdot \hat{J}_{\text{ext}}$. By using $x_r = r/R$, the previous expression can be written as

$$F_{\text{ext}} = K_F \cdot R^2 L^2 \cdot (1 - x_r) \cdot \hat{J}_{\text{ext}}, \quad (2.11)$$

where K_F is the force constant and the current density is given with (2.9). Hence, the force density for the tubular actuator with exterior rotor is obtained as

$$f_{\text{ext}} = \frac{K_F K_J}{\pi} \cdot \sqrt{L} \cdot \sqrt{\frac{1 - x_r}{1 + x_r}} \cdot \frac{1}{\sqrt{\frac{1}{\lambda_{\text{fe}}} \frac{L}{x_r^2} + \frac{2}{h}}}. \quad (2.12)$$

The force density f_{ext} only depends on the absolute length L and increases when the length L of the actuator increases. The influence of the thermal parameters λ_{fe} and h is analyzed and shown in **Fig. 2.9(a)**, while the verification by FEM simulation is shown in **Fig. 2.9(b)**.

In general, for the tubular actuator with exterior rotor and therefore internal axial heat flow, the consideration of the thermal aspects is very important, since they influence the actuator geometry significantly as shown in **Fig. 2.8(a)** and **Fig. 2.9(a)**.

2.5 Scaling Law Constants

In this section, the absolute values of the scaling law constants K_T and K_F are given and briefly discussed. **Tab. 2.3** summarizes the constants for the

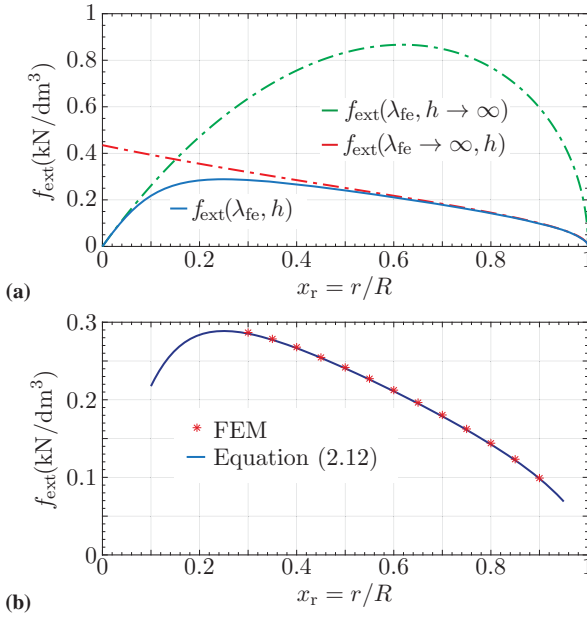


Fig. 2.9: Scaling law of the achievable force for the *Exterior Rotor* actuator. **(a)** Overall force density f_{ext} (blue), and influence of the thermal parameters λ_{fe} (red) and h (green) onto the force density f_{ext} . **(b)** Force density f_{ext} verified with FEM simulations with parameters given in **Tab. 2.2**.

actuators with {R,L,S}-Rotor and {R,L}-Stator for the interior rotor and with {R,L}-Rotor and {R,L}-Stator for the exterior rotor. The actuator constants for the rest of the actuator arrangements from **Fig. 2.3** will be analyzed in future work.

As intuitively expected, the actuator constants for the S-Rotor are around 2 times lower compared to the R-Rotor and L-Rotor. This is the consequence of the 2 times lower PM cross section area, and therefore around 2 times lower flux linkage. More detailed analysis of the S-Rotor and its application in high dynamic positioning systems is explained in [15].

2.6 Design Example Discussion

As an example, in this section, the two possible realization options of the LiRA-1 (MB, L, R, MB) with interior rotor are compared, i.e. where either a combination of an L- and R-Rotor or a S-Rotor is used (cf. **Fig. 2.1** and **Fig. 2.3**). In a first step, the magnetic bearings are not considered, since on the one hand the MBs are not yet considered in the scaling laws, and on the other hand the scaling laws are also applicable to machines with conventional bearings. Furthermore, the design discussion is conducted for the dimensions also used for the FEM simulations as given in **Tab. 2.2**. Thereby, the length L equals the total length of the complete actuator, which means that the axial stroke (Δz), the rotary actuator length L_R and the linear actuator length L_L have to be accommodated in the total length L . As already discussed, for the combined LR-Rotor the distance Δz between the linear and rotary machines must be at least as large as the specified maximum stroke z_{stroke} , while for the S-Rotor no distance between the machines is needed ($\Delta z = 0$). However, it also must be mentioned that with the S-Rotor lower torque and force constants are achieved (cf. **Tab. 2.3**), and therefore the volumes of the rotary machine V_R and linear machine volume V_L are bigger in order to achieve the same absolute torques and forces. Hence, considering the volume between the machines defined by Δz as additional actuator volume V_z , the question arises for which range of stroke z_{stroke} which machine realization results in a smaller overall actuator volume V_A if a given absolute torque T and force F must be achieved. The total actuator volume is actually defined as $V_A = V_R + V_L + V_z$, which, based on the assumption of a constant outer radius R for all machines, corresponds to $L = L_R + L_L + \Delta z$. Accordingly, in case of the RL-Rotor with increasing Δz , the remaining length for L_R and L_L is reduced, which in consequence also leads to a reduction of the maximum achievable force and torque performance, while for the S-Rotor always the

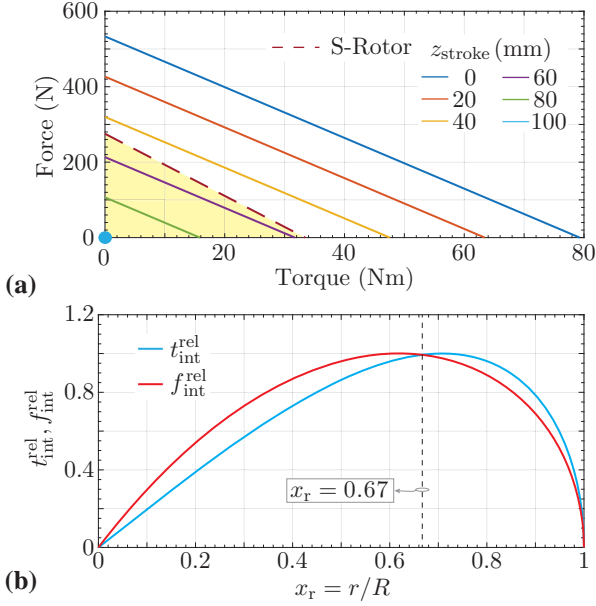


Fig. 2.10: (a) Achievable absolute forces and torques of the LiRA-1 with interior rotor arrangement for different lengths of stroke z_{stroke} . The performance of the LiRA-1 with combined LR-Rotor depends on the stroke (solid lines), while it is independent from the stroke when realized with a S-Rotor. (b) Determining the relative parameter x_r by using the normalized torque and force densities $t_{\text{int}}^{\text{rel}} = t_{\text{int}}/\max(t_{\text{int}})$ and $f_{\text{int}}^{\text{rel}} = f_{\text{int}}/\max(f_{\text{int}})$. For the LR-rotor the optimum radius ratios are found at $x_r = 0.711$ for rotary machine and at $x_r = 0.624$ for the linear machine. For the S-Rotor a sub-optimal value of $x_r = 0.67$ is selected, which however for the given dimensions hardly decreases the achievable torque and force densities.

full actuator length L can be shared between the two machines. Moreover, for both actuator realizations, the length distribution between L_R and L_L can be selected arbitrarily. E.g. in the extreme case, where $L_L = 0$ and $L_R = L - \Delta z$, the actuator achieves the maximum torque but no axial force is obtained, i.e. only constitutes a rotary machine. However, if now L_R is decreased, also the maximum achievable torque decreases linearly, since $T = t \cdot V_R \sim t \cdot L_R$, and the axial force linearly increases, since $F = f \cdot V_L \sim f \cdot L_L$. This behavior is visualized in **Fig. 2.10(a)** for different stroke lengths z_{stroke} . As can be clearly noticed, for the LR-Rotor, the achievable torque-force-ratio decreases with increasing z_{stroke} and for a maximum stroke of $z_{\text{stroke}} = 100$ mm neither an axial force nor a torque can be achieved. On the other hand, for the S-Rotor, a stroke-independent torque-force-ratio is obtained. In this case, the break even in performance is roughly found at the half of the total actuator length $L/2 = 50$ mm, which means that for axial strokes smaller than $L/2$ the LR-Rotor performs better, while for $z_{\text{stroke}} > L/2$ the S-Rotor should be used (cf. yellow shaded area in **Fig. 2.10(b)**). The factor $1/2$ actually originates from the ratio of the torque and force constants K_T and K_F , which for the two rotor types roughly differs by this factor. Hence, z_{stroke} of the break-even point can easily be estimated by writing

$$L_{R,LR} + L_{L,LR} + \Delta z = L_{R,S} + L_{L,S} + \Delta z,$$

where $K_{T,LR} \cdot L_{R,LR} = K_{T,S} \cdot L_{R,S}$ and $K_{F,LR} \cdot L_{F,LR} = K_{F,S} \cdot L_{F,S}$ must be guaranteed in order to achieve the same absolute torque and force values. For the sake of completeness, it must be mentioned that also the relative parameter x_r can strongly influence this break-even point, since for the combined LR-Rotor both machines can be designed independently, which means that the rotor radius r can be optimized for each machine, i.e. always the optimum x_r can be selected, while for the S-Rotor the same x_r for both machines must be used. This is explained by **Fig. 2.10(b)**, where the two normalized torque and force densities, achievable for the specifications given **Tab. 2.2**, are shown. Accordingly, the LR-rotor would be realized with two different diameters, where for the rotary machine the optimum radius ratio is $x_r = 0.711$ and for the linear machine $x_r = 0.624$. For the S-rotor a compromise between torque and force has to be made, which for the given actuator dimensions is found at $x_r = 0.67$. As can be noticed, this sub-optimal radius ratio is hardly decreasing the achievable force and torque densities, however, for other actuator dimensions can be much larger, which means that the break-even point concerning achievable performance is shifted to even larger strokes z_{stroke} .

2.7 Summary

This chapter gives an overview of possible realization concepts to build a linear-rotary actuator (LiRAs) with magnetic bearings (MBs), i.e. a self-bearing electric machine that can realize coupled linear and rotary movements. In order to help the designer to easily compare different realization options and to simplify the selection of the appropriate actuator concept for a given application, general scaling laws concerning torque and forces considering also the heat flow inside and outside the actuator are deduced for interior and exterior rotor arrangements. All the findings are verified with FEM simulations. The scaling laws are also applicable to special actuators (checkerboard or double stator) as well as to standard rotary and/or linear actuators with conventional bearings, as was also done for a design example in this chapter. The comparison of linear-rotary actuators realized with either separate linear and rotary machines or a combined linear-rotary machine showed, that the separate realization outperforms the combined actuator with respect to the total actuator volume as long as the linear stroke is smaller than half the length of the total actuator. Furthermore, depending on the outer dimensions given by the underlying application, this break-even point can be even shifted to larger stroke values, since for the separate realization both machines can be optimized independently, while for the combined actuator a compromise has to be made.

The derived scaling laws have importance in an initial design decision making, as discussed in the design example **Section 2.6** of this chapter. Therefore, they are used later in the thesis, in an initial design of the MALTA in **Section 4.5** of **Chapter 4** to make a decision on the mover diameter range that in the next step should be optimized using 3D-FEM.

The following **Chapter 3** deals with complex space vector modeling for linear-rotary machines, which is necessary to understand their behavior in stationary dq reference frame. These models are finally used for the position and the current controller designs in the later chapters.

3

Generic Complex Space Vector Modeling

To decouple the control of the torque, drive force and/or bearing force of a magnetically coupled linear-rotary actuator, a modeling of phase windings and rotor flux linkage in a stationary dq -coordinate system is needed, which is given in this chapter. The material presented in this chapter is also detailed in [18].

3.1 Introduction

Actuators that can achieve rotary, linear or coupled linear-rotary motion are used in many versatile applications [38] such as pick-and-place robots [24, 39], active suspension systems [40], compressors [41], wave energy harvesting [42], to mention a few. One of the main parts that limits the performance of the linear-rotary actuators are the bearings. Most of the conventional actuators use mechanical bearings, either ball or slider bearings. These bearings introduce drawbacks such as particle generation and the need for lubrication, which is a limiting factor for purity sensitive applications. In high-precision applications (\sim nm range), the thermal expansions of the mechanical bearings limit the precision of the system and make it temperature dependent. Moreover, mechanical bearings limit the lifetime of the actuator [43]. In order to partially overcome these issues, in some applications air bearings are used [30, 44], which on the other hand increase the system complexity due to the needed external air supply and the operation in low pressure environments is not possible. All the above mentioned issues may be solved with magnetic bearings (MBs) [22], which are already largely employed in

high-purity [45], high-speed applications [46], ultra high-speed systems [47] or nanometer precision planar actuators [48]. However, the usage of MBs in linear-rotary actuator systems has not been thoroughly studied in literature. In [34] and [35], tubular linear actuators with separate and integrated MBs are shown, but mainly focusing on the magnetic design without extensive details about the models used for control system design and implementation. In [35], the integration of the two machines (the linear and the rotary MB machine) results in a winding similar to the magnetically coupled linear-rotary machine winding [19]. Such a machine, having the winding used for the magnetic levitation that is at the same time magnetically coupled with the linear motion, requires a decoupling transformation that clearly indicates the current components contributing only to the MB forces or only to the thrust force. Only in this case, an independent and decoupled control of the mentioned forces can be achieved. Therefore, in this chapter an enhanced complex space vector model is derived which allows to control any linear-rotary machine with/without MBs based on only one space vector, which is actually rotating in two complex planes, one for the rotary and one for the linear movement. This model may also directly be applied to a linear machine with integrated MBs [35], which is a special case of the linear-rotary machine with zero rotational speed. Moreover, in order to easily follow the derivations, standard complex space vector models of the rotary and linear machines with and without MBs are revisited and a general three-phase machine model used throughout the chapter is established. To my best knowledge, for the first time in the literature, a complex space vector of the coupled linear-rotary machine is formulated and used to explain the torque, thrust force and the magnetic bearing force generation principles.

3.2 Complex Space Vector Model

In general, complex space vector theory may be used to model symmetric, asymmetric, sinusoidal and non-sinusoidal steady state and transient phenomena of three-phase electric machines [49]. More frequently the algorithm is used for three-phase machines, but may be also used for multi-phase machines, with a phase number higher than 3, which are gaining more and more attention [50], [51], [52], [53], [54]. Moreover, it can also model the saturation effects in machines [55]. Mainly, it is developed to describe the transient behavior of electric machines, where traditional single-phase equivalent circuits cannot be used [56], especially in modern actuator systems, where electric machines rarely operate in a steady-state sinusoidal regime

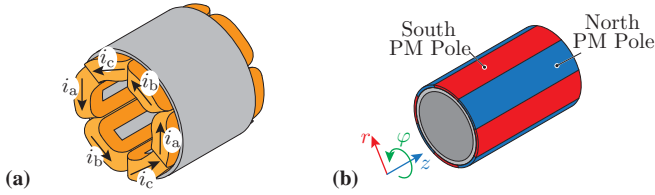


Fig. 3.1: Example of a rotary machine realization with (a) 6 concentrated coils in the stator and (b) 8 poles in the rotor, i.e. the number of the pole pairs is $N_{pp,R} = 4$. The mechanical rotational speed of the rotor is Ω_{mech} , and it is related to the electrical angular speed as $\omega_R = N_{pp,R} \Omega_{\text{mech}}$.

with constant amplitude and electrical frequency of the supply voltage. For the first time, the space vector theory was introduced in [57] and the purpose was to model alternating current (AC) machines. Today, in modern industry, complex space vector theory is used to model three-phase systems, such that in three-phase power converters, which are either connected to a three-phase electric grid [58] or to a three-phase electric machine [59–63], the phase currents and voltages are properly controlled. Compared to the other approaches, e.g. generalized machine theory where a pure mathematical formalism is applied and an electric machine is viewed 'from outside' as 'black box', with electric currents at the input and torque and/or force at the output, space vector theory allows to view a machine 'from inside' and model the spatial field distribution in the air gap [64].

Based on this, in this section the complex space vector models of three-phase electric machines, focusing on the magnetic coupling of the rotary and linear motion [19] with MBs, are derived. In order to introduce a general three-phase electric machine model, the derivation starts with the conventional rotary machine and develops further towards the linear-rotary machine with MBs.

For the sake of clarity, i and j are used to denote complex units of the two different complex planes related to rotation/magnetic levitation and linear motion, respectively. For the notation of electric currents always either indices or the complex space vector notation \underline{i} or \underline{j} is used.

3.3 Rotary Machine: Torque

An example of a three-phase electric machine with 6 teeth in the stator and 8 poles in the rotor is shown in Fig. 3.1. For different machines these

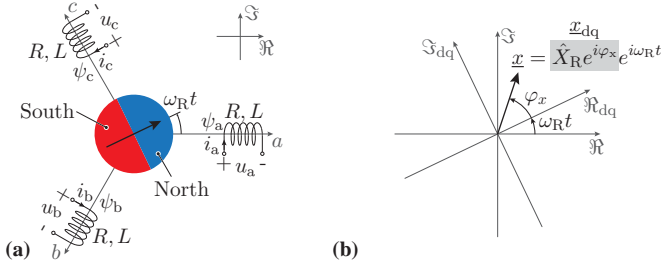


Fig. 3.2: (a) Three-phase electric machine model with the 3 coils spatially displaced by 120° and a 2-pole rotor. The mechanical rotational speed of the rotor is equal to the electrical angular speed of the modeled machine (for the rotary machine ω_R). (b) The complex space vector machine model represented either in the stationary reference frame $(\mathcal{R}, \mathcal{J})$ or in the rotary reference frame $(\mathcal{R}_{dq}, \mathcal{J}_{dq})$.

numbers may differ, but they would still have a three-phase system in the stator. In order to simplify and generalize the analysis of three-phase electric machines, a model with 3 stator coils and a 2-pole rotor is used, as shown in **Fig. 3.2(a)**. It should be noted that this model can resemble concentrated and distributed stator windings, with or without iron teeth, i.e. slotted or slotless windings, which are spatially displaced by 120° . Furthermore, also the electrical quantities such as the voltages on the terminals $u_{\{a,b,c\}}$, the currents in the coils $i_{\{a,b,c\}}$ and the flux linkages of the coils $\psi_{\{a,b,c\}}$ are shifted by 120° in time (cf. **Fig. 3.2(a)**). These quantities are described by their amplitude \hat{X}_R and phase $\omega_R t + \varphi_x$ as

$$\begin{bmatrix} x_a \\ x_b \\ x_c \end{bmatrix} = \hat{X}_R \cdot \begin{bmatrix} \cos(\omega_R t + \varphi_x + \gamma_a) \\ \cos(\omega_R t + \varphi_x + \gamma_b) \\ \cos(\omega_R t + \varphi_x + \gamma_c) \end{bmatrix}, \quad (3.1)$$

where x can be any of the quantities u, i or ψ denoted as $x \in \{u, i, \psi\}$ with the amplitude $\hat{X}_R \in \{\hat{U}_R, \hat{I}_R, \hat{\Psi}_R\}$. The initial phase angle is given as φ_x while $\gamma_a = 0^\circ$, $\gamma_b = -120^\circ$ and $\gamma_c = 120^\circ$ are the electrical angles that determine the three-phase system, where the three phases for the rotation are denoted with lowercase letters as 'a', 'b' and 'c'. For symmetric electric machines, the sum of the quantities is equal to zero, i.e. $x_a + x_b + x_c = 0$. Consequently, the three-phase system $\{x_a, x_b, x_c\}$ is determined by knowing only 2 out of 3 quantities (e.g. if the first two quantities are given, the third one is $x_c = -x_a - x_b$). This allows to model the three-phase system in a two-dimensional coordinate system, i.e. the complex plane $(\mathcal{R}, \mathcal{J})$, which is extensively used

in the analysis of three-phase electric machines. As shown in **Fig. 3.2(a)**, the complex plane ($\mathfrak{R}, \mathfrak{I}$) is superimposed to the general three-phase electric machine model. Based on that, a complex space vector may be defined using the positions of the coils in the model and the instantaneous values of the three-phase quantities as

$$\underline{x} \triangleq \frac{2}{3} \begin{bmatrix} 1 & \underline{a} & \underline{a}^2 \end{bmatrix} \begin{bmatrix} x_a \\ x_b \\ x_c \end{bmatrix} \quad (3.2)$$

where $\underline{a} = e^{i(2\pi/3)}$ is a complex number and i the imaginary unit. This results in a space vector rotating in the complex plane ($\mathfrak{R}, \mathfrak{I}$) which fully describes the three-phase quantities present in the windings. The amplitude of the space vector is the magnitude $|\underline{x}| = \hat{X}_R$ and its argument equals the phase of the quantities $\arg(\underline{x}) = \omega_R t + \varphi_x$, which is graphically represented in **Fig. 3.2(b)**. This can be directly seen by writing the space vector in its exponential form

$$\underline{x} = \hat{X} e^{i\varphi_x} e^{i\omega_R t}.$$

The instantaneous values of the quantities are again simply obtained as

$$x_a = \Re\{\underline{x}\}, \quad x_b = \Re\{\underline{a}^2 \underline{x}\}, \quad x_c = \Re\{\underline{a} \underline{x}\}.$$

The space vector model of the three-phase electric machine can be further simplified by its representation in the rotary complex frame ($\mathfrak{R}_{dq}, \mathfrak{I}_{dq}$), also known as dq -frame. The complex space vector in the dq -frame rotating with the angular frequency ω_R removes the electrical angular speed from its representation and it is equal to $\underline{x}_{dq} = \underline{x} e^{-i\omega_R t} = \hat{X} e^{i\varphi_x}$ (cf. **Fig. 3.2(b)**). Its real and imaginary components ($\underline{x}_{dq} = x_d + ix_q$) are known as dq -components and are related to the amplitude and phase angle as $\hat{X}_R = \sqrt{x_d^2 + x_q^2}$ and $\varphi_x = \text{atan2}(x_q/x_d)$, where atan2 is the function that calculates the angle between the \underline{x}_{dq} and the d -axis considering also the periodicity between $\pm\pi/2$ of the tangent function [65].

In summary, the three-phase electric machine quantities may be represented either with the three-phase electric machine model shown in **Fig. 3.2(a)** in combination with the system of equations given in (3.1), or with the complex space vector model from **Fig. 3.2(b)**, which is equal to \underline{x} in the stationary complex frame or \underline{x}_{dq} in the rotary reference frame.

The established three-phase electric machine complex space vector representation may also be used to determine the electromagnetic torque T_z

of the machine. For this purpose, in the first step the instantaneous input electric power is determined. By using the three-phase quantities given in (3.1), the instantaneous electrical power is calculated as $p_{\text{el}} = \sum_{k=\{a,b,c\}} u_k i_k$. The same power may be obtained by using the complex space vectors of the voltage and current as $p_{\text{el}} = \Re\{3/2 \underline{u} \underline{i}^*\} = \Re\{3/2 \underline{u}_{\text{dq}} \underline{i}_{\text{dq}}^*\}$, where $*$ denotes the conjugate complex number. In both cases, it is necessary to determine the voltage equation. The three-phase model will have 3 voltage equations (i.e. one equation per coil), which can be put together into a single complex space vector equation by using the transformation defined in (3.2) as

$$\underline{u} = R \underline{i} + L \frac{d\underline{i}}{dt} + \frac{d\underline{\psi}}{dt}, \quad (3.3)$$

where R is the resistance of the coils and L is the inductance (cf. **Fig. 3.2(a)**). It should be noted that the mutual inductance between the coils in **Fig. 3.2(a)** is neglected in order to have a clearer presentation, but can be easily included while (3.3) would have the same form. By using (3.3), the electric power is equal to

$$p_{\text{el}} = \frac{3}{2} R \hat{I}_{\text{R}}^2 + \frac{3}{2} L \Re \left\{ \frac{d\underline{i}}{dt} \underline{i}^* \right\} + \frac{3}{2} \Re \left\{ \frac{d\underline{\psi}}{dt} \underline{i}^* \right\}. \quad (3.4)$$

The first term $3/2 R \hat{I}_{\text{R}}^2$ models the copper losses in the stator winding, the second term $3/2 L \Re \{d\underline{i}/dt \underline{i}^*\}$ represents the power used to change the magnetic energy in the machine, while the third term $3/2 \Re \{d\underline{\psi}/dt \underline{i}^*\}$ is further analyzed. The space vector of the flux linkage $\underline{\psi}$ can be expressed as $\underline{\psi} = \hat{\Psi}_{\text{R}} e^{i\varphi_{\psi}} e^{i\omega_{\text{R}} t} = (\psi_{\text{d}} + i\psi_{\text{q}}) e^{i\omega_{\text{R}} t}$. Usually, the rotating complex frame, the dq -frame, is positioned such that the d -axis \Re_{dq} coincides with the flux linkage space vector $\underline{\psi}$, which leads to $\varphi_{\psi} = 0^\circ$ (cf. **Fig. 3.2(b)**). Therefore, the flux linkage space vector in the stationary complex frame is $\underline{\psi} = \hat{\Psi}_{\text{R}} e^{i\omega_{\text{R}} t}$, while in the rotary dq -frame $\underline{\psi}_{\text{dq}} = \psi_{\text{d}} = \hat{\Psi}_{\text{R}}$. Similarly, the conjugate complex space vector of the current in the stationary complex frame is $\underline{i}^* = (\underline{i}_{\text{dq}} e^{i\omega_{\text{R}} t})^* = \underline{i}_{\text{dq}}^* e^{-i\omega_{\text{R}} t}$, where the complex conjugate in the dq -frame is $\underline{i}_{\text{dq}}^* = i_{\text{d}} - i i_{\text{q}}$. Using these expressions for $\underline{\psi}$ and \underline{i}^* , the third term of (3.4) is further developed as

$$\frac{3}{2} \Re \left\{ \frac{d\underline{\psi}}{dt} \underline{i}^* \right\} = \frac{3}{2} \frac{d\hat{\Psi}_{\text{R}}}{dt} i_{\text{d}} + \omega_{\text{R}} \frac{3}{2} \hat{\Psi}_{\text{R}} i_{\text{q}}, \quad (3.5)$$

where the first term only results when also a change in the flux linkage magnitude $\hat{\Psi}_{\text{R}}$ is considered. Hence, this term represents the power necessary

to change the flux linkage $\hat{\Psi}_R$, e.g. used for field weakening operation of the electric machine and may be changed with the d -component of the current i_d . The second term represents the converted power of the machine, which at the shaft is equal to $p_{\text{mech}} = \Omega_{\text{mech}} T_z$, where Ω_{mech} is the mechanical rotational speed of the rotor in rad/s and T_z is the electromagnetic torque. Having in mind the relation of the electrical angular speed and the mechanical speed $\omega_R = N_{\text{pp,R}} \Omega_{\text{mech}}$, where $N_{\text{pp,R}}$ is the number of pole pairs in the rotor, the mechanical torque is equal to

$$T_z = \frac{3}{2} N_{\text{pp,R}} \hat{\Psi}_R i_q. \quad (3.6)$$

Therefore, the mechanical torque is controlled by the q -current component (i_q).

3.4 Rotary Machine: Bearing Force

Rotary machines are mainly used to generate torque, but may also be used to generate the bearing force if the winding configuration, i.e. the interconnection between several phase windings is accordingly adjusted. For a given number of stator teeth and pole pairs $N_{\text{pp,R}}$ in the rotor, the winding configuration for the torque generation can be optimized and is well documented in literature [66] and there are even online tools for the winding configuration calculation [67]. For the bearing force generation the same winding arrangement as for the torque generation can be used, while only the winding interconnections have to be reconfigured. This actually results in a different virtual number of pole pairs of the stator winding, which means that depending on the winding interconnection a different stator field harmonic is pronounced by the three-phase currents. For example, if the number of the pole pairs in the rotor is $N_{\text{pp,R}}$, the winding configuration optimized for the torque generation with $N_{\text{pp,B}} = N_{\text{pp,R}} \pm 1$ pole pairs should be used to generate the bearing force. In literature, this is known as the self-bearing motor $N_{\text{pp,R}} \pm 1$ type [22, 68]. To show this in an example, the winding configuration of the machine shown in **Fig. 3.1**, which has concentrated windings with 6 teeth and a rotor with $N_{\text{pp,R}} = 4$, is analyzed and reconfigured, i.e. changing the interconnection of phase windings, such that the rotary machine can also generate the bearing force. Hence, in order to generate torque, the stator winding should be connected such that the three-phase currents in the coils have directions as denoted in **Fig. 3.1(a)**, which can be represented with the set as $W_T = \{i_a, i_b, i_c, i_a, i_b, i_c\}$. As already mentioned, to use the same winding

for the bearing force generation, a winding configuration for $N_{pp,B} = 4 \pm 1$ pole pairs should be used. Since it is not possible to have a concentrated winding with 6 teeth and 3 pole pairs [67], a winding configuration that is able to generate $N_{pp,B} = 5$ pole pairs has to be used, which in this case means that the coils are connected as $W_B = \{i_a, -i_b, i_c, -i_a, i_b, -i_c\}$. In contrast to W_T , the winding configuration W_B actually means that now the two corresponding phase windings are connected in anti-series instead of being connected in series, thus by applying the three-phase currents to the rotary electric machine shown in **Fig. 3.1**, with the W_B winding configuration the bearing force onto the rotor is generated.

In order to control the magnetic bearing forces (F_x and F_y), a three-phase model of the magnetic bearing machine similar to the one shown in **Fig. 3.2(a)** is established. The difference between the torque machine winding and the bearing machine winding is that now due to this anti-series connection of the phase windings the overall flux linkage in the bearing winding, i.e. the sum of the flux linked with both phase coils, is equal to 0 when the rotor is in its center position, i.e. when there is no radial displacement of the rotor, $x = 0$ and $y = 0$, independent from the angular position of the rotor. A non-zero flux linkage in the bearing winding only appears when a radial displacement of the rotor is present. To model this, the coils in the three-phase electric machine model from **Fig. 3.2(a)** are split in half, placed at both sides of the rotor and are connected in anti-series as shown in **Fig. 3.3(a)**. As will be explained in the following, with this arrangement the total flux linkage in all coils becomes non-zero when the rotor is displaced from the center, i.e. $x \neq 0$ and/or $y \neq 0$, and can be calculated as

$$\begin{aligned} \psi_{\{a,b,c\}} = & \frac{d\hat{\Psi}_R}{dx} x \cos(\omega_R t + \varphi_\psi + \{\gamma_a, \gamma_b, \gamma_c\}) - \\ & \frac{d\hat{\Psi}_R}{dy} y \sin(\omega_R t + \varphi_\psi + \{\gamma_a, \gamma_b, \gamma_c\}), \end{aligned} \quad (3.7)$$

where $d\hat{\Psi}_R/dx$ and $d\hat{\Psi}_R/dy$ are the change of the flux linkage with respect to the radial displacement. The deduction of this radial displacement-dependent flux linkage given in (3.7) is explained for phase ‘a’ based on **Fig. 3.3(b-d)**.

In a first step, a displacement in x -direction is assumed, while the rotor flux is also pointing in positive x -direction. As shown in **Fig. 3.3(c)**, a displacement in positive x -direction leads to an increased flux linkage in the right coil, while the flux linkage with the left coil is reduced, thus the total flux linkage with both coils is increasing. Assuming a certain constant sensitivity $d\hat{\Psi}_R/dx = \chi_{pm,x}$ the resulting flux linkage can be calculated as $(d\hat{\Psi}_R/dx) x = \chi_{pm,x} x$. As

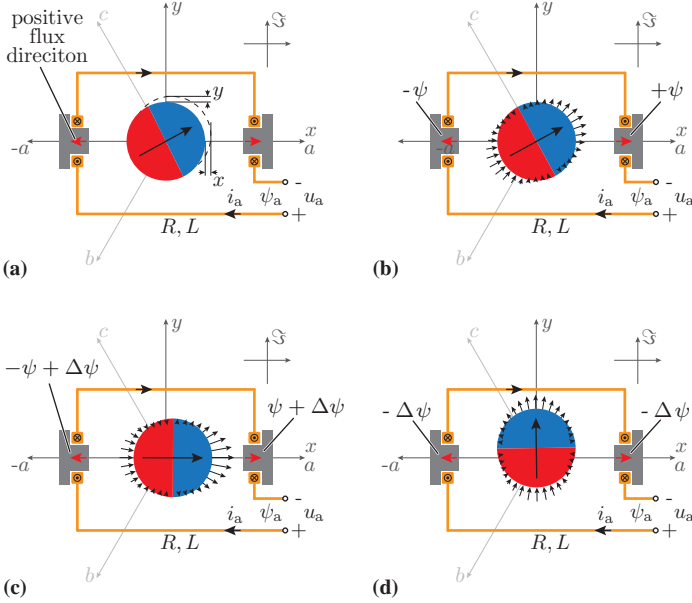


Fig. 3.3: (a) Three-phase electric machine bearing force model where a radial displacement of the rotor in x - and y -direction is allowed. It is derived from the three-phase machine model shown in Fig. 3.2(a) by splitting the coils in half, placing them at both sides of the rotor and connecting them in anti-series. This allows to model the bearing winding, in which the flux linkage only exists when the rotor is displaced from its center. (b) Radial flux density component of the rotor PMs. The rotor is in the center and, therefore, the flux linkage of the first phase $\psi_a = +\psi - \psi = 0$. (c) The rotor is displaced in x -direction by x with the rotary orientation $(\omega_R t + \varphi_\psi) = 0$. Consequently, there is a non-zero flux linkage in the first winding $\psi_a = +\psi + \Delta\psi - \psi + \Delta\psi = 2\Delta\psi$, which we model with the sensitivity $d\hat{\Psi}_R/dx$. This results in the flux linkage of the first phase $\psi_a = (d\hat{\Psi}_R/dx) x$. (d) The rotor is displaced in y -direction by y with the rotary orientation $(\omega_R t + \varphi_\psi) = \pi/2$. Both winding sides experience negative flux increase, resulting in the flux linkage $\psi_a = -\Delta\psi - \Delta\psi = -2\Delta\psi$. Again, we model it with the sensitivity $d\hat{\Psi}_R/dy$, resulting in the flux linkage of $\psi_a = -(d\hat{\Psi}_R/dy) y$.

can be noticed, however, this is only true when the rotor's angular position is equal to $(\omega_R t + \varphi_\psi) = 0^\circ$. If e.g. the rotor is rotated by 180° , the flux linkage would be the same as with 0° , but in the negative direction, which means a multiplication by -1 . Furthermore, at the angular positions 90° and 270° a displacement in x -direction ideally does not result in any total flux linkage. Consequently, the arbitrary rotational position of the rotor (cf. **Fig. 3.3(c)**) has to be considered, which for an x -displacement can be done by multiplying $(d\hat{\Psi}_R/dx) x = \chi_{pm,x} x$ with $\cos(\omega_R t + \varphi_\psi + \gamma_a)$.

In analogy to the x -displacement, the influence of a y -displacement can be analyzed. As it may be imagined based on **Fig. 3.3(d)**, when the rotor flux is pointing in y -direction, the resulting flux linkage of the phase 'a' is $(-d\hat{\Psi}_R/dy) y = -\chi_{pm,y} y$, if again a certain constant sensitivity $d\hat{\Psi}_R/dy = \chi_{pm,y}$ is assumed. Furthermore, the flux linkage again depends on the rotating position, which for a y -displacement has to be considered with $\sin(\omega_R t + \varphi_\psi + \gamma_a)$ and thus leads to the second term of (3.7). By applying now the transformation given in (3.2) and assuming that $\chi_{pm,x} = \chi_{pm,y} = \chi_{pm,R}$, the complex space vector of the bearing flux linkage in the stationary complex frame is obtained

$$\underline{\psi} = \chi_{pm,R} (x + iy) e^{i\varphi_\psi} e^{i\omega_R t}, \quad (3.8)$$

where x and y equal the radial displacements [69]. The complex space vector of the flux linkage in the rotary dq -frame is $\underline{\psi}_{dq} = \chi_{pm,R} (x + iy) e^{i\varphi_\psi}$. Since the rotating dq -frame is positioned such that $\varphi_\psi = 0$, the complex space vector of the flux linkage is then equal to $\underline{\psi}_{dq} = \chi_{pm,R} (x + iy)$.

To obtain the expressions for the mechanical bearing forces F_x and F_y , similar as for the mechanical torque, the expression of the instantaneous electric power p_{el} is analyzed. The electric power may be obtained by using the complex space vectors as $p_{el} = \Re\{3/2 \underline{u} \underline{i}^*\} = \Re\{3/2 \underline{u}_{dq} \underline{i}_{dq}^*\}$, which results in the same expression found in (3.4). Accordingly, for the mechanical bearing force analysis only the last term given in (3.4) is needed, which leads to

$$\begin{aligned} \frac{3}{2} \Re \left\{ \frac{d\underline{\psi}}{dt} \underline{i}^* \right\} &= \frac{3}{2} \chi_{pm,R} (v_x i_d + v_y i_q) + \\ &\quad \frac{3}{2} \chi_{pm,R} \omega_R (x i_q - y i_d), \end{aligned} \quad (3.9)$$

where $v_x = dx/dt$ and $v_y = dy/dt$ are the rotor velocities in x - and y -direction. The total mechanical power with the allowed radial displacement of the rotor

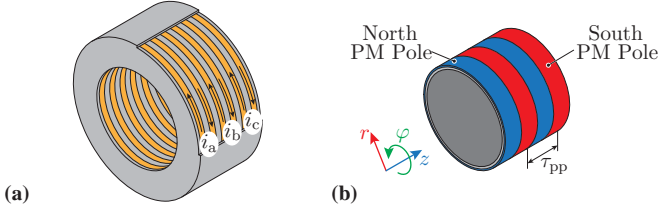


Fig. 3.4: (a) A three-phase electric linear machine stator realization with 6 teeth single layer winding. (b) Rotor (also called 'mover' for linear machines) with 4 poles. The pole pair width (twice the pole pitch) is denoted as τ_{pp} .

is $p_{\text{mech}} = v_x F_x + v_y F_y + \Omega_{\text{mech}} T_z$. Comparing the terms of p_{mech} with the terms in (3.9), the bearing forces are

$$F_x = \frac{3}{2} \chi_{\text{pm,R}} i_d, \quad F_y = \frac{3}{2} \chi_{\text{pm,R}} i_q. \quad (3.10)$$

As can be noted, the radial force components can be independently controlled with i_d and i_q current components of the bearing winding. In addition, there is a parasitic torque created when the rotor radial displacement is non-zero, which is equal to $T_z = (3/2) N_{\text{pp,R}} \chi_{\text{pm,R}} (x i_q - y i_d)$ and has to be compensated by the controller.

3.5 Linear Machine: Thrust Force

An example of the three-phase electric linear machine realization is shown in Fig. 3.4. It should be noted that instead of the pole pair number for the rotary machine, the pole pair width τ_{pp} is given for the linear machine.

From the perspective of the electrical machine analysis, the three-phase linear electric machine is similar to the rotary machine, i.e. the stator winding is characterized by the three-phase voltage, current and the flux linkage

$$\begin{bmatrix} x_A \\ x_B \\ x_C \end{bmatrix} = \hat{X}_L \cdot \begin{bmatrix} \cos(\omega_L t + \theta_x + \gamma_A) \\ \cos(\omega_L t + \theta_x + \gamma_B) \\ \cos(\omega_L t + \theta_x + \gamma_C) \end{bmatrix}, \quad (3.11)$$

where $\hat{X}_L \in \{\hat{U}_L, \hat{I}_L, \hat{\Psi}_L\}$ is the amplitude, ω_L is the linear machine electrical angular speed, θ_x is the phase angle and $\gamma_A = 0^\circ$, $\gamma_B = -120^\circ$ and $\gamma_C = 120^\circ$ are the electrical angles that determine the three-phase system, where the

three phases for linear motion are denoted with uppercase letters as ‘A’, ‘B’ and ‘C’. Therefore, the same model as depicted in **Fig. 3.2** may be used for the linear machine analysis. In the rotary machine the rotational mechanical speed Ω_{mech} is related to the electrical angular speed ω_R , while for the linear machine the linear mechanical speed v_z is related to the linear machine electrical angular speed as

$$\omega_L = \frac{2\pi}{\tau_{\text{pp}}} v_z. \quad (3.12)$$

Similar to the rotary machine, where the electrical power is analyzed based on (3.4) to get the expression for the mechanical torque, for the linear machine the same expression can be used, just with the linear machine quantities. Therefore, the last term of (3.4) is

$$\frac{3}{2} \Re \left\{ \frac{d\psi}{dt} i^* \right\} = \frac{3}{2} \frac{d\hat{\Psi}_L}{dt} i_d + \omega_L \frac{3}{2} \hat{\Psi}_L i_q, \quad (3.13)$$

where $\hat{\Psi}_L$ is the flux linkage of the linear machine. The first term again describes the magnetic power to change the flux linkage (flux weakening), while the second term is related to the mechanical output power. By using (3.12) and the mechanical power $p_{\text{mech}} = v_z F_z$, the thrust force is obtained as

$$F_z = \frac{3\pi}{\tau_{\text{pp}}} \hat{\Psi}_L i_q. \quad (3.14)$$

In analogy to the mechanical torque obtained in a rotary machine, the thrust force is controlled by the q -current component i_q .

3.6 Linear Machine: Bearing Force

In order to generate and control the bearing force onto the rotor of a linear machine, the air gap flux density has to be controlled around the rotor circumference such that a ‘radial pull’ is created in the desired direction. However, the three-phase linear machine has a winding that is circumferentially homogeneous (cf. **Fig. 3.4(a)**). Consequently, the air gap flux density around the circumference cannot be adjusted with the linear machine winding. Therefore, the conventional linear machine cannot be used as a bearing machine.

3.7 Linear-Rotary Machine: Torque + Thrust Force

A linear-rotary machine may be realized by coupling a rotary and a linear machine either mechanically or magnetically. The analysis of the linear-rotary machine with the mechanical coupling may be split into the separate analyses of the rotary and linear machines explained in **Section 3.3** and **Section 3.5**, respectively. The analysis of the linear-rotary machine with the magnetic coupling is clarified in this section. A realization example of such a machine is shown in **Fig. 3.5**. Since the stator windings have to be able to generate torque and thrust force at the same time, concentrated stator coils are needed, which can be seen as a combination of the winding arrangements used for the rotary machine (denoted with lowercase letters $\{a,b,c\}$) and the linear machine (denoted with uppercase letters $\{A,B,C\}$). As illustrated in **Fig. 3.5(a)**, the concentrated coils of the linear-rotary machine resemble the rotary machine in rotary direction and the linear machine in linear direction. Similarly, the rotor's PM arrangement results from a combination of the PM arrangement needed for the rotary machine and the linear machine, which leads to a checkerboard-type PM arrangement (cf. **Fig. 3.5(b)**). Therefore, the number of pole pairs in rotary direction is again $N_{pp,R}$, and the pole pair width in linear direction is τ_{pp} .

Finally, also the voltages and currents which have to be applied to the magnetically coupled linear-rotary machine windings can be seen as a combination of the quantities needed for the rotary machine and the linear machine. Compared to a conventional rotary machine, for example, this means that for the linear-rotary machine also a rotating flux density has to be generated by the stator windings in order to produce torque, however, in this case also the linear position of the rotor has to be considered, since for each rotary three-phase winding set (e.g. $\{aA, bA, cA\}$ compared to $\{aB, bB, cB\}$) the PM alignment below each three-phase winding set is different and therefore different torque-generating currents have to be injected into the rotary three-phase windings. Accordingly, the same is also true in linear direction, which means that for the generation of thrust force, for each linear three-phase winding set (e.g. $\{aA, aB, aC\}$ compared to $\{bA, bB, bC\}$) the rotation angle has to be considered, since the PM alignment for each linear three-phase winding set is different. This can be achieved by multiplying the rotary three-phase quantities (e.g. $\cos(\omega_R t)$) with the linear three-phase quantities (e.g. $\cos(\omega_L t)$), which corresponds to a modulation of the rotary quantities in linear direction with the electrical angular speed ω_L and a modulation of the linear quantities

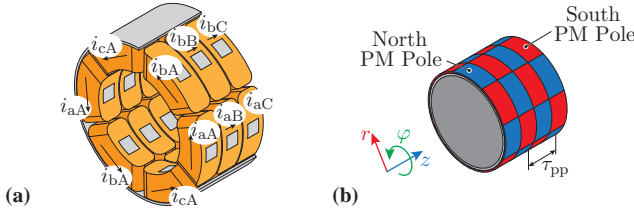


Fig. 3.5: (a) A linear-rotary machine stator realization with 6 teeth for the rotation and 3 teeth for the linear motion. (b) The rotor of the linear-rotary machine with $N_{pp,R} = 4$ pole pairs for the rotation and with a pole pair width of τ_{pp} for the linear motion.

in rotary direction with the electrical angular speed ω_R . Therefore, the phase quantities of the linear-rotary machine have the following form

$$x_{\{a,b,c\}\{A,B,C\}} = \hat{X}_{RL} \cos(\omega_R t + \varphi_x + \{\gamma_a, \gamma_b, \gamma_c\}) \times \cos(\omega_L t + \theta_x + \{\gamma_A, \gamma_B, \gamma_C\}), \quad (3.15)$$

where $\hat{X}_{RL} \in \{\hat{U}_{RL}, \hat{I}_{RL}, \hat{\Psi}_{RL}\}$ is the amplitude, φ_x is the rotary initial phase angle and θ_x is the linear initial phase angle. It should be noted again that the lowercase letters $\{a, b, c\}$ denote the rotary component, while the uppercase letters $\{A, B, C\}$ denote the linear component.

In order to unify the analysis of the linear-rotary machines and apply the same techniques as for the rotary and linear machines, the complex space vector of the magnetically coupled linear-rotary machine is defined. Hence, two complex planes are needed, one for the rotary component (with the complex unit i) and another for the linear component (with the complex unit j). The complex space vector for the magnetically coupled linear-rotary machine is defined with the following transformation

$$\underline{\underline{x}} \triangleq \frac{4}{9} \begin{bmatrix} 1 & \underline{a} & \underline{a}^2 \end{bmatrix} \begin{bmatrix} x_{aA} & x_{aB} & x_{aC} \\ x_{bA} & x_{bB} & x_{bC} \\ x_{cA} & x_{cB} & x_{cC} \end{bmatrix} \begin{bmatrix} 1 \\ \underline{b} \\ \underline{b}^2 \end{bmatrix}, \quad (3.16)$$

where $\underline{\underline{x}} \in \{\underline{\underline{u}}, \underline{\underline{i}}, \underline{\underline{\psi}}\}$, $\underline{a} = e^{i(2\pi/3)}$ and $\underline{b} = e^{j(2\pi/3)}$ are complex numbers. It should be noted that the ‘double underline’ $\underline{\underline{x}}$ denotes the complex space vector with the two different complex units. This results in the space vector rotating simultaneously in two complex planes, (\Re^i, \Im^i) and (\Re^j, \Im^j) , and fully describing the phase quantities of the linear-rotary machine. The amplitude of the complex space vector is the magnitude $|\underline{\underline{x}}| = \hat{X}_{RL}$ and its arguments

are the rotary and linear phases of the phase quantities, i.e. $\arg^i(\underline{x}) = \omega_R t + \varphi_x$ and $\arg^j(\underline{x}) = \omega_L t + \theta_x$. This can be seen by writing the complex space vector in its exponential form as

$$\underline{\underline{x}} = \underbrace{\hat{X}_{RL} e^{i\varphi_x} e^{j\theta_x}}_{\underline{\underline{x}}_{dq}} e^{i\omega_R t} e^{j\omega_L t}, \quad (3.17)$$

where $\underline{\underline{x}}_{dq}$ is the complex space vector in the double-rotary dq -frame. The defined complex space vector (3.16) has 4 components

$$\underline{\underline{x}}_{dq} = x_{dd} + ix_{qd} + jx_{dq} + ijx_{qq}, \quad (3.18)$$

which may be obtained by applying Euler's formula (e.g. $e^{i\omega_R t} = \cos(\omega_R t) + i \sin(\omega_R t)$) on each of the exponents in (3.17). The first index of each component belongs to the rotary and the second index to the linear machine. Accordingly, the component x_{dd} equals in both complex planes, i.e. for the rotary and linear machine, to a real component and thus in both complex planes is pointing in d -direction. The component ix_{qd} is purely imaginary for the rotary machine (first index q) and purely real for the linear machine (second index d), while for the component jx_{qd} it is exactly opposite. Finally, the component ijx_{qq} is a component which in both complex planes is purely imaginary, therefore in both frames points in q -direction.

In order to obtain instantaneous values given with (3.15) from the complex space vector $\underline{\underline{x}}$, a similar procedure as for the complex space vector \underline{x} is applied. Namely, depending on the desired instantaneous component ($x_{\{a,b,c\}\{A,B,C\}}$) the complex space vector is multiplied at first with either 1 , \underline{a} , \underline{a}^2 , \underline{b} and/or \underline{b}^2 and then the real part \Re is taken, which can be written as

$$\begin{bmatrix} x_{aA} & x_{aB} & x_{aC} \\ x_{bA} & x_{bB} & x_{bC} \\ x_{cA} & x_{cB} & x_{cC} \end{bmatrix} = \Re \left\{ \begin{bmatrix} 1 \\ \underline{a}^2 \\ \underline{a} \end{bmatrix} \underline{\underline{x}} \begin{bmatrix} 1 & \underline{b}^2 & \underline{b} \end{bmatrix} \right\}. \quad (3.19)$$

After defining the complex space vector of the linear-rotary machine, further calculations are similar as for the rotary or linear machines. Hence, in order to obtain the expressions for the torque and the thrust force of the linear-rotary machine, again the power balance, i.e. the conversion from electrical input power to mechanical output power, is analyzed. The input electrical power is the sum of the powers of each phase, which can be written using the double sum operators $p_{el} = \sum_{m=\{a,b,c\}} \sum_{n=\{A,B,C\}} u_{mn} i_{mn}$. It also

can be calculated using the complex space vectors as $p_{\text{el}} = \Re\{9/4 \underline{\underline{u}}_{\text{dq}} \underline{\underline{i}}_{\text{dq}}^*\} = \Re\{9/4 \underline{\underline{u}}_{\text{dq}} \underline{\underline{i}}_{\text{dq}}^*\}$, which together with the voltage space vector equation given in (3.3) results in

$$p_{\text{el}} = \frac{9}{4} R \hat{I}_{\text{RL}}^2 + \frac{9}{4} L \Re \left\{ \frac{d\underline{\underline{i}}_{\text{dq}}}{dt} \underline{\underline{i}}_{\text{dq}}^* \right\} + \frac{9}{4} \Re \left\{ \frac{d\underline{\underline{\psi}}}{dt} \underline{\underline{i}}_{\text{dq}}^* \right\}. \quad (3.20)$$

Similar to the analysis of the electric power expression for the rotary machine (cf. (3.4)), the first two terms do not contribute to the mechanical power but consider either the losses in the windings or the change in magnetic energy. Therefore, the third term $9/4 \Re \left\{ \frac{d\underline{\underline{\psi}}}{dt} \underline{\underline{i}}_{\text{dq}}^* \right\}$ is further analyzed. As the dq -frames are oriented in such a way that $\varphi_{\psi} = 0$ and $\theta_{\psi} = 0$, the complex space vector of the flux linkage is then equal to $\underline{\underline{\psi}} = \hat{\Psi}_{\text{RL}} e^{i\omega_{\text{R}} t} e^{j\omega_{\text{L}} t}$. The conjugate complex space vector of the current is equal to $\underline{\underline{i}}_{\text{dq}}^* = \hat{I}_{\text{RL}} e^{-i\varphi_i} e^{-j\theta_i} e^{-i\omega_{\text{R}} t} e^{-j\omega_{\text{L}} t} = \underline{\underline{i}}_{\text{dq}}^* e^{-i\omega_{\text{R}} t} e^{-j\omega_{\text{L}} t}$, where $\underline{\underline{i}}_{\text{dq}}^* = i_{\text{dd}} - ii_{\text{qd}} - ji_{\text{dq}} + jji_{\text{qq}}$. Using these expressions, the last term in (3.20) is equal to

$$\frac{9}{4} \Re \left\{ \frac{d\underline{\underline{\psi}}}{dt} \underline{\underline{i}}_{\text{dq}}^* \right\} = \frac{9}{4} \frac{d\hat{\Psi}_{\text{RL}}}{dt} i_{\text{dd}} + \omega_{\text{R}} \frac{9}{4} \hat{\Psi}_{\text{RL}} i_{\text{qd}} + \omega_{\text{L}} \frac{9}{4} \hat{\Psi}_{\text{RL}} i_{\text{dq}}. \quad (3.21)$$

The first term is the power used to change the flux linkage $\hat{\Psi}_{\text{RL}}$, e.g. used for field weakening. The other two terms correspond to the mechanical power of the rotation and the linear motion. Considering the expression for the total mechanical power obtained at the shaft $p_{\text{mech}} = \Omega_{\text{mech}} T_z + v_z F_z$ and the ratios between the electrical and mechanical angular speeds $\omega_{\text{R}} = N_{\text{pp,R}} \Omega_{\text{mech}}$ and $\omega_{\text{L}} = 2\pi/\tau_{\text{pp}} v_z$, the torque and the thrust force are calculated as

$$T_z = \frac{9}{4} N_{\text{pp,R}} \hat{\Psi}_{\text{RL}} i_{\text{qd}}, \quad F_z = \frac{9\pi}{2\tau_{\text{pp}}} \hat{\Psi}_{\text{RL}} i_{\text{dq}}. \quad (3.22)$$

As can be noted, the mechanical torque and the thrust force in the linear-rotary machine can be fortunately controlled with two independent current components i_{qd} and i_{dq} , which for the corresponding machine part, i.e. rotary or linear machine, equals to the q -current (torque or force generation) and in the other machine part results in a d -component (field weakening/amplification). The torque T_z and the F_z generation is decoupled, i.e. i_{qd} current

component does not cause any axial force, while i_{dq} current component does not cause any torque. It should be mentioned that this result agrees with the torque and the thrust force expressions derived in [19].

3.8 Linear-Rotary Machine: Bearing Force

Similar to the rotary machine discussed in **Section 3.4**, the bearing force may also be generated with the linear-rotary machine. In analogy to the rotary machine, for the linear-rotary machine the winding configuration has to be adjusted. Consequently, in order to generate the torque, the winding configuration in rotary direction is $W_T = \{i_{aX}, i_{bX}, i_{cX}, i_{aX}, i_{bX}, i_{cX}\}$, where ‘ X ’ in the index denotes any of the linear phase components $X \in \{A, B, C\}$, and to generate the bearing force, the winding configuration in rotary direction should be $W_B = \{i_{aX}, -i_{bX}, i_{cX}, -i_{aX}, i_{bX}, -i_{cX}\}$ (cf. **Section 3.4**).

The flux linkage modeling considerations are similar as for the rotary machine given with (3.7) and shown in **Fig. 3.3**, while for the linear-rotary machine in addition to the rotation angle, which is already considered in (3.7), also the linear position of the rotor has to be taken into account. Hence, (3.7) has to be multiplied with $\cos(\omega_L t + \theta_\psi + \{\gamma_A, \gamma_B, \gamma_C\})$, which in other words corresponds to a modulation of the flux linkage in linear direction, and results in the following expression

$$\begin{aligned} \psi_{\{a,b,c\}\{A,B,C\}} = \chi_{\text{pm,RL}} & \left(x \cos(\omega_R t + \varphi_\psi + \{\gamma_A, \gamma_B, \gamma_C\}) - \right. \\ & y \sin(\omega_R t + \varphi_\psi + \{\gamma_A, \gamma_B, \gamma_C\}) \Big) \times \\ & \cos(\omega_L t + \theta_\psi + \{\gamma_A, \gamma_B, \gamma_C\}), \end{aligned} \quad (3.23)$$

where $\chi_{\text{pm,RL}}$ is the flux linkage radial sensitivity of the linear-rotary machine. By applying the proposed complex space vector transformation for the linear-rotary machines (cf. (3.16)), the bearing flux linkage vector is

$$\underline{\underline{\psi}} = \chi_{\text{pm,RL}} (x + jy) e^{i\varphi_\psi} e^{j\theta_\psi} e^{i\omega_R t} e^{j\omega_L t}. \quad (3.24)$$

The complex space vectors of the voltage $\underline{\underline{u}}$ and the current $\underline{\underline{i}}$ are the same as for the linear-rotary machine (cf. (3.17)).

To determine the bearing forces F_x and F_y of the linear-rotary machine, similar to the previous analysis for the rotary machine, the expressions for the electrical and mechanical powers are used. The electric power may be calculated using the complex space vectors (cf. (3.20)). Similar as for the

torque and the thrust force calculation, the last term in (3.20) is further analyzed

$$\frac{9}{4} \Re \left\{ \frac{d\psi}{dt} \underline{i}^* \right\} = \frac{9}{4} \chi_{\text{pm,RL}} \left(v_x i_{\text{dd}} + v_y i_{\text{qd}} + \omega_{\text{R}} (x i_{\text{qd}} - y i_{\text{dd}}) + \omega_{\text{L}} (x i_{\text{dq}} + y i_{\text{qq}}) \right), \quad (3.25)$$

where $v_x = dx/dt$, $v_y = dy/dt$, $\omega_{\text{R}} = N_{\text{pp,R}} \Omega_{\text{mech}}$ and $\omega_{\text{L}} = 2\pi/\tau_{\text{pp}} v_z$. The mechanical power is equal to $p_{\text{mech}} = v_x F_x + v_y F_y + v_z F_z + \Omega_{\text{mech}} T_z$. By comparing these coefficients with (3.25), the bearing forces of the linear-rotary machine are obtained as

$$F_x = \frac{9}{4} \chi_{\text{pm,RL}} i_{\text{dd}}, \quad F_y = \frac{9}{4} \chi_{\text{pm,RL}} i_{\text{qd}}. \quad (3.26)$$

Again, the radial force components of the linear-rotary machine can be independently controlled with i_{dd} and i_{qd} current components of the bearing winding, which in both cases means that the bearing forces are generated with the linear d -current component. In addition, there are parasitic torque and thrust force components created when the rotor radial displacement is non-zero. They are equal to $T_z = (9/4) N_{\text{pp,R}} \chi_{\text{pm,RL}} (x i_{\text{qd}} - y i_{\text{dd}})$ and $F_z = (9\pi/2\tau_{\text{pp}}) \chi_{\text{pm,RL}} (x i_{\text{dq}} + y i_{\text{qq}})$ and have to be compensated by the controller.

3.9 Linear Machine: Thrust Force + Bearing Force

As shown in **Section 3.6**, the linear machine analyzed in **Section 3.5** cannot generate any bearing forces and, therefore, cannot be operated as a self-bearing machine.

In contrast, the linear machine analyzed in this section can be operated as a self-bearing machine and can be derived either from the standard linear machine shown in **Fig. 3.4**, by interrupting the linear machine winding in circumferential direction and creating the three new coils as shown in **Fig. 3.6(a)**, or from the rotary-linear machine discussed in the previous section. Hence, the resulting machine is a combination of a rotary-linear machine winding and a linear machine rotor (cf. **Fig. 3.6**).

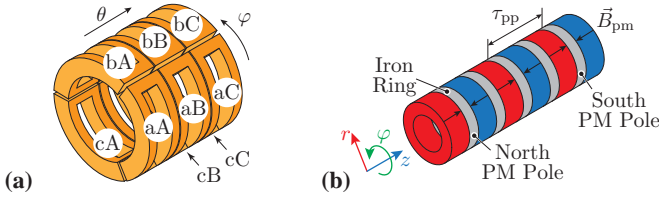


Fig. 3.6: (a) Stator winding arrangement of the MALTA with 9 phase windings. (b) The MALTA rotor is similar to the rotor of a linear machine (cf. **Fig. 3.4**). Due to simpler manufacturing, the MALTA rotor has axially magnetized PMs in combination with iron rings.

This machine type, also called MALTA (Magnetically Levitated Tubular Actuator), is for the first time proposed in [35], where the magnetic design and hardware realization are discussed.

The achievable thrust and the bearing forces of the MALTA are determined by using the complex space vector models derived for the linear and linear-rotary machines. It should be noted that they are first analyzed separately, i.e. it is assumed that the MALTA winding is carrying only the thrust force current or only the bearing force current, which in the literature is known as separate winding arrangement [70]. In a second step, the superposition of the thrust and bearing force currents is analyzed in **Section 6.5**.

3.9.1 MALTA Thrust Force Generation

From the thrust force generation point of view, the MALTA winding (cf. **Fig. 3.6(a)**) behaves the same as the winding of the linear machine analyzed in **Section 3.5** (cf. **Fig. 3.4(a)**). Therefore, the currents in the MALTA winding are equal in circumferential (rotary) direction, i.e. $i_{aX} = i_{bX} = i_{cX}$, where $X \in \{A, B, C\}$. Consequently, it is enough to analyze one third (one circumferential third) of the MALTA winding (e.g. coils $\{aA, aB, aC\}$). Accordingly, the findings can afterwards also be applied to the rest of the windings.

Furthermore, the analysis concerning thrust force, which was conducted for the linear machine (cf. **Section 3.5**) can also be applied to one third of the MALTA winding. Therefore, the phase quantities in the MALTA responsible for the thrust force will have the same waveform as the ones for the linear machine (cf. (3.11)). After transforming the three-phase currents into the rotating dq -frame, the i_q current component will contribute to the thrust force generation as $3\pi/\tau_{pp} \hat{\Psi}_M i_q$, where τ_{pp} is the pole pair width in the MALTA

rotor (cf. **Fig. 3.6(b)**) and $\hat{\Psi}_M$ is the flux linkage of the MALTA coil. However, since only one third of the MALTA winding is considered, the total thrust force of the MALTA is obtained by multiplying the linear machine force expression with 3, which gives

$$F_z = \frac{9\pi}{\tau_{pp}} \hat{\Psi}_M i_q. \quad (3.27)$$

This expression is verified with measurements on the MALTA prototype [35]. The term $(9\pi/\tau_{pp}) \hat{\Psi}_M$ represents the MALTA thrust force constant. The pole pair width in the MALTA prototype is $\tau_{pp} = 30$ mm and the measured flux linkage is $\hat{\Psi}_M = 8.35$ mWb. By using these two values, the MALTA thrust force constant is calculated to be $(9\pi/\tau_{pp}) \hat{\Psi}_M = 7.8$ N/A. On the other hand, using the external force sensor in the test bench, the value of the MALTA thrust force constant is measured to be 7.6 N/A (cf. (6) in [35]). The calculated and the measured value differ only $\approx 2.6\%$, which verifies (3.27).

3.9.2 MALTA Bearing Force Generation

The generation of the bearing forces in the MALTA is very similar to the linear-rotary machine analyzed in **Section 3.8**. The waveforms of the MALTA bearing voltage and current match with (3.15), while only $\omega_R = 0$. Applying the transformation (3.16), the complex space vector of the voltage and the current is

$$\underline{\underline{x}} = \hat{X}_{M,b} e^{i\varphi_x} e^{j\theta_x} e^{j\omega_L t} = \underline{\underline{x}}_{dq} e^{j\omega_L t}, \quad (3.28)$$

where $x \in \{u, i\}$ and $\underline{\underline{x}}_{dq} = \hat{X}_{M,b} e^{i\varphi_x} e^{j\theta_x}$. Similarly, for the flux linkage, (3.23) may be used, where $\omega_R = 0$. With (3.16) this results in the complex space vector of the MALTA bearing flux linkage as

$$\underline{\underline{\psi}} = \chi_{pm,M} (x + iy) e^{i\varphi_\psi} e^{j\theta_\psi} e^{j\omega_L t}, \quad (3.29)$$

where $\chi_{pm,M}$ is the MALTA flux linkage radial sensitivity. In order to determine the bearing forces F_x and F_y of the MALTA, similar to the linear-rotary machine, the electric power and the mechanical power expressions are compared. The term of the electric power that contributes to the mechanical power is the same as for the linear-rotary machine (cf. (3.25)), just replacing $\omega_R = 0$. Therefore, the radial forces of the MALTA are generated as

$$F_x = \frac{9}{4} \chi_{pm,M} i_{dd}, \quad F_y = \frac{9}{4} \chi_{pm,M} i_{qd}, \quad (3.30)$$

which are the same bearing forces as obtained in (3.26) and are again independently controlled with the i_{dd} and i_{qd} current components of the MALTA winding. In addition, a parasitic thrust force component is created when the rotor radial displacement is non-zero, which is equal to $F_z = (9\pi/2\tau_{pp})\chi_{pm,M}(xi_{dq} + yi_{qq})$ and has to be compensated by the controller.

In order to verify (3.30) and to estimate the impact of the parasitic thrust force, the flux linkage radial sensitivity for the MALTA prototype from [35] is estimated with FEM. For the MALTA prototype, where each coil has 205 turns, the average flux linkage radial sensitivity is $\chi_{pm,M} \approx 2.56$ Wb/m. Using (3.30), the term $(9/4)\chi_{pm,M} \approx 5.75$ N/A is the MALTA average bearing constant, since the effective value also depends on the displacement direction, i.e. whether the rotor is displaced either towards a stator tooth or towards the stator winding, as explained and measured in [35]. The average thrust force constant is then 5.94 N/m, which is very close to the value calculated using (3.30). The value for the flux linkage radial sensitivity $\chi_{pm,M}$ may also be used to check for the expected parasitic thrust force. For the MALTA prototype $\tau_{pp} = 30$ mm and if a radial displacement of $x = 10$ μ m and an electrical current of $i_{dq} = 6$ A are assumed, the parasitic thrust force is calculated to be $F_z = (9\pi/2\tau_{pp})\chi_{pm,M}(xi_{dq} + yi_{qq}) = 0.07$ N, which is negligible compared to the MALTA continuous forces ~ 20 N (cf. [35]). For the sake of clarity, the assumed current $i_{dq} = 6$ A is twice the continuous current allowed by the thermal limit, and only occurs e.g. during transients.

3.10 Summary

This chapter focuses on the complex space vector modeling of electric machines with permanent magnet (PM) rotor covering all possible movements such as rotary, linear and radial, i.e. magnetic bearing (MB). To the best knowledge of the author, for the first time in literature a complex space vector model of the linear-rotary machine with MBs is formulated, allowing to apply known complex space vector techniques used for years for modeling of electric machines. For example, the phase winding of the linear-rotary machine may be described with a single complex space vector voltage equation using the proposed transformation, which has the same form as the complex space vector voltage equation of the conventional rotary or linear machine. The torque, the thrust force and the radial (bearing) forces onto the rotor can be easily calculated using the proposed complex space vector model, which is

of interest for understanding the machine operation and implementing the control system.

The derived models of the linear-rotary machines in stationary dq reference frame are used in the later chapters for the control system design. More specifically, in **Chapter 6** for the MALTA controller design and in **Chapter 10** for the DS LiRA controller design.

Based on the derived scaling laws (**Chapter 2**) and dq models (**Chapter 3**), a design of a bearingless linear actuator (MALTA) will be discussed in the following **Chapter 4**, while in the further **Chapter 8** the design of a bearingless linear-rotary actuator with double stators is given.

4

Design of the Linear Machine with Integrated Magnetic Bearings

To understand and verify the concept of the tubular linear machine with integrated magnetic bearings (also called MALTA), the machine topology derivation is explained in detail in this chapter. Moreover, various winding realizations that result in different required numbers of half-bridges in the inverter are compared. The MALTA prototype with the winding realization featuring the highest force density is realized in hardware and FEM design models are verified with measurements. Parts of the material presented in this chapter are published in [35].

4.1 Introduction

Tubular linear actuators (TLAs) offer certain benefits compared to flat linear actuators such as better exploitation of the permanent magnet (PM) flux, absence of asymmetric attractive forces between the stator and the mover, and higher power density [71]. Therefore, there is a growing trend in using TLAs in many versatile applications such as pick-and-place robots used in packaging lines or very precise component mounting on printed circuit boards [72, 73], surgery robots [74, 75], active suspension of vehicles [76], electrical power generation [42, 77, 78], linear compressors [79–81] and walking robots [82]. Because of their closed construction, TLAs are also convenient for underwater [83] or high-purity applications [84].

Bearings used in TLAs today are mainly mechanical bearings. These bearings feature drawbacks such as friction, risk of contamination due to wear and limited lifetime [43]. Moreover, their use in high-accuracy positioning

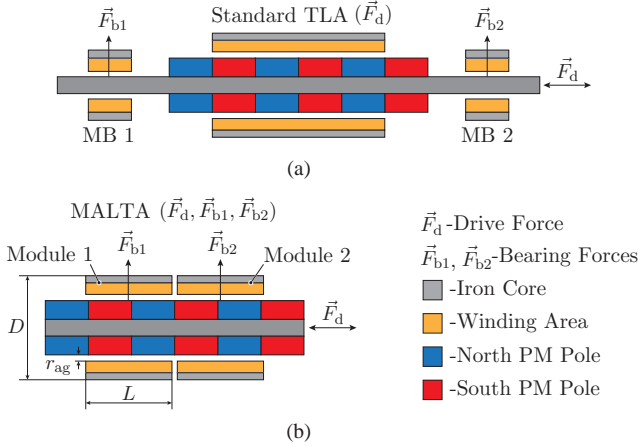


Fig. 4.1: Magnetic support of the mover in TLA: (a) with two standalone MBs and (b) the proposed MALTA.

systems is limited due to thermal disturbance. In order to overcome some of these issues, higher-end TLAs feature air bearings, which, on the other hand, increase system complexity since a pressurized air supply is necessary. Moreover, air bearings prohibit operation in vacuum.

Even though magnetic bearings (MBs) would overcome the issues mentioned earlier, their integration into a TLA system has not been analyzed thoroughly in literature. In [34], a system with two standalone MBs used at each axial end of a TLA is analyzed, see **Fig. 4.1(a)**. This system, compared to the standard TLA, is characterized by a bulkier design, a higher complexity and a longer mover.

In this chapter, the integration of MBs into the TLA, which results in a magnetically levitated tubular actuator (MALTA), is analyzed and an actuator prototype is built. The concept is illustrated in **Fig. 4.1(b)**. The MB integration is achieved by introducing slits in the circumferential direction in the teeth of the standard TLA stator, which are normally not interrupted in the circumferential direction. A new winding arrangement is proposed, which can alter the air gap magnetic field distribution both in the circumferential and axial directions. This is achieved by replacing the circumferentially uninterrupted coils of a standard TLA with concentrated windings wound around the teeth, which are now separated by the newly introduced slits. The proposed MALTA features lower mass and inertia of the moving parts and higher compactness

compared to a standard TLA with additional MBs. Even though the detailed discussion of the suitable control strategies is not the topic of this chapter, the actuator design is carried out with a controlled magnetic levitation in mind. For instance, in order to control the tilting of the mover, the stator of the MALTA consists of two modules (module 1 and module 2, see **Fig. 4.1(b)**) that can generate two independent bearing forces (\vec{F}_{b1} and \vec{F}_{b2}). Moreover, design aspects affecting the levitation controller, such as the radial pull force and the circumferential dependency of the bearing force constant are also studied.

4.2 Derivation of the MALTA Winding

In **Fig. 4.1** two TLA concepts are shown: **(a)** with standalone MBs, which employs windings that can solely generate the drive force \vec{F}_d and windings that can solely generate the bearing forces \vec{F}_{b1} and \vec{F}_{b2} and **(b)** with integrated MBs, which uses windings that can generate both, the drive and the bearing forces. It should be noted that generation of two independent bearing forces is needed, in order to control the tilting of the mover. Going from the solution shown in **Fig. 4.1(a)** to the one shown in **Fig. 4.1(b)** involves the integration of MBs into the TLA, where the fundamental characteristic of the TLA, i.e. the drive force generation, should be kept. This results in a so-called *self-bearing* or *bearingsless* actuator. This terminology is also used for rotary machines/actuators, cf. [85]. Therefore, MALTA could be referred to as a self-bearing TLA or a bearingsless TLA.

In **Fig. 4.2**, various three-phase actuator types are shown, (tubular) rotary actuator (RA), flat linear actuator (FLA) and tubular linear actuator (TLA). In general, RAs are capable of generating a torque \vec{T} and a bearing force \vec{F}_b on the rotor. Unfolding the RA results in FLA, where the tangential force that generates the torque in the RA now acts as a linear driving force \vec{F}_d on the mover of the FLA. Generation of the bearing force on the mover is also possible. A drawback of single-sided PM FLAs are rather large attraction forces between the mover PMs and the stator iron, which makes this solution unpractical for MBs due to constant bearing forces needed to levitate the mover. This issue can be solved by using an iron-less (slot-less) stator [86, 87], or by attaching a FLA on top where the weight of the load would compensate the attraction force. By further folding of the FLA in the direction of the slots as shown in **Fig. 4.2**, a TLA is achieved. This actuator can generate the drive force in the same way as the FLA, since the magnetic coupling between

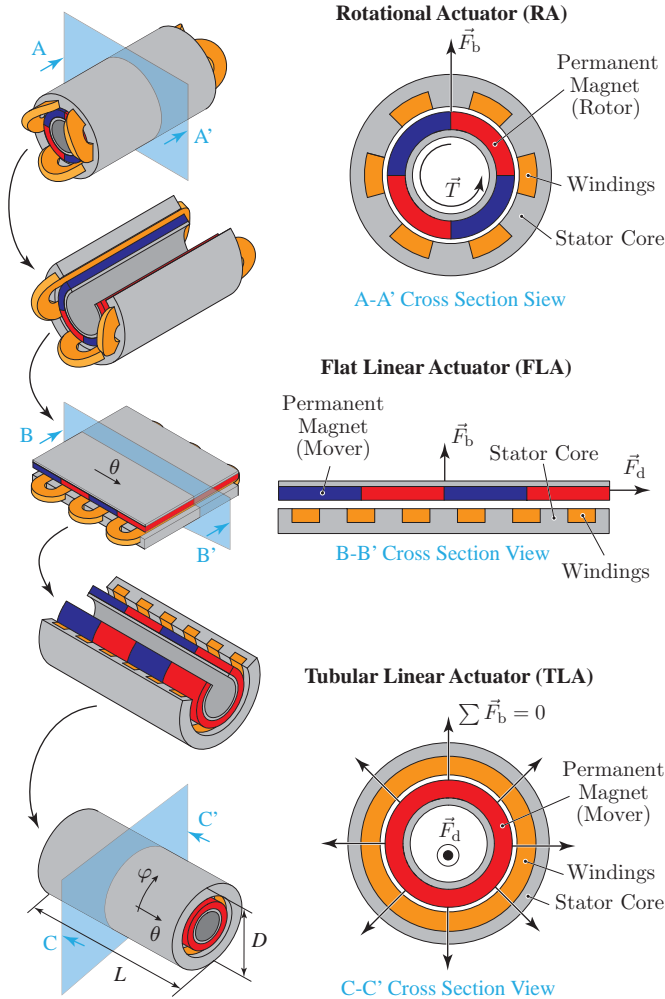


Fig. 4.2: Evolution of a self-bearing (bearingless) FLA from a self-bearing RA through unfolding in circumferential direction. Folding back in axial direction yields the TLA, but the self-bearing capability cannot be maintained.

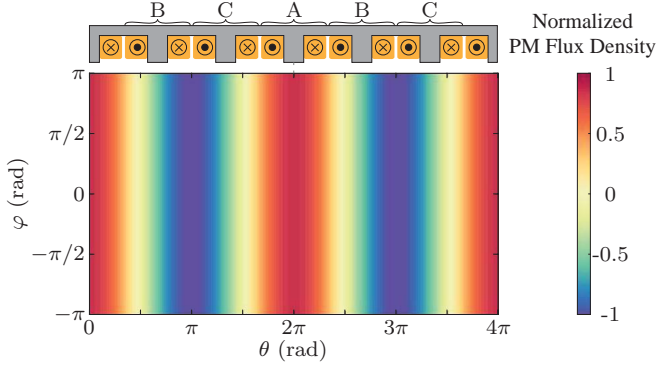


Fig. 4.3: Normalized fundamental component of the radial air gap PM flux density in the TLA. The electrical angles θ and φ are indicated in **Fig. 4.2**. θ denotes the electrical angle in axial (z) direction, while φ is the electrical angle in circumferential direction. Since in circumferential direction there are no PM poles, φ is equal to the mechanical angle.

the stator winding and the mover PMs did not change by folding the FLA. Additionally, in the TLA there is no parasitic attraction forces, as they are compensated by the circumferential symmetry of the actuator.

The radial air gap flux density in the TLA is shown in **Fig. 4.3**, where the angles θ and φ are indicated in **Fig. 4.2**. Additionally, in **Fig. 4.3** the TLA stator is shown. It is positioned such that the first phase A is aligned with the maximum PM flux density. Therefore, the fundamental component of the three-phase flux linkage may be written as

$$\begin{bmatrix} \psi_A \\ \psi_B \\ \psi_C \end{bmatrix} = \hat{\Psi}_M \begin{bmatrix} \cos(\theta) \\ \cos(\theta - 2\pi/3) \\ \cos(\theta + 2\pi/3) \end{bmatrix}, \quad (4.1)$$

where $\hat{\Psi}_M$ is the TLA flux linkage. To generate the drive force with the TLA, the three-phase currents existing in the stator should have the the following waveforms

$$\begin{bmatrix} i_A \\ i_B \\ i_C \end{bmatrix} = \hat{I}_M \begin{bmatrix} \cos(\theta + \pi/2) \\ \cos(\theta + \pi/2 - 2\pi/3) \\ \cos(\theta + \pi/2 + 2\pi/3) \end{bmatrix}. \quad (4.2)$$

If the reluctance force component in the MALTA is neglected, this phase of the current, being $\pi/2$ shifted with respect to the flux linkage gives the

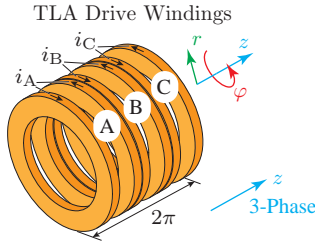


Fig. 4.4: Three-phase TLA winding where 3 stator slots span along a single pole pair of the mover PMs. The winding is symmetric in circumferential direction (ϕ -direction).

maximum drive force per copper loss. The TLA three-phase windings are shown in **Fig. 4.4**. The TLA windings have ϕ symmetry, therefore, the field generated by the TLA windings does not change along the circumference, which is shown in **Fig. 4.5**. As expected, the two field components in the TLA, from the PMs (cf. **Fig. 4.3**) and from the drive currents (cf. **Fig. 4.5**), which interact in the air gap of the TLA, are shifted by $\pi/2$ electrical radians. The two fields tend to align, which creates the drive force onto the mover.

In general, the radial force in electric machines that acts onto the rotor/mover is generated if the air gap field is not symmetric in circumferential direction. As in the TLA, the both fields, from the PMs and the stator currents (cf. **Fig. 4.3** and **Fig. 4.5**), have circumferential symmetry, it is not possible to generate any radial force. Therefore, it is not possible to implement MBs with the TLA geometry of the windings.

To generate the bearing force, the magnetic field in the air gap must be modulated in circumferential direction. In **Fig. 4.6** an interaction between the mover PM field at the axial position $\theta = 2\pi$ and the field with two poles is shown, resulting in a bearing force onto the mover. The force direction can be controlled by controlling the field orientation. Therefore, in order to allow bearing force control in the TLA, its stator should be modified such that it can generate the field shown in **Fig. 4.6(b)**. Additionally, at the positions where the mover radial flux density is zero, e.g. $\{\pi/2, 3\pi/2, 5\pi/2, 7\pi/2\}$ in **Fig. 4.3**, it is not possible to generate any radial forces, therefore, the stator should not create a field in these zones. Also, the field in these zones would create a drive force (cf. **Fig. 4.5**), which is not desirable as it would introduce coupling between the drive and the bearing forces. Therefore, the stator field that should generate the bearing forces is modulated in both directions, axial θ and circumferential ϕ . An example of such field is shown in **Fig. 4.7**, where

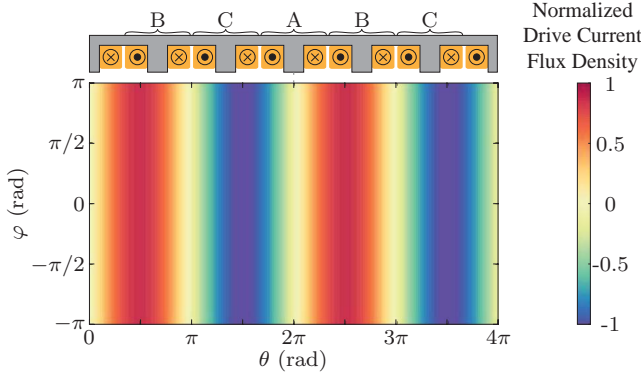


Fig. 4.5: Normalized fundamental component of the radial air gap flux density in the TLA, originating from the drive currents given in (4.2). The electrical angles θ and φ are denoted in **Fig. 4.2**. θ denotes the electrical angle in axial (z) direction, while φ is the electrical angle in circumferential direction.

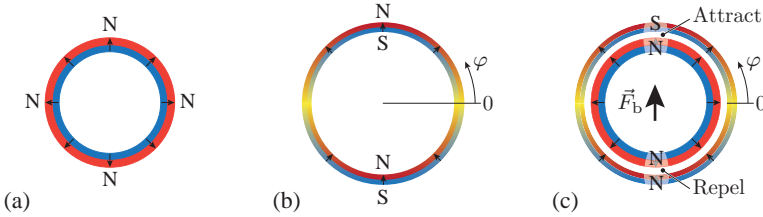


Fig. 4.6: (a) PM field from the MALTA mover at the axial position $\theta = 2\pi$, cf. **Fig. 4.3**. The field lines close axially, therefore, along the outer circumference the North pole N exists. (b) A two pole magnetic field which lines close circumferentially resulting in the North N and the South S poles. From inner side, the S pole is located at $\varphi = 90^\circ$, while the N pole at $\varphi = -90^\circ$. (c) Interaction of the two fields results in the bearing force \vec{F}_b in the direction of $\varphi = 90^\circ$. Since the mover PM field is constant for any $\varphi \in [-\pi, \pi]$, the bearing force direction can be controlled by controlling the direction of the field from (b).

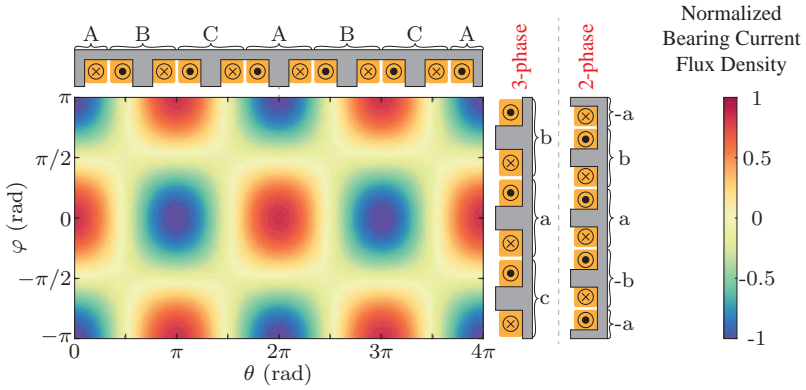


Fig. 4.7: Normalized fundamental component of the radial air gap flux density from the MALTA winding, created by the bearing current. θ denotes the electrical angle in axial (z) direction, while φ is the electrical angle in circumferential direction.

the alternation of the poles in θ - and φ -direction is achieved. To create such a field distribution, a simultaneous action from the stator in θ - and φ -direction is needed. In θ -direction, the same stator as for the TLA is kept, i.e. with three-phases A, B and C. The field alternation/modulation in φ -direction may be achieved either with a three- or two-phase stator, as shown in **Fig. 4.7**. This requirement, to keep the three-phases in θ -direction and to consider three- and two-phases in φ -direction, results in the winding realizations shown in **Fig. 4.8**, which are called the MALTA windings. It should be mentioned that the notation of the phases in θ -direction is done with capital letters (ABC), while in φ -direction with small letters (abc). The MALTA windings are derived from the TLA windings, by interrupting them in circumferential direction, i.e. from a single TLA coil three or four MALTA winding coils are created. For example, the coil from the first phase A in TLA (cf. **Fig. 4.4**) is interrupted/split in circumferential direction into more coils, either aA-bA-cA for the three-phase or aA-bA-cA-dA for the two-phase option (cf. **Fig. 4.8**).

In order to create the air gap field shown in **Fig. 4.7** that would generate the bearing force, the currents in the MALTA winding should have proper waveforms. For the 3×3 -phase MALTA winding (cf. **Fig. 4.8(a)**), the currents

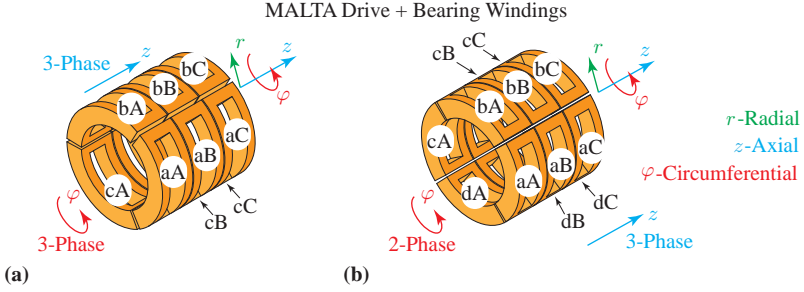


Fig. 4.8: Schematic representation of the MALTA winding that can generate the drive and the bearing force: **(a)** the winding with three-phases in circumferential direction and three-phases in axial direction (3×3 -phase winding) and **(b)** the winding with two-phases in circumferential direction and three-phases in axial direction (2×3 -phase winding).

are equal to

$$\begin{aligned}
 i_{aA} &= \hat{I}_{Mb} \cos(\varphi) \cos(\theta) \\
 i_{bA} &= \hat{I}_{Mb} \cos(\varphi - 2\pi/3) \cos(\theta) \\
 i_{cA} &= \hat{I}_{Mb} \cos(\varphi + 2\pi/3) \cos(\theta) \\
 i_{aB} &= \hat{I}_{Mb} \cos(\varphi) \cos(\theta - 2\pi/3) \\
 i_{bB} &= \hat{I}_{Mb} \cos(\varphi - 2\pi/3) \cos(\theta - 2\pi/3) \\
 i_{cB} &= \hat{I}_{Mb} \cos(\varphi + 2\pi/3) \cos(\theta - 2\pi/3) \\
 i_{aC} &= \hat{I}_{Mb} \cos(\varphi) \cos(\theta + 2\pi/3) \\
 i_{bC} &= \hat{I}_{Mb} \cos(\varphi - 2\pi/3) \cos(\theta + 2\pi/3) \\
 i_{cC} &= \hat{I}_{Mb} \cos(\varphi + 2\pi/3) \cos(\theta + 2\pi/3)
 \end{aligned} \tag{4.3}$$

For the 2×3 -phase MALTA winding (cf. **Fig. 4.8(b)**), the currents are equal to

$$\begin{aligned}
 i_{aA} &= \hat{I}_{Mb} \cos(\varphi) \cos(\theta) \\
 i_{bA} &= \hat{I}_{Mb} \sin(\varphi) \cos(\theta) \\
 i_{aB} &= \hat{I}_{Mb} \cos(\varphi) \cos(\theta - 2\pi/3) \\
 i_{bB} &= \hat{I}_{Mb} \sin(\varphi) \cos(\theta - 2\pi/3) \\
 i_{aC} &= \hat{I}_{Mb} \cos(\varphi) \cos(\theta + 2\pi/3) \\
 i_{bC} &= \hat{I}_{Mb} \sin(\varphi) \cos(\theta + 2\pi/3)
 \end{aligned} \tag{4.4}$$

It should be noted that the drive currents i_A , i_B and i_C given in (4.2) are $+\pi/2$ shifted compared to the θ -component of the bearing currents given in (4.3) and (4.4). Therefore, the bearing current component will not generate any drive force.

The simultaneous action of the drive and the bearing current components in the creation of the air gap field is shown in **Fig. 4.9** for different values of the bearing and the drive current amplitudes.

4.3 MALTA Winding Realizations

In **Fig. 4.8** two possible MALTA windings are shown, with either two- or three-phases in circumferential φ -direction and three-phases in axial θ -direction. In this section, a step further is analyzed, where the possible MALTA winding realizations are considered and compared with respect to the inverter effort (required number of half-bridges) and the achievable bearing and drive forces.

The MALTA windings shown in **Fig. 4.8** may be used to control the bearing and the drive force, simultaneously. In that case, the total current in the winding consists of two components: the bearing and the drive current component. This winding is typically called *combined winding*. The MALTA windings (cf. **Fig. 4.8**) may be used in the combination with the TLA drive windings (cf. **Fig. 4.4**), where the two winding systems would be physically separated in the MALTA stator. The MALTA winding would carry only the bearing current component, while the drive winding would carry the drive current component. Such winding realization is called *separated winding*. Both winding realizations are shown in **Fig. 4.10**. In the following, the required phase current and the resulting inverter effort are analyzed for each of the MALTA winding realizations.

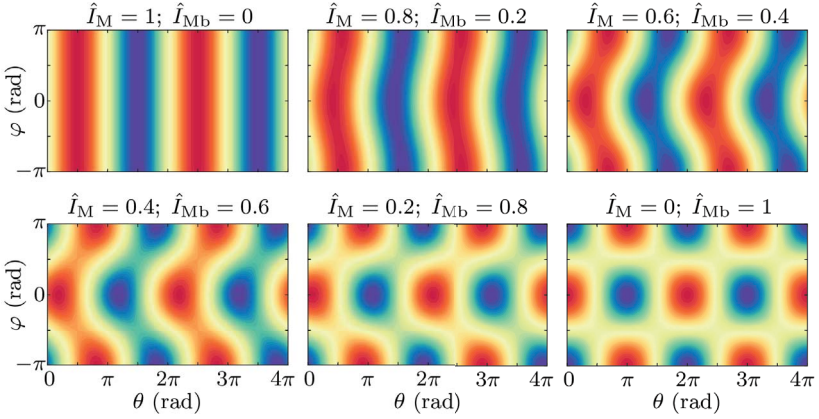


Fig. 4.9: Normalized radial air gap flux density of the MALTA windings created by the drive and the bearing current components acting simultaneously. The fields are shown for different ratios of the drive \hat{I}_M and the bearing currents \hat{I}_{Mb} , starting from only a drive current and no bearing current, till only a bearing current existing and no drive current. It should be noted that the drive and the bearing field distributions are shifted by $\pi/2$ in axial θ -direction.

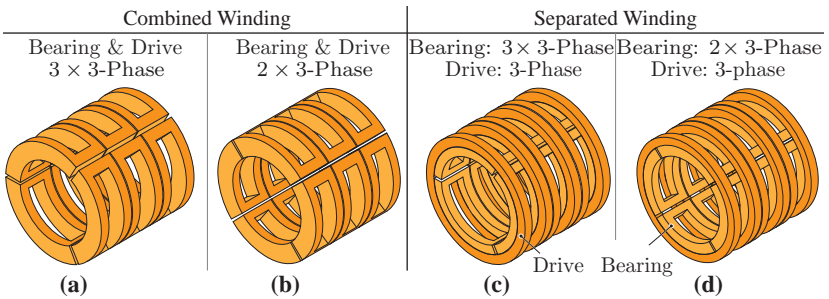


Fig. 4.10: Two types of MALTA winding realizations are possible: combined windings (a,b) and separated windings (c,d). The coils in the combined windings contain both current components, bearing and drive, while the separated windings have these two current components physically separated with dedicated bearing and drive winding.

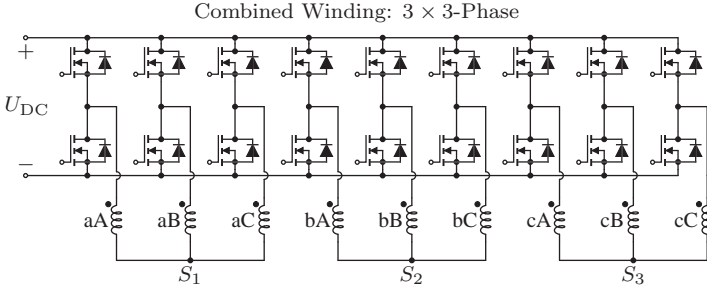


Fig. 4.11: The required number of half-bridges in the inverter for the MALTA combined winding with 3×3 -phases (cf. **Fig. 4.10(a)**) is 9 half-bridges per module. In total, at least 2 modules are needed to control the tilting of the mover (cf. **Fig. 4.1(b)**), therefore, an inverter with 18 half-bridges is needed to supply this MALTA winding.

Combined Winding: 3×3 -Phase

The winding realization is shown in **Fig. 4.10(a)**. The winding current has two components, the bearing and the drive component, and therefore, the total current is the superposition of the two components

$$\begin{bmatrix} i_{aA} + i_A & i_{aB} + i_B & i_{aC} + i_C \\ i_{bA} + i_A & i_{bB} + i_B & i_{bC} + i_C \\ i_{cA} + i_A & i_{cB} + i_B & i_{cC} + i_C \end{bmatrix}, \quad (4.5)$$

where the current component waveforms are given in (4.3) and (4.2). An inverter with 18 half-bridges is required to supply this MALTA winding realization, cf. **Fig. 4.11**. The star points S_1 , S_2 and S_3 should be kept unconnected, such that the potential occurrence of a low frequency zero sequence current (common mode (CM) current) is prevented.

Combined Winding: 2×3 -Phase

The winding realization is shown in **Fig. 4.10(b)**. The winding current has two components, the bearing and the drive component, and therefore, the total current is the superposition of the two components

$$\begin{bmatrix} i_{aA} + i_A & i_{aB} + i_B & i_{aC} + i_C \\ i_{bA} + i_A & i_{bB} + i_B & i_{bC} + i_C \\ -i_{aA} + i_A & -i_{aB} + i_B & -i_{aC} + i_C \\ -i_{bA} + i_A & -i_{bB} + i_B & -i_{bC} + i_C \end{bmatrix}, \quad (4.6)$$

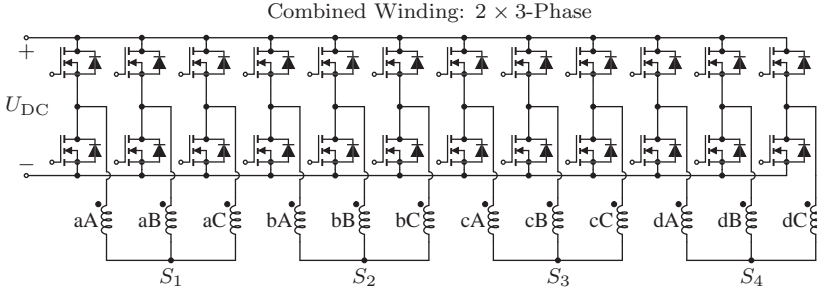


Fig. 4.12: The required number of half-bridges in the inverter for the MALTA combined winding with 2×3 -phases (cf. **Fig. 4.10(b)**) is 12 half-bridges per module. In total, at least 2 modules are needed to control the tilting of the mover (cf. **Fig. 4.1(b)**), therefore, an inverter with 24 half-bridges is needed to supply this MALTA winding.

where the current component waveforms are given in (4.4) and (4.2). An inverter with 24 half-bridges is required to supply this MALTA winding realization, cf. **Fig. 4.12**. The star points S_1 , S_2 , S_3 and S_4 should be kept unconnected, such that the potential occurrence of a low frequency zero sequence current (common mode (CM) current) is prevented.

Separated Winding: 3×3 -Phase + 3-Phase

The winding realization is shown in **Fig. 4.10(c)**. The two current components, the bearing and the drive component, exist in separate winding sections of the MALTA stator

$$\text{bearing: } \begin{bmatrix} i_{aA} & i_{aB} & i_{aC} \\ i_{bA} & i_{bB} & i_{bC} \\ i_{cA} & i_{cB} & i_{cC} \end{bmatrix}, \quad \text{drive: } \begin{bmatrix} i_A \\ i_B \\ i_C \end{bmatrix}, \quad (4.7)$$

where their waveforms are given in (4.3) and (4.2). An inverter with 21 half-bridges is required to supply this MALTA winding realization, cf. **Fig. 4.13**. The star points S_1 , S_2 , S_3 and S should be kept unconnected, such that the potential occurrence of a low frequency zero sequence current (common mode (CM) current) is prevented.

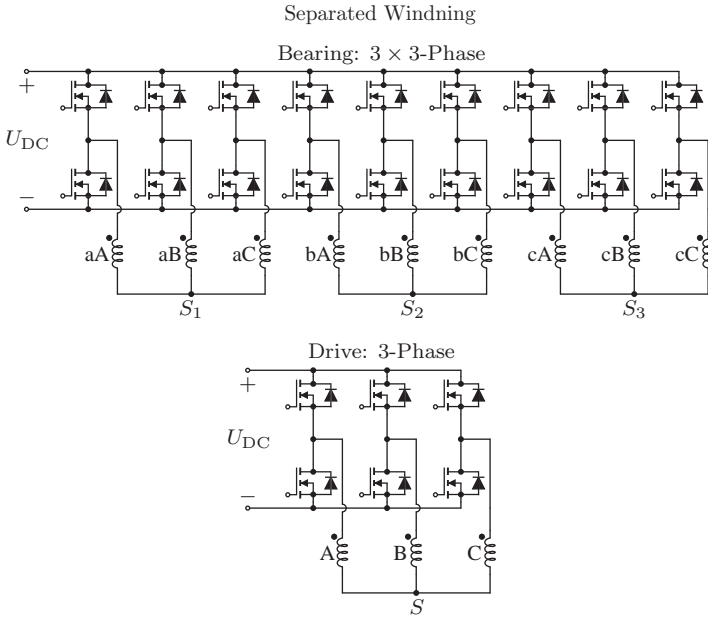


Fig. 4.13: The required number of half-bridges in the inverter for the bearing part of the MALTA separated winding with 3×3 -phases is 9 half-bridges per module. At least 2 modules are needed to control the tilting of the mover (cf. **Fig. 4.1(b)**), therefore, 18 half-bridges are needed to supply the bearing part of this MALTA winding. For the drive part of the winding 3 half-bridges are needed. Therefore, in total an inverter with 21 half-bridges is needed to supply this winding, which realization is shown in (cf. **Fig. 4.10(c)**).

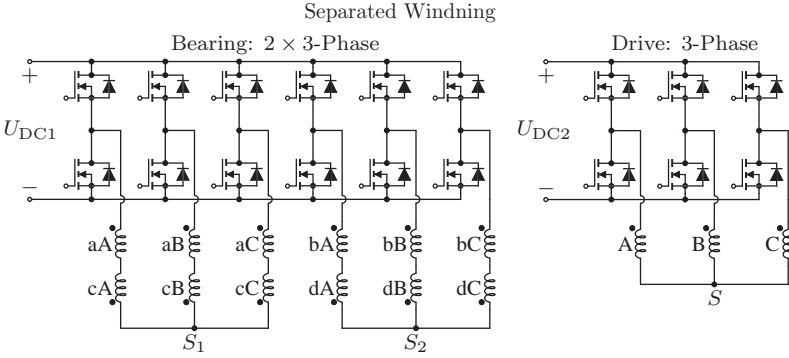


Fig. 4.14: The required number of half-bridges in the inverter for the bearing part of the MALTA separated winding with 2×3 -phases is 6 half-bridges per module. At least 2 modules are needed to control the tilting of the mover (cf. **Fig. 4.1(b)**), therefore, 12 half-bridges are needed to supply the bearing part of this MALTA winding. For the drive part of the winding 3 half-bridges are needed. Therefore, in total an inverter with 15 half-bridges is needed to supply this winding, which realization is shown in (cf. **Fig. 4.10(d)**).

Separated Winding: 2×3 -Phase + 3-Phase

The winding realization is shown in **Fig. 4.10(d)**. The two current components, the bearing and the drive component, exist in separate winding sections of the MALTA stator

$$\text{bearing: } \begin{bmatrix} i_{aA} & i_{aB} & i_{aC} \\ i_{bA} & i_{bB} & i_{bC} \\ -i_{aA} & -i_{aB} & -i_{aC} \\ -i_{bA} & -i_{bB} & -i_{bC} \end{bmatrix}, \quad \text{drive: } \begin{bmatrix} i_A \\ i_B \\ i_C \end{bmatrix}, \quad (4.8)$$

where their waveforms are given in (4.4) and (4.2). An inverter with 15 half-bridges is required to supply this MALTA winding realization, cf. **Fig. 4.14**. The star points S_1 , S_2 and S should be kept unconnected, such that the potential occurrence of a low frequency zero sequence current (common mode (CM) current) is prevented.

It should be noted that the flux linkage in the coils at the same axial position is equal, since the PM field from the mover does not change around the circumference φ , cf. **Fig. 4.3**. Consequently, the induced voltage is equal in the coils around the circumference and due to anti-series connection of $a\{A,B,C\}$ - $c\{A,B,C\}$ and $b\{A,B,C\}$ - $d\{A,B,C\}$ in the bearing winding (cf. **Fig. 4.14**)

Tab. 4.1: Comparison of the winding realizations.

Winding Realization	Shown	Force/ $F_{d,TLA}$		Number of Half-Bridges
		Drive	Bearing	
Combined				
3×3 -Phase	Fig. 4.11(a)	0.78	1.12	18
2×3 -Phase	Fig. 4.12(b)	0.76	1.1	24
Separated				
3×3 -Phase +3-Phase	Fig. 4.13(c)	0.57	0.81	21
2×3 -Phase +3-Phase	Fig. 4.14(d)	0.29	0.46	15

it cancels out. Therefore, the two-level inverter supplied from the U_{DC1} will not see any induced voltage. This allows to use eventually different DC-link voltages, e.g. U_{DC1} may be lower than U_{DC2} and the bearing inverter may be realized with lower blocking voltage semiconductors than for the drive inverter.

4.4 Comparison of the MALTA Winding Realizations

In this section the MALTA winding realizations shown in **Fig. 4.10** are compared with respect to the achievable drive and the bearing force. The benchmark actuator in the comparison is the conventional TLA (cf. **Fig. 4.2** and **Fig. 4.3**). The goal is to obtain a relative comparison among the MALTA winding realizations such that the best performing one could be chosen. Therefore, the absolute values of the forces are currently not of interest. In order to perform an as fair as possible comparison, the magnetic circuits of all the actuator options are the same, which includes the outer diameter of the stator and the tooth depth, the air gap, the mover geometry and the material properties. For the separated windings, the winding depth space is divided equally between the drive and the bearing windings. Additionally, the copper losses of each winding realization are fixed to the same value. Therefore, the current amplitudes \hat{I}_M and \hat{I}_{Mb} are set such that the drive force generation as well as the bearing force generation result in the same amount of copper losses for each MALTA winding realization. Iron core losses are neglected in this comparison.

In **Tab. 4.1** the relative comparison between the MALTA winding realizations is shown. The benchmark force value is the TLA drive force $F_{d,TLA}$, achieved with the same stator and the mover geometrical parameters and

Tab. 4.2: MALTA design constraints.

Symbol	Quantity	Value
Geometrical		
L	Module active length	60 mm
D	Stator diameter	60 mm
r_{ag}	Air gap radial size	2 mm
Materials		
-Solid steel CK45 used as iron core material		
μ_r	Relative permeability	500
B_{max}	Saturation flux density	1.3 T
-Neodymium PM used in the mover		
B_r	PM remanent flux density	1.18 T
-Copper used for windings		
σ_{Cu}	Copper conductivity (20 °C)	58.5 S/m

the copper losses as for the MALTA winding realizations, just having TLA windings (cf. **Fig. 4.4**) and the stator teeth with no circumferential slots. The results are obtained by using 3D-FEM models of the analyzed actuators.

The winding realization with the highest drive and the bearing force is the MALTA **3 × 3-phase combined winding**. Therefore, this winding realization is further considered.

4.5 Machine Design

Key design aspects of the MALTA are addressed in this section. By choosing the key geometry parameters, the goal of the design is to maximize the axial force and the bearing forces and to minimize the mover mass, i.e. to maximize the axial and sustainable radial accelerations¹.

The constraints in the MALTA design are the outer dimensions, radial air gap size and material properties as summarized in **Tab. 4.2**. Additionally, practical limitations such as simple manufacturing of windings, off-the-shelf available PM shapes, easily accessible and machinable core materials are all boundaries that are considered in this design.

FEM analysis is used in the design procedure. The reason for not using analytic models is their typical limitation to cylindrical coordinate systems,

¹A linear actuator can be mounted on a kinematic system that moves it radially with high accelerations. This translates into a sustainable radial acceleration, i.e. a MB force requirement that depends on the mover's mass and the acceleration of the whole MALTA in the radial direction.

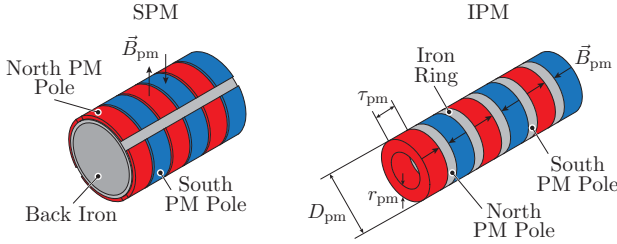


Fig. 4.15: SPM and IPM mover.

i.e. the models cannot account for radial displacement, i.e. cannot calculate the radial pull force.

4.5.1 Mover Design

Two different mover configurations are considered in the design procedure, i.e. surface-mounted PMs (SPM) and interior PMs (IPM), as shown in **Fig. 4.15**. The SPM mover consists of PMs magnetized in radial direction, as denoted with arrows pointing radially outwards (North PM pole) and radially inwards (South PM pole). In the IPM mover type, PMs are magnetized axially. Therefore, the iron rings are used to form the poles in this mover type.

The range of the considered PM dimensions, especially their outer diameter is determined based on the scaling laws for the thrust force interior mover actuator, derived in **Chapter 2**. More specifically, in **Fig. 2.6** it can be seen that the optimum ratio of the outer winding diameter ($D - 2r_{bi}$, cf. **Fig. 2.4**) and the inner winding diameter ($D_{pm} + 2r_{ag}$) depends on the cooling of the actuator. If conditions close to natural convection are assumed, which is justified since the MALTA is not considered to have water cooling, the optimum ratio of the winding inner and outer diameters should be in the range

$$\frac{D_{pm} + 2r_{ag}}{D - 2r_{bi}} = [0.5, 0.7] \quad (4.9)$$

where r_{bi} is the back-iron thickness. If a back-iron thickness of $r_{bi} = 2$ mm is assumed, the suggested optimum diameter range of the PMs is

$$\begin{aligned} D_{pm} &= (D - 2r_{bi}) \cdot [0.5, 0.7] - 2r_{ag} \\ &= [24 \text{ mm}, 35.2 \text{ mm}] \end{aligned} \quad (4.10)$$

Tab. 4.3: Considered PMs for the mover design.

Number	Pole Size	D_{pm}	r_{pm}	τ_{pm}
SPM (radially magnetized PMs)				
1	10 mm	35.75 mm	1.5 mm	9 mm
2	7.5 mm	22.6 mm	1.3 mm	6.5 mm
IPM (axially magnetized PMs)				
3	10.5 mm	23 mm	5.15 mm	7 mm
4	15 mm	25 mm	2.5 mm	10 mm
5	15 mm	27 mm	5.5 mm	10 mm
6	15 mm	27 mm	3 mm	10 mm
7	15 mm	34 mm	6.5 mm	10 mm

Highlighted geometry is the chosen design.

Therefore, the considered PM dimensions are given in **Tab. 4.3**. These PMs define different mover geometries, and each of them is evaluated with two 3D-FEM magnetostatic simulations, one for axial force, and one for bearing force. Axial and sustainable radial accelerations are calculated in post processing based on the obtained forces. No additional load is considered, i.e. the actuator is used only for levitating and accelerating its mover, which is a very reasonable assumption e.g. considering the use of a MALTA in pick-and-place robots in semiconductor industry, where the mass of the potential load is negligible compared to that of the mover itself. The forces are determined by the electrical loading, which is limited by the maximum allowed winding temperature and the actuator's thermal properties. In order to provide quantitative results, the electrical loading is set such that the mean copper losses are 15 W, which is based on a simplified thermal model that is given in [16] for an actuator with similar outer dimensions. However, since the final performance of the MALTA will depend strongly on the actual cooling performance, the thermal properties of the actuator will be studied experimentally in **Section 4.7.2**. A winding fill factor of 0.6 is assumed based on earlier experience with electrical machines of similar size.

The performance of different mover geometries is shown in **Fig. 4.16**. This analysis shows the contradiction between the forces and accelerations, which is an expected behavior as more PMs in the mover guarantee higher flux density in the air gap and consequently higher forces. On the other hand, more PMs increase the mover mass and reduce the accelerations. A mover geometry that is a good compromise between high forces and high accelerations is chosen as final mover design, which is the IPM mover topology that is denoted in **Fig. 4.16** and its dimensions are highlighted in **Tab. 4.3**.

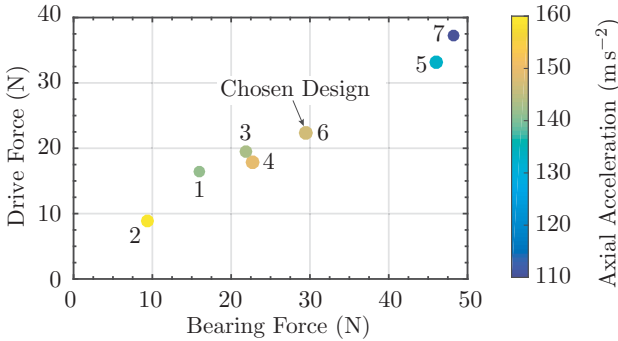


Fig. 4.16: Performance comparison of different mover geometries defined with **Tab. 4.3**. The numbers next to the dots denote the number in **Tab. 4.3**. The chosen design is number 6 and it is highlighted in **Tab. 4.3**.

4.5.2 Stator Design

A key aspect in the MALTA stator design is the trade-off between the achievable drive and bearing forces, and the radial pull force when the mover is radially displaced. The effect of two key geometrical parameters, tooth thickness τ_t and tooth depth r_t (cf. **Fig. 4.17(a)**), on this trade-off is studied. Since the start-up is the most critical for the MBs, i.e. requires the highest radial pull force, this scenario is used to determine the stator teeth size.

Two groups of 3D-FEM simulations are performed for the MALTA in the scenario where the mover touches the touch-down bearing (a touch-down bearing is used in machines with MBs to avoid a damage of the mover or the stator in case the MBs stop working or are overloaded [22]). In one group the tooth thickness τ_t has a fixed value and the tooth depth r_t is changed. In the other group, the tooth thickness τ_t is changed while the tooth depth r_t is fixed. The outer dimensions of the windings are fixed, see **Fig. 4.17(a)**.

In the first group of simulations, the influence of the tooth depth on the drive, bearing and the radial pull forces is examined. If the tooth depth is equal to the radial size of the windings ($r_t = 12.5$ mm), the radial pull force is much higher than the continuous bearing force. In order to reduce the radial pull force, the tooth depth is reduced and its influence on the forces is shown in **Fig. 4.18(a)**. As a consequence, the continuous drive and bearing forces are lower. The tooth depth of $r_t = 11$ mm is chosen for the final design, since

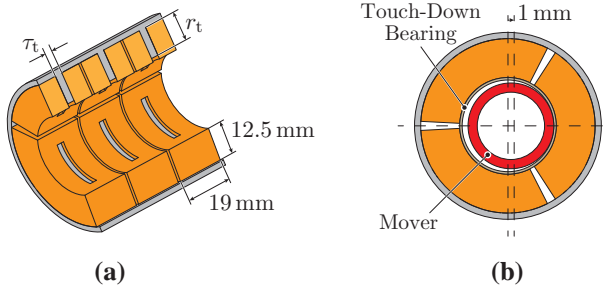


Fig. 4.17: (a) Cross section of the MALTA module with denoted teeth size and size of the winding. (b) Stator teeth design scenario: mover displaced such that it touches the touch-down bearing (1 mm displacement). The thickness of the touch-down bearing is 1 mm.

the pull force is significantly reduced and close to the continuous bearing force.

In the second group of the simulations, see **Fig. 4.18(b)**, the influence of the tooth thickness on the drive, bearing and radial pull forces is examined. Increasing the tooth thickness leads to an increased radial pull force, but results in no increase of the drive and bearing forces since the copper volume and hence the electric loading are decreasing. Therefore, the tooth thickness of $\tau_t = 3$ mm is chosen for the final design.

Generally, in systems with short stroke movement the average speed is rather low. Consequently, eddy-current losses due to the PM movement are low compared to copper losses, which justifies building these systems from solid iron [44]. Additionally, this is shown once more here, using a worst case 2D-FEM model.

Because of the transverse flux in the stator iron and complicated geometry, lamination is not considered. The stator is built of solid steel CK45, which magnetic properties are measured and reported in [88]. In order to check the order of eddy-current losses in the stator iron, a 2D-FEM model is utilized, see **Fig. 4.19**. A very high axial acceleration of $20g$ is assumed. The acceleration is intentionally selected above values which the machine can continuously deliver, such that the eddy-currents are calculated for the absolute worst case. The 2D-FEM model is axis-symmetric, therefore the slits between the teeth of the MALTA are neglected, which is another worst-case approximation, as both the total flux and the eddy-current loop are larger. Hence, the eddy-current losses in the actual MALTA will be lower for the same speed profile.

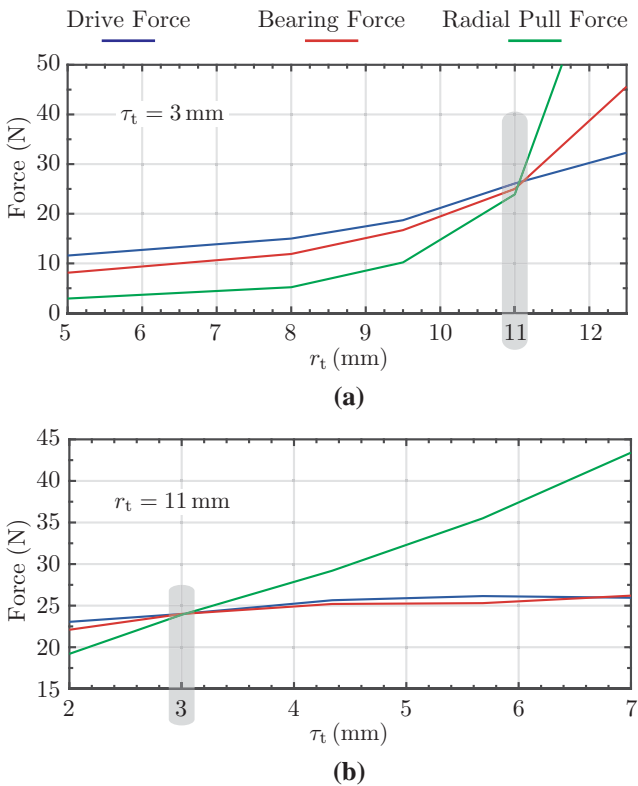


Fig. 4.18: Two groups of 3D-FEM simulations that examine the influence of the tooth depth (r_t) and the tooth thickness (τ_t) on the drive, bearing and radial pull forces: **(a)** tooth thickness is constant, while tooth depth is swept, and **(b)** tooth thickness is swept, while tooth depth is constant.

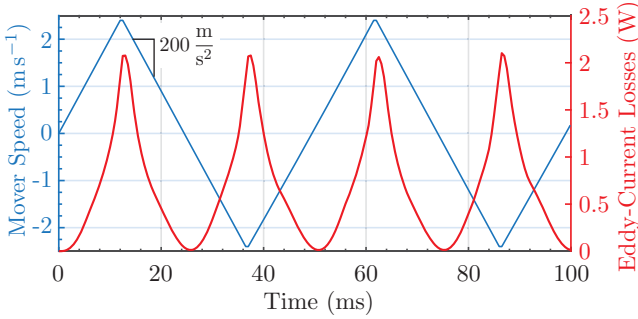


Fig. 4.19: Simulated eddy-current losses in the stator teeth and back iron for a speed profile (blue curve) in the extreme case where the mover accelerates and decelerates with $20g$ for an axial stroke of 30 mm. The obtained average eddy-current losses are ≈ 0.7 W.

The average eddy-current losses are 0.7 W, which is only 4.7 % of the assumed copper losses. Therefore, it is expected that the eddy-current losses will not have a significant influence on the temperature rise of the MALTA and will not impair its performance.

4.6 MALTA Prototype

4.6.1 Mover

The mover is of IPM type (see **Fig. 4.15** on the right) and its geometrical parameters are highlighted in **Tab. 4.3**. In the prototype, the PMs and the iron rings are stacked on a light-weight carbon rod, see **Fig. 4.20**. The total number of poles (iron rings) in the mover prototype is 10. Each module covers 4 poles (8 poles for the two modules) and the length of the 2 poles covers the stroke, such that a constant active length of the MALTA is kept during the operation.

The aluminum sleeve that shields the mover is used to protect the PMs from breaking if the touch-down bearing is hit. Additionally, the smooth conductive surface of the sleeve is used for eddy-current radial position sensing [89].

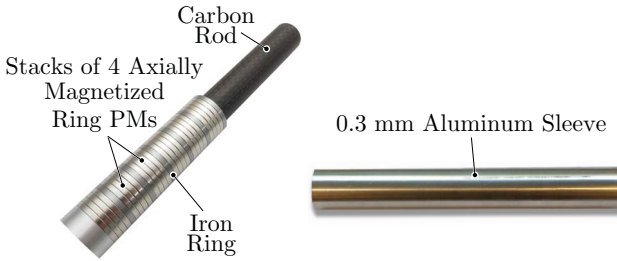


Fig. 4.20: Built mover prototype: axially magnetized ring PMs are stack on a light-weight carbon rod. Finally, the whole assembly is inserted into a 0.3 mm thick aluminum sleeve that protects the PMs. The smooth conductive surface of the sleeve is be used for eddy-current radial position sensing.

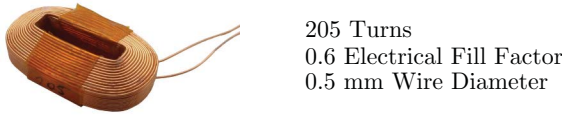


Fig. 4.21: Built coil prototype of the MALTA winding (cf. schematic representation shown in **Fig. 4.8(a)**).

4.6.2 Windings

A manufactured coil prototype is shown in **Fig. 4.21**. Its shape differs from the schematic representation of the MALTA winding depicted in **Fig. 4.8(a)** due to manufacturing constraints. It is built using 0.5 mm wire and consists of 205 turns. The achieved fill factor is 0.6.

In order to determine the maximum expected voltage across the winding terminals, phase resistance and inductance are measured and the back electromotive force (EMF) is estimated from the 3D-FEM simulation. In the simulation, a constant linear mover speed of 2 m/s is assumed as a worst-case scenario, since 2 m/s is the peak speed during the oscillating motion of the actuator. Accordingly, a peak induced back-EMF per turn of 26 mV is obtained. The winding resistance and inductance are measured as 2.2 Ω and 2 mH, once the windings are inserted into the stator and the stator is potted. The measurement is taken at 66.7 Hz, which is the worst-case electrical frequency corresponding the mover's peak instantaneous linear speed of 2 m/s (pole length is 15 mm).

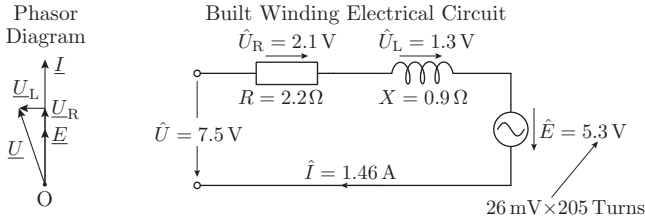


Fig. 4.22: Phasor diagram and electrical circuit of the built winding (\underline{X} - phasor quantity; \hat{X} - amplitude).

The electrical loading of the windings is obtained from the stator design (see **Section 4.5**), as 300 Ampere–turns. For 205 winding turns, this corresponds to a phase current amplitude of 1.46 A. Consequently, the amplitude of the phase voltage is estimated to be around 7.5 V, see **Fig. 4.22**. The peak-to-peak value of this voltage is ≈ 15 V, which implies that an inverter with 24 V DC-link voltage can be used to drive the actuator.

4.6.3 Stator

As already mentioned in **Section 4.5.2**, the stator is built from solid steel. It is divided into three stator sections, one of which is depicted in **Fig. 4.23(a)**. In order to monitor the temperature in the machine, three NTC thermal sensors are inserted in the radially innermost surface of one winding in each stator section. From the inner side, a 3D printed touch-down bearing is inserted, which protects mover and stator windings from damaging in case the MBs stop working [22], and is furthermore used as a mold in the potting procedure.

In order to fix the module in the test bench, it is inserted into an aluminum case shown in **Fig. 4.23(b)**. Further, the stator is potted with epoxy, which holds windings and stator sections together and ensures better cooling of the windings. A PCB connector is designed that gathers all $9 \times 2 = 18$ power winding connections and 6 connections for the three NTC thermal sensors.

4.6.4 Test Bench

A prototype of the MALTA is built in order to verify its concept and the FEM models. As the mover is magnetically levitated, a verification of the actual system without closed loop control, sensors and power electronics is not

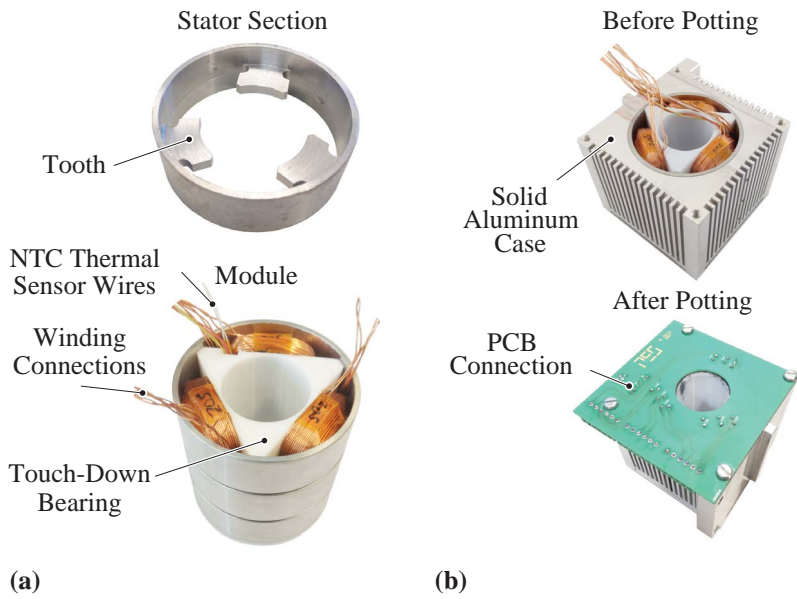


Fig. 4.23: (a) Stator section and module. (b) Module inside the aluminum case, before and after potting.

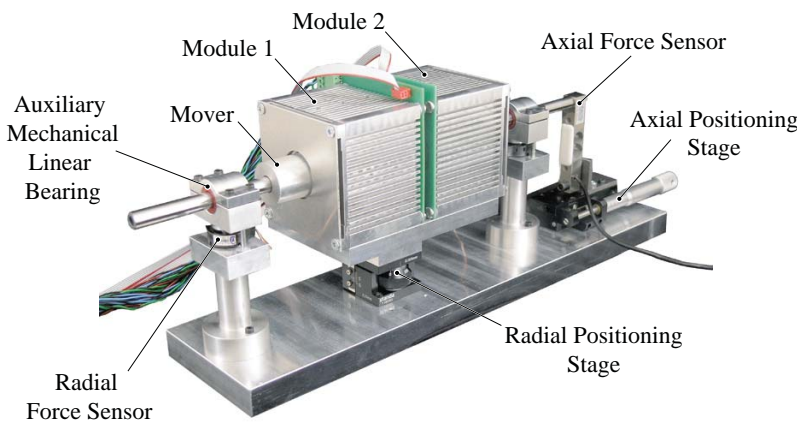


Fig. 4.24: MALTA test bench.

possible. Therefore, a custom test bench shown in **Fig. 4.24** is built, in which mechanical bearings are used to suspend the mover. The mechanical bearings are used only during the initial measurement and verification stage. Later on, they are removed and MBs are used in regular operation. The two radial force sensors, located beneath each linear bearing, are used to measure the bearing force. The drive force is measured with one sensor, which is attached to one end of the mover and to the axial positioning stage that is used for setting the axial position of the mover. The axial position of the modules (module 1 and module 2) is fixed, while its radial position is set with the radial positioning stage. The radial position of the mover is guaranteed by the fixture with embedded force sensors. Sensors used in the measurements are given in **Tab. 4.4**.

Tab. 4.4: Sensors used in the test bench.

Measurement	Manufacturer / Model
Temperature sensor	see [90]
Drive force sensor	see [91]
Bearing force sensor	see [92]

4.7 Machine Constant Measurement Results

4.7.1 Flux Linkage

Flux linkage is obtained by integrating the induced back-EMF, which is measured across the open-circuited machine terminals while the mover travels its complete stroke back and forth several times, actuated manually. Obtained flux linkage values are given in **Fig. 4.25**. The flux linkage is lower in the outer coils than in the middle coils due to the lower flux leakage of the outer coils. 3D-FEM simulation results for the flux linkage of the outer and the inner coils are provided and a good match with the measurements is achieved.

4.7.2 Temperature Rise

The continuous drive and bearing forces of the MALTA are limited by the maximum allowable winding temperature. So far, the electrical loading has been calculated according to a simplified thermal model presented in [16]. However, in order to assess the actual performance limit of the built prototype,

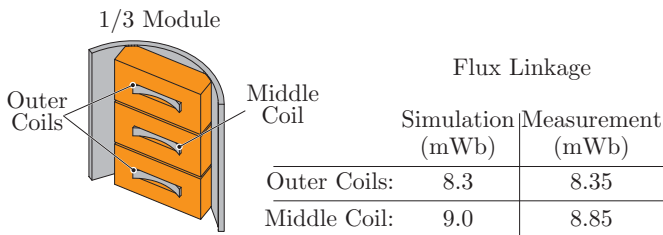


Fig. 4.25: Measured flux linkage of the outer and the middle coils in the MALTA module and its comparison to the 3D-FEM simulation results.

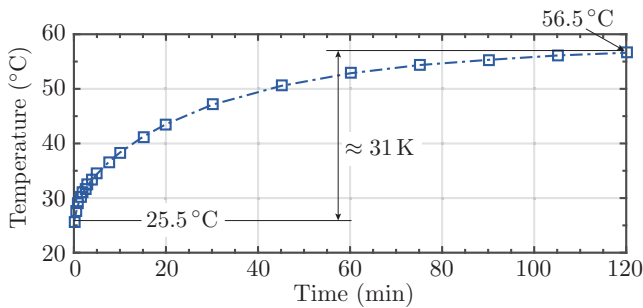


Fig. 4.26: Winding temperature rise measurement for 20.5 W of copper losses in the MALTA windings of a module.

a winding temperature rise measurement is performed for determining the actual thermal properties in detail, and consequently, for determining the maximum permissible electrical loading.

At standstill, a DC voltage is applied to the windings and total copper losses of 20.5 W are dissipated. Note that this is an arbitrary value and is only used to estimate the thermal properties of the prototype. The measured winding temperature is shown in **Fig. 4.26**. The thermal resistance of the test bench setup, in which the MALTA is enclosed with an aluminum case, can be roughly estimated as $R_{th} \approx 31^\circ\text{C}/20.5\text{ W} = 1.51^\circ\text{C}/\text{W}$. The obtained thermal resistance of the test bench closely resembles the thermal properties of the MALTA in a real life application. The casing has fins and it is connected with the radial positioning stage to the aluminum base plate, which resembles the MALTA that is held by a robot arm.

With the estimated thermal resistance of $R_{th} \approx 1.51^\circ\text{C}/\text{W}$, and a given maximum continuous winding temperature, the admissible continuous electrical loading of the MALTA can be calculated, which directly allows to specify its performance. Setting the maximum winding temperature to 100°C , continuous copper losses of $(100^\circ\text{C} - 28^\circ\text{C})/1.51^\circ\text{C}/\text{W} \approx 47\text{ W}$ are obtained, where 28°C is the assumed ambient temperature. This value will be used in the following sections to specify the expected performance of the MALTA prototype.

4.7.3 Drive Force Constant

The MALTA drive force constant (drive force divided by the current amplitude) is determined in this subsection. The measurement is performed with one module. Hence, for the actual MALTA with two modules (module 1 and module 2, see **Fig. 4.24**), the drive force constant is doubled.

In this measurement, the difference between the electrical angles of the current vector and the PM flux linkage vector is $\pi/2$ in axial direction. In order to simplify this measurement, the position of the current vector is chosen such that some of the coils have zero current. E.g. $\theta = 5\pi/6$ (cf. (4.2) and (4.5)), results in the following currents in the MALTA winding

$$I_M \begin{bmatrix} -\sqrt{3}/2 & 0 & \sqrt{3}/2 \\ -\sqrt{3}/2 & 0 & \sqrt{3}/2 \\ -\sqrt{3}/2 & 0 & \sqrt{3}/2 \end{bmatrix}, \quad (4.11)$$

where I_M is the current amplitude that can be arbitrary chosen and $I_{Mb} = 0$. The columns and the rows denote the current in the MALTA winding, as explained in **Section 4.3**. In the following, the axial position of the mover is changed, e.g. in steps of 1 mm, while the current in the MALTA winding is kept constant according to (4.11). The measured drive force is shown in **Fig. 4.27(a)**. The axial positions of the mover that give the $\pm\pi/2$ electrical distance between the current vector given with (4.11) and the mover flux vector are $\pm 7.5\text{ mm}$. In the sense of the well known dq -transformation, the direct current component is equal to zero at this positions, i.e. the force-per-copper-loss is maximized. Additionally, a 15 mm pole size in the mover can be observed, which agrees with the designed mover pole size, see **Tab. 4.3**.

In the next measurement the drive force constant is obtained. The axial position of the mover is fixed to -7.5 mm , while the current vector amplitude I_M is changed, see **Fig. 4.27(b)**. The drive force constant is estimated from

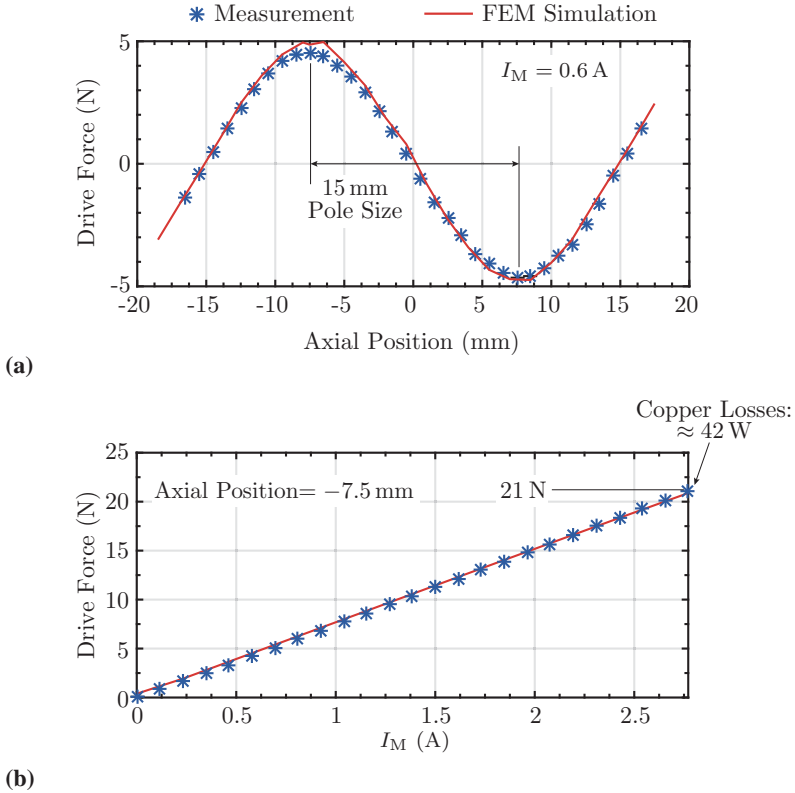


Fig. 4.27: Drive force constant measurement and comparison with FEM simulations: **(a)** Synchronization of the constant DC-current vector given in (4.11) with the mover flux vector by changing the mover's axial position. **(b)** Drive force constant measurement by changing the DC-current vector amplitude I_M for a fixed axial position of the mover at -7.5 mm that results in $\pi/2$ electrical distance between the DC-current vector and PM flux linkage vector.

the measurement as

$$K_d = \frac{\text{Axial Force}}{I_M} \approx 7.6 \text{ N/A}. \quad (4.12)$$

A drive force of 21 N per module can be achieved with copper losses of 42 W in continuous operation, see **Fig. 4.27(b)**. The maximum continuous electrical loading with copper losses of ≈ 47 W per module of the MALTA prototype is obtained in **Section 4.7.2**. The drive force per module for these losses is 22.2 N. Therefore, the continuous drive force with two modules is $2 \times 22.2 \text{ N} = 44.4 \text{ N}$. The mass of the mover without the extension that is required solely for the temporary linear bearings is 0.35 kg, which results in an achievable continuous axial acceleration of the MALTA with two modules of $\approx \pm 12.5g$.

4.7.4 Bearing Force Constant

This measurement is conducted in a similar fashion as the drive force constant measurement, i.e. a current vector at fixed axial position is applied, its amplitude is changed and the bearing force is recorded. In order to examine the MB properties of the MALTA in circumferential direction, a FEM simulation is conducted, whose result is shown in **Fig. 4.28**. In this simulation the magnitude of the bearing force along the circumference is obtained ($\varphi = [0^\circ, \dots, 360^\circ]$), where the current amplitude is kept constant and equal to $\hat{I}_{Mb} = 3 \text{ A}$ (cf. (4.5) and (4.3)). The circumferential position at the MALTA stator is defined as in **Fig. 4.29**.

The three denoted points in the plot shown in **Fig. 4.28** are further verified with measurements on the prototype. These measurement points capture critical bearing force magnitude values, i.e. its maximum for $\varphi = 0^\circ$, its average value for $\varphi = 30^\circ$ and its minimum value for $\varphi = 60^\circ$. For each of these circumferential directions, the bearing force measurements for different bearing current amplitudes ($\hat{I}_{Mb} = 0 \dots 3 \text{ A}$) are conducted, in order to capture the machine bearing constant. In order not to generate any parasitic drive force, the bearing force is measured at 0 mm axial position, see **Fig. 4.27(a)**, which is electrically 90° away from the position where the drive force is measured, i.e. in the phase with the PM flux linkage.

The bearing force constant measurement for $\varphi = 0^\circ$ direction is conducted in the following setup. The current vector is formed by applying the currents in the coils given with (4.5) and (4.3). The electrical angle in the axial direction

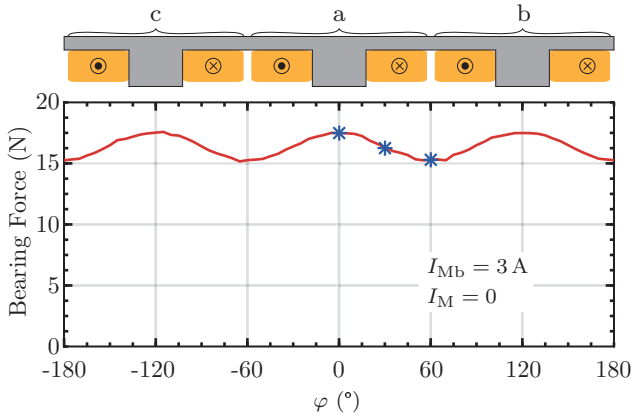


Fig. 4.28: Bearing force magnitude dependency on the circumference of the MALTA stator shown in **Fig. 4.29**. The results are obtained with 3D-FEM simulation. The desired bearing force may vary up to around 13 % depending on the circumferential direction. The three denoted points (blue stars) are further verified with measurements.

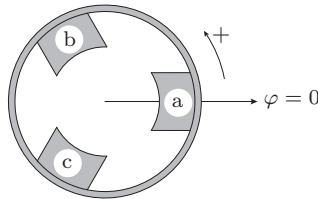


Fig. 4.29: Force circumferential position used in **Fig. 4.30**.

is set to $\theta = 0^\circ$. This results in the following currents in the MALTA windings:

$$I_{Mb} \begin{bmatrix} 1 & -1/2 & -1/2 \\ -1/2 & 1/4 & 1/4 \\ -1/2 & 1/4 & 1/4 \end{bmatrix}. \quad (4.13)$$

The amplitude $I_{Mb} = [0 \dots 3 \text{ A}]$ is varied and the bearing force is measured and shown in **Fig. 4.30(a)** and compared to 3D-FEM simulation results. From this measurement the bearing force constant for the $\varphi = 0^\circ$ direction is calculated as

$$K_b^{0^\circ} = \frac{\text{Bearing Force}}{I_{Mb}} \approx 5.6 \text{ N/A}. \quad (4.14)$$

Copper losses in the last measurement point are $\approx 28 \text{ W}$, see **Fig. 4.30(a)**. According to the above described temperature rise measurements, copper losses of $\approx 47 \text{ W}$ can be continuously dissipated in the module. Consequently, a maximum continuous bearing force of $\approx 21.9 \text{ N}$ per module in the $\varphi = 0^\circ$ circumferential direction can be achieved.

The second bearing force constant measurement is conducted for $\varphi = 30^\circ$ direction, see **Fig. 4.29**. Also here, the current vector has the same fixed axial position argument of $\theta_d = 0^\circ$, which results in

$$I_{Mb} \begin{bmatrix} \sqrt{3}/2 & -\sqrt{3}/4 & -\sqrt{3}/4 \\ 0 & 0 & 0 \\ -\sqrt{3}/2 & \sqrt{3}/4 & \sqrt{3}/4 \end{bmatrix}. \quad (4.15)$$

The current amplitude $I_{Mb} = [0 \dots 3.1 \text{ A}]$ is varied and the bearing force is measured, as shown in **Fig. 4.30(b)**. From this measurement, the bearing force constant for $\varphi = 30^\circ$ circumferential direction is calculated as

$$K_b^{30^\circ} = \frac{\text{Bearing Force}}{I_{Mb}} \approx 5.96 \text{ N/A}. \quad (4.16)$$

In the last measurement point the copper losses are $\approx 29 \text{ W}$, see **Fig. 4.30(b)**. A maximum continuous bearing force for $\varphi = 30^\circ$ direction of 23.2 N per module is obtained assuming the copper losses of 47 W .

The bearing force constant measurement for $\varphi = 60^\circ$ direction is conducted with the current vector equal to

$$I_{Mb} \begin{bmatrix} 1/2 & -1/4 & -1/4 \\ 1/2 & -1/4 & -1/4 \\ -1 & 1/2 & 1/2 \end{bmatrix}. \quad (4.17)$$

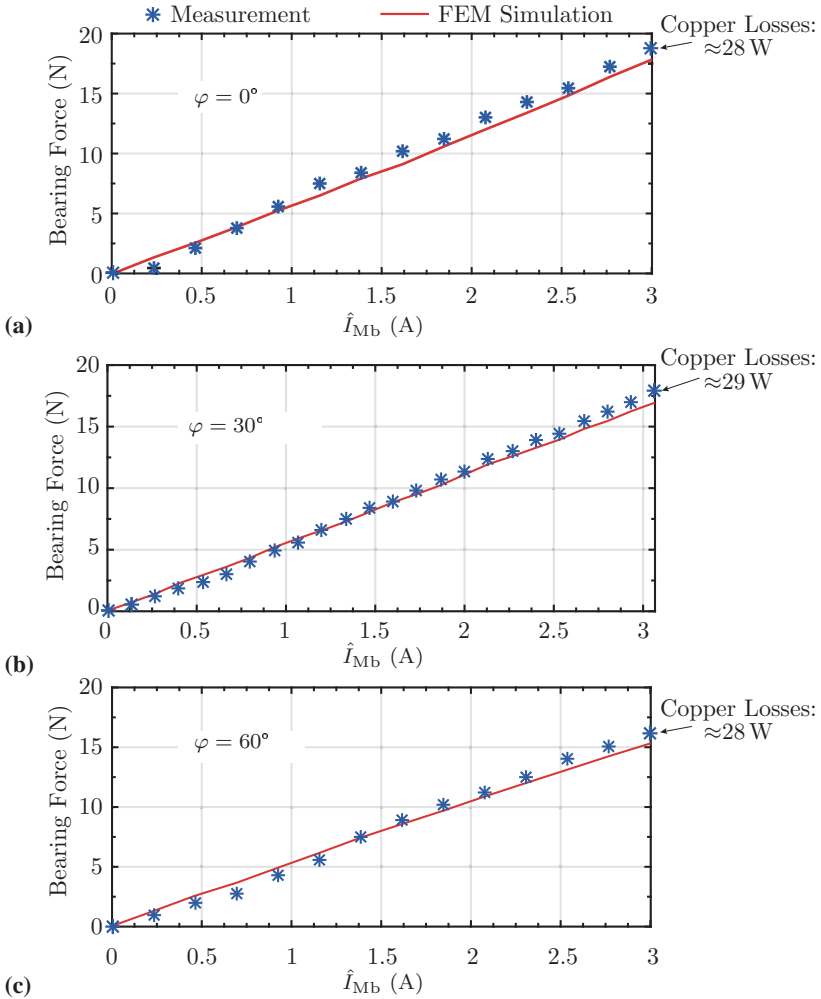


Fig. 4.30: Bearing force constant measurement for different circumferential directions. For these measurements, the drive current component is kept at zero, i.e. $\hat{I}_M = 0$. (a) Bearing force constant measurement for $\varphi = 0^\circ$. (b) Bearing force constant measurement for $\varphi = 30^\circ$. (c) Bearing force constant measurement for $\varphi = 60^\circ$.

The current amplitude $I_{Mb} = [0 \dots 3 \text{ A}]$ is varied and the bearing force is measured, as shown in **Fig. 4.30(c)**. From this measurement, the bearing force constant for $\varphi = 60^\circ$ circumferential direction is calculated as

$$K_b^{60^\circ} = \frac{\text{Bearing Force}}{I_m} \approx 6.26 \text{ N/A}. \quad (4.18)$$

A maximum continuous bearing force for $\varphi = 60^\circ$ direction of 24.4 N per module can be generated assuming the copper losses of 47 W.

The bearing force constant depends on the bearing force circumferential direction, which is shown with FEM simulations in **Fig. 4.28** and confirmed with measurements for 0° , 30° and 60° circumferential directions. The maximal measured bearing force constant $K_b^{0^\circ}$ and the minimal one $K_b^{60^\circ}$ differ by $\approx 11.8\%$.

Additionally, the bearing force constant depends on the radial displacement of the mover from its center position. This dependence is $\approx 2 \text{ N/A/mm}$ (per mm of the radial displacement). As typical radial displacements in MB machines of this size are in the range of only several μm , the influence of radial mover displacements on the bearing force constant is very low.

An important aspect for the MALTA is the decoupled control of the drive and bearing forces, which is achieved by proper determination of the phase currents (see **Section 4.2**). Measurements and FEM simulation results in **Fig. 4.31** show that the cross coupling between the drive and the bearing forces is negligible when a bearing force is commanded. Negligible cross coupling between the forces when a drive force is commanded is clear as it reduces the MALTA operation to a standard TLA in which the bearing force is always zero.

4.7.5 Radial Pull Force

The radial pull force measurement for one module is shown in **Fig. 4.32** and compared with 3D-FEM magnetostatic simulation results. This measurement is important for the self-bearing operation of the MALTA, since it will act as radial position disturbance if the mover is not in the center position. Additionally, if the mover is continuously displaced for $\approx 0.5 \text{ mm}$, the radial pull force would have to be balanced by a MB force, which would raise the copper losses per module by up to $\approx 2.5 \text{ W}$.

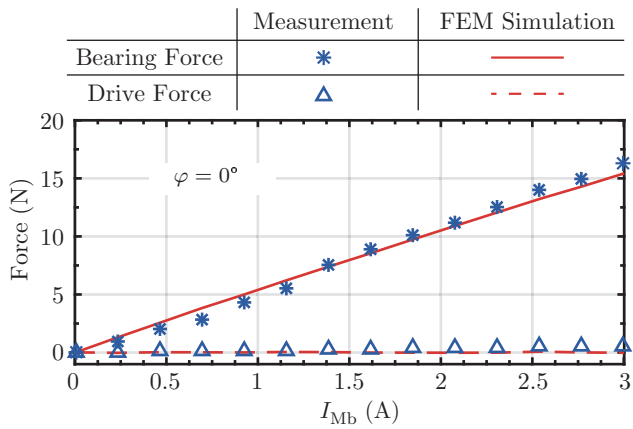


Fig. 4.31: Measurements and FEM simulations that show decoupled control of the drive and bearing forces, when a bearing force is commanded.

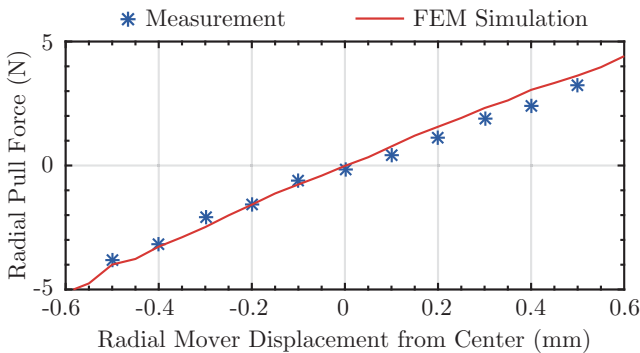


Fig. 4.32: Radial pull force measurement and comparison with 3D-FEM magnetostatic simulation results when the mover is displaced from its center position.

Tab. 4.5: MALTA performance with two modules. For 0° , 30° and 180° directions see **Fig. 4.29**.

Quantity	Value
Continuous drive/axial/thrust/linear force	44.4 N
Continuous bearing force, $\varphi = 0^\circ$ position	43.7 N
Continuous bearing force, $\varphi = 30^\circ$ position	46.4 N
Linear/axial acceleration	12.5g
Sustainable radial acceleration, $\varphi = 0^\circ$ direction	12.5g
Sustainable radial acceleration, $\varphi = 30^\circ$ direction	13.3g
Sustainable radial acceleration, $\varphi = 180^\circ$ direction	13.9g

4.7.6 MALTA Performance

The MALTA performance with both modules is determined in this section. The results rely on the measurements of the temperature rise (see **Section 4.7.2**), drive force constant (see **Section 4.7.3**) and bearing force constant (see **Section 4.7.4**) of one module.

The MALTA performance is summarized in **Tab. 4.5**. The mass of the mover is 0.35 kg without the extension that is required solely for the temporary linear bearings.

4.8 Summary

Tubular linear actuators (TLAs) can realize linear reciprocal motion as a direct drive, i.e. no mechanical transmissions are needed like in the conversion from rotational to translational motion. Therefore, higher compactness and efficiency can be achieved with TLAs in systems with linear reciprocal motion.

Standard bearings used in TLAs are either mechanical bearings or air bearings. These bearings feature drawbacks such as friction, risk of contamination due to wear or limited lifetime of the mechanical bearings, increased system volume and complexity due to pressurized air supply for air bearings. Furthermore, operation in low pressure environments is not possible for air bearings. These issues can be avoided if magnetic bearings (MBs) are used in TLA systems. MBs could be used as two separate machines on each axial side of a TLA, which would increase its length and complexity. Therefore, in this chapter, a novel self-bearing (bearingless) TLA is analyzed, resulting in a magnetically levitated tubular actuator (MALTA). The outer dimensions of the stator, i.e. active length and diameter, are 120 mm and 50 mm, respectively. Flux linkage measurements, drive, bearing and radial pull forces measure-

ments are shown and a good agreement with FEM simulations is achieved. The maximum feasible drive force in continuous operation is ≈ 44 N and a maximum axial acceleration of $\approx 12.5g$ can be achieved in continuous operation. This force is roughly 40 % lower compared to a standard TLA, because in the standard TLA the flux linkage is higher as there are no slits in the teeth.

As a next step in the following **Chapter 5** the MALTA inverter supply and the position sensor are designed and realized in hardware.

5

Linear Machine Inverter Supply and Position Sensor

In order to test and verify the proposed tubular linear machine with integrated magnetic bearings (MALTA), an inverter supply and position sensors are needed, which realization is described in this chapter. Parts of the material presented in this chapter are published in [93].

5.1 Introduction

This chapter summarizes the most important design aspects of the MALTA inverter supply and its position sensor. Derivation of the inverter specification from the MALTA requirements is explained. The current measurement circuit of the inverter features external ADC ICs to minimize the analog circuitry area.

The position sensor is capable of measuring the MALTA mover axial and radial positions. A technique to reduce an influence of the mover's radial displacements onto the axial position measurement is shown. Finally, the measurements from the sensor prototype calibration are given.

5.2 MALTA Inverter Supply

After building the MALTA prototype, the flux linkage of the stator phase coil and the PM's flux from the mover are measured, cf. **Section 4.7**. With this, for the maximum assumed mover linear speed of 2 m/s the maximum expected induced voltage amplitude of ≈ 5.3 V is estimated, cf. **Fig. 4.21**. Therefore, the supply inverter with a DC-link voltage of 45 V would be suitable, i.e. a certain

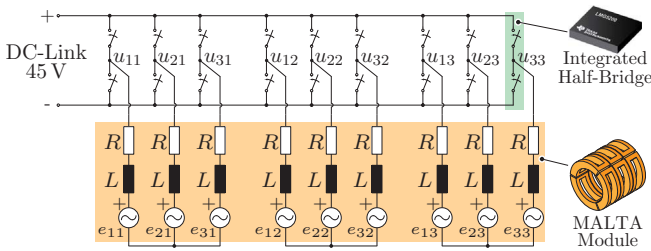


Fig. 5.1: Schematic of the MALTA inverter supplying a single MALTA module.

margin for eventually higher speeds is left, as well as a room for current control. The thermal measurements on the MALTA prototype revealed that the continuous phase current has an amplitude ≈ 3 A, resulting in so called continuous or RMS drive force of 22.2 N per module. As in the operation of the actuator the mechanical loads should be accelerated and decelerated, it is typical to overload the actuator for these periods of time, constituting so called intermittent operation. On average, the RMS value of the overload force waveform should not exceed its continuous value, where in overload the forces may be $3\times$ higher. Therefore, the inverter should be able to supply at least ≥ 9 A.

For the above discussed specifications of the MALTA prototype, a choice of the inverter semiconductor should be done such that it can block 45 VDC and supply the phase current with an amplitude of minimum 9 A. A suitable semiconductor arrangement for implementing the inverter half-bridges for this purpose is GaN LMG5200 from *Texas Instruments*, cf. [94], whose specifications are given in **Tab. 5.1**. The schematic of the inverter supplying a single MALTA module which comprising 9 half-bridges is shown in **Fig. 5.1**.

The schematic of a single phase current measurement circuit is shown in **Fig. 5.2**. For the current measurement the voltage over the shunt resistor is

Tab. 5.1: LMG5200 half-bridge specification.

Quantity/Feature	Value
Semiconductor technology	GaN
Max. drain-source blocking voltage	80 V
Nominal drain-source current	10 A
Drain-source electrical resistance	15 m Ω
Integrated gate driver	Yes

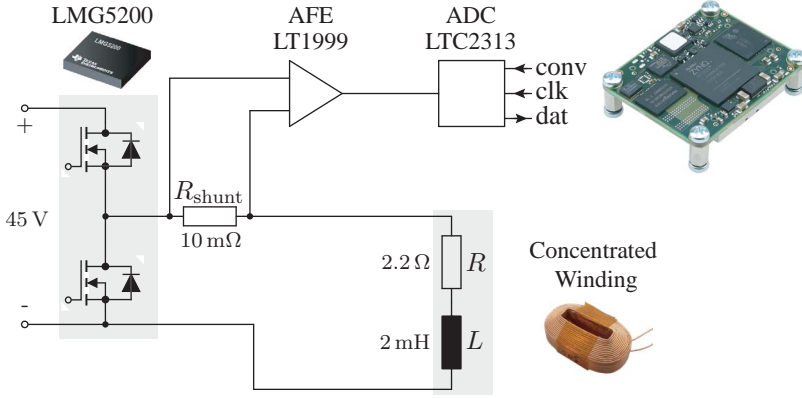


Fig. 5.2: Schematic of the MALTA inverter half-bridge with current measurement scheme.

sensed and amplified with the analog front end (AFE) implemented in the IC LT1999 [95]. The AFE provides insulation as well, since its input is connected to the switching node. The amplified analog signal is digitized with 12-bit ADC LTC2313 [96], which over the serial link transmits the data to the high-performance digital signal processing platform from Xilinx, Zynq Z-7020 [97]. The control system is discretized and implemented in C code on the processing platform and executed at a rate of 20 kHz, which is limited by the available processing capability. In each control interrupt the current measurements of all 18 half-bridges are taken and transferred to the platform's memory simultaneously. The 18 integrated GaN half-bridges required to drive the MALTA are controlled by 18 individual pulse-width modulators implemented in the fabric of the FPGA processing platform. The MALTA inverter prototype is shown in **Fig. 5.3**.

In MALTA operation, the mover exhibits accelerations and decelerations, which reflects onto the electrical part of the system by consumption or generation of electrical energy that might cause oscillations of the DC-link voltage. Therefore, a rather large capacitance of $4 \times 22 \text{ mF} = 88 \text{ mF}$ is used in the DC-link. For example, if the mover has a linear speed of 5 m/s, it has accumulated kinetic energy of

$$\frac{1}{2} \cdot m \cdot (5 \text{ m/s})^2 = 4.5 \text{ J},$$

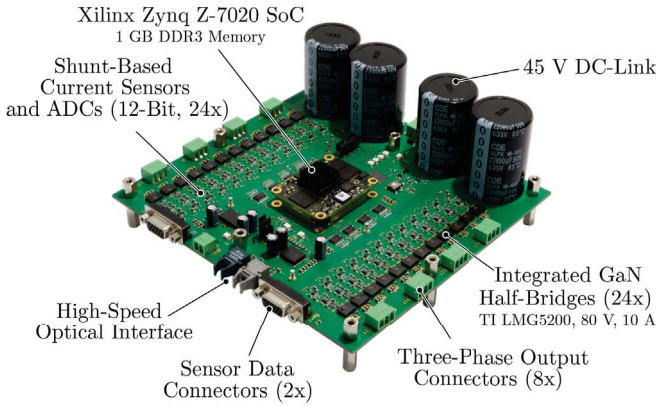


Fig. 5.3: Two-level 45 VDC inverter supply with 24 half-bridges.

where $m = 0.36 \text{ kg}$ is the mover mass. If the losses in the inverter and the MALTA are neglected, this kinetic energy will be added to the electric energy in the DC-link caps and would cause a voltage oscillation of $\sim 1.12 \text{ V}$, which is around 2.5 % of the 45 VDC and is an acceptable value. This issue could be also addressed by e.g. adding a braking resistor in the DC-link, which would allow to use a lower DC-link capacitance value. This approach is not used as it was simpler to implement larger DC-link capacitance.

5.3 MALTA Position Sensor

The MALTA position sensors are realized on PCBs and placed with respect to the stator modules as shown in **Fig. 5.4(a)**. For the axial position detection, the signals from the Hall-effect sensors located on both sensor planes, SP1 and SP2, are used. This is a very well known method where ‘sin’ and ‘cos’ of the PM field need to be measured such that linear position may be detected [98]. In conventional linear machines where the radial position of the mover is governed, e.g. by mechanical bearings, the PM field sensed by the Hall-effect sensors can change only if the mover moves in linear z -direction. Since in the MALTA, the mover is capable also to move radially (for the MALTA from approx. -0.6 mm to 0.6 mm), which is allowed by the integrated MBs, the change of the PM field detected by the Hall-effect sensor due to radial motion cannot be distinguished from the PM field change due to linear motion, which may lead to an inaccurate linear position detection. Therefore, for the linear

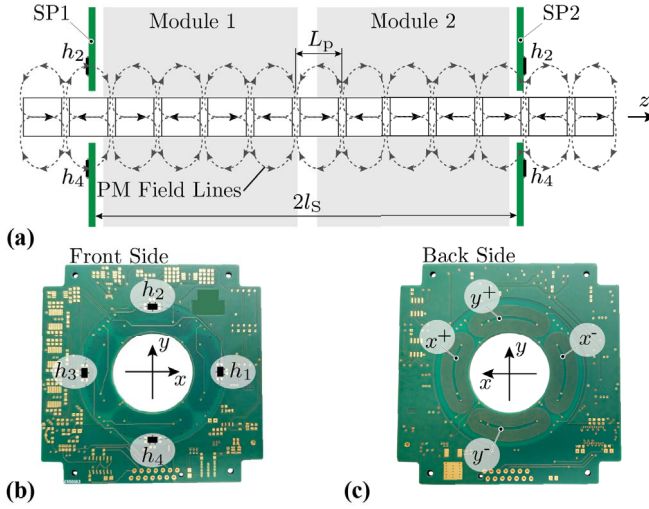


Fig. 5.4: (a) Illustration of the PM field lines used to sense the axial position of the mover and the sensor planes SP1 and SP2, at axial distance $2l_s$. (b) Front side of the sensor prototype with four Hall-effect sensors, denoted as h_1 , h_2 , h_3 and h_4 . The Hall-effect sensors can sense the z -component (axial) of the PM field. The displacement $2l_s$ is such that the sensed PM field from SP1 and SP2 Hall sensors is shifted by half the PM pole size $L_p/2$. (c) Back side of the PCB integrated sensor prototype. The eddy-current sensor coils for x -direction (x^+ , x^-) are connected in anti-series, as well as (y^+ , y^-) for y -direction. The physical size of sensor PCBs is 8×8 cm.

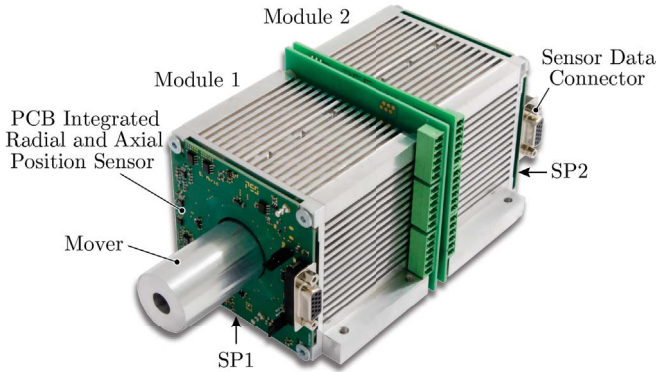


Fig. 5-5: MALTA prototype consisting of two stator modules that contain the phase coils, a mover comprising permanent magnets, and two PCB-integrated position sensors (SP1 and SP2). The shaft diameter is 27 mm, while the actuator active length is 170 mm. The machine design procedure is described in detail in [35]. The MALTA modules (stator) can act onto the mover with the bearing (radial) forces $f_{x,B\{1,2\}}$ and $f_{y,B\{1,2\}}$ in x - and y -direction and with the drive (linear) force f_D in z -direction.

position detection of the MALTA, the ‘sin’ and ‘cos’ signals are formed by the average sum of the four Hall-effect sensors, i.e. $(h_1 + h_2 + h_3 + h_4)/4$. This mitigates the sensitivity of the sensed PM field change to the radial motions of the MALTA mover. For example, if the mover moves in the positive y -direction (cf. **Fig. 5.4(b)**), the PM field sensed by h_2 would increase while the field for h_4 reduces, i.e. their average sum stays approximately constant. Finally, in total 8 Hall-effect sensors (4 per sensor plane) are used for the linear position detection of the MALTA’s mover. The sensors implemented in the MALTA prototype are shown in **Fig. 5-5**.

The radial position is detected by the PCB integrated eddy-current position sensor, shown in **Fig. 5.4(c)**. The explanation about the sensor operating principles and its equivalent circuit are given in **Section 9.2**. Also, in [89, 99] a similar sensor approach is analyzed. Here, the operation of the sensor will be discussed only briefly. The eddy-current sensor consists of a so-called injection coil and pick-up coils. In the injection coil exists an AC-current with an amplitude of ≈ 100 mA and a frequency of ≈ 3.5 MHz. It should be mentioned that this frequency is selected as large as possible, but still below the injection coil resonance frequency, i.e. the frequency where the injection

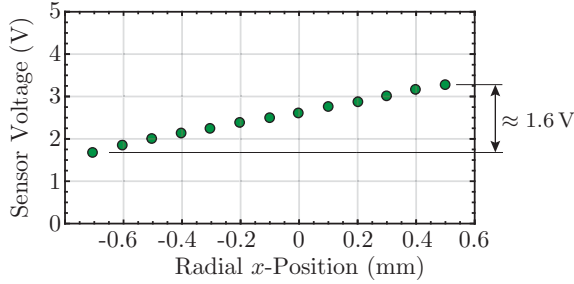


Fig. 5.6: Measured sensor output voltage as a function of the radial mover displacement in x -direction.

coil impedance turns from inductive to capacitive behavior. The current in the injection coil creates the HF field that is coupled with the pick-up coils and induces voltage whose amplitude depends on the mover's radial position. The mover's surface is made out of non-ferromagnetic electrically conductive material (e.g. aluminum or stainless steel). The analog signal of the induced HF AC voltage in pick-up coils is further processed by electronic components and transformed into a DC-signal that depends on the mover's radial position, as shown in **Fig. 5.6**.

The measured voltage signal in **Fig. 5.6** changes around $\Delta u = 1.6$ V when the mover is moved from $x = -0.7$ mm to $x = 0.5$ mm, i.e. for a step of $\Delta x = 1.2$ mm. This voltage signal is digitized with 12-bit ADC (LTC2313, cf. [96]) in which 1 mV suits to a single bit. Therefore, the resolution of the radial position measurement is around

$$\frac{1.2 \text{ mm}}{1600 \text{ bit}} = 0.75 \mu\text{m/bit}.$$

To assess the quality of the sensor signal, the voltage noise is measured with a precision FFT spectrum analyzer [100], and its RMS noise value is around $52 \mu\text{V}$. The measurement frequency range is 10 – 5000 Hz. Therefore, the best signal to noise ratio (SNR) is

$$20 \log_{10} \left(\frac{1.6 \text{ V}/\sqrt{2}}{52 \mu\text{V}} \right) = 86.7 \text{ dB}.$$

5.4 Summary

In this chapter details of the MALTA inverter and the position sensor design and hardware realization are shown. Based on the analysis and measurements in the previous **Chapter 4**, a specification for the MALTA inverter design is derived, resulting in 45 VDC and 10 A_{peak} of the output current. Therefore, for this purpose the GaN integrated half-bridge from Texas Instruments LMG5200 is used and an inverter with 24 half-bridges is realized, where only 18 are used to drive the MALTA. The inverter is designed with 24 half-bridges such that it can also drive other actuators with 24 phases, e.g. a 2×3 phases MALTA with the combined windings (cf. **Chapter 4**). The MALTA radial position sensor is based on the eddy-current principle, while the linear position sensor is based on Hall-effect elements that sense the mover PM field.

At this point, the realization of the MALTA hardware parts is complete, i.e. the MALTA machine prototype realization is shown in **Chapter 4** and the inverter and position sensor realizations are shown in this chapter. In a next step a control system must be designed and implemented, which is the topic of the following **Chapter 6**.

6

Dynamic Model and Controller Design of the Linear Machine

To verify the MALTA concept a position controller is necessary. As the MALTA represents a system with coupled dynamics, the controller design finally results in a LQG MIMO controller. Parts of the material presented in this chapter are published in [93].

6.1 Introduction

In applications that require repetitive linear motion, the usage of direct drive tubular linear actuators (TLAs) is beneficial compared to systems where gear-boxes are used to generate linear motion from a rotary actuator [101, 102]. Direct drive TLAs achieve higher dynamics, are more precise, and feature less moving parts that are subject to wear. They are gaining attention in numerous applications, such as actuators for pick-and-place robots in the semiconductor or electronics manufacturing industries [24, 39, 103], active and semi-active suspension systems [40], compressors [41], tubular linear generators [42], steering systems [104] or rehabilitation robots [105]. Nevertheless, in precision sensitive applications, accuracy and fast motion control of the direct-drive actuators may be affected by friction of the bearings and/or thermal expansions (e.g. in robotic arms that move the actuator). As a step forward in the actuator area, a contact-less TLA was proposed in [35] that features integrated active magnetic bearings (AMBs). With such an actuator, friction is removed and any thermal expansion may be compensated by adjusting the radial position of the AMB [22]. In addition, the stiffness of the bearings and the tilting of the mover may be actively controlled. The proposed

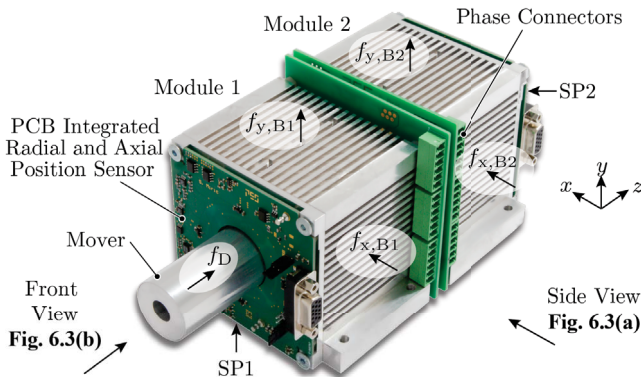


Fig. 6.1: MALTA prototype consisting of two stator modules that contain the phase coils, a mover comprising permanent magnets, and two PCB-integrated position sensors (SP1 and SP2). The shaft diameter is 27 mm, while the actuator active length is 170 mm. The machine design procedure is described in detail in [35]. The MALTA modules (stator) can act onto the mover with the bearing (radial) forces $f_{x,B\{1,2\}}$ and $f_{y,B\{1,2\}}$ in x - and y -direction and with the drive (linear) force f_D in z -direction.

actuator is called MALTA (Magnetically Levitated Tubular Actuator) and its hardware prototype is shown in **Fig. 6.1**. In addition to the linear motion and magnetic bearings, to obtain rotation, the MALTA concept may be extended and adapted, e.g. by adding a rotary machine, cf. [23].

In industry, PID position controllers are widely adopted for conventional TLAs [106], which are in general well suited for single-input single-output control schemes. However, they are unsuitable for the considered MALTA system, as for the positioning of the magnetically levitated mover five degrees of freedom have to be controlled simultaneously (instead of just a single position), resulting in a multiple-input multiple-output (MIMO) control problem. The controlled five degrees of freedom refer to: *forward-back*, *right-left*, *up-down*, *pitch* and *yaw*, whereas the sixth degree of freedom of the MALTA's mover, *rotation*, is not controllable. Therefore, a dynamic model of the mechanical subsystem of the MALTA is developed, which is used to design an appropriate MIMO feedback controller structure, which is assisted by additional feed-forward compensation components.

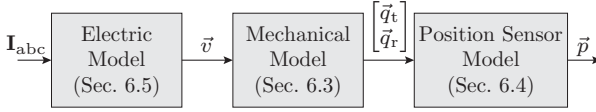


Fig. 6.2: Overview of the MALTA system models: electric, mechanical and position sensor model.

6.2 MALTA System Model

The MALTA system model consists of three parts: the electric model, the mechanical model and the position sensor model, as shown in **Fig. 6.2**.

The electric model elaborates the bearing and the drive force generation from the phase currents \mathbf{I}_{abc} . For the derivation of the electric model of the MALTA, two electrical angles, the linear electrical angle θ and the circumferential electrical angle φ are used, whose directions are shown in **Fig. 6.3**.

The mechanical model is a nonlinear dynamic model, which allows to determine the mover's position (output of the model) depending on the total net forces \vec{v} that act on the mover (input of the model). The input of the mechanical model, the bearing and the drive force that act onto the MALTA mover is written in vector form as

$$\vec{v} = [f_{xB1} \ f_{yB1} \ f_{xB2} \ f_{yB2} \ f_D]^T, \quad (6.1)$$

whose components are denoted in **Fig. 6.1**.

The position sensor model relates the center of gravity (COG) mover coordinates \tilde{q}_t and \tilde{q}_r (cf. equation (6.2)) to the displacements \vec{p} that are measured in the position sensor planes SP1 and SP2 (cf. **Fig. 6.1**). The mass distribution of the mover is assumed to be even. A potential influence of the picked component mass in pick-and-place application is neglected, as the component mass is assumed to be much smaller than the mass of the mover (e.g. this applies for SMD components to be mounted onto a printed circuit board). For the derivation of the dynamic model, two coordinate reference frames, the inertial \mathcal{I} and the rotary \mathcal{R} reference frame (cf. **Fig. 6.3**) are used, which are described in more detail in the following subsection.

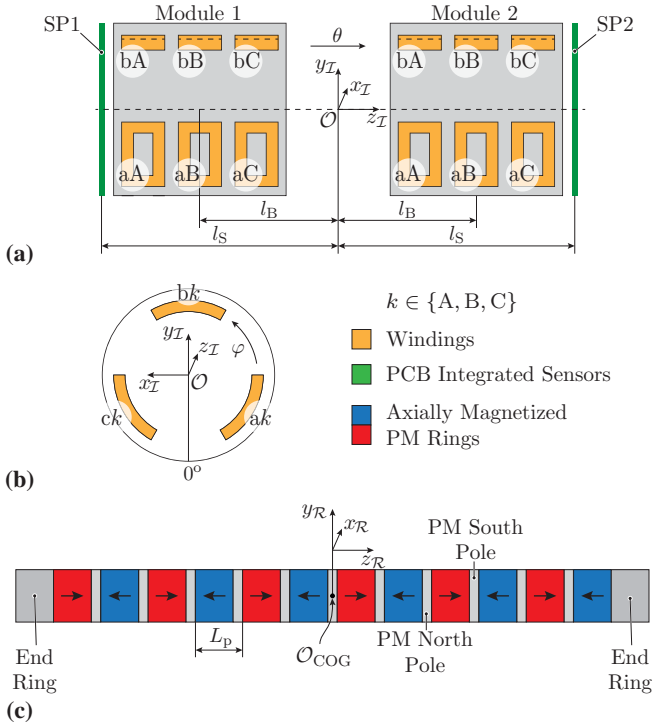


Fig. 6.3: Mechanical setup of the MALTA with inertial (I) and rotary (R) reference frames: (a) side view as denoted in Fig. 6.1; (b) front view on the sensor plane 1 (SP1) as denoted in Fig. 6.1; (c) mover construction showing the arrangement of the PMs and their flux density directions.

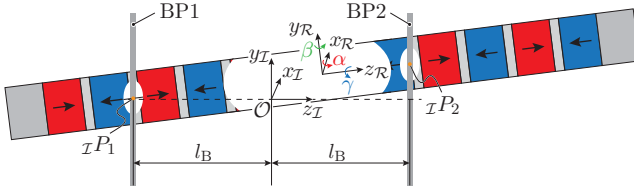


Fig. 6.4: Simplified mechanical setup showing the bearing planes 1 and 2 (BP1 and BP2) in the center of the modules 1 and 2, respectively (cf. **Fig. 6.3(a)**). The intersection points 1 and 2 are denoted by ${}_I\vec{P}_1$ and ${}_I\vec{P}_2$.

6.3 Mechanical Model

The mechanical model is nonlinear and dynamic and assumes a rigid mover of the MALTA. The inertial reference frame \mathcal{I} is fixed to the origin O and the z_I -axis is oriented along the axial direction of the MALTA stator, whereas the rotary reference frame \mathcal{R} is fixed to the mover's center of gravity (COG) O_{COG} and the z_I -axis is aligned with its principal axis, as shown in **Fig. 6.4**. The tilting of the mover in **Fig. 6.4** is used to illustrate the position of the \mathcal{R} frame and it does not correspond to the tilting possible in reality. The motion of the mover is described in terms of *translation* and *rotation* of the frame \mathcal{R} with respect to the frame \mathcal{I} . The translation and rotation may be parametrized using a set of Cartesian coordinates \vec{q}_t and a set of Cardan angles \vec{q}_r as

$$\vec{q}_t = \begin{bmatrix} x \\ y \\ z \end{bmatrix}, \quad \vec{q}_r = \begin{bmatrix} \alpha \\ \beta \\ \gamma \end{bmatrix}. \quad (6.2)$$

The angles in \vec{q}_r are three subsequent elementary rotations around the x_R , y_R and z_R axes (cf. **Fig. 6.4**). Once the motion of the mover is parametrized, the equations of motion can be derived, for example by using the *Newton-Euler equations* [107], which can describe combined translation and rotation of a rigid body,

$$m \frac{\partial^2 \vec{q}_t}{\partial t^2} = {}_I\vec{F}_{\text{tot}} \quad (6.3)$$

$${}_{\mathcal{R}}\mathbf{I}_m \cdot \frac{\partial {}_{\mathcal{R}}\vec{\omega}}{\partial t} + {}_{\mathcal{R}}\vec{\omega} \times {}_{\mathcal{R}}\mathbf{I}_m \cdot {}_{\mathcal{R}}\vec{\omega} = {}_{\mathcal{R}}\vec{T}_{\text{tot}},$$

where the translation is described in the inertial frame \mathcal{I} and the rotation in the rotary frame \mathcal{R} . \vec{F}_{tot} and \vec{T}_{tot} are the total force and the total torque acting

Tab. 6.1: Mechanical parameters of the MALTA.

Symbol	Quantity	Value
Mass and Moment of Inertia		
m	Mover mass	0.360 kg
I_{xx}	Mover x -axis MoI	$1.3805 \times 10^{-3} \text{ kg m}^2$
I_{yy}	Mover y -axis MoI	$1.3805 \times 10^{-3} \text{ kg m}^2$
I_{zz}	Mover z -axis MoI	$4.7707 \times 10^{-5} \text{ kg m}^2$
Force Constant		
K_D	Drive constant per module	5.2 N/A
K_B	Bearing constant per module	5.2 N/A
K_A	Attraction constant per module	8330 N/m

on the mover, respectively. The mass of the mover is m , while

$$\mathcal{R}\mathbf{I}_m = \begin{bmatrix} I_{xx} & 0 & 0 \\ 0 & I_{yy} & 0 \\ 0 & 0 & I_{zz} \end{bmatrix}$$

is the Moment of Inertia (MoI) diagonal matrix, expressed in the mover frame \mathcal{R} . The values of these parameters are given in the **Tab. 6.1**. The angular speed in the rotary frame $\mathcal{R}\omega$ is given by the following angular rotations

$$\mathcal{R}\vec{\omega} = \begin{bmatrix} 0 \\ 0 \\ \mathcal{I}\omega_z \end{bmatrix} + \mathbf{R}_z(\beta) \begin{bmatrix} 0 \\ \mathcal{I}\omega_y \\ 0 \end{bmatrix} + \mathbf{R}_z(\beta)\mathbf{R}_y(\alpha) \begin{bmatrix} \mathcal{I}\omega_x \\ 0 \\ 0 \end{bmatrix}, \quad (6.4)$$

where $\mathcal{I}\omega_x = \partial\alpha/\partial t$, $\mathcal{I}\omega_y = \partial\beta/\partial t$, $\mathcal{I}\omega_z = \partial\gamma/\partial t$. Furthermore, a small angle approximation is used, i.e. for any angle ξ it applies $\sin \xi \approx \xi$ and $\cos \xi \approx 1$. The rotation matrices $\mathbf{R}_y(\beta)$ and $\mathbf{R}_z(\alpha)$ are equal to

$$\mathbf{R}_y(\beta) = \begin{bmatrix} \cos(\beta) & 0 & \sin(\beta) \\ 0 & 1 & 0 \\ -\sin(\beta) & 0 & \cos(\beta) \end{bmatrix}, \quad \mathbf{R}_z(\alpha) = \begin{bmatrix} \cos(\alpha) & -\sin(\alpha) & 0 \\ \sin(\alpha) & \cos(\alpha) & 0 \\ 0 & 0 & 1 \end{bmatrix}, \quad (6.5)$$

where a detailed outline of the rotation procedure is given in [108].

The total force on the mover is the superposition of the two net forces from the modules 1 and 2, acting at the points ${}_I\vec{P}_1$ and ${}_I\vec{P}_2$, which are in the middle of each module. These points are shown in **Fig. 6.4** and may be described analytically as

$${}_I\vec{P}_1 = \begin{bmatrix} x - \beta(l_B + z) \\ y + \alpha(l_B + z) \\ -l_B \end{bmatrix}, \quad {}_I\vec{P}_2 = \begin{bmatrix} x + \beta(l_B - z) \\ y - \alpha(l_B - z) \\ l_B \end{bmatrix}. \quad (6.6)$$

These expressions are derived from

$${}_I\vec{P}_1 = {}_I\vec{O}_{\text{COG}} + \mathbf{R}_{I\mathcal{R}} {}_{\mathcal{R}}\vec{P}_1$$

and

$${}_I\vec{P}_2 = {}_I\vec{O}_{\text{COG}} + \mathbf{R}_{I\mathcal{R}} {}_{\mathcal{R}}\vec{P}_2,$$

where the points in the rotary reference frame are equal to

$${}_{\mathcal{R}}\vec{P}_1 = \begin{bmatrix} 0 & 0 & (-l_B - z) \end{bmatrix}^\top$$

and

$${}_{\mathcal{R}}\vec{P}_2 = \begin{bmatrix} 0 & 0 & (l_B - z) \end{bmatrix}^\top,$$

and the 3×3 transformation matrix $\mathbf{R}_{I\mathcal{R}} = \mathbf{R}_{\mathcal{R}I}^{-1}$, where $\mathbf{R}_{\mathcal{R}I} = \mathbf{R}_z(\alpha)\mathbf{R}_y(\beta)\mathbf{R}_x(\gamma)$ (cf. [108]), is considered. The rotation matrix $\mathbf{R}_x(\gamma)$ is equal to

$$\mathbf{R}_x(\gamma) = \begin{bmatrix} 1 & 0 & 0 \\ 0 & \cos(\gamma) & -\sin(\gamma) \\ 0 & \sin(\gamma) & \cos(\gamma) \end{bmatrix}. \quad (6.7)$$

Based on the position of these interaction points, the total forces and torques applied to the mover are discussed in the following.

6.3.1 Total Force in Inertial Reference Frame

The total force \vec{F}_{tot} acting on the mover consists of three force types: the drive, the bearing and the attraction force (also called *magnetic pull* or *detent* force). As the inertial frame \mathcal{I} is fixed to the stator, the total force may be readily expressed in the \mathcal{I} frame as ${}_I\vec{F}_{\text{tot}}$, where ${}_I\vec{F}_{\text{tot}}$ is composed of the two components which are generated by module 1 and module 2, acting as a net force in the points ${}_I\vec{P}_1$ and ${}_I\vec{P}_2$,

$${}_I\vec{F}_{\text{tot}} = {}_I\vec{F}_1 + {}_I\vec{F}_2. \quad (6.8)$$

The forces of each module, ${}_I\vec{F}_1$ and ${}_I\vec{F}_2$, are further split into a drive, a bearing and an attraction force,

$${}_I\vec{F}_1 = {}_I\vec{F}_{D1} + {}_I\vec{F}_{B1} + {}_I\vec{F}_{A1}$$

and

$${}_I\vec{F}_2 = {}_I\vec{F}_{D2} + {}_I\vec{F}_{B2} + {}_I\vec{F}_{A2}.$$

It should be mentioned that these considered force vectors are analyzed in the Cartesian coordinate system (with the axes x , y and z) and, therefore, the vectors have a dimension of 3×1 .

The drive force component is an active component controlled by the drive currents in the stator and acts in the z_I -axis direction. Therefore, it corresponds to the third component of the drive force vectors

$${}_I \vec{F}_{D1} = \begin{bmatrix} 0 \\ 0 \\ f_{D1} \end{bmatrix} \quad \text{and} \quad {}_I \vec{F}_{D2} = \begin{bmatrix} 0 \\ 0 \\ f_{D2} \end{bmatrix}.$$

The total drive force may be expressed as a superposition of the individual drive forces ${}_I \vec{F}_{D1}$ and ${}_I \vec{F}_{D2}$ as

$$\begin{aligned} {}_I \vec{F}_D &= {}_I \vec{F}_{D1} + {}_I \vec{F}_{D2} \\ &= \begin{bmatrix} 0 \\ 0 \\ f_{D1} + f_{D2} \end{bmatrix}. \end{aligned} \quad (6.9)$$

The bearing forces are also actively controlled by the bearing current component in the stator windings. They act as net forces in x_I - and y_I -direction at the interaction points ${}_I \vec{P}_1$ and ${}_I \vec{P}_2$. Therefore, these forces constitute the first and the second component of the force vectors

$${}_I \vec{F}_{B1} = \begin{bmatrix} f_{x,B1} \\ f_{y,B1} \\ 0 \end{bmatrix} \quad \text{and} \quad {}_I \vec{F}_{B2} = \begin{bmatrix} f_{x,B2} \\ f_{y,B2} \\ 0 \end{bmatrix}.$$

The total bearing force may be expressed as a superposition of ${}_I \vec{F}_{B1}$ and ${}_I \vec{F}_{B2}$ as

$$\begin{aligned} {}_I \vec{F}_B &= {}_I \vec{F}_{B1} + {}_I \vec{F}_{B2} \\ &= \begin{bmatrix} f_{xB1} + f_{xB2} \\ f_{yB1} + f_{yB2} \\ 0 \end{bmatrix}. \end{aligned} \quad (6.10)$$

The attraction forces are radial reluctance forces, which only generate a resulting attraction force on the mover if it is displaced from its center position, otherwise they cancel each other out. Thereby, it can be assumed that for a small displacement the resulting attraction forces acting at the

interaction points ${}_I\vec{P}_1$ and ${}_I\vec{P}_2$ are proportional to the radial displacement at these points. Therefore, the modules 1 and 2 are generating the attraction forces

$${}_I\vec{F}_{A1} = K_A \cdot {}_I\vec{P}_1$$

and

$${}_I\vec{F}_{A2} = K_A \cdot {}_I\vec{P}_2$$

which can be written as

$${}_I\vec{F}_{A1} = K_A \begin{bmatrix} x - \beta(l_B + z) \\ y + \alpha(l_B + z) \\ 0 \end{bmatrix}, \quad (6.11)$$

and

$${}_I\vec{F}_{A2} = K_A \begin{bmatrix} x + \beta(l_B - z) \\ y - \alpha(l_B - z) \\ 0 \end{bmatrix}. \quad (6.12)$$

There, K_A equals the attraction constant per module, whose measured value of the prototype is given in **Tab. 6.1**. The total attraction force is then given as the superposition of the forces ${}_I\vec{F}_{A1}$ and ${}_I\vec{F}_{A2}$, i.e.

$${}_I\vec{F}_A = {}_I\vec{F}_{A1} + {}_I\vec{F}_{A2}. \quad (6.13)$$

6.3.2 Total Torque in Rotary Reference Frame

By its magnetic design, the MALTA is designed as a linear motor (with integrated MBs). Therefore, it is not able to generate any drive torque (the torque around the z -axis, which ‘drives’ the rotation of conventional rotary machines). Consequently, the total drive torque component is equal to zero. On the other hand, certain net forces (drive, bearing and attraction) may act on the mover at the interaction points ${}_I\vec{P}_1$ and ${}_I\vec{P}_2$ points, which may generate a certain net torque \vec{T}_{tot} . This net total torque is first determined in the \mathcal{I} frame, and then transformed into the \mathcal{R} frame.

In a first step, the lever arms are determined at the interaction points ${}_I\vec{P}_1$ and ${}_I\vec{P}_2$. The lever arms are vectors describing the distance between the force interaction point and the mover’s center of gravity O_{COG} . In the inertial reference frame \mathcal{I} , for the MALTA mover two lever arms are defined as ${}_I\vec{L}_1 = {}_I\vec{P}_1 - {}_I\vec{O}_{\text{COG}}$ and ${}_I\vec{L}_2 = {}_I\vec{P}_2 - {}_I\vec{O}_{\text{COG}}$, which results in the following

expressions

$${}_I\vec{L}_1 = \begin{bmatrix} -\beta(l_B + z) \\ \alpha(l_B + z) \\ -l_B - z \end{bmatrix}, \quad {}_I\vec{L}_2 = \begin{bmatrix} \beta(l_B - z) \\ -\alpha(l_B + z) \\ l_B - z \end{bmatrix}. \quad (6.14)$$

The net torques ${}_I\vec{T}_1$ and ${}_I\vec{T}_2$ generated by the MALTA modules 1 and 2, may be calculated then as

$${}_I\vec{T}_1 = {}_I\vec{L}_1 \times {}_I\vec{F}_1, \quad {}_I\vec{T}_2 = {}_I\vec{L}_2 \times {}_I\vec{F}_2. \quad (6.15)$$

Finally, the total torque acting on the mover in the rotary \mathcal{R} reference frame is obtained as

$$\mathcal{R}\vec{T}_{\text{tot}} = \mathbf{R}_{\mathcal{R}I}({}_I\vec{T}_1 + {}_I\vec{T}_2). \quad (6.16)$$

6.4 Position Sensor Model

In order to realize a closed-loop position control of the MALTA mover, the axial and radial positions have to be measured. Here, it should be mentioned that the radial position has to be measured at two distinct axial locations, such that any tilting of the mover can be controlled. Therefore, two PCB integrated sensors are located at a certain distance l_S in z -direction from the origin O of the inertial frame I , as shown in **Fig. 6.3(a)**. The position measurement vector of SP1 and SP2 (which are denoted in **Fig. 6.1** and **Fig. 6.3**) may then be written as

$$\vec{p} = \begin{bmatrix} x_1 \\ y_1 \\ x_2 \\ y_2 \\ z \end{bmatrix},$$

and the position of the mover described in terms of translation and rotation of the COG, may be related to the measured positions as

$$\vec{p} = \mathbf{P}_0(z) \begin{bmatrix} \vec{q}_t \\ \vec{q}_r \end{bmatrix},$$

where \vec{q}_t and \vec{q}_r are given in (6.2) and

$$\mathbf{P}_0(z) = \begin{bmatrix} 1 & 0 & 0 & 0 & -(l_S + z) & 0 \\ 0 & 1 & 0 & (l_S + z) & 0 & 0 \\ 1 & 0 & 0 & 0 & (l_S - z) & 0 \\ 0 & 1 & 0 & -(l_S - z) & 0 & 0 \\ 0 & 0 & 1 & 0 & 0 & 0 \end{bmatrix}, \quad (6.17)$$

can be deduced in analogy to the relations given in (6.6) for the two force interaction points, where in this case the measurement points l_S instead of l_B have to be used.

The hardware implementation of the two eddy-current sensors, which output a voltage that is proportional to the radial displacement, is shown in **Fig. 6.1**. Hence, the two position sensors, denoted as SP1 and SP2 in **Fig. 6.3(a)**, can measure the radial positions of the mover at their axial locations $z = \pm l_S$, i.e. x_1 and y_1 are measured by SP1 at $-l_S$ and x_2 and y_2 are measured by SP2 at l_S . Furthermore, the axial position of the mover z is measured with Hall-effect sensors, as explained in **Section 5.3**.

6.5 Electrical Model

The drive force ${}_I\vec{F}_D$ and the bearing force ${}_I\vec{F}_B$, are controlled by the electric currents in the multiple three-phase windings of the MALTA, as shown in **Fig. 6.5(a)**. In conventional linear machines, the appropriate drive current to generate the desired thrust is typically obtained by performing a dq -transformation out of the three-phase currents in the axially arranged three-phase windings. The resulting q -current component is proportional to the generated thrust, and the resulting d -current component is used for field-weakening; however, it is typically controlled to zero.

For electric machines like the MALTA, which can also control the radial bearing forces on the mover (rotor), the same principle, i.e. the dq -transformation, can be applied to the radially arranged three-phase systems, whose obtained d - and q -current components directly control the resulting bearing forces in x - and y -direction. Hence, for electric machines which can either simultaneously generate drive and bearing forces or simultaneously rotate and move in linear direction, a dq -transformation for both systems should be applied, i.e. for the rotational and the linear motion, which results in a so-called two-directional dq -transformation [18, 19]. Such a transformation has 4 components, dd , dq , qd and qq , where the components dq , qd may provide decoupled torque and axial force control (the first index is related to the rotation, while the second index corresponds to the linear motion, e.g. dq is the d -component for rotation and the q -component for the linear motion). As explained in [18], the MALTA drive current component is a zero-sequence component in rotary direction, and therefore, its q -component is denoted as $0q$ in the two-directional transformation, which is also shown in **Fig. 6.5(b)**. The bearing components have only a d -component in axial direction and both d - and q -components in rotary direction, which gives dd -

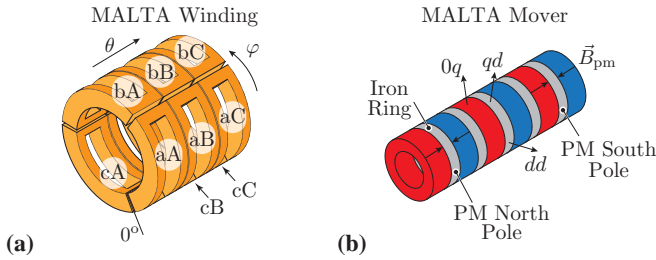


Fig. 6.5: Electrical system of the MALTA: (a) Winding system of a single module consisting of 9 concentrated coils. The complete MALTA prototype with module 1 and module 2 has $2 \times 9 = 18$ coils. (b) Mover with labelled two-directional dq -transformation axes (the first index for radial direction (bearing) and the second index for the linear direction).

and qd -components for control of the bearing forces in x - and y -direction. The mentioned zero-sequence component in rotary direction cannot be represented by the two dimensional complex dq -transformation (3.16). Therefore, for the control implementation in this section, matrix notation is used.

In general, in electric machines that can generate torque and/or thrust force in combination with magnetic bearing forces, the windings are realized either as separate or combined windings [70, 85]. The separated winding arrangement contains a drive winding dedicated to the torque and/or thrust force generation and a bearing winding dedicated to the bearing force generation (i.e. a bearing winding). On the other hand, the combined winding arrangement employs only one winding, where the drive and bearing currents are superimposed. Usually, the separated winding is more difficult to manufacture than the combined winding, as the two different winding systems have to be arranged on the same magnetic core. On the other hand, with the separated winding the control system implementation is simpler compared to the combined winding, as the drive and bearing quantities (voltages, currents and flux linkages) are inherently decoupled.

The comparison of the MALTA winding realizations (separated versus combined) is conducted in **Section 4.4**. The 3×3 -phase combined MALTA winding realization (cf. **Fig. 6.5**) provides the highest drive and bearing force per copper loss compared to the other realization options. Therefore, this winding realization is used in the built prototype. Consequently, the two components of the voltage (u), current (i) and the flux (ψ) linkage, the drive component (for the thrust force generation) and the bearing component (for

the magnetic bearing force generation) are superimposed, and the MALTA phase quantities may be written in the following form

$$\mathbf{X}_{abc} = \begin{bmatrix} x_A + x_{aA} & x_B + x_{aB} & x_C + x_{aC} \\ x_A + x_{bA} & x_B + x_{bB} & x_C + x_{bC} \\ x_A + x_{cA} & x_B + x_{cB} & x_C + x_{cC} \end{bmatrix}, \quad (6.18)$$

where $x_{\{A,B,C\}}$ is the drive component and $x_{\{a,b,c\}\{A,B,C\}}$ is the bearing component and $x \in \{u, i, \psi\}$ may represent any of the phase quantities (voltage, current or flux linkage). According to a conventional linear machine, the drive component of the MALTA phase quantities is equal to

$$x_{\{A,B,C\}} = \hat{X}_M \cos(\omega_L t + \theta_x + \{\gamma_A, \gamma_B, \gamma_C\}), \quad (6.19)$$

where $x \in \{u, i, \psi\}$, $\hat{X}_M \in \{\hat{U}_M, \hat{I}_M, \hat{\Psi}_M\}$ is the drive amplitude, ω_L is the electrical angular speed, θ_x is the initial drive phase angle, $\gamma_A = 0^\circ$, $\gamma_B = -120^\circ$ and $\gamma_C = 120^\circ$. As can be noted, the drive component results in an offset, i.e. a zero-sequence component, added to the bearing components of each rotary three-phase system (cf. each column in (6.18)). These zero-sequence components appear due to the MALTA combined winding, i.e. each winding has drive and bearing current components. E.g. the first three axial windings aA, bA and cA have the same drive current component which forms zero-sequence, whereas the bearing component currents form a three-phase system. Therefore, to ensure a uniform modeling, linear algebra notation (vectors and matrices) is used for the MALTA electric model rather than complex numbers, since representing zero-sequence components is simpler. The bearing component of the MALTA voltage and current quantities is given as

$$x_{\{a,b,c\}\{A,B,C\}} = \hat{X}_{Mb} \cos(\varphi_x + \{\gamma_a, \gamma_b, \gamma_c\}) \times \cos(\omega_L t + \theta_{x,b} + \{\gamma_A, \gamma_B, \gamma_C\}), \quad (6.20)$$

where $x \in \{u, i\}$, $\hat{X}_{Mb} \in \{\hat{U}_{Mb}, \hat{I}_{Mb}\}$ is the bearing amplitude and φ_x is the direction in which the current space vector has to point in order to counteract the displacement, which together with \hat{X}_{Mb} is later defined by the bearing current controller. Furthermore, since not all stator windings are facing the same PM in axial direction, the linear position of the rotor has to be considered for the bearing current and voltage, which is achieved by the multiplication with $\cos(\omega_L t + \theta_{x,b} + \{\gamma_A, \gamma_B, \gamma_C\})$ in (6.20). Hence, the superposition of the three bearing components to the drive component can be interpreted as a redistribution of the drive current to the three circumferential windings of

one linear phase in order to generate bearing forces, while at the same time the average drive component in linear direction is not changed.

As already discussed in **Section 3.9.2**, in contrast to the bearing components of the current and voltage, the bearing component of the flux linkage also depends on the radial displacement. Since for the MALTA there is no dependency on the rotation angle, i.e. $\omega_R t + \varphi_\psi = 0$, based on (3.23) the flux linkage can be written as

$$\psi_{\{a,b,c\}\{A,B,C\}} = \chi_{\text{pm},M} (x \cos\{\gamma_a, \gamma_b, \gamma_c\} - y \sin\{\gamma_a, \gamma_b, \gamma_c\}) \times \cos(\omega_L t + \theta_\psi + \{\gamma_A, \gamma_B, \gamma_C\}), \quad (6.21)$$

where $\chi_{\text{pm},M}$ is the MALTA flux linkage radial sensitivity.

6.5.1 MALTA Transformation

As shown in **Section 3.9.2**, for the MALTA only the currents i_q , i_{dd} and i_{qd} have to be controlled to generate the thrust and the bearing force, respectively. Furthermore, as shown in the following, also the i_d -component must be controlled to zero such that the drive current is kept to a minimum and is not weakening the PM field. Hence, In order to obtain these quantities, first the 9 MALTA phase quantities (*abc*-quantities) have to be transformed into 9 stationary *dq0*-quantities as

$$\mathbf{X}_{dq0} = \mathbf{K}_{R0} \cdot \mathbf{X}_{abc} \cdot \mathbf{K}_{L0}, \quad (6.22)$$

where \mathbf{K}_{R0} is the rotary electrical angle transformation

$$\mathbf{K}_{R0} = \frac{2}{3} \begin{bmatrix} \cos \gamma_a & \cos \gamma_b & \cos \gamma_c \\ -\sin \gamma_a & -\sin \gamma_b & -\sin \gamma_c \\ 1/2 & 1/2 & 1/2 \end{bmatrix}, \quad (6.23)$$

and \mathbf{K}_{L0} is the linear electrical angle transformation

$$\mathbf{K}_{L0} = \frac{2}{3} \begin{bmatrix} \cos(\omega_L t + \gamma_a) & -\sin(\omega_L t + \gamma_a) & 1/2 \\ \cos(\omega_L t + \gamma_b) & -\sin(\omega_L t + \gamma_b) & 1/2 \\ \cos(\omega_L t + \gamma_c) & -\sin(\omega_L t + \gamma_c) & 1/2 \end{bmatrix}. \quad (6.24)$$

It should be noted that these transformation matrices also consider the zero sequence components for rotation and for linear motion, since, as already seen, e.g. the drive component in linear direction is a zero-sequence component

for the bearing component (cf. (6.18)). Hence, the $dq0$ -quantities have the following components

$$\mathbf{X}_{dq0} = \begin{bmatrix} x_{dd} & x_{dq} & x_{d0} \\ x_{qd} & x_{qq} & x_{q0} \\ x_{0d} & x_{0q} & x_{00} \end{bmatrix}, \quad (6.25)$$

where in the double index notation $x_{\{d,q,0\}\{d,q,0\}}$, the first index denotes the respective rotary component (d , q or 0) while the second index denotes the linear component, i.e. the rows in \mathbf{X}_{dq0} represent the rotary direction while the columns represent the linear direction. Furthermore, it should be noted that three types of the zero sequence components may be identified: (1) rotary zero sequence components x_{0d} and x_{0q} , (2) linear zero sequence components x_{d0} and x_{q0} and (3) rotary-linear zero sequence component x_{00} . By transforming the abc -quantities of the MALTA voltage and the current into the $dq0$ -quantities, i.e. inserting (6.19) and (6.20) into (6.18) and applying the transformation given in (6.22), the following components are obtained

$$\mathbf{X}_{dq0} = \begin{bmatrix} \hat{X}_{Mb} \cos \varphi_x \cos \theta_{x,b} & \hat{X}_{Mb} \cos \varphi_x \sin \theta_{x,b} & 0 \\ \hat{X}_{Mb} \sin \varphi_x \cos \theta_{x,b} & \hat{X}_{Mb} \sin \varphi_x \sin \theta_{x,b} & 0 \\ \hat{X}_M \cos \theta_x & \hat{X}_M \sin \theta_x & 0 \end{bmatrix}. \quad (6.26)$$

This expression clearly shows that the drive components of the voltage and the current ($\hat{X}_M \cos \theta_x$ and $\hat{X}_M \sin \theta_x$) are ‘seen’ as a zero component (x_{0d} and x_{0q}) for the rotary direction, which also corresponds to (6.18) where the drive component is the same in all rows of the matrix \mathbf{X}_{abc} . Accordingly, also the abc flux linkage Ψ_{abc} is transformed into the $dq0$ -flux linkage which results in

$$\Psi_{dq0} = \begin{bmatrix} x \chi_{pm,M} \cos \theta_\psi & x \chi_{pm,M} \sin \theta_\psi & 0 \\ y \chi_{pm,M} \cos \theta_\psi & y \chi_{pm,M} \sin \theta_\psi & 0 \\ \hat{\Psi}_M \cos \theta_\psi & \hat{\Psi}_M \sin \theta_\psi & 0 \end{bmatrix}. \quad (6.27)$$

The dq -frame is usually oriented such that $\theta_\psi = 0^\circ$, which leads to only three non-zero flux linkage components

$$\Psi_{dq0} = \begin{bmatrix} x \chi_{pm,M} & 0 & 0 \\ y \chi_{pm,M} & 0 & 0 \\ \hat{\Psi}_M & 0 & 0 \end{bmatrix}. \quad (6.28)$$

As already done in **Section 3.9.2** for separate windings, in order to identify the $dq0$ -current components that contribute to the radial forces (F_x and F_y)

and the thrust force (F_z) generation in matrix notation for the combined winding, the electrical and mechanical powers are compared. The electrical power of the MALTA winding is $p_{el} = \sum_{m=\{a,b,c\}} \sum_{n=\{A,B,C\}} u_{mn} i_{mn}$, which can be expressed by the Frobenius inner product [109] of matrices, i.e. the sum of the element by element multiplication, as

$$p_{el} = \langle \mathbf{U}_{abc}, \mathbf{I}_{abc} \rangle_F, \quad (6.29)$$

where the MALTA voltage \mathbf{U}_{abc} is given as

$$\mathbf{U}_{abc} = \mathbf{R}_{abc} \mathbf{I}_{abc} + \mathbf{L}_{abc} \frac{d\mathbf{I}_{abc}}{dt} + \frac{d\mathbf{\Psi}_{abc}}{dt}. \quad (6.30)$$

The resistance \mathbf{R}_{abc} and the inductance \mathbf{L}_{abc} matrices are diagonal matrices, i.e. $\mathbf{R}_{abc} = \text{diag}(R, R, R)$ and $\mathbf{L}_{abc} = \text{diag}(L, L, L)$. Hence, the electrical power is equal to

$$\begin{aligned} p_{el} = & \frac{9}{4} \left\{ R \hat{I}_{Mb}^2 + L \frac{d\hat{I}_{Mb}}{dt} \hat{I}_{Mb} + \right. \\ & \left. \chi_{pm,M} (v_x i_{dd} + v_y i_{qd}) + \omega_L \chi_{pm,M} (x i_{dq} + y i_{qq}) \right\} + \\ & \frac{9}{2} \left\{ R \hat{I}_M^2 + L \frac{d\hat{I}_M}{dt} \hat{I}_M + \frac{d\hat{\Psi}_M}{dt} i_{0d} + \omega_L \hat{\Psi}_M i_{0q} \right\}, \end{aligned} \quad (6.31)$$

where $d\chi_{pm,M}/dt = 0$ is assumed. From (6.31), the power parts that contribute to the copper losses (containing R), change of the magnetic energy (containing L or $d\hat{\Psi}_M/dt$) and the mechanical power (containing v_x , v_y or ω_L) can be easily identified. It should be noted that

$$\omega_L = \frac{2\pi}{\tau_{pp}} v_z.$$

On the other hand, the mechanical power of the MALTA is equal to

$$p_{mech} = v_x F_x + v_y F_y + v_z F_z.$$

Therefore, the thrust force in the MALTA with the combined winding is generated as

$$F_z = \frac{9\pi}{\tau_{pp}} \hat{\Psi}_M i_{0q}, \quad (6.32)$$

while the bearing forces are generated as

$$F_x = \frac{9}{4} \chi_{\text{pm},\text{M}} i_{\text{dd}}, \quad F_y = \frac{9}{4} \chi_{\text{pm},\text{M}} i_{\text{qd}}, \quad (6.33)$$

which agrees with the analysis conducted using complex space vectors (cf. (3.26) and (3.27)). Additionally, the parasitic thrust force is created when the rotor radial displacement is non-zero, which is equal to

$$F_{z,\text{par}} = (9\pi/2\tau_{\text{pp}}) \hat{\Psi}_{\text{M}}(x i_{\text{dq}} + y i_{\text{qq}}),$$

which has to be compensated by the controller.

6.5.2 MALTA Reduced Transformation

In a second step, now a transformation has to be found which transforms the 9 $dq0$ -quantities into only 4 $dq0$ -quantities, which are needed to control the forces generated in the MALTA. From (6.32) and (6.33) it can be seen that the thrust force F_z and the bearing forces F_x and F_y are controlled with three different $dq0$ -current components. The rest of the current components has to be kept to zero by the current controller. Hence, \mathbf{I}_{dq0} reference has the following form

$$\mathbf{I}_{\text{dq0}} = \begin{bmatrix} i_{\text{dd}} \rightarrow F_x/K_{\text{B}} & i_{\text{dq}} \rightarrow 0 & i_{\text{d0}} \rightarrow 0 \\ i_{\text{qd}} \rightarrow F_y/K_{\text{B}} & i_{\text{qq}} \rightarrow 0 & i_{\text{q0}} \rightarrow 0 \\ i_{\text{0d}} \rightarrow 0 & i_{\text{0q}} \rightarrow F_z/K_{\text{L}} & i_{\text{00}} \rightarrow 0 \end{bmatrix}, \quad (6.34)$$

where $K_{\text{L}} = (9\pi/\tau_{\text{pp}}) \hat{\Psi}_{\text{M}}$ and $K_{\text{B}} = (9/4) \chi_{\text{pm},\text{M}}$ are the MALTA drive and bearing constants (cf. (6.32) and (6.33)). It should be noted that by keeping the current components in (6.34) to zero, the electrical angles φ_x , θ_x and $\theta_{x,\text{b}}$ of the phase currents have to be controlled. Comparing (6.34) and (6.26), it can be seen that when controlling $i_{\text{0d}} \rightarrow 0$, the drive current phase angle $\theta_i = \pi/2$ is achieved and when controlling $i_{\text{dq}} \rightarrow 0$ or $i_{\text{qq}} \rightarrow 0$, the bearing current phase angle $\theta_{i,\text{b}} = 0$ results. Finally, the phase angle φ_i is determined by the current components i_{dd} and i_{qd} ($i_{\text{dd}} = \hat{I}_{\text{Mb}} \cos \varphi_i$ and $i_{\text{qd}} = \hat{I}_{\text{Mb}} \sin \varphi_i$) as

$$\varphi_i = \text{atan2}(i_{\text{qd}}, i_{\text{dd}}),$$

which can be also obtained as

$$\varphi_i = \text{atan2}(F_y, F_x)$$

due to the proportionality between the currents i_{qd} , i_{dd} and F_y , F_x , respectively, (cf. (6.33)).

Since \mathbf{I}_{dq0} has nine current components, the control system of the MALTA would need nine independent current controllers per MALTA module (the complete MALTA system consists of two such independently controllable modules, since a possible tilting of the long MALTA rotor has to be counteracted). In order to reduce the number of the required current controllers, a reduced transformation that requires only four current controllers per MALTA module is proposed. Since there is no rotation in the MALTA (i.e. the mover cannot rotate $\omega_R = 0$, and therefore all bearing control quantities are positioned in circumferential direction, but not rotated), the three-phase system in the rotary direction resembles a DC-quantity, i.e. it does not alternate its values over time with a certain angular frequency like in typical electric machines. Therefore, it is enough to control only its amplitude \hat{I}_{Mb} , while the information about the phase and the electrical angle φ_i is given by the radial position controllers that output the bearing forces F_x and F_y . Hence, the angle φ_i is always pointing in the direction in which the bearing force has to act. The transformation that gives only 4 dq -components is defined as

$$\mathbf{X}_{dq} = \begin{bmatrix} \hat{X}_M \cos \theta_x & \hat{X}_M \sin \theta_x \\ \hat{X}_{Mb} \cos \theta_{x,b} & \hat{X}_{Mb} \sin \theta_{x,b} \end{bmatrix} = \mathbf{K}_R(\varphi_x) \cdot \mathbf{X}_{abc} \cdot \mathbf{K}_L, \quad (6.35)$$

where the transformation matrices $\mathbf{K}_R(\varphi_x)$ and \mathbf{K}_L are

$$\mathbf{K}_R(\varphi_x) = \frac{2}{3} \begin{bmatrix} 1/2 & -\sin(\varphi_x - \pi/2 + \gamma_a) \\ 1/2 & -\sin(\varphi_x - \pi/2 + \gamma_b) \\ 1/2 & -\sin(\varphi_x - \pi/2 + \gamma_c) \end{bmatrix}^T, \quad (6.36)$$

and

$$\mathbf{K}_L = \frac{2}{3} \begin{bmatrix} \cos(\omega_L t + \gamma_a) & -\sin(\omega_L t + \gamma_a) \\ \cos(\omega_L t + \gamma_b) & -\sin(\omega_L t + \gamma_b) \\ \cos(\omega_L t + \gamma_c) & -\sin(\omega_L t + \gamma_c) \end{bmatrix}. \quad (6.37)$$

The pseudoinverse transformation matrices are equal to

$$\mathbf{K}_R^{-1}(\varphi_x) = \begin{bmatrix} 1 & -\sin(\varphi_x - \pi/2 + \gamma_a) \\ 1 & -\sin(\varphi_x - \pi/2 + \gamma_b) \\ 1 & -\sin(\varphi_x - \pi/2 + \gamma_c) \end{bmatrix}, \quad (6.38)$$

and

$$\mathbf{K}_L^{-1} = \begin{bmatrix} \cos(\omega_L t + \gamma_a) & -\sin(\omega_L t + \gamma_a) \\ \cos(\omega_L t + \gamma_b) & -\sin(\omega_L t + \gamma_b) \\ \cos(\omega_L t + \gamma_c) & -\sin(\omega_L t + \gamma_c) \end{bmatrix}^T. \quad (6.39)$$

Comparing the new dq -components in \mathbf{X}_{dq} given with (6.35) to the $dq0$ -components in \mathbf{X}_{dq0} given with (6.26), it can be seen that the rotary zero sequence components x_{0d} and x_{0q} are moved to the first row of the \mathbf{X}_{dq} . In the second row the components proportional to the bearing amplitude \hat{X}_{Mb} are found. In order not to generate any thrust force F_z with the bearing current component, the electrical angle is $\theta_{i,b} = 0$. Similarly, to maximize the thrust force generation with the drive current component \hat{X}_M , the electrical angle is $\theta_i = \pi/2$. In order to achieve these electrical angles, the components $\mathbf{X}_{dq}(1, 1)$ and $\mathbf{X}_{dq}(2, 2)$ are controlled to zero

$$\mathbf{I}_{dq} = \begin{bmatrix} i_{0d} \rightarrow 0 & i_{0q} \rightarrow F_z/K_L \\ i_{bd} \rightarrow F_B/K_B & i_{bq} \rightarrow 0 \end{bmatrix}, \quad (6.40)$$

where $i_{bd} = \hat{I}_{Mb} \cos \theta_{x,b}$, $i_{bq} = \hat{I}_{Mb} \sin \theta_{x,b}$ and $F_B = \sqrt{F_x^2 + F_y^2}$. The force angle $\varphi_i = \text{atan2}(F_y/F_x)$ is calculated from the bearing force references F_x and F_y , which are provided from the radial position controller as shown in the following section.

6.6 MALTA Mechanical Model Linearization

The nonlinear mechanical model given with the equations of motion (6.3), together with the model of the position sensing and the electrical model, may be used for numerical simulation of the MALTA dynamics. To use the nonlinear mechanical model (6.3) for the position controller design, the model is first linearized. In order to formally represent the linearization process a function from the equations of motion (6.3) is defined as

$$\begin{aligned} \vec{F}_{\text{EoM}} \left(\frac{\partial^2 \vec{q}}{\partial t^2}, \frac{\partial \vec{q}}{\partial t}, \vec{q}, \vec{v} \right) &= \begin{bmatrix} - & - & - & - & m \frac{\partial^2 \vec{q}_i}{\partial t^2} - \mathcal{I} \vec{F}_{\text{tot}} & - & - & - & - \\ \mathcal{R} \mathbf{I}_m \cdot \frac{\partial \mathcal{R} \vec{\omega}}{\partial t} + \mathcal{R} \vec{\omega} \times \mathcal{R} \mathbf{I}_m \cdot \mathcal{R} \vec{\omega} - \mathcal{R} \vec{T}_{\text{tot}} & - & - & - & - & - & - & - & - \end{bmatrix} \\ &= \mathbf{0}_{6 \times 1}, \end{aligned} \quad (6.41)$$

which is identically equal to zero. $\mathbf{0}_{6 \times 1}$ represents a 6×1 zero matrix. The position (state) \vec{q} and the force (input) \vec{v} vectors are equal to

$$\vec{q} = \begin{bmatrix} x \\ y \\ z \\ \alpha \\ \beta \\ \gamma \end{bmatrix}, \quad \vec{v} = \begin{bmatrix} f_{xB1} \\ f_{yB1} \\ f_{xB2} \\ f_{yB2} \\ f_D \end{bmatrix},$$

where $f_D = f_{D1} + f_{D2}$. The resulting *linear equation of motion* is

$$\mathbf{M} \frac{\partial^2 \vec{q}}{\partial t^2} + \mathbf{G} \frac{\partial \vec{q}}{\partial t} = \mathbf{S} \vec{q} + \mathbf{V} \vec{v}, \quad (6.42)$$

where the linearization matrices are calculated as

$$\begin{aligned} \mathbf{M}_{6 \times 6} &= \mathbf{J} \left(\vec{F}_{\text{EoM}}, \frac{\partial^2 \vec{q}}{\partial t^2} \right) \bigg|_{\text{at ss}} & \mathbf{G}_{6 \times 6} &= \mathbf{J} \left(\vec{F}_{\text{EoM}}, \frac{\partial \vec{q}}{\partial t} \right) \bigg|_{\text{at ss}} \\ \mathbf{S}_{6 \times 6} &= -\mathbf{J} \left(\vec{F}_{\text{EoM}}, \vec{q} \right) \bigg|_{\text{at ss}} & \mathbf{V}_{6 \times 5} &= -\mathbf{J} \left(\vec{F}_{\text{EoM}}, \vec{v} \right) \bigg|_{\text{at ss}} \end{aligned}$$

$\mathbf{J}(\vec{f}, \vec{n})$ computes the Jacobian matrix of the function $\vec{f}_{m \times 1}$ with respect to $\vec{r}_{n \times 1}$, where the Jacobian matrix size is $m \times n$, which is then evaluated at the given steady-state point. At the steady-state point, the mover can be displaced in axial direction, but should be in the radial center and not tilted. Therefore, the linearization is conducted for the following values of the position and force vectors:

$$\vec{q}_{ss} = \begin{bmatrix} 0 \\ 0 \\ z_{ss} \\ 0 \\ 0 \\ 0 \end{bmatrix}, \quad \vec{v}_{ss} = \begin{bmatrix} 0 \\ -g \cdot m \cdot \frac{z_{ss} - l_B}{2l_B} \\ 0 \\ g \cdot m \cdot \frac{z_{ss} + l_B}{2l_B} \\ 0 \\ 0 \end{bmatrix}.$$

Additionally, at the steady-state point, the position derivatives are set to zero, i.e.

$$\frac{\partial^2 \vec{q}_{ss}}{\partial t^2} = \mathbf{0} \in \mathbb{R}^{6 \times 1}, \quad \frac{\partial \vec{q}_{ss}}{\partial t} = \mathbf{0} \in \mathbb{R}^{6 \times 1}.$$

The matrix $\mathbf{G} = \mathbf{0}_{6 \times 6}$ in the linearized equation of motion (6.42), also called *gyroscopic effect matrix* [22], is equal to zero as the rotation of the mover in the steady-state is neglected. The rest of the matrices in (6.42) are equal to

$$\mathbf{M} = \begin{bmatrix} m & 0 & 0 & 0 & 0 & 0 \\ 0 & m & 0 & 0 & 0 & 0 \\ 0 & 0 & m & 0 & 0 & 0 \\ 0 & 0 & 0 & I_{xx} & 0 & 0 \\ 0 & 0 & 0 & 0 & I_{yy} & 0 \\ 0 & 0 & 0 & 0 & 0 & I_{zz} \end{bmatrix}, \quad (6.43)$$

$$\mathbf{S} = \begin{bmatrix} 2K_A & 0 & 0 & 0 & -2K_A \cdot z_{ss} & 0 \\ 0 & 2K_A & 0 & 2K_A \cdot z_{ss} & 0 & 0 \\ 0 & 0 & 0 & 0 & 0 & 0 \\ 0 & 2K_A \cdot z_{ss} & g \cdot m & 2K_A(z_{ss}^2 + l_B^2) & 0 & 0 \\ -2K_A \cdot z_{ss} & 0 & 0 & 0 & 2K_A(z_{ss}^2 + l_B^2) & 0 \\ 0 & 0 & 0 & 0 & 0 & 0 \end{bmatrix}, \quad (6.44)$$

$$\mathbf{V} = \begin{bmatrix} 1 & 0 & 1 & 0 & 0 \\ 0 & 1 & 0 & 1 & 0 \\ 0 & 0 & 0 & 0 & 1 \\ 0 & l_B + z_{ss} & 0 & l_B - z_{ss} & 0 \\ -l_B - z_{ss} & 0 & l_B - z_{ss} & 0 & 0 \\ 0 & 0 & 0 & 0 & 0 \end{bmatrix}. \quad (6.45)$$

6.6.1 Reduced MALTA Model

Since rotation of the MALTA mover cannot be actively controlled, therefore, the dynamics of γ are not considered for the controller design. Consequently, the matrices in the linearized equation of motion (6.42) are reduced, i.e. the last rows and columns in (6.43), (6.44) and (6.45) are omitted. Therefore, in further analysis the matrices \mathbf{M} , \mathbf{S} and \mathbf{V} have the following dimensions

$$\mathbf{M} \in \mathbb{R}^{5 \times 5}, \quad \mathbf{S} \in \mathbb{R}^{5 \times 5}, \quad \mathbf{V} \in \mathbb{R}^{5 \times 5}.$$

The most favorable form of MIMO system for controller design is the state-space form of the linear equations, where the first derivatives of the states are expressed as functions of the states itself and the inputs (drive and bearing forces). In order get the state-space form, the second derivatives from the linearized equations of motions are removed by augmenting the state vector as

$$\vec{\xi} = \begin{bmatrix} \vec{q} \\ \frac{\partial \vec{q}}{\partial t} \end{bmatrix} \in \mathbb{R}^{10},$$

where

$$\vec{q} = \begin{bmatrix} x \\ y \\ z \\ \alpha \\ \beta \end{bmatrix} \in \mathbb{R}^5,$$

Tab. 6.2: Poles (eigenvalues) of the linearized MALTA system.

Symbol	Mode	Eigenvalue
$\lambda_{1,2}$	x	± 218.92
$\lambda_{3,4}$	y	± 218.92
$\lambda_{5,6}$	z	0
$\lambda_{7,8}$	α	± 157.53
$\lambda_{9,10}$	β	± 157.53

since y is neglected for the further analysis. This gives a system in a standard state-space form

$$\begin{aligned}\frac{\partial \vec{\xi}}{\partial t} &= \mathbf{A} \vec{\xi} + \mathbf{B} \vec{v}, \\ \vec{p} &= \mathbf{C} \vec{\xi},\end{aligned}\tag{6.46}$$

where the state-space matrices are obtained as

$$\mathbf{A} = \mathbf{E}^{-1} \begin{bmatrix} \mathbf{0} & \mathbf{I} \\ \mathbf{S} & \mathbf{0} \end{bmatrix} \quad \mathbf{B} = \mathbf{E}^{-1} \begin{bmatrix} \mathbf{0} \\ \mathbf{V} \end{bmatrix} \quad \mathbf{C} = [\mathbf{P} \quad \mathbf{0}], \tag{6.47}$$

where $\mathbf{A} \in \mathbb{R}^{10 \times 10}$, $\mathbf{B} \in \mathbb{R}^{10 \times 5}$, $\mathbf{C} \in \mathbb{R}^{5 \times 10}$ and the matrix $\mathbf{P} \in \mathbb{R}^{5 \times 5}$ is obtained from (6.17) by removing the last column and adding the zero-matrix $\mathbf{0} \in \mathbb{R}^{5 \times 5}$.

6.6.2 Poles of the Reduced MALTA Model

From the linearized state-space system representation (6.46), the poles of the system are determined as eigenvalues of the matrix \mathbf{A} , which are given in **Tab. 6.2** for the case $z_{ss} = 0$. The linearization was also studied for $z_{ss} \in [-15, 15]$ mm, revealing that the pole locations do not vary significantly. The system is open-loop unstable, since there exist positive poles. These are caused by the destabilizing attraction forces, which act on the mover in a ‘negative-stiffness spring’ fashion. The largest unstable pole imposes a minimum requirement on the closed-loop bandwidth of the position control system (as a rule of thumb, the closed-loop system bandwidth should at least be twice the frequency of the largest unstable pole [110]). For example, from **Tab. 6.2** the largest frequency is 218.92 rad/s and it is associated to the unstable pole $\lambda_1 = 218.92$.

Tab. 6.3: Maximum expected values of positions and forces used for normalization.

Symbol	Description	Value
Position		
x_{\max}	Radial distance from center to touchdown bearing	0.65 mm
y_{\max}	Radial distance from center to touchdown bearing	0.65 mm
z_{\max}	Axial stroke amplitude	15 mm
α_{\max}	Cardan angle	0.0154 rad
β_{\max}	Cardan angle	0.0154 rad
Speed		
\dot{x}_{\max}	Translational velocity	0.335 m/s
\dot{y}_{\max}	Translational velocity	0.335 m/s
\dot{z}_{\max}	Translational velocity	1.904 m/s
$\dot{\alpha}_{\max}$	Angular velocity	5.315 rad/s
$\dot{\beta}_{\max}$	Angular velocity	5.315 rad/s
Force		
$f_{B\max}$	Maximum bearing force per module	15 N
$f_{D\max}$	Maximum drive force per module	21 N

6.6.3 Normalization

Normalization (scaling) is very important for practical implementations of the control systems, as it allows to ensure for all the states $\vec{\xi}$, inputs \vec{v} and the outputs \vec{p} numerical values ≤ 1 . Therefore, the absolute values in the vectors are divided by their maximum expected value, which may be written in the following form using the normalization matrices

$$\vec{\xi}_{\text{pu}} = \mathbf{D}_{\xi}^{-1} \vec{\xi} \in \mathbb{R}^{10}, \quad \vec{v}_{\text{pu}} = \mathbf{D}_v^{-1} \vec{v} \in \mathbb{R}^5, \quad \vec{p}_{\text{pu}} = \mathbf{D}_p^{-1} \vec{p} \in \mathbb{R}^5, \quad (6.48)$$

where the normalization matrices are diagonal and equal to

$$\begin{aligned} \mathbf{D}_{\xi} &= \begin{bmatrix} \mathbf{D}_q & \mathbf{0} \\ \mathbf{0} & \mathbf{D}_{\dot{q}} \end{bmatrix}, \\ \mathbf{D}_q &= \text{diag} (x_{\max} \quad y_{\max} \quad z_{\max} \quad \alpha_{\max} \quad \beta_{\max}), \\ \mathbf{D}_{\dot{q}} &= \text{diag} (\dot{x}_{\max} \quad \dot{y}_{\max} \quad \dot{z}_{\max} \quad \dot{\alpha}_{\max} \quad \dot{\beta}_{\max}), \\ \mathbf{D}_v &= \text{diag} (f_{B\max} \quad f_{B\max} \quad f_{B\max} \quad f_{B\max} \quad 2f_{D\max}), \\ \mathbf{D}_p &= \text{diag} (x_{\max} \quad y_{\max} \quad x_{\max} \quad y_{\max} \quad z_{\max}). \end{aligned} \quad (6.49)$$

The maximum values for the positions and the forces are given in **Tab. 6.3**. The cardan angles are calculated as

$$\alpha_{\max} = \text{atan} \left(\frac{x_{\max}}{l_B} \right), \quad \beta_{\max} = \text{atan} \left(\frac{y_{\max}}{l_B} \right).$$

The speeds are derived from the maximum displacements and the maximum forces. The derivation is given for the x -direction, but is analog for the y - and z -direction. Assuming the mover is initially at rest at the origin, the movement is described with

$$\ddot{x}(t) = \frac{F}{m}, \quad \dot{x}(t) = \frac{F}{m} t, \quad x(t) = \frac{F}{2m} t^2,$$

where F is assumed to be the total force accelerating the mover in the respective direction, m is the mover mass and t time. In order to find the maximum occurring speed, the last equation is solved for the maximum time t_{\max} , where the mover hits the touchdown bearing, i.e.

$$t_{\max} = \sqrt{\frac{2m x_{\max}}{F}}.$$

This results in the maximum velocity

$$\dot{x}(t_{\max}) = \sqrt{\frac{2F x_{\max}}{m}}.$$

Therefore, the translational velocities are calculated as

$$\dot{x}_{\max} = \sqrt{\frac{4f_{B\max} x_{\max}}{m}}, \quad \dot{y}_{\max} = \sqrt{\frac{4f_{B\max} y_{\max}}{m}}, \quad \dot{z}_{\max} = \sqrt{\frac{4f_{D\max} z_{\max}}{m}},$$

where the force F that accelerates the mover in the respective direction is twice the maximum force per module, since the MALTA has the two modules acting on the mover.

For the angular velocities, the considerations are similar. If α is taken as an example, the following expressions that describe the rotation result

$$\ddot{\alpha}(t) = \frac{r F}{I_{xx}}, \quad \dot{\alpha}(t) = \frac{r F}{I_{xx}} t, \quad \alpha(t) = \frac{r F}{2I_{xx}} t^2,$$

where F is the total force that rotates the mover over the radius r . The maximum rotational velocities are equal to

$$\dot{\alpha}_{\max} = \sqrt{\frac{4l_B f_{B\max} \alpha_{\max}}{I_{xx}}}, \quad \dot{\beta}_{\max} = \sqrt{\frac{4l_B f_{B\max} \beta_{\max}}{I_{yy}}}.$$

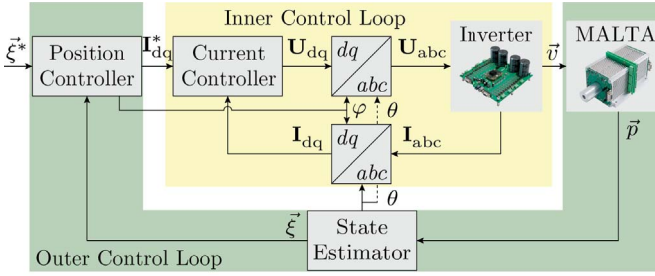


Fig. 6.6: Overview of the cascaded MALTA control structure with inner current control loop and outer position control loop.

The normalization of the state vector $\vec{\xi}$ and the input vector \vec{v} results in the normalized (scaled) system of the state-space equations

$$\begin{aligned} \frac{\partial \vec{\xi}_{\text{pu}}}{\partial t} &= \mathbf{A}_{\text{pu}} \vec{\xi}_{\text{pu}} + \mathbf{B}_{\text{pu}} \vec{v}_{\text{pu}}, \\ \vec{p}_{\text{pu}} &= \mathbf{C}_{\text{pu}} \vec{\xi}_{\text{pu}} \end{aligned} \quad (6.50)$$

where the normalized state-space matrices are calculated using (6.47) and (6.49) as

$$\mathbf{A}_{\text{pu}} = \mathbf{D}_{\xi}^{-1} \mathbf{A} \mathbf{D}_{\xi}, \quad \mathbf{B}_{\text{pu}} = \mathbf{D}_{\xi}^{-1} \mathbf{B} \mathbf{D}_v, \quad \mathbf{C}_{\text{pu}} = \mathbf{D}_p^{-1} \mathbf{C} \mathbf{D}_{\xi}. \quad (6.51)$$

6.7 Position Controller Design

The overall MALTA control scheme is presented in **Fig. 6.6**. It features a cascaded structure, with inner current control loop and outer position control loop. This is a common choice for the control of electromechanical actuators as the mechanical time constants are typically much larger than the electrical ones, thus exhibiting a dynamic separation in the frequency domain. This allows a largely independent design of both control loops. In the following, first the position controller and next the current controller are described.

6.7.1 State-Space Augmenting for Integral Control

For the outer position loop a COG control strategy [22] is chosen, which consists in controlling position and orientation of the mover frame \mathcal{R} , rather

than axial and radial positions \vec{p} sensed at the sensor planes (i.e. output control or *decentralized* approach). The controlled states $\vec{\xi}_{\text{pu}}$ contain positions and their derivatives, which allows to realize a controller with *proportional* and *derivative* action on the state's dynamics. Such controller may result in non-zero steady-state errors that may be caused by unmodeled disturbances such as cogging or radial pull forces or any other external mechanical load. The main aim is to bring the measured positions \vec{p} to the desired reference values \vec{p}^* . Therefore, the vector representing the integral of the error

$$\vec{v}(t) = \int_0^t (\vec{p}^*(\tau) - \vec{p}(\tau)) d\tau \in \mathbb{R}^5, \quad (6.52)$$

is considered. It should be noted that

$$\frac{\partial \vec{v}(t)}{\partial t} = \vec{p}^*(t) - \vec{p}(t).$$

For the implementation, the normalized state-space, i.e. per unit, equations are considered (cf. (6.50)). Consequently, the integral error vector \vec{v} should also be normalized. As \vec{v} has the same dimension and units as \vec{p} , it is normalized with the same normalization matrix (cf. (6.48))

$$\vec{v}_{\text{pu}} = \mathbf{D}_p^{-1} \vec{v} \in \mathbb{R}^5. \quad (6.53)$$

The augmented per unit state-space equations are equal to

$$\underbrace{\frac{\partial}{\partial t} \begin{bmatrix} \vec{\xi}_{\text{pu}} \\ \vec{v}_{\text{pu}} \end{bmatrix}}_{=\vec{\xi}_{\text{aug,pu}}} = \underbrace{\begin{bmatrix} \mathbf{A}_{\text{pu}} & \mathbf{0}_{10 \times 5} \\ -\mathbf{C}_{\text{pu}} & \mathbf{0}_{5 \times 5} \end{bmatrix}}_{=\mathbf{A}_{\text{aug,pu}}} \cdot \underbrace{\begin{bmatrix} \vec{\xi}_{\text{pu}} \\ \vec{v}_{\text{pu}} \end{bmatrix}}_{=\vec{\xi}_{\text{aug,pu}}} + \underbrace{\begin{bmatrix} \mathbf{B}_{\text{pu}} \\ \mathbf{0}_{5 \times 5} \end{bmatrix}}_{=\mathbf{B}_{\text{aug,pu}}} \cdot \vec{u}_{\text{pu}} \quad (6.54)$$

$$\vec{p}_{\text{pu}} = \underbrace{\begin{bmatrix} \mathbf{C}_{\text{pu}} & \mathbf{0}_{5 \times 5} \end{bmatrix}}_{=\mathbf{C}_{\text{aug,pu}}} \cdot \begin{bmatrix} \vec{\xi}_{\text{pu}} \\ \vec{v}_{\text{pu}} \end{bmatrix}$$

where the dimensions of the new state-space system are

$$\vec{\xi}_{\text{aug,pu}} \in \mathbb{R}^{15} \quad \mathbf{A}_{\text{aug,pu}} \in \mathbb{R}^{15 \times 15} \quad \mathbf{B}_{\text{aug,pu}} \in \mathbb{R}^{15 \times 5} \quad \mathbf{C}_{\text{aug,pu}} \in \mathbb{R}^{5 \times 15}.$$

6.7.2 Controller Structure and Components

The position controller structure is shown in **Fig. 6.7**, realized in the normalized, i.e. per unit, system of values. The control action comprises three components:

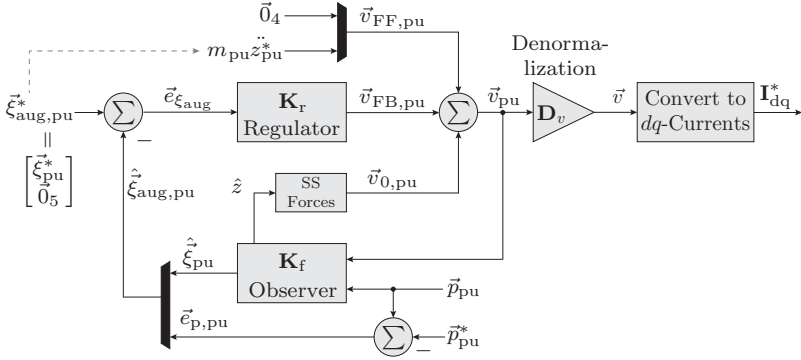


Fig. 6.7: Structure of the MALTA position controller. From the output measurements \vec{p} , the state $\vec{\xi}$ is estimated with the state estimator (Kalman Filter) and used for LQR feedback control. To enhance the performance, the feed-forward force commands \vec{v}_{FF} (for tracking) and \vec{v}_0 (steady-state compensation) are added to the feedback-only component \vec{v}_{FB} resulting in the total force command \vec{v} . This is finally converted into the desired dq -currents \mathbf{i}_{dq}^* .

- $\vec{v}_{FB,pu}$ is the feedback component, which is the outcome of the MIMO controller action $\vec{v}_{FB,pu} = -\mathbf{K}_f \vec{\xi}_{aug,pu}$;
- $\vec{v}_{FF,pu}$ is the feed-forward component, which is used only in the z -direction;
- $\vec{v}_{0,pu}$ is the zero force component, i.e. the steady-state value of the force. This component compensates for any parasitic forces such as gravity, cogging or radial pull forces. This force vector is saved in the control memory as a function of the axial z -component $\vec{v}_{0,pu}(z)$.

The most important controller component is the feedback component $\vec{v}_{FB,pu}$, which is described based on the knowledge of the MALTA mover dynamics. With the feedback controller action, the MALTA mechanical dynamics reduce to

$$\frac{\partial \vec{\xi}_{aug,pu}}{\partial t} = (\mathbf{A}_{aug,pu} - \mathbf{B}_{aug,pu} \mathbf{K}_r) \vec{\xi}_{aug,pu}. \quad (6.55)$$

Therefore, the design of the control reduces to the determination of the feedback matrix \mathbf{K}_r , which once the linearized mechanical state-space model

Tab. 6.4: LQR control weights for \mathbf{K}_r design.

q_x, q_y	3.25	q_{dx}, q_{dy}	10	q_{ex1}, q_{ey1}	80	r_{fx1}, r_{fy1}	1
q_α, q_β	15	$q_{d\alpha}, q_{d\beta}$	12	q_{ex2}, q_{ey2}	80	r_{fx2}, r_{fy2}	1
q_z	0.3	q_{dz}	0.3	q_{ez}	30	r_{fz}	0.1

of the MALTA is formed, cf. (6.54), is straightforward. The position controller gain matrix \mathbf{K}_r is obtained by using the MATLAB's built-in function `lqr()` as

$$\mathbf{K}_r = \text{lqr}(\mathbf{A}_{\text{aug,pu}}, \mathbf{B}_{\text{aug,pu}}, \mathbf{Q}_{\text{aug}}, \mathbf{R}_{\text{aug}}), \quad (6.56)$$

where $\mathbf{A}_{\text{aug,pu}}$ and $\mathbf{B}_{\text{aug,pu}}$ are given in (6.54), $\mathbf{Q}_{\text{aug}} \in \mathbb{R}^{15 \times 15}$ and $\mathbf{R}_{\text{aug}} \in \mathbb{R}^{5 \times 5}$ are equal to

$$\begin{aligned} \mathbf{Q}_{\text{aug}} &= \text{diag}(q_x, q_y, q_z, q_\alpha, q_\beta, q_{dx}, q_{dy}, q_{dz}, q_{d\alpha}, q_{d\beta}, q_{ex1}, q_{ey1}, q_{ex2}, q_{ey2}, q_{ez}), \\ \mathbf{R}_{\text{aug}} &= \text{diag}(q_{fx1}, q_{fy1}, q_{fx2}, q_{fy2}, q_{fz}), \end{aligned} \quad (6.57)$$

where \mathbf{Q}_{aug} and \mathbf{R}_{aug} minimize the cost function

$$J(\vec{v}_{\text{pu}}) = \int_0^\infty \left(\vec{\xi}_{\text{aug,pu}}^\top \mathbf{Q}_{\text{aug}} \vec{\xi}_{\text{aug,pu}} + \vec{v}_{\text{pu}}^\top \mathbf{R}_{\text{aug}} \vec{v}_{\text{pu}} \right) dt. \quad (6.58)$$

An example of the control weights for the \mathbf{K}_r feedback matrix design is given in **Tab. 6.4**. As there is an infinite number of combinations to choose the values of \mathbf{K}_r , tuning the feedback controller component is an iterative process. For example, if the actuator should reject unknown external mechanical force disturbances very fast, the weights of the position error $q_{ex1}, q_{ey1}, q_{ex2}, q_{ey2}, q_{ez}$ should be increased. A regulator where the gain matrix \mathbf{K}_r is tuned using `lqr()` is called multi-input multi-output (MIMO) Linear Quadratic Regulator (LQR) [111], which is based on *full state feedback*. As with the sensor it is only possible to measure \vec{p} it is necessary to build a state observer, which is explained in the following section.

The performances of the position controller are enhanced with feed-forward components $\vec{v}_{\text{FF,pu}}$, which are added directly after feedback control action computation. More specifically, feed-forward control is provided along the axial direction z in order to improve the transient response to known references. This is possible with an appropriate force component obtained through inversion of the plant's dynamics. If z_{pu}^* is the axial position reference to be tracked, then $m_{\text{pu}} \ddot{z}_{\text{pu}}^*$ is the feed-forward component, the controller

knows in advance. Therefore, it can act to follow the commanded reference, instead of reacting after it has already changed. This allows speeding up the transient response and tracking faster references, relieving the feedback part from this task. The feed-forward control in radial direction may be provided via the first four components of $\vec{v}_{\text{FF,pu}}$, which can be used to counteract any known radial disturbances, e.g. when the MALTA is moved with parallel kinematics in pick-and-place robots.

The feed-forward action includes an additional component $\vec{v}_{0,\text{pu}}(z)$ to adjust in advance steady-state forces according to the current axial position z . These include for example a gravity compensation with the two bearing forces f_{yB1} and f_{yB2} and a compensation of irregularities in the radial pull forces due to asymmetries and manufacturing tolerances. Nevertheless, the feed-forward steady-state action $\vec{v}_{0,\text{pu}}(z)$ includes also a linear (axial) cogging force component, which is already passively reduced to very low value by choosing a distance between the two MALTA stator modules that minimizes cogging. These components are recorded from the position controller reference signal in steady-state.

6.7.3 Full State Observer

In order to realize the LQR regulator, explained in the previous section, it is necessary to have information about the entire state vector $\vec{\xi}_{\text{aug,pu}}$. Since the sensor only provides measurements of the radial and axial displacements, it is necessary to build a state observer as shown in **Fig. 6.7**. The state observer equation that obtains the estimated states $\hat{\xi}_{\text{pu}} \in \mathbb{R}^{10}$ is

$$\frac{\partial \hat{\xi}_{\text{pu}}}{\partial t} = \mathbf{A}_{\text{pu}} \hat{\xi}_{\text{pu}} + \mathbf{B}_{\text{pu}} \vec{v}_{\text{pu}} + \mathbf{K}_f \left(\vec{p}_{\text{pu}} - \mathbf{C}_{\text{pu}} \hat{\xi}_{\text{pu}} \right), \quad (6.59)$$

where $\mathbf{K}_f \in \mathbb{R}^{10 \times 10}$ is a constant matrix and the only unknown in the equation and calculated as

$$\mathbf{K}_f = \left(\text{lqr} \left(\mathbf{A}_{\text{pu}}^\top, \mathbf{C}_{\text{pu}}^\top, \mathbf{Q}_{\text{obs}}, \mathbf{R}_{\text{obs}} \right) \right)^\top. \quad (6.60)$$

The design weights $\mathbf{Q}_{\text{obs}} \in \mathbb{R}^{10 \times 10}$ and $\mathbf{R}_{\text{obs}} \in \mathbb{R}^{5 \times 5}$ are obtained from the variances of the process and sensor noise, respectively, which are assumed to be normally distributed. They have the following form

$$\begin{aligned} \mathbf{Q}_{\text{obs}} &= \mathbf{B}_{\text{pu}} \text{diag}(\sigma_{fx1}^2, \sigma_{fy1}^2, \sigma_{fx2}^2, \sigma_{fy2}^2, \sigma_{fz}^2) \mathbf{B}_{\text{pu}}^\top \\ \mathbf{R}_{\text{obs}} &= \text{diag}(\sigma_{x1}^2, \sigma_{y1}^2, \sigma_{x2}^2, \sigma_{y2}^2, \sigma_z^2) \end{aligned} \quad (6.61)$$

Tab. 6.5: Control weights for \mathbf{K}_f design.

$\sigma_{x1}^2, \sigma_{x2}^2$	$7.06 \cdot 10^{-10}$	$\sigma_{fx1}^2, \sigma_{fx2}^2$	$2.5 \cdot 10^{-3}$
$\sigma_{y1}^2, \sigma_{y2}^2$	$4.53 \cdot 10^{-10}$	$\sigma_{fy1}^2, \sigma_{fy2}^2$	$2.5 \cdot 10^{-3}$
σ_z^2	$1.55 \cdot 10^{-8}$	σ_{fz}^2	$4.9 \cdot 10^{-3}$

The values of the variances, given in **Tab. 6.5**, are determined from open-loop measurements in order to prevent correlation of the two kinds of noise. As without feedback control the mover cannot levitate, position sensors are statistically characterized with no phase currents, i.e. with the mover resting on the touchdown bearing. Concerning input forces, it is equivalent to statistically characterize the input currents, as they are directly proportional. In this case the mover is removed from the machine and DC-currents of 1 A in dq -frame for the bearing and the drive force generation are applied (cf. (6.4o)). This way, the variances in **Tab. 6.4** are obtained.

It should be mentioned that a state observer is not mandatory for COG control. In fact, in most AMBs setups the measurement matrix is square and invertible. Hence, it is possible to explicitly map measurements back into COG coordinates as $\vec{q} = \mathbf{P}_0^{-1}(z) \vec{p}$. For the MALTA, as $\mathbf{P}_0(z)$ in (6.17) is not invertible, the Moore-Penrose pseudoinverse $\mathbf{P}_0^\dagger(z)$ should be used instead. Nevertheless, the use of the (full) state estimate for feedback control is advantageous. Not only it allows filtering out noise from measurement data in an optimal sense, but also it provides speed estimates, which can be used to implement derivative control action. This is highly beneficial, as it avoids the direct computation of discrete derivatives from the measurement data, which would result in noise amplification for noisy signals.

6.7.4 Tuning of the Controller

The LQR position controller is tuned by choosing the design weights \mathbf{Q}_{aug} and \mathbf{R}_{aug} as reported in **Tab. 6.4**. LQR design often includes some trial and error, as it is a matter of trade-off between penalization of large state or large input magnitudes. In the case at hand, in order to gain some insight on the closed loop system, the controller is tuned iteratively by shaping the singular value decomposition of the complementary sensitivity function (i.e. the closed loop transfer function), using the established linearized dynamic model.

The modes x and y , as well as α and β are tuned in the same way, whereas different weights are chosen specifically for z . With these choices, the resulting MIMO position controller closed-loop bandwidth is around 400 rad/s. To

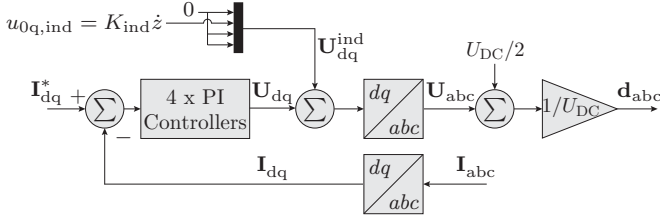


Fig. 6.8: Structure of the MALTA current controller. Only one module is considered for simplicity. There are 4 dq -quantities to be controlled: i_{0d} , i_{0q} , i_{bd} , and i_{bq} . Hence, 4 PI-controllers, all designed and tuned in the same way, are used.

further increase the bandwidth of the position controller, an increased bandwidth of the inner current control is required such that dynamic decoupling between the inner and outer control loops is guaranteed.

6.8 Current Controller

The structure of the current control is shown in **Fig. 6.8**. The control is designed and implemented in dq -coordinates [112]. Alternatively, a current controller implementation in abc -coordinates would also be possible. The control actions are the dq -voltages U_{dq} , which are transformed into phase voltages U_{abc} according to the transformation introduced in **Section 6.5.2**. These are finally converted into equivalent duty cycles d_{abc} for pulse-width modulation. The switching frequency of the MALTA inverter is $f_{sw} = 100$ kHz.

The current controller is designed using the linearized steady-state electrical model in stationary dq -coordinates, i.e. with $\dot{\varphi} = 0$ and $\dot{\theta} = 0$. The model is of the form

$$\frac{di_k(t)}{dt} = -\frac{R_k}{L_k} i_k(t) + \frac{1}{L_k} u_k(t), \quad (6.62)$$

where $k \in \{0d, 0q, bd, bq\}$ denotes the stationary coordinate axes, cf. **Fig. 6.5(b)**. The PI current controllers are tuned such that the crossover frequency is $\omega_c^{cc} = 3000$ rad/s, which is considerably higher than the crossover frequency of the position controller. The phase margin is 60° in order to ensure a low overshoot of the transient response. The voltages u_{0q1} and u_{0q2} also include an additional feed-forward correction factor $u_{0q,ind} = K_{ind} \dot{z}$, to compensate for the induced voltage due to non-zero linear speed along the z -axis during operation.

6.9 Summary

In this chapter, the dynamic operation of the Magnetically Levitated Tubular Actuator (MALTA) is analyzed. The analysis starts with the dynamic mechanical modeling of the MALTA system by using Newton-Euler equations that can describe combined translation and rotation of the MALTA rigid mover. All force types (drive, bearing or attraction) that act on the mover are modeled, as well as the torques that they create. As the mover position is described by the translation and rotation of its center of gravity and the position sensor provides measurements of the radial and axial positions, the sensor system is modeled and the mapping with the center of gravity coordinates is given. A LQR feedback controller assisted with feed-forward compensations of the nonlinearities due to the cogging force and the induced voltage due to linear motion is employed. The control features a cascaded structure with an inner (faster) current control loop and an outer position control loop. Additionally, a mechanical model based observer is designed, which is used to provide information about the states and state derivatives (speeds) such that high-frequency noise amplification due to measurement signal differentiation is avoided.

The implementation of the control system presented in this chapter and the measurements on the MALTA prototype are shown in the following **Chapter 7**.

7

Experimental Analysis of the Linear Machine

This chapter summarizes the experimental analysis conducted on the MALTA prototype, which shows successful operation of the control system and operation of the proposed MALTA. Additionally, an experiment is conducted where the mover tilting is controlled, which shows superiority of the MALTA over the conventional tubular linear actuators. The material presented in this chapter is also published in [93].

7.1 Introduction

The shown measurements are conducted on the MALTA prototype with the controller structure described in **Section 6.7**. In order to record the shown measurement results, the MALTA prototype was fixed in a stable test-bench where the commissioning of the MALTA prototype was conducted. Commissioning assumes determination of the force constants (drive, bearing and attraction) and cogging force, as well as sensor commissioning. This data is then used in the implemented controller, either in the form of the parameters (cf. **Tab. 6.1**) or the lookup table (cf. $\vec{v}_{0,pu}$ in **Fig. 6.7**). Three different types of measurement experiments were conducted in which (1) axial position reference tracking is studied; (2) the statistical metrics of the closed loop position control are determined and (3) an application example where the advantages of the MALTA compared to the conventional linear actuators are shown by radial position reference tracking capabilities.

7.2 Axial Reference Tracking

In this section the MALTA performs an axial 10 mm stroke. The commanded stroke shows a successful operation of the MALTA LQG position controller, which beside the reference tracking maintains the mover's radial position. The commanded step is shown in **Fig. 7.1(a)**. The non-zero steady-state drive force/current that can be observed in **Fig. 7.1(d)** from around 40 ms onwards is needed to counteract the cogging force, guaranteeing average steady-state errors in the order of $1\text{ }\mu\text{m}$ (cf. also **Tab. 7.1**). Due to feed-forward control, the controller tracks the assigned sigmoid position reference z without overshoot, which is seen from the measurements in **Fig. 7.1(a)**. It should be mentioned that typically linear actuators are not allowed to overshoot, as this could result in damaging mechanical parts/tools.

In **Fig. 7.2**, the radial position responses to the same axial step of **Fig. 7.1(a)** are shown. The radial position control rejects effectively the disturbances occurring during fast axial motion, maintaining the deviations within $\pm 20\text{ }\mu\text{m}$ (cf. **Fig. 7.2(a),(b)**). In **Fig. 7.2(c),(d)** the commanded radial forces are shown. Also in this case, after reaching steady-state they have a non-zero value. In particular, f_{yB1} and f_{yB2} are needed to keep the mover levitated and their sum corresponds in fact to $m \cdot g \approx 3.25\text{ N}$. As the mover is unbalanced towards the first stator module (at the steady-state axial position of 5 mm), f_{yB1} is larger than f_{yB2} . It should be mentioned that additional unknown radial disturbances, e.g. external vibrations, could cause higher radial position deviations.

In both, **Fig. 7.1** and **Fig. 7.2** the dashed lines are the simulated responses to the same smooth reference as obtained from a MATLAB Simulink model. This is built according to the modelling of **Section 6.2**, derived from first physical principles. By allowing for the expected differences between model and measurements due to manufacturing tolerances, unmodeled dynamics and noise, it can be assessed that the two are in good agreement. An exception are the measured x_1 and x_2 positions, which according to the model should not be affected by an axial motion. This mismatch could be explained with the irregular magnetic field distribution inside the two stator modules and tolerances in the strengths of the permanent magnets of the mover.

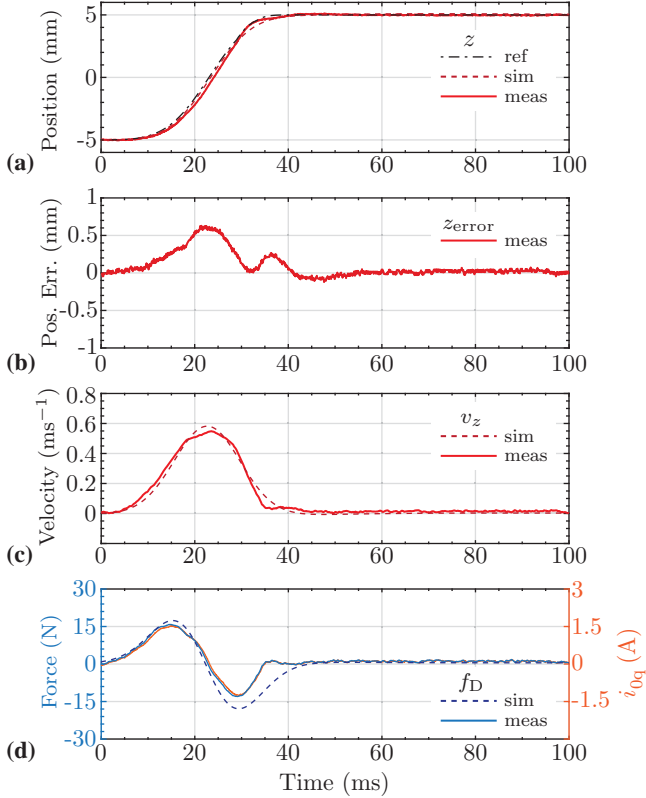


Fig. 7.1: Measurements of the MALTA response for a 10 mm axial stroke. **(a)** Reference axial position, simulation and actual response. The reference for z , shown as a black dashed line, is shaped with a sigmoid profile to improve tracking performances. The actual z response is shown in red and it tracks the reference with 16.2 ms rise time and $\leq 1.5\%$ overshoot. **(b)** Axial position tracking error which stays below 0.6 mm **(c)** Axial speed profile. **(d)** Axial driving force (total) and associated dq -component (only for Module 1). It is possible to verify the value of the drive constant of $K_D \approx 5 \text{ N/A}$.

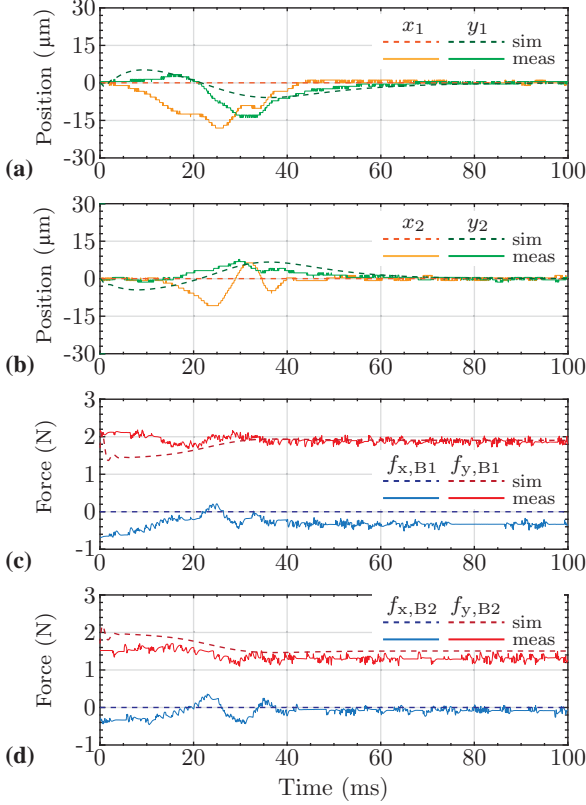


Fig. 7.2: Measurements of the MALTA response for a 10 mm axial stroke corresponding to **Fig. 7.1**. **(a-b)** Radial responses in x - and y -directions for Module 1 and Module 2. The maximum deviation is contained within $\pm 20 \mu\text{m}$. According to simulations of the dynamical model, deviations y_1 and y_2 are expected, whereas this is not the case for x_1 and x_2 . This mismatch can be explained by manufacturing tolerances. **(c-d)** Commanded forces from the position controller for Module 1 and Module 2. f_{yB1} is larger than f_{yB2} at steady-state as the mover is unbalanced towards Module 1. Their sum compensates the gravity force $m \cdot g \approx 3.25 \text{ N}$.

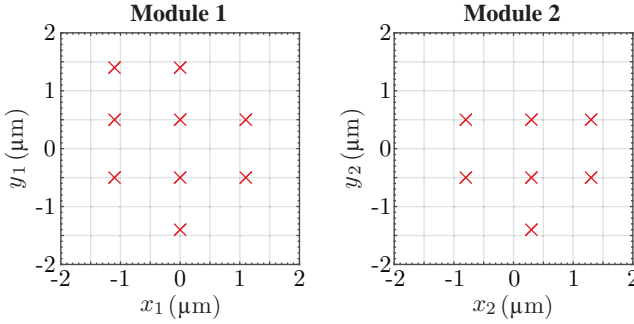


Fig. 7.3: Distribution of the measurement values of the steady-state radial positions of Module 1 and Module 2. Axial position reference is $z^* = 0$, i.e. the mover is positioned in the middle. From the 2000 measured samples, the sensor resolution is clearly visible to be around $1\ \mu\text{m}$.

Tab. 7.1: Statistical metrics (mean and standard deviation, STD) of the steady-state position measurements calculated from 2000 measured samples.

Position (Symbol)	Mean (μm)	STD (μm)	Motion Range (μm)
Axial (z)	-0.5224	15.4277	$\pm 15 \times 10^3$
Module 1			
x -direction (x_1)	0.0335	0.3883	± 600
y -direction (y_1)	-0.0212	0.5579	± 600
Module 2			
x -direction (x_2)	0.0579	0.4827	± 600
y -direction (y_2)	-0.0735	0.4956	± 600

7.3 Steady-State Positioning Performance

Positioning performances may be further investigated in steady-state with the measurements shown in **Fig. 7.3** for the case of

$$\vec{p}^*(t) = \begin{bmatrix} 0 & 0 & 0 & 0 & 0 \end{bmatrix}^T,$$

i.e. for a mover position in the middle. It can be clearly seen that the measured radial positions are very close to the sensor resolution of $\approx 1\ \mu\text{m}$. This is a good result offered by the chosen eddy-current sensor technique. **Tab. 7.1** finally summarizes the statistical metrics of all the measured position signals. The noticeably higher variance of the axial z position is due to the Hall-effect sensor technique employed, which is more prone to noise.

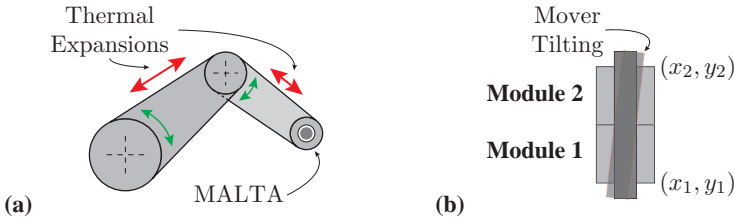


Fig. 7.4: (a) Setup of a typical application with MALTA mounted as an end-effector of a robot arm. If the robot arm experiences thermal expansions during operation, the overall precision of the positioning system is compromised. (b) Active tilting and radial control to provide an appropriate correction of the compromised position.

7.4 Mover Tilting Capability

A special characteristic of the MALTA system is a possibility of actively controlling the tilting of the mover, cf. **Fig. 7.4**, which is not possible with conventional tubular linear machines. This can be exploited for advanced positioning systems. For instance, in a typical application, an actuator like the MALTA would be mounted as an end-effector of a robotic arm, cf. **Fig. 7.4(a)**, for instance in a pick-and-place robot application. If during the operation the whole setup heats up, thermal expansions of the supporting robotic arm occur. For example, a robotic arm of 0.5 m length would extend in length by around $\approx 65 \mu\text{m}$, if the temperature rises for 10°C (temperature expansion coefficient of steel equal to $13 \times 10^{-6}/^\circ\text{C}$ is assumed). This would totally compromise precise positioning of the end-effector if no correction is applied. However, with the MALTA, these thermal disturbances may be completely decoupled by active magnetic bearings with the radial precision determined by the precision of the radial eddy-current position sensor. The thermal expansions may be measured, e.g. by measuring the position of the MALTA mover with a laser sensor mounted on a support that is not affected by the thermal expansions. This feature may justify an effort of integrating MBs into the actuators, as some of the conventional solutions have water cooling systems in the robotic arms, which limit temperature changes and thermal expansions.

This concept is demonstrated with the experiment shown in **Fig. 7.5**. In this case, a circumference of radius $S = 200 \mu\text{m}$ is assigned as a reference to be tracked along the SP1 plane, whereas the mover should be kept fixed at the center of the SP2. The reference

$$\vec{p}^*(t) = [S \cos(2\pi f_p^* t) \quad S \sin(2\pi f_p^* t) \quad 0 \quad 0 \quad 0]^T \quad (7.1)$$

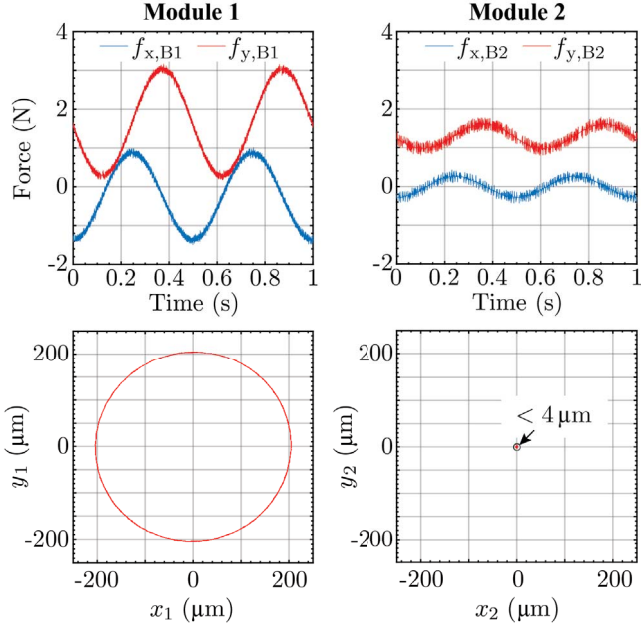


Fig. 7.5: Measurements of the mover tilting control. The assigned reference is given with the expression (7.1).

is then directly used for integral control and transformed into the appropriate state reference $\vec{\xi}^* = [\vec{q}^* \quad \partial\vec{q}^*/\partial t]^\top$, with $\vec{q}^* = \mathbf{P}_0^{-1}(z)\vec{p}^*$ for full state feedback. The controller is employed to track the circumference at $f_p^* = 2$ Hz. The measurements in **Fig. 7.5** show the response of the system for both modules. It can be seen how the radial motions in Module 1 affect Module 2, where the controller commands the forces f_{xB2} and f_{yB2} that keep the radial position deviation from the reference center position below $4\text{ }\mu\text{m}$.

7.5 Summary

The measurement experiments on the MALTA prototype show good axial reference tracking for a 10 mm axial stroke amplitude with 16.2 ms rise time. During this axial movement, the radial position of the mover is disturbed and its deviation from the center is below $20\text{ }\mu\text{m}$. By studying statistical metrics of the controlled positions in the steady-state, the radial positions exhibit a standard deviation of $\approx 0.5\text{ }\mu\text{m}$ and the axial position of $\approx 15\text{ }\mu\text{m}$. This difference between the radial and the axial standard deviations originates from the larger noise of the axial position sensor.

In the final measurement experiment an application example is proven, in which mover tilting control of the proposed MALTA is used to compensate for any thermal expansions that would deteriorate positioning accuracy, e.g. in a pick-and-place robot application. In this experiment, the mover's radial position follows successfully a sinusoidal reference.

With this chapter, the analysis of the MALTA is completed, from its machine design in **Chapter 4** and the inverter and the sensor design in **Chapter 5** and finally with the MIMO control system design and implementation in **Chapter 6** and measurements presented in this chapter. Additionally, the MALTA is tested with the SISO position controller, whose design and implementation and experimental verification are shown in **Appendix A**. The purpose of the SISO controller implementation is to show that the MALTA can be operated with the SISO controller that does not consider couplings. The relative gain number of the dynamic model suggests exactly this: both MIMO and SISO implementations at 400 Hz closed-loop frequency are possible. In the next chapters, in addition to the linear motion and MBs considered for the MALTA, rotation is considered, resulting in a linear-rotary actuator. The analyzed actuator topology is a double stator linear-rotary actuator.

8

Design of the Double Stator Machine

As a step towards the linear-rotary actuator with magnetic bearings (MBs), a double stator linear-rotary actuator is considered in this chapter, where its principle of operation, design and optimization details are shown.

8.1 Introduction

Linear-rotary actuators (LiRAs) are used in many applications requiring coupled linear and rotary motion, such as gearbox control actuation in vehicles [113], tooling machines such as drills [114], robotics [115], and industrial pick-and-place machines [39], [103]. In order to achieve linear and rotary motion, linear and rotary actuators can be coupled in different ways. In usual LiRA arrangements, standalone linear and rotary actuators that share the same mover [103], [39] are displaced axially. The mover consists of two axially displaced parts (linear and rotary) that produce force and torque by interacting with the respective part of the two stators. In order to keep the overlapping area and magnetic interaction between the mover and the stators constant, the latter are placed apart by an axial distance, which has to be larger than the axial stroke of the mover. Consequently, this results in an increased length of the LiRA.

Another approach is to stack the stators radially instead of axially [14], [116], i.e. by placing them on the inside and outside of a hollow mover. Such a setup is commonly referred to as a double stator (DS) machine and is shown in **Fig. 8.1**. The PMs are arranged such that their North and South poles alternate in the axial and circumferential direction for the linear and rotary actuator,

respectively. Further DS LiRA realization options and their force/torque capabilities are analyzed in **Appendix B**.

8.2 Machine Topology

The DS LiRA topology, whose design is described in this chapter, is shown in **Fig. 8.1**. It has two radially displaced stators:

- Inner Linear Stator: used to generate a linear drive force on the mover.
- Outer Rotary Stator: used to generate the torque and the bearing forces on the mover. The two outer rotary stators are needed, such that the bearing force may be generated at two distant axial positions (cf. **Fig. 8.2**), which is required to control the tilting of the mover.

The summary of the forces and torques acting on the mover from the two stators is given in **Fig. 8.2**.

A degree of freedom in the design of a DS LiRA (cf. **Fig. 8.1**) is to choose the arrangement of the inner and outer stators, i.e. whether the actuator has an inner rotary or linear stator. In the literature [14], the DS LiRA is designed with the inner rotary and outer linear stator. In this specific case, the actuator does not have a magnetic bearing feature. If the DS LiRA rotary stator needs to provide bearing forces on the mover, from the manufacturing point of

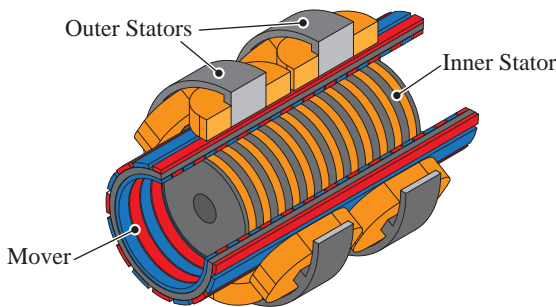


Fig. 8.1: Double stator linear-rotary actuator (DS LiRA) with rotary outer stators and linear inner stator. The outer stators generate torque and the bearing forces on the mover, while the inner stator generates the linear drive force. Therefore, the mover consists of two sets of PMs (for rotation and linear motion) and a back iron.

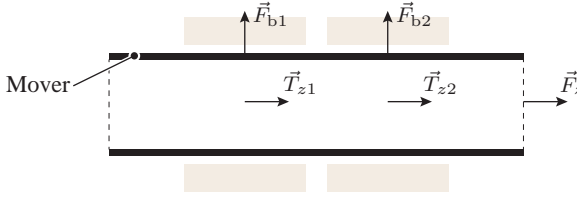


Fig. 8.2: Forces and torques acting on the mover from the outer rotary stators: \vec{F}_{b1} , \vec{F}_{b2} (bearing forces); \vec{T}_{z1} , \vec{T}_{z2} (axial torques) and from the inner linear stator: \vec{F}_z (drive axial force).

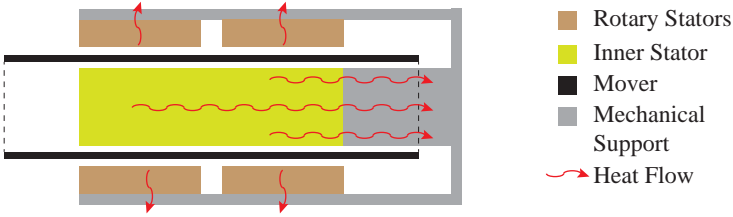


Fig. 8.3: Illustration of the heat flows in the DS LiRA excited with the stator losses. Inner stator exhibits axial heat flow.

view it is beneficial to employ rotary stators, as the radial force is directly transmitted to the mechanical fixation.

It should be noted that thickness of the mover should be as small as possible, since it is reducing the space for stator windings. Consequently, this imposes limit on the PM size, i.e. too thick PM would saturate the mover's back iron.

Another challenge in the design of the DS LiRA from **Fig. 8.1** is the cooling of the inner linear stator. If the radial heat flow through the inner air gap is neglected, all the inner stator heat, generated by its losses, have axial flow through the stator as shown in **Fig. 8.3**. To better illustrate this, a numerical example is considered. In **Fig. 8.4** two realizations of the inner stator are shown, without and with the copper pipe inserted inside the iron core. For both realizations only copper losses are considered and calculated as

$$\begin{aligned} p_{cu} &= \frac{1}{2} \rho_{cu} \hat{j}^2 \\ &= 4.1 \times 10^5 \text{ W/m}^3 \end{aligned} \quad (8.1)$$

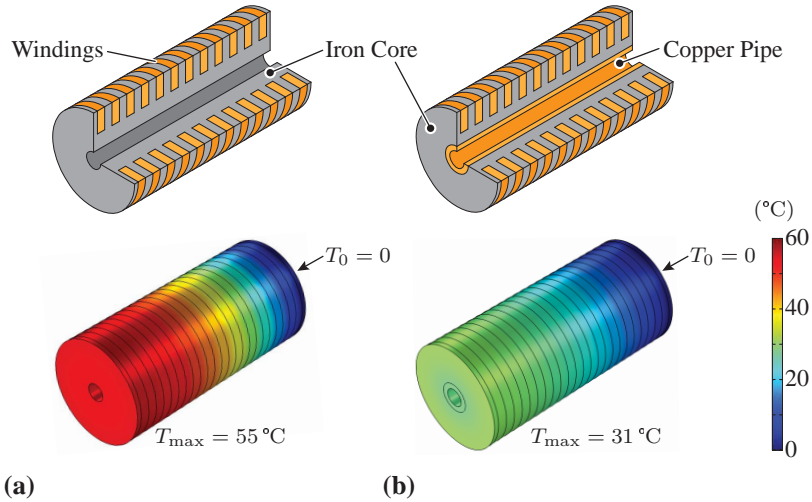


Fig. 8.4: Inner stator realizations and respective temperature distributions where one axial end is attached to a fixed temperature $T_0 = 0$ and the rest is assumed thermally insulated. Only copper losses of 0.41 W/cm^3 are assumed. The assumed thermal conductivities are: iron core: 20 W/(mK) , windings: 2 W/(mK) and copper pipe: 400 W/(mK) . The hole in the middle of the inner stator is used for the sensor cables. **(a)** The inner stator with the iron core resulting in rather large temperature difference between the two axial ends. **(b)** The inner stator with the iron core and an inserted copper pipe in order to reduce the temperature difference. The copper pipe wall thickness is 2.5 mm .

where $\rho_{\text{cu}} = 2.27 \times 10^{-8} \Omega\text{m}$ is the specific electrical resistance of copper considered at 110°C (assumed possible average winding temperature) and $\hat{j} = 6 \text{ A/mm}^2$. In **Fig. 8.4(a)** the temperature distribution in the inner stator without the copper pipe is obtained with 3D-FEM simulation, where at the one axial end the constant temperature boundary condition $T_0 = 0$ is applied, while all the other boundaries are assumed thermally insulated. A rather large temperature difference between the two axial ends of the inner stator can be noted, which is a consequence of the axial heat flow. In a real machine, this would cause unequal temperature in the stator windings and, therefore, unequal winding resistances. This could increase the losses in the hotter windings, which would further increase the temperature difference.

In order to attenuate this parasitic effect of the axial heat flow, a hollow copper pipe is inserted inside the inner stator as shown in **Fig. 8.4(b)**. As can be seen from the temperature distribution, the temperature difference reduces by almost a factor 2 compared to the case without copper pipe. As the permeability of copper is μ_0 equal to vacuum, the copper pipe reduces the stator iron core cross section available for the flux guiding, increasing the risk of the inner stator core saturation. Therefore, one of the design requirements of the inner stator involves a compromise between the magnetic and thermally conductive materials. This will be included in the Pareto optimization, which is shown in the coming sections.

It should be mentioned that the temperature differences in **Fig. 8.4** are the worst case temperature differences, since a complete thermal insulation of the stator is assumed. In the real machine, heat dissipation from all sides will be possible (e.g. by convection and/or radiation), not just conduction through the stator, which will help to reduce the temperature difference.

8.3 Optimization and Design Space

In order to build the DS LiRA shown in **Fig. 8.1**, its geometry, e.g. size of the PMs, coils size, copper pipe thickness, to mention a few, should be determined such that:

- ▶ the torque per Watt of outer rotary stator copper loss is maximized,
- ▶ the linear drive force per Watt of inner stator copper loss is maximized and
- ▶ no saturation of the iron parts occurs.

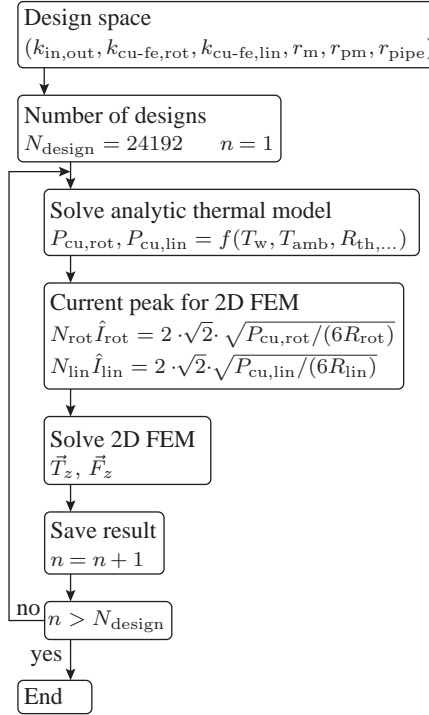


Fig. 8.5: DS LiRA grid search optimization algorithm.

The optimization algorithm is shown in **Fig. 8.5**, rendering a well known grid search optimization method. In other words, each point of the discrete design space is evaluated with the established model and the resulting performance is saved, which allows to directly choose the best performing designs. The optimization starts with the definition of the discrete design space, which is given in **Tab. 8.1**. Also, in **Tab. 8.1**, a set of fixed parameters, important for the optimization is given. The fixed geometrical parameter values can come from a certain application where it is necessary to fit the actuator into the available space. In case a desired force/torque are given, the parameters determining the outer dimensions (L and D) could not be fixed and would have to be a part of the swept parameters set. The geometrical parameters are defined in **Fig. 8.6**. Most of the swept parameters are relative numbers, which are related to the geometrical absolute parameters. One of the most

Tab. 8.1: DS LiRA geometrical discrete design space.

Symbol	Description	Value
Fixed parameters		
Geometrical		
L	Active length	100 mm
D	Outer diameter	100 mm
Δz	Mover axial stroke	30 mm
r_{ag}	Inner and outer air gaps	0.7 mm
D_{hole}	Copper pipe inner diameter	8 mm
Thermal		
T_{amb}	Ambient temperature	35 °C
T_{w}	Winding hot spot temperature	140 °C
λ_{w}	Thermal conductivity of the winding	2 W/(mK)
λ_{cu}	Thermal conductivity of copper	385 W/(mK)
λ_{fe}	Thermal conductivity of iron core	20 W/(mK)
λ_{alu}	Thermal conductivity of the aluminum	200 W/(mK)
λ_{ex}	Thermal conductivity of the potting epoxy	0.1 W/(mK)
Magnetic		
B_{r}	Permanent magnet remanent magnetization	1.3 T
$\mu_{\text{r,fe}}$	Stator core relative permeability	400
Electric		
k_{ff}	Winding feel factor	0.6
$N_{\text{p,rot}}$	Number of rotary poles	16
$N_{\text{p,lin}}$	Number of linear poles	16
$N_{\text{s,rot}}$	Number of rotary slots	6
$N_{\text{s,lin}}$	Number of linear slots	12
Swept parameters		
$k_{\text{in,out}}$	Ratio of the mover diameter and the outer stator diameters	0.46 : 0.02 : 0.6
$k_{\text{cu-fe,rot}}$	Ratio of copper and iron in the outer rotary stator	0.78 : 0.02 : 0.9
$k_{\text{cu-fe,lin}}$	Ratio of copper and iron in the inner linear stator	0.5, 0.6, 0.7
$k_{\text{pm,rot}}$	Relative rotary PM size	0.7 : 0.1 : 0.9
$k_{\text{pm,lin}}$	Relative linear PM size	0.8, 0.9
r_{m}	Mover back iron thickness	2.5 : 0.5 : 4 mm
r_{pm}	PM thickness, rotary and linear	2, 2.5 mm
r_{pipe}	Copper pipe thickness	2 : 0.5 : 3 mm

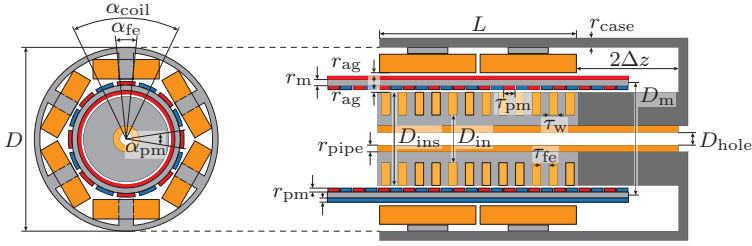


Fig. 8.6: Geometry parameters of the DS LiRA used in the optimization.

important relative parameters is the ratio of the mover diameter and the outer stator diameter

$$k_{\text{in,out}} = \frac{D_m}{D},$$

which determines the volume distribution between the inner and the outer stator. In other words, this parameter compromises between the torque and the linear force of the DS LiRA. Another important relative parameter is the ratio of copper and iron core in the rotary and linear stators

$$k_{\text{cu-fe,rot}} = 1 - \frac{\alpha_{\text{fe}}}{\alpha_{\text{coil}}} \quad k_{\text{cu-fe,lin}} = \frac{\tau_w}{\tau_w + \tau_{\text{fe}}}$$

where the geometrical parameters are illustrated in **Fig. 8.6**. The coil's angle α_{coil} is equal to

$$\alpha_{\text{coil}} = 0.96 \cdot \frac{2\pi}{N_{\text{s,rot}}} = \frac{25\pi}{72} \text{ rad},$$

where $N_{\text{s,rot}} = 6$ is the number of slots in the outer rotary machine, cf. **Tab. 8.1**. For the linear machine it should be noted that the sum

$$\tau_w + \tau_{\text{fe}} = \frac{L}{N_{\text{s,lin}}} = 8.33 \text{ mm},$$

is constant and L and $N_{\text{s,lin}}$ are given in **Tab. 8.1**. Similar to the ratio of copper and iron in the stators, a relative size of the PMs within a pole is given as

$$k_{\text{pm,rot}} = \frac{\alpha_{\text{pm}}}{2\pi/N_{\text{p,rot}}} \quad k_{\text{pm,lin}} = \frac{\tau_{\text{pm}}}{L/N_{\text{p,lin}}}$$

where L , $N_{\text{p,rot}}$ and $N_{\text{p,lin}}$ are given in **Tab. 8.1**.

Once the discrete set of optimization parameters is defined, a total number of designs may be obtained as a combination of all the vectors in the swept parameters in **Tab. 8.1** and it is equal to

$$N_{\text{design}} = 24192.$$

After this, the optimization algorithm starts to loop through the possible discrete designs, where n represents the number of the current design.

In the first step of the optimization loop, a steady-state thermal model, based on a lumped parameter thermal circuit is solved for the rotary and linear stator. The thermal model relates the ambient temperature T_{amb} and the winding hot spot temperature T_{w} as a function of the copper losses ($P_{\text{cu,rot}}$ and $P_{\text{cu,lin}}$). It should be noted that only copper losses are assumed in the optimization, as the DS LiRA is intended to be operated in actuator mode, i.e. to position the mover from one reference position to another, which leads to rather low speeds and therefore, the eddy-current losses are neglected. The thermal model allows to calculate the allowed copper losses, $P_{\text{cu,rot}}$ and $P_{\text{cu,lin}}$, for the analyzed DS LiRA geometry n .

The calculated copper losses are used in the next step to determine the current in the DS LiRA rotary and linear stators. The DS LiRA stators have three-phases and therefore the currents have the following waveforms

$$\begin{aligned} i_a &= \hat{I}_{\text{rot}} \cos(\omega_{\text{R}}t + \varphi_i) \\ i_b &= \hat{I}_{\text{rot}} \cos(\omega_{\text{R}}t + \varphi_i - 2\pi/3) \\ i_c &= \hat{I}_{\text{rot}} \cos(\omega_{\text{R}}t + \varphi_i + 2\pi/3) \end{aligned} \tag{8.2}$$

for the rotary stator, and

$$\begin{aligned} i_A &= \hat{I}_{\text{lin}} \cos(\omega_{\text{L}}t + \theta_i) \\ i_B &= \hat{I}_{\text{lin}} \cos(\omega_{\text{L}}t + \theta_i - 2\pi/3) \\ i_C &= \hat{I}_{\text{lin}} \cos(\omega_{\text{L}}t + \theta_i + 2\pi/3) \end{aligned} \tag{8.3}$$

for the linear stator. In **Fig. 8.7** the rotary and linear winding connections are shown.

The current peak values, \hat{I}_{rot} and \hat{I}_{lin} , used in the optimization are two times higher than the continuous DS LiRA current, i.e. they would cause 4 times higher copper losses. By using twice the current in the 2D-FEM simulation, where the flux density distributions and the resulting torques and forces are calculated, the chosen design is guaranteed to have twice the

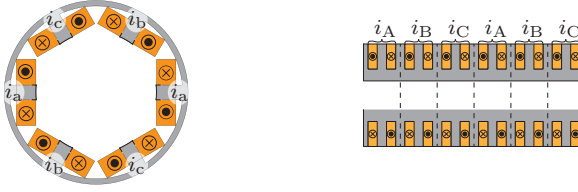


Fig. 8.7: Three-phase currents in the rotary and linear stator. The electrical resistance of a single coil in the rotary stator is R_{rot} , while R_{lin} is the electrical resistance of the series connection of the two concentrated coils wound in a slot.

current overload capability, i.e. with twice the nominal current the iron parts will not saturate.

At the end of each optimization loop, the results are saved in an array of structures, such that they can be loaded later and plotted to view the available performance. The optimization procedure ends once all design combinations have been evaluated, i.e. when $n > N_{\text{design}}$.

8.3.1 Thermal Model

When changing internal geometry dimensions of a machine, its capability to dissipate losses changes and therefore, different geometries would have different losses that cause the same hot spot temperature in the winding. In order to account for this, a thermal model of the DS LiRA is established that is evaluated in each optimization loop pass and used to calculate the current peak values \hat{I}_{rot} and \hat{I}_{lin} .

A simplified lumped parameter steady-state thermal model circuit of the outer rotary stator is shown in **Fig. 8.8**. The model assumes that the hot spot in the winding is on its inner radial surface, denoted in the figure as T_{w1}, \dots, T_{w12} , and therefore the losses of a coil pass through the whole coil in radial direction. The heat flow through the teeth is neglected. In reality, there would be a heat flow through the teeth and the hot spot would be inside the winding volume. Therefore, the model assumptions are conservative and in reality the DS LiRA should be able to dissipate the losses assumed by the model.

The thermal resistance of the potted DS LiRA coil in the outer rotary actuator is equal to

$$R_{\text{th},w1} = \frac{h_{w1}}{\lambda_w A_{w1}},$$

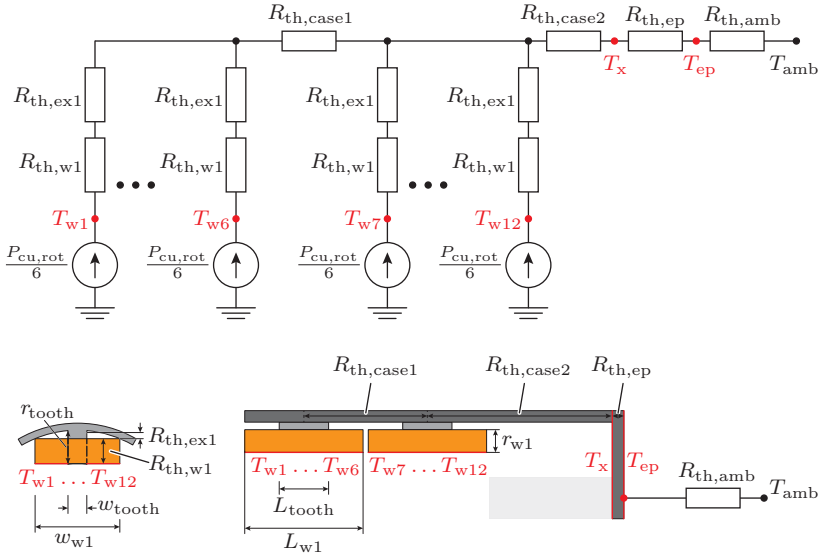


Fig. 8.8: Steady-state lumped parameter thermal model of the outer rotary stator. In the point with the temperature T_x the thermal model couples with the inner linear stator thermal model. Due to circumferential symmetry the assumed hot spot temperatures of each rotary stator are equal, i.e. $T_{w1} = \dots = T_{w6}$ and $T_{w7} = \dots = T_{w12}$ holds.

where the heat flow area is

$$A_{w1} = w_{w1} L_{w1} - w_{tooth} L_{tooth}.$$

The thermal resistance of the epoxy layer between the winding and the aluminum case is calculated similarly as

$$R_{th,ex1} = \frac{h_{ex1}}{\lambda_{ex} A_{w1}},$$

where

$$h_{ex1} = \frac{r_{tooth} - r_{coil}}{2}.$$

The thermal resistance of the first part of the outer aluminum case is equal to

$$R_{th,case1} = \frac{L/2}{\lambda_{al} A_{case}},$$

where the case area is

$$A_{case} = \frac{\pi}{4} ((D + 2r_{case})^2 - D^2).$$

The thermal resistance of the second part of the outer aluminum case is

$$R_{th,case2} = \frac{L/4 + 2\Delta z}{\lambda_{al} A_{case}}.$$

By considering the rotary stator thermal model circuit in **Fig. 8.8**, it can be noticed that the stator temperatures T_{w1}, \dots, T_{w6} are higher than T_{w7}, \dots, T_{w12} , cf. **Fig. 8.9(a)**. As in the optimization it is of interest to identify the maximum temperature spot, these temperatures are further considered. Therefore, an equivalent thermal resistance of interest, between the T_{w1-6} and T_x may be calculated as

$$R_{th,rot} = \frac{R_{th,w1} + R_{th,ex1}}{12} + \frac{R_{th,case1}}{2} + R_{th,case2}.$$

The thermal model circuit of the linear stator is shown in **Fig. 8.10**. Similar to the rotary stator thermal model, it is assumed that the heat due to copper losses passes entirely through the potted coils. Also, heat flow through the teeth is neglected. From **Fig. 8.10** it can be seen that the most critical is the last coil with the temperature T_{c12} , i.e. $T_{c12} > T_{c11} > \dots > T_{c1}$. The temperature

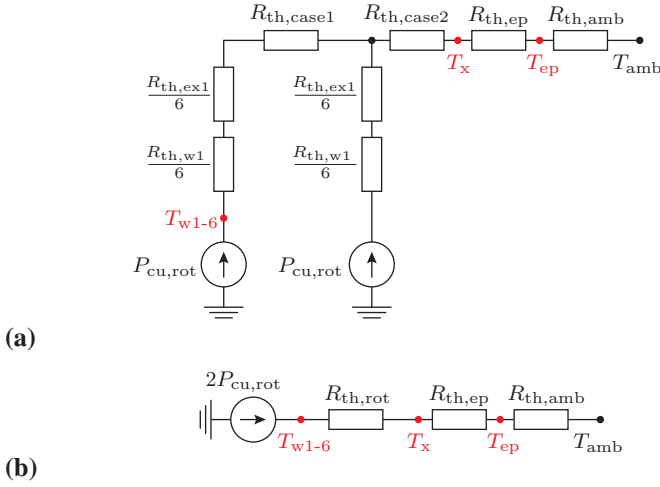


Fig. 8.9: (a) Modification of the rotary stator thermal circuit from Fig. 8.8 where $T_{w1-6} = T_{w1} = \dots = T_{w12}$ is used. (b) Equivalent thermal resistance between the T_{w1-6} and T_x .

difference between the hot spot of the most critical coil and the front of the end plate is equal to

$$T_{c12} - T_x = P_{cu,lin} \left(R_{th,eq2} + R_{th,eq1} \sum_{k=1}^{11} k + \frac{R_{th,c1}}{12} \right),$$

where the equivalent thermal resistances are calculated as

$$R_{th,eq1} = \frac{R_{th,fe1} R_{th,cu1}}{R_{th,fe1} + R_{th,cu1}}$$

and

$$R_{th,eq2} = \frac{(R_{th,fe1}/2 + R_{th,fe2}) \cdot (R_{th,cu1}/2 + R_{th,cu2})}{R_{th,fe1}/2 + R_{th,fe2} + R_{th,cu1}/2 + R_{th,cu2}}.$$

Therefore, the equivalent rotary thermal resistance used in the DS LiRA equivalent thermal circuit (cf. Fig. 8.11) is equal to

$$R_{th,lin} = \frac{R_{th,c1}}{12} + 66 R_{th,eq1} + R_{th,eq2}.$$

The individual thermal resistances are calculated from the geometry, where

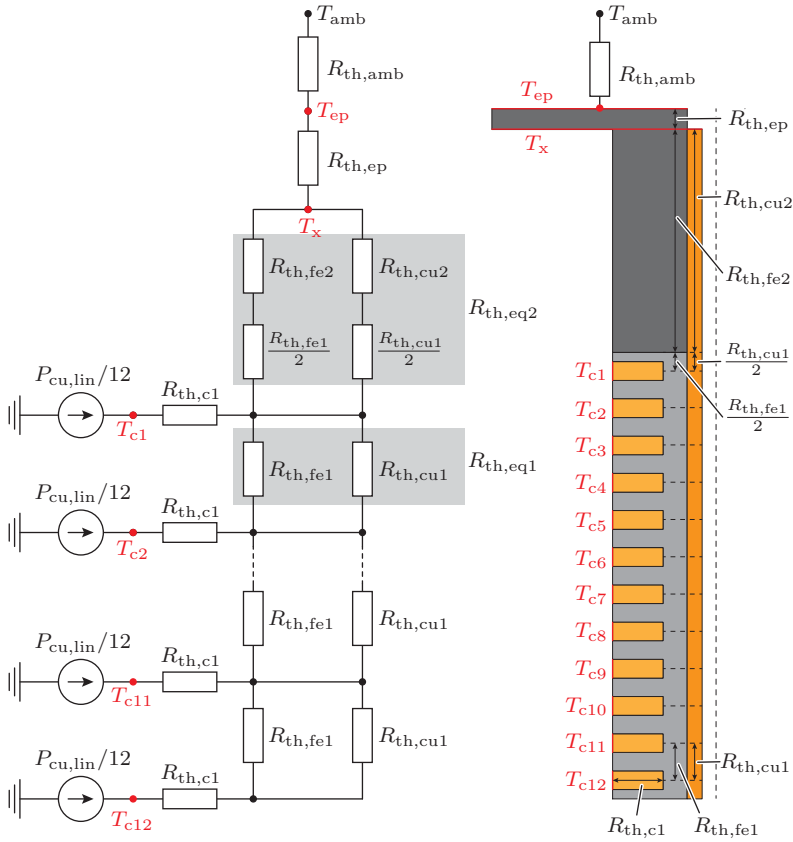


Fig. 8.10: Steady-state lumped parameter thermal model of the inner linear stator. In the point with the temperature T_x the thermal model couples with the outer rotary stator thermal model.

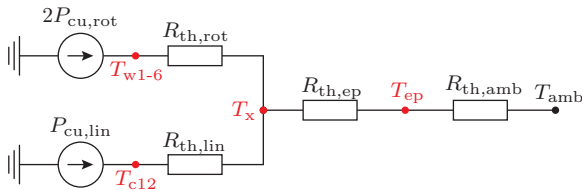


Fig. 8.11: Equivalent thermal model circuit of the DS LiRA.

the coil radial thermal resistance is

$$R_{th,c1} = \frac{\ln(D_{ins}/D_{in})}{2\pi \lambda_w \tau_w}.$$

The thermal resistance of the iron part that models the axial heat flow is obtained as

$$R_{th,fe1} = \frac{\tau_w + \tau_{fe}}{\lambda_{fe} A_{fe1}},$$

where the area is equal to

$$A_{fe1} = \frac{\pi}{4} (D_{in}^2 - (D_{hole} + 2r_{pipe})^2).$$

The thermal resistance of the copper pipe part that models the axial heat flow through the pipe is

$$R_{th,cu1} = \frac{\tau_w + \tau_{fe}}{\lambda_{fe} A_{cu1}},$$

where the cross section of the copper pipe is equal to

$$A_{cu1} = \frac{\pi}{4} ((D_{hole} + 2r_{pipe})^2 - D_{hole}^2).$$

Since the maximum winding temperature should be T_w , in the circuit from **Fig. 8.11** the following expression holds

$$T_{w1-6} = T_{c12} = T_w.$$

This allows to write a system of two equations from which the unknown copper losses ($P_{cu,rot}$ and $P_{cu,lin}$) may be calculated

$$\begin{aligned} R_{th,rot} 2P_{cu,rot} - R_{th,lin} P_{cu,lin} &= 0 \\ 2P_{cu,rot} + P_{cu,lin} &= \frac{T_w - T_{amb}}{R_{th,eq3}}, \end{aligned} \quad (8.4)$$

where the equivalent thermal resistance $R_{th,eq3}$ is equal to

$$R_{th,eq3} = \frac{R_{th,rot} R_{th,lin}}{R_{th,rot} + R_{th,lin}}.$$

By solving the system of equations (8.4), the copper losses are obtained as

$$\begin{aligned} P_{cu,rot} &= \frac{R_{th,lin}}{2R_{th,eq3}(R_{th,rot} + R_{th,lin})} (T_w - T_{amb}) \\ P_{cu,lin} &= \frac{R_{th,rot}}{R_{th,eq3}(R_{th,rot} + R_{th,lin})} (T_w - T_{amb}) \end{aligned} \quad (8.5)$$

In the next step of the optimization loop the Ampere-turn peak values are calculated, by using the obtained copper losses in (8.5). They are used as an input for the 2D-FEM models of the rotary and linear actuators, where the torque \vec{T}_z and the linear drive force \vec{F}_z are calculated.

8.4 Pareto Plots and Selection of the Optimum Design

In this section the results of the optimization are analyzed and a design of the DS LiRA is chosen. Since the DS LiRA can rotate the loads and drive them in linear direction simultaneously, the goal of the optimization is to

- ▶ maximize the torque,
- ▶ maximize the drive force and
- ▶ maximize the circumferential and linear accelerations.

The first two requirements are reasonable performance choices. The last one helps to balance the first two, i.e. if only the first two are considered, the resulting design may have a bulky mover that could be difficult to levitate. It should be mentioned that force and acceleration are the two contradicting performances, e.g. a larger PM volume in the mover results in higher force, but lowers the acceleration due to increased mass.

The achievable torque and the drive force of the DS LiRA are shown in **Fig. 8.12** and **Fig. 8.13**, where the color of the dots represents the circumferential and linear accelerations. The shown data is deduced from the $N_{\text{design}} = 24192$ designs by considering restrictions on the flux density in the iron core parts. The following restrictions on the flux density for each point of the volume are applied

- ▶ Outer stator: $< 2.1 \text{ T}$ - (Electrical steel)
- ▶ Inner stator: $< 1.4 \text{ T}$ - (Steel ST52)
- ▶ Mover: $< 2.1 \text{ T}$ - (Soft iron)

After applying the restrictions only 158 designs are left, which are plotted in **Fig. 8.12** and **Fig. 8.13**. From the plotted data, a trade-off between the torque and the linear force can be noticed, which is expected as the DS LiRA volume is fixed and by changing the mover diameter the volume distributes between the rotary and the linear stators.

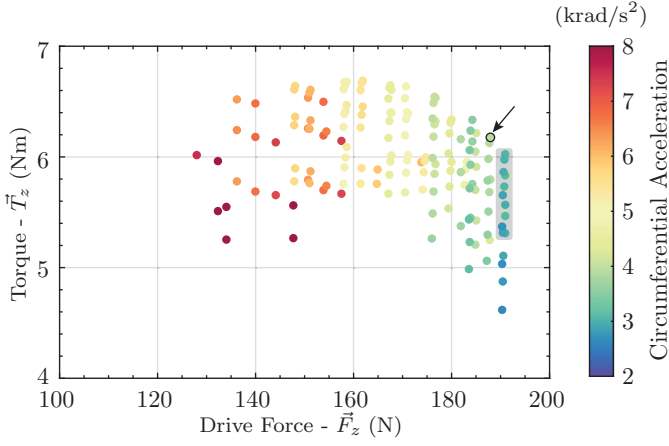


Fig. 8.12: Achievable torque \vec{T}_z and linear force \vec{F}_z of the DS LiRA. The circumferential acceleration is denoted with the color of the dots.

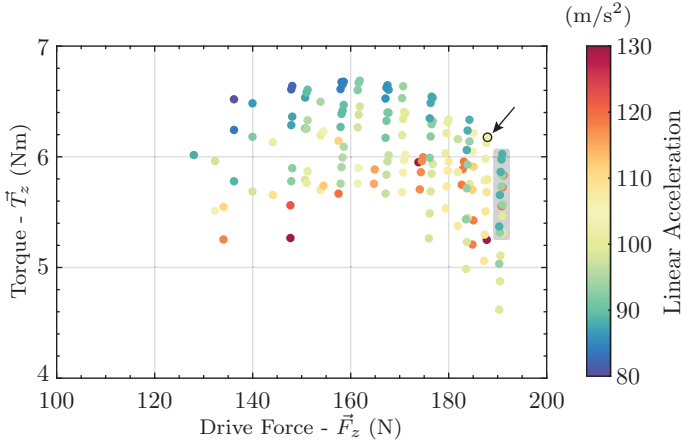


Fig. 8.13: Achievable torque \vec{T}_z and linear force \vec{F}_z of the DS LiRA. The linear acceleration is denoted with the color of the dots.

Tab. 8.2: DS LiRA chosen design performance.

Symbol	Description	Value
T_z	Torque	6.24 Nm
F_z	Linear force	181.5 N
$\ddot{\gamma}$	Circumferential acceleration	5.3 krad/s ²
\ddot{z}	Linear acceleration	123.5 m/s ²
$2P_{\text{cu,rot}}$	Copper losses of the outer rotary stators	97 W
$P_{\text{cu,lin}}$	Copper losses of the inner linear stator	18 W

Tab. 8.3: DS LiRA chosen design parameters.

Symbol	Description	Value
Swept parameters		
$k_{\text{in,out}}$	Ratio of the mover diameter and the outer stator diameters	0.56
$k_{\text{cu-fe,rot}}$	Ratio of copper and iron in the outer rotary stator	0.8
$k_{\text{cu-fe,lin}}$	Ratio of copper and iron in the inner linear stator	0.5
$k_{\text{pm,rot}}$	Relative rotary PM size	0.8
$k_{\text{pm,lin}}$	Relative linear PM size	0.9
r_m	Mover back iron thickness	3 mm
r_{pm}	PM thickness, rotary and linear	2 mm
r_{pipe}	Copper pipe thickness	2.5 mm

The chosen design is encircled and denoted with an arrow. From the shown feasible designs, the chosen one does not have the highest drive force possible, as can be seen in **Fig. 8.12** and **Fig. 8.13** where a group of designs that has higher drive force is denoted. This small drive force compromise is made because the denoted designs have lower accelerations. The chosen design performance is given in **Tab. 8.2**. In **Tab. 8.3** the parameters of the chosen design are given.

The DS LiRA design optimization is performed using 2D-FEM simulations, where models for the outer rotary machine and the inner linear machine are analyzed separately as it is assumed that the mover back iron provides magnetic insulation. This is true as long as the mover back iron is not saturated. Therefore, to check for the simultaneous influence of the rotary and linear PMs onto the mover's back iron flux density, a 3D-FEM model of the DS LiRA is built and analyzed. 3D-FEM models take much longer time to solve than 2D-FEM ones. Consequently, 3D-FEM analysis of only the chosen design is performed, which is shown in **Fig. 8.14**. It can be seen that for the analyzed

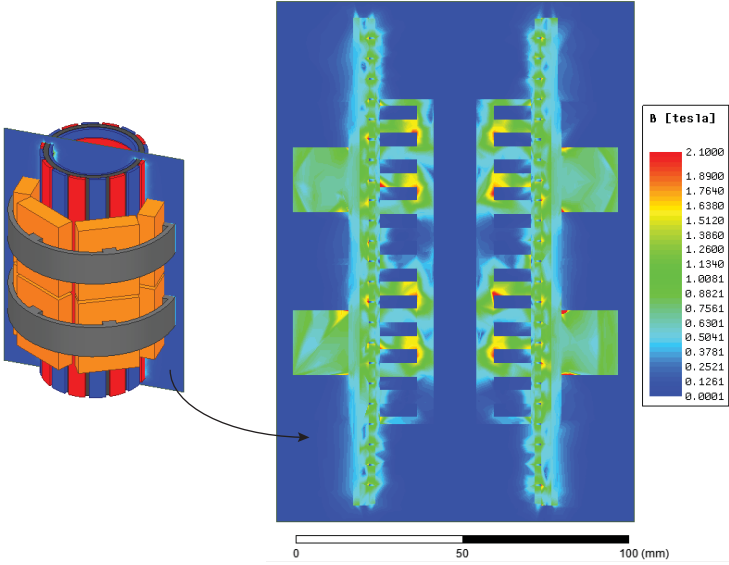


Fig. 8.14: 3D-FEM simulation of the chosen design whose parameters are given in **Tab. 8.3**. The simulation is conducted for twice the value of the Ampere-turns that are continuously possible, which are equal to $N_{\text{rot}} \hat{I}_{\text{rot}} = 2028.6 \text{ A turns}$ and $N_{\text{lin}} \hat{I}_{\text{lin}} = 685.2 \text{ A turns}$.

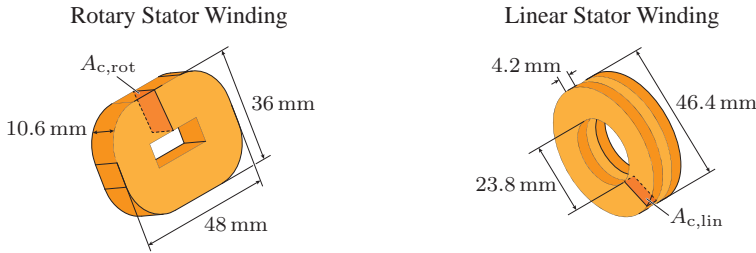


Fig. 8.15: The volume available for the winding realization of the outer rotary and inner linear stator. The winding window area is $A_{c,rot} = 148.7 \text{ mm}^2$ and $A_{c,lin} = 47.1 \text{ mm}^2$.

cross section the flux density in the DS LiRA is the highest in the rotary stator tooth and reaches around 1.6 T.

8.5 Winding Design

After the optimization, the geometry of the magnetic parts, such as PMs and the stator iron core are determined. With it, also the volume available for the winding realization is known, which in **Fig. 8.15** is shown for the rotary and the linear stators. The goal of this section is to determine a wire diameter that should be used for the realization of the windings, such that for the expected operating regimes, e.g. maximum torque and/or speed, the resulting induced voltages and phase currents suit to the inverter supply.

8.5.1 Rotary Stator Winding

The rotary stator winding has a twofold role, the torque and the bearing force control on the mover, which is achieved by controlling its phase currents. These currents are controlled with the inverter voltage supply, which has limited maximum voltage and current that it can generate. Therefore, in the winding design it is important that these maximum values of the inverter voltage and current are not exceeded. In the design at hand, it is assumed that the inverter supply may provide a maximum voltage amplitude of 200 V_{peak} , which suits to the DC-link voltage of 400 V. A maximum inverter phase current of 10 A_{peak} is assumed, cf. **Fig. 8.16**. It should be noted that each coil of the rotary DS LiRA stator winding is supplied with a dedicated half-bridge of the inverter.

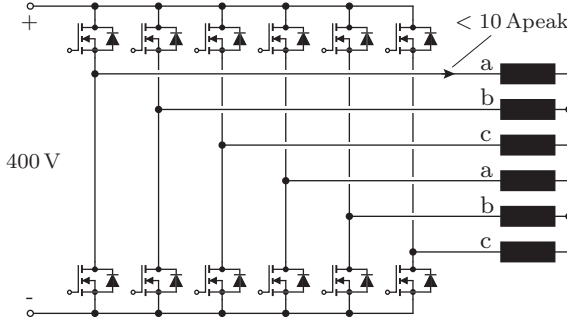


Fig. 8.16: Outer rotary stator inverter supply. Each coil of the rotary stator is supplied with a dedicated inverter half-bridge.

An additional aspect to consider is that the phase inductance increases with the number of turns as $\sim N_{\text{rot}}^2$. A too high value could limit the current control bandwidth and take direct influence on the magnetic bearing stiffness. Therefore, to have an as low as possible number of turns N_{rot} in the coil, a maximum possible diameter $D_{\text{wire,rot}}$ of the wire is chosen.

The upper limit on the wire diameter is determined by the manufacturing (too large wire diameter is difficult to bend when winding the coil), which is here set to 1 mm. Another upper limit comes from the skin effect in the conductors. The skin depth is calculated as

$$\delta_{\text{cu,rot}} = \sqrt{\frac{2\rho_{\text{cu}}}{\omega\mu_0}} \sqrt{\sqrt{1 + (\rho_{\text{cu}}\omega\epsilon_0)^2} + \rho_{\text{cu}}\omega\epsilon_0} = 3.26 \text{ mm}, \quad (8.6)$$

where $\rho_{\text{cu}} = 1.68 \times 10^{-8} \Omega\text{m}$, $\mu_0 = 4\pi \times 10^{-7} \text{ H/m}$, $\epsilon_0 = 8.854 \times 10^{-12} \text{ F/m}$ and the electrical angular frequency is equal to

$$\omega = \omega_{\text{R}} = N_{\text{p,rot}} \frac{\pi}{30} 3000 \text{ rpm} = 2513.3 \text{ rad/s},$$

which is the electrical angular frequency that suits to the maximum assumed mechanical speed of the mover of 3000 rpm that has $N_{\text{p,rot}} = 16$ PM poles. To safely ignore the skin effect in the DS LiRA windings, the wire diameter should be

$$D_{\text{wire,rot}} < \frac{\delta_{\text{cu}}}{4} = 0.81 \text{ mm}.$$

With the conducted considerations, $D_{\text{wire,rot}} = 0.8 \text{ mm}$ would be a reasonable choice for the wire diameter, just the resulting induced voltage in the coil

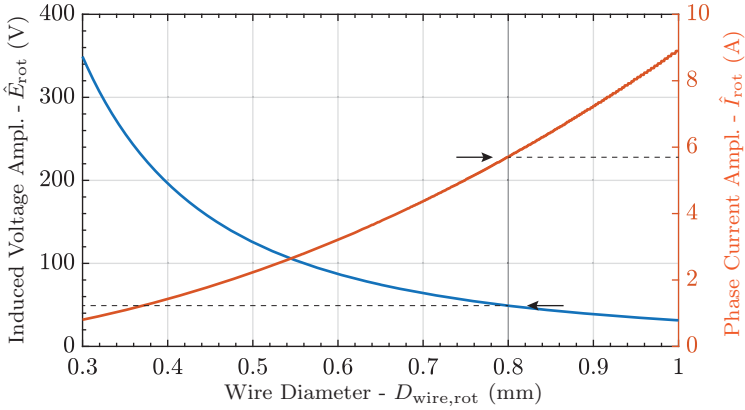


Fig. 8.17: Induced voltage amplitude for 3000 rpm mover rotational speed and a current amplitude of 1014 A turns (twice the continuous value of the current) versus wire diameter of the coil.

and the phase current should be checked. In **Fig. 8.17** voltage and current are plotted for different wire diameters. The induced voltage is calculated as

$$\hat{E}_{\text{rot}} = N_{\text{rot}} \cdot \omega_R \hat{\phi}_{\text{rot}}.$$

The number of turns of the rotary coil N_{rot} is calculated as

$$N_{\text{rot}} = \text{round} \left(\frac{k_{\text{ff}} A_{\text{c,rot}}}{A_{\text{wire,rot}}} \right),$$

where $k_{\text{ff}} = 0.6$ is the winding fill factor, $A_{\text{c,rot}} = 148.7 \text{ mm}^2$ is available coil window area (cf. **Fig. 8.15**) and $A_{\text{wire,rot}} = \pi D_{\text{wire,rot}}^2 / 4 = 0.5 \text{ mm}^2$ is the wire cross section. The flux amplitude $\hat{\phi}_{\text{rot}} = 0.11 \text{ mWb}$ in the rotor tooth carrying the coil, is obtained from 3D-FEM simulations and given in **Fig. 8.18**. In **Fig. 8.15** the phase current amplitude \hat{I}_{rot} is calculated as

$$\hat{I}_{\text{rot}} = \frac{1014 \text{ A turns}}{N_{\text{rot}}}$$

where 1014 A turns is the Ampere-turn value that in the chosen design results in copper losses that are twice the continuous losses allowed by the thermal model, such that the inverter can provide the overload current to the DS LiRA.

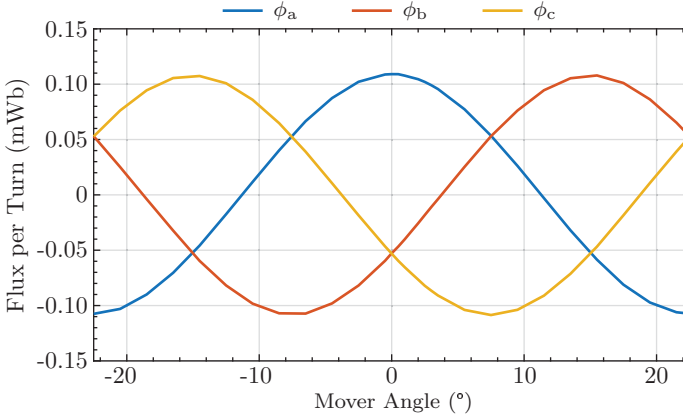


Fig. 8.18: Total flux in different teeth of the outer rotary stator, i.e. flux per winding turn.

As can be seen in **Fig. 8.15**, a wire diameter of $D_{\text{wire,rot}} = 0.8 \text{ mm}$ would result in an induced voltage much lower ($\hat{E}_{\text{rot}} = 50 \text{ V}$) than the 200 V , i.e. the maximum the inverter may provide. Also, the resulting phase current $\hat{I}_{\text{rot}} = 5.7 \text{ A}$ is lower than 10 A , the maximum inverter current. Therefore, finally a wire diameter of

$$D_{\text{wire,rot}} = 0.8 \text{ mm} \quad (8.7)$$

is chosen, which should result in around $N_{\text{rot}} = 187$ turns.

8.5.2 Linear Stator Winding

For the linear stator supply, the same inverter as for the rotary stator is used, therefore, the limit for the phase voltage amplitude is $\hat{E}_{\text{lin}} \leq 200 \text{ V}$ and the phase current amplitude limit is $\hat{I}_{\text{lin}} \leq 10 \text{ A}$.

The maximum assumed speed of the mover is $v_z = 4 \text{ m/s}$, which results in an electrical frequency in the winding of

$$\omega_L = \frac{2\pi}{\tau_{\text{pp}}} v_z = 1005.3 \text{ rad/s},$$

where the pole pair size τ_{pp} is equal to

$$\tau_{\text{pp}} = \frac{L}{N_{\text{p,lin}}/2} = 12.5 \text{ mm}.$$

In order to check for the maximum allowable wire diameter limited by the skin depth in the wire, (8.6) is used, where the resulting skin depth is $\delta_{\text{cu,lin}} = 5.2 \text{ mm}$, which limits the wire diameter to

$$D_{\text{wire,lin}} < \frac{\delta_{\text{cu,lin}}}{4} = 1.3 \text{ mm}.$$

Due to easier manufacturing, a wire diameter of the linear stator winding of

$$D_{\text{wire,lin}} = 0.5 \text{ mm} \quad (8.8)$$

is chosen. This winding diameter results in

$$N_{\text{lin}} = \text{round} \left(\frac{k_{\text{ff}} A_{\text{c,lin}}}{A_{\text{wire,lin}}} \right) = 144 \text{ turns},$$

where the winding factor is $k_{\text{ff}} = 0.6$, the winding window area $A_{\text{c,lin}} = 47.1 \text{ mm}^2$ and the wire cross section area $A_{\text{c,lin}} = \pi D_{\text{wire,lin}}^2 / 4 = 0.2 \text{ mm}^2$.

The induced voltage amplitude \hat{E}_{lin} due to flux linkage with the linear stator coil is

$$\hat{E}_{\text{lin}} = N_{\text{lin}} \cdot \omega_{\text{L}} \hat{\phi}_{\text{lin}} = 98.5 \text{ V},$$

where a magnetic flux amplitude in the tooth of $\hat{\phi}_{\text{lin}} = 0.672 \text{ mWb}$ is obtained from 2D-FEM simulation. The phase current amplitude is equal to

$$\hat{I}_{\text{lin}} = \frac{342.6 \text{ A turns}}{N_{\text{lin}}} = 2.4 \text{ A},$$

where the used Ampere-turns value is twice the Ampere-turns value that can exist continuously in the winding, i.e. the inverter may supply the actuator even in overload condition.

8.5.3 Summary of the Winding Design

The DS LiRA winding design details are summarized in **Tab. 8.4**.

8.6 Prototype Manufacturing

A DS LiRA prototype of the chosen design (cf. **Section 8.4**) is built. In the following sections, the manufactured prototype design is shown and described.

Tab. 8.4: DS LiRA winding design.

Symbol	Description	Value
Rotary stator		
N_{rot}	Expected number of turns	187 turns
$D_{\text{wire,rot}}$	Wire diameter	0.8 mm
\hat{E}_{rot}	Max. expected back-EMF	50 V
\hat{I}_{rot}	Overload phase current	5.7 A
Linear stator		
N_{lin}	Expected number of turns	144 turns
$D_{\text{wire,lin}}$	Wire diameter	0.5 mm
\hat{E}_{lin}	Max. expected back-EMF	98.5 V
\hat{I}_{lin}	Overload phase current	2.4 A

Rotary Stator Winding



190 turns
0.8 mm wire diameter

Linear Stator Winding



2×150 turns
0.5 mm wire diameter

Fig. 8.19: Concentrated windings of the rotary stator and the linear stator. The rotary stator winding is wound using a coil former, while the linear stator winding is wound directly on the stator core.

8.6.1 Windings for Rotary and Linear Stators

The rotary and the linear stator windings are shown in Fig. 8.19

The rotary stator winding is wound using a customized winding former made out of brass. The coil wire is self-bonding, which means that it has a glue around it that activates at certain temperature and glues the winding turns. Therefore, the winding does not need a coil former. After winding 190 turns, the coil is baked in an oven at 200 °C for around 30 min. The achieved winding fill factor is

$$k_{\text{ff,rot}} = \frac{190 \cdot A_{\text{wire,rot}}}{A_{\text{c,rot}}} = 0.642,$$

where $A_{\text{wire,rot}} = 0.5 \text{ mm}^2$ and $A_{\text{c,rot}} = 148.7 \text{ mm}^2$. Therefore, the assumed winding fill factor of 0.6 in the design is a good choice.

The linear stator winding is wound directly onto the stator iron core and cured in the oven at 160°C for 30 min. The achieved winding fill factor is

$$k_{\text{ff,lin}} = \frac{150 \cdot A_{\text{wire,lin}}}{A_{\text{c,lin}}} = 0.625,$$

where $A_{\text{wire,lin}} = 0.2 \text{ mm}^2$ and $A_{\text{c,lin}} = 47.1 \text{ mm}^2$. Once more here, the assumed winding fill factor of 0.6 in the design is a good choice.

8.6.2 Rotary Stator Assembly

The 3D-CAD model of the rotary stator assembly is shown in **Fig. 8.20**. It consists of

- ▶ 2 stator cores,
- ▶ 12 rotary stator concentrated coils,
- ▶ 2 position sensor PCBs and
- ▶ a power connection PCB where 24 coil wires are soldered.

The assembly ensures circumferential alignment of the stator cores, the axial distance between the rotary stator cores and the axial alignment with the inner stator core. To ensure the mechanical stability of the rotary stator assembly and its alignment with the inner stator, it is inserted into an aluminum case as shown in **Fig. 8.21**.

The stator core is built from laminated sheets and the winding coils are mounted onto it without coil former, cf. **Fig. 8.22**. The rotary stator cores are potted with the windings, where the potting mold is shown in **Fig. 8.23**. In the first step of the potting procedure the WEVOPOX 2513 and WEVODUR HC 1003 are mixed in 100 : 13 ratio. The stator and the epoxy are preheated to 60°C , such that the epoxy gets more liquid and fills each corner of the stator. After the epoxy is poured in the stator mold, it is cured for 4 hours at room temperature and after that for 4 hours at 120°C in the oven.

8.6.3 Linear Stator Assembly

The linear stator assembly is shown in **Fig. 8.24**. As already described in **Section 8.2** a copper pipe is used for heat conduction and is press fitted into

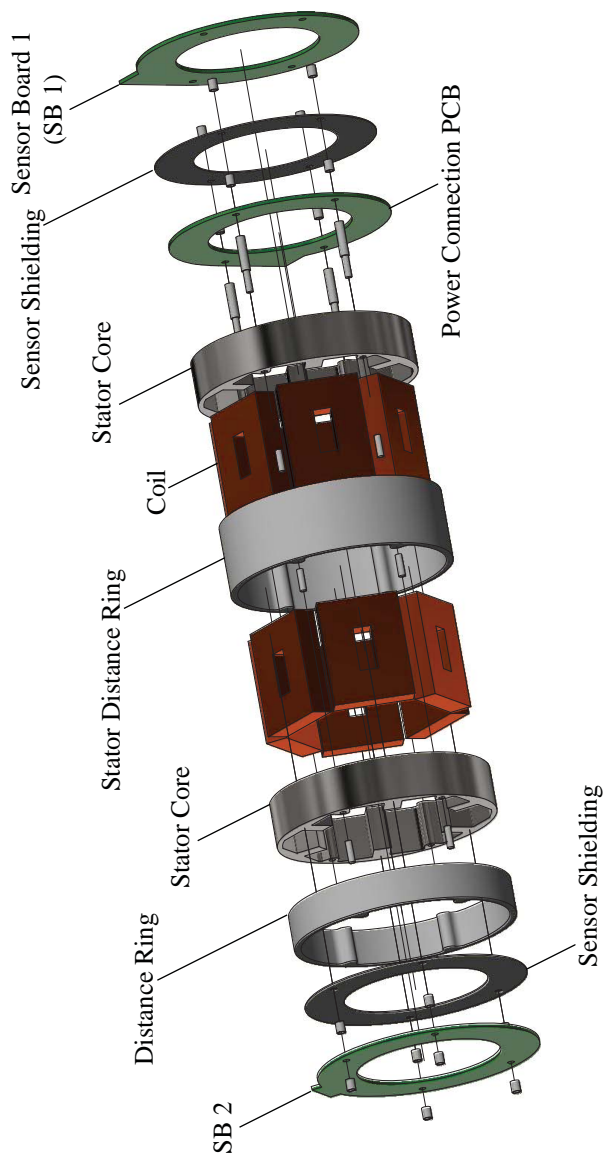


Fig. 8.20: Exploded view of the outer rotary stator assembly with sensor PCBs and the power connection PCB.

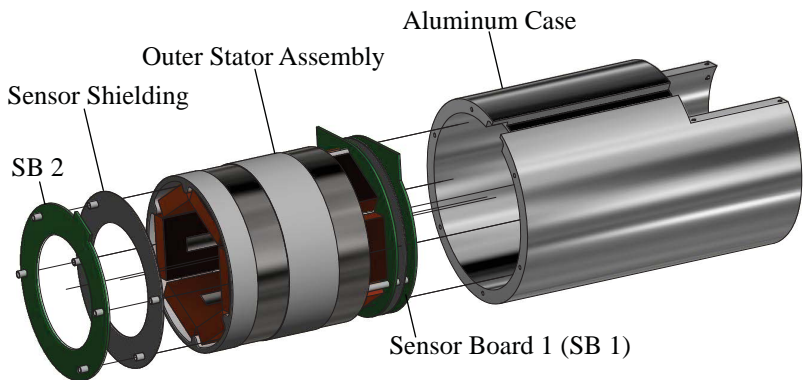


Fig. 8.21: Outer rotary stator insertion into the outer aluminum case that mechanically supports the assembly and positions the outer stator with respect to the inner stator.

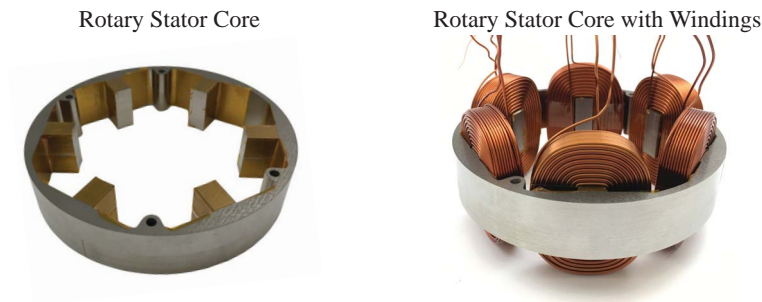


Fig. 8.22: Rotary stator core built from laminated steel. The lamination thickness is 0.35 mm. Kapton tape is used for the electrical insulation between the winding and the stator core.

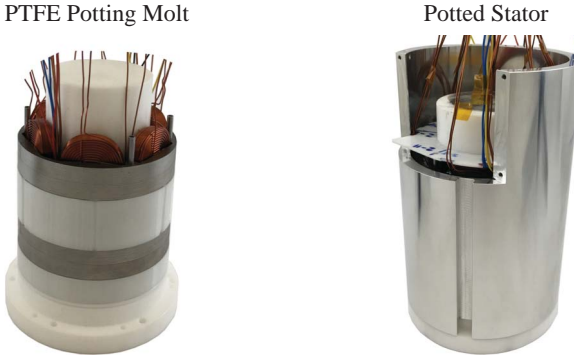


Fig. 8.23: The potting molt is made out of Teflon and is placed through the rotary stator. The stator is potted with epoxy WEVOPOX 2513 mixed with WEVODUR HC1003 in a ratio 100 : 13. The epoxy thermal conductivity is 1.4 W/(mK).

the iron core part as shown in **Fig. 8.24**. This press fit is done by heating up the iron core (to $\approx 150^\circ\text{C}$) and cooling down the copper pipe (to $\approx -20^\circ\text{C}$) and then pressing the copper pipe into the iron core. The inner stator core is built from multiple pieces, i.e. segments, which are stacked on the iron core and finally pressed with the face pin nut. The linear stator prototype is shown in **Fig. 8.25**.

8.6.4 DS LiRA Stator Assembly

The DS LiRA assembly is shown in **Fig. 8.26**. The assembly shows the positioning of the two stators, the outer rotary stator and the inner linear stator. The linear stator is attached to the end plate, which is then pressed into the aluminum case of the rotary stator. At the end of the linear stator, opposite to the end plate, a PCB integrated position sensor with Hall-effect elements is designed to sense the linear position of the mover. The sensor is connected with the cables that pass through the copper pipe hole, cf. **Fig. 8.25**. In total, the whole assembly employs three PCB integrated sensors (two at both axial ends of the rotary stator and one in the linear stator). The two cable glands are used for the power and the data cable. The power cable has $25 \times 1\text{ mm}^2$ wires and its outer diameter is 15.8 mm. The data cable has 25 twisted pairs and an outer diameter of 11.2 mm. The prototype of the DS LiRA with the rotary and the linear stators assembled is shown in **Fig. 8.27**.

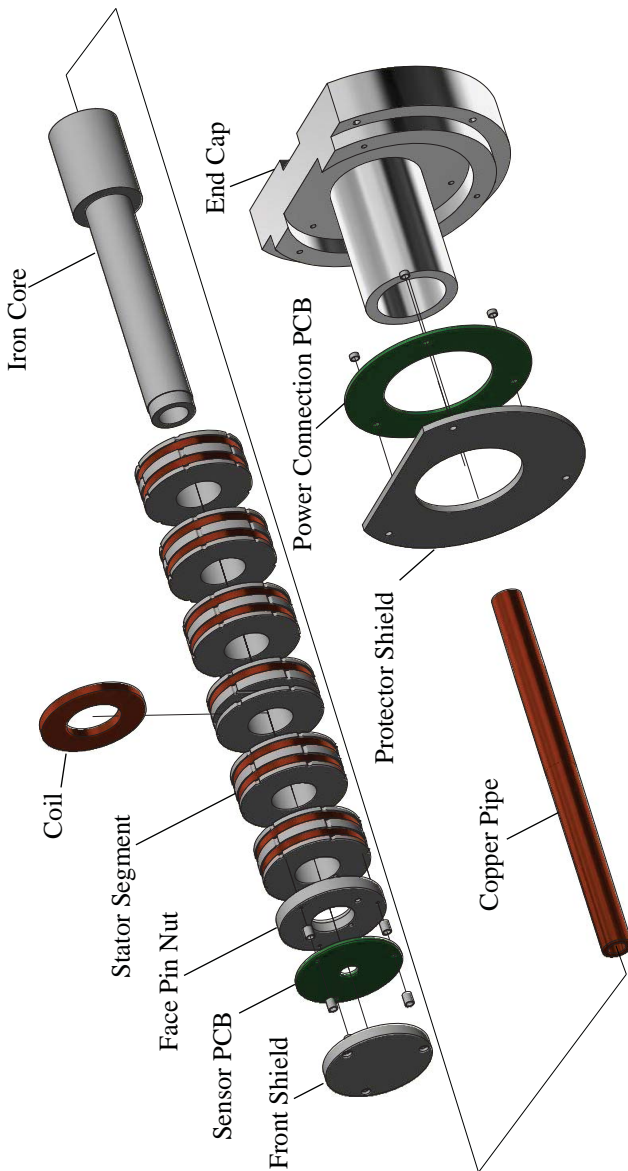


Fig. 8.24: Exploded view of the inner linear stator assembly with the sensor PCB and the power connection PCB.

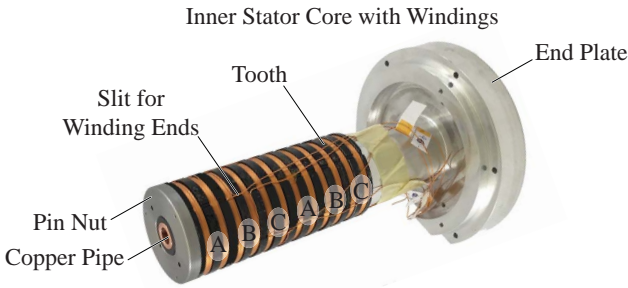


Fig. 8.25: Three-phase linear stator prototype attached to the end plate. The stator core material is machined from ST52 steel. The small slits in the teeth are used for the winding ends that are brought towards the end plate.

8.6.5 Mover Prototype

The mover of the DS LiRA consists of the iron core (cf. **Fig. 8.28**) that is sandwiched between the two sets of PMs, used by the outer rotary stator and the inner linear stator. For the assembling of the outer rotary stator PMs, the mover has specially made slits for the PMs, such that precise positioning of the PMs and gluing is possible. The poles of these PMs (North and South) are alternated in circumferential direction, as denoted in **Fig. 8.28**.

From the inner side of the mover core the inner linear stator PMs are assembled, cf. **Fig. 8.29**. The PMs are at first glued onto an aluminum form that has slits in axial direction. During the gluing process an iron pipe is used inside the aluminum form such that the PMs get attracted. Otherwise, it would not be possible to glue PMs next to each other due to strong attraction/repulsive forces. Due to mechanical tolerances in manufacturing, the PMs radial sizes may differ by ± 0.1 mm. As the PMs should fit inside the mover core, each PM piece is measured and sorted, such that the ones with larger radial dimension are dropped out and not used. In the last step, the PMs glued onto the aluminum form are pushed inside the mover core and glued.

The fully assembled mover is shown in **Fig. 8.30**. On top of the outer rotary PMs, the 0.4 mm thick aluminum shield is pulled on the mover over the PMs. This shield has a twofold role: (1) to mechanically protect the PMs in case the mover hits the touchdown bearing and (2) it is used by an eddy-current sensor to sense the mover's radial position. The same eddy-current sensor principle as for the MALTA is used, cf. **Section 5.3**.

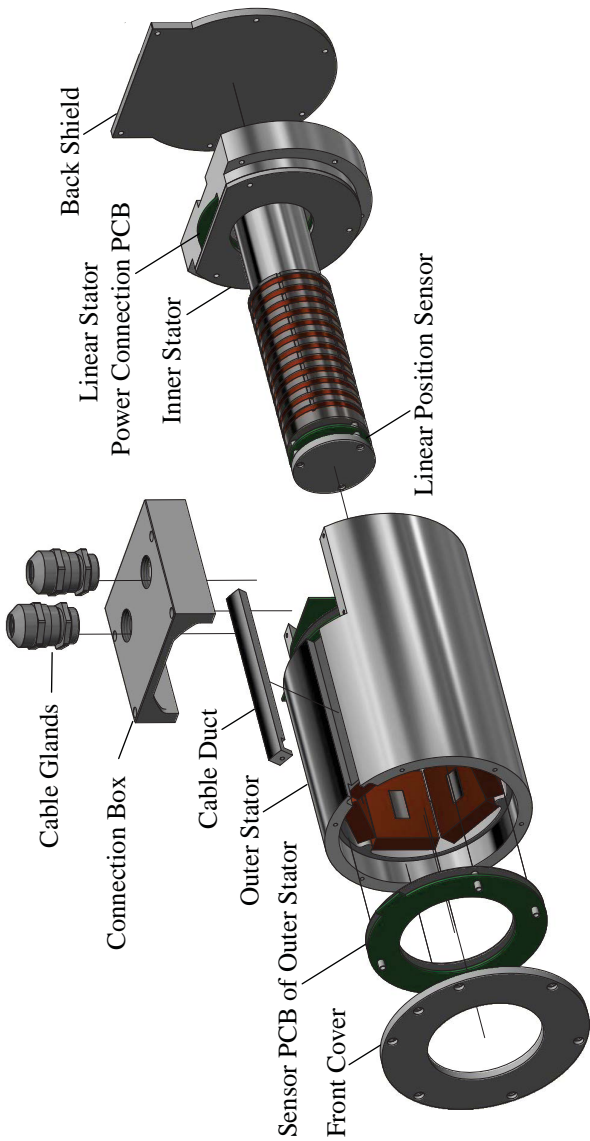


Fig. 8.26: Exploded view of the rotary and linear stators of the DS LiRA. The two cable glands are used for the power connection cable and the sensor twisted pair cable. The cable duct is used to connect the outer rotary position sensor PCB located at the axial end opposite to the connection box.

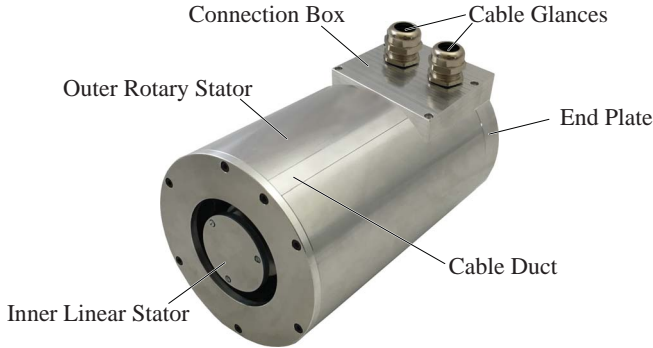


Fig. 8.27: DS LiRA prototype with outer rotary and inner linear stator assembled.

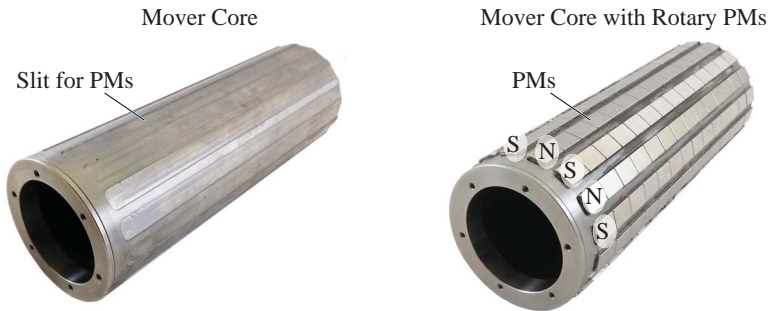


Fig. 8.28: Mover back iron core (steel ST52, cf. **Section 8.4**) with 0.2 mm deep slits for the PMs and iron core with glued rotary PMs. The PM piece sizes are $(2 \times 9.2 \times 34)$ mm, since the PM poles may not be manufactured from a single piece because of mechanical fragility.

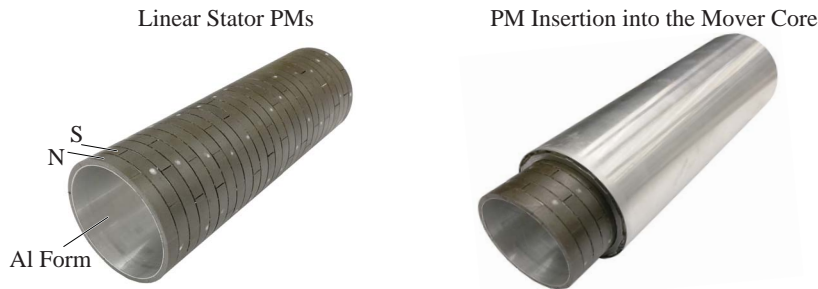


Fig. 8.29: Linear stator PMs are glued onto the Al form with 0.4 mm wall thickness and inserted from inner side into the mover iron core.



Fig. 8.30: DS LiRA mover with the aluminum shields from the inner and outer sides.

8.6.6 Summary

In this chapter the DS LiRA machine topology is introduced, optimized and built in hardware. The main challenge in the design is to reduce the temperature difference between the first and the last coil of the inner linear stator, which is caused by the axial heat flow. A solution where a copper pipe is inserted into the inner stator core structure is introduced and later on included in the optimization based on an analytic model of the heat flow. The applied optimization algorithm is a grid search method, where at first a design space is generated, i.e. DS LiRA geometrical parameters are varied within a certain range and the resulting performance is evaluated for each combination of these parameters. A 3D-CAD model of the chosen design is built with the assembly of all machine parts including sensor and power connection PCBs. The manufactured and assembled prototype of the DS LiRA is shown.

As a next step, the inverter and the position sensor for the DS LiRA are designed and realized in hardware, which is shown in the following **Chapter 9**.

9

Inverter Supply and Position Sensor of the Double Stator Machine

To test and drive the DS LiRA, an inverter supply and a position sensor are needed. This chapter summarizes their main design aspects and the used specifications.

9.1 Inverter Design Considerations

The inverter driving the DS LiRA should be able to supply its two rotary stators and the linear stator. The two rotary stators have 2×6 phases and the linear stator has three-phases. Therefore, the inverter should provide in total at least 15 phases. In order for the inverter to be able to supply the MALTA stators as well, the number of phases is chosen to be $N_{ph} = 18$. In literature, such multi-phase inverters are used to supply multi-phase machines, where the number of phases is higher than 3, cf. [117]. The specifications of the inverter are given in **Tab. 9.1**. The inverter is operated in pulse width modulation (PWM, cf. [118]) mode with constant switching frequency.

The schematic of a single inverter phase is shown in **Fig. 9.1**. The inverter phase employs an output filter, such that a smooth sinusoidal voltage is supplied to the corresponding DS LiRA winding. Thus several parasitic effects are eliminated such as, reflections and/or surge voltages at the winding terminals in case of a longer supply cable, HF capacitive currents through the mover, grounding parts and the machine integrated position sensors, which would increase the SNR of the position sensors. But, it should be mentioned that the output filter increases the inverter cost the additional hardware components are needed. Also, the measurement and control effort is increased

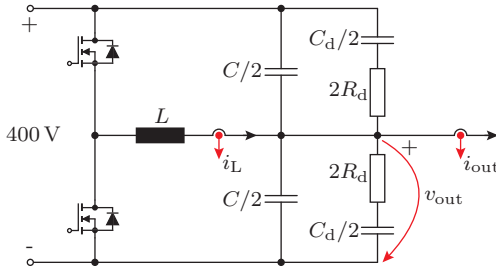


Fig. 9.1: Schematic of the power circuit of an inverter phase, comprising a GaN power semiconductor half-bridge and an LC output filter. The power semiconductors are 600 V, 70 m Ω CoolGaN-MOSFETs from Infineon [119]. The output filter capacitor is divided and attached to the DC+ and DC- rails. R_d and C_d are used for damping of the filter. In each inverter phase, three measurements are conducted: (1) inductor current i_L , (2) the output voltage v_{out} and (3) the output current i_{out} .

from a single current controller and measurement to 3 measurements and cascaded control loops for i_L , v_{out} and i_{out} and the bandwidth of the output current is limited.

For the whole inverter with 18 phases, $18 \times 2 = 36$ current measurement and 18 voltage measurement circuits are needed. Therefore, in total there are 54 measurements conducted at each current/voltage control interrupt.

9.1.1 Filter Inductor Design

One of the most important elements of the output filter is the inductor L . The inductance value of L influences the losses in the semiconductors, e.g. a too large inductance value increases the switching losses while reducing the conduction losses. A low inductance value might reduce switching losses as

Tab. 9.1: DS LiRA inverter specifications.

Symbol	Description	Value
V_{dc}	DC-link voltage	400 V
\hat{V}_{out}	Output voltage peak for 100 % modulation index	200 V
\hat{I}_{out}	Output current peak	10 A
f_{out}	Output fundamental frequency	400 Hz
f_{sw}	Switching frequency	140 kHz
N_{ph}	Number of phases	18

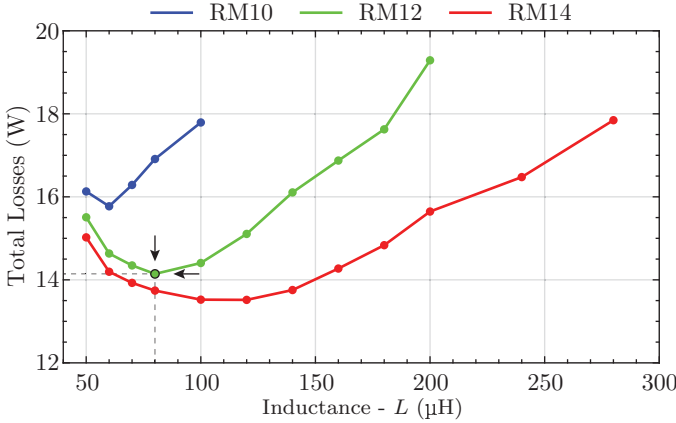


Fig. 9.2: Total inverter losses including: semiconductor (switching and conduction) and inductor (copper and core) losses. The RM12 core inductor design that provides minimum total losses is chosen. The design with the RM14 core is omitted, as the RM12 core better suits width of the PCB layout of a half-bridge. The inductor design details are given in **Tab. 9.2**.

a large inductor current ripple would result in soft switching for low values of i_{out} , while the conduction losses would increase. Additionally, an inductor with a fixed inductance value might be realized in many different ways, e.g. using different numbers of wire turns and different wire types, different types of cores and core sizes, with a typical trend of lower losses for larger volume designs.

The inductor is chosen based on an optimization for the nominal operating point, cf. **Tab. 9.1**. Three different inductor core options are considered (RM10, RM12 and RM14) with different inductance values in the range from 50 μH to 280 μH , in the steps of 10 μH . In **Fig. 9.2** different inductor design options are indicated also considering influence on the total losses in the inverter, i.e. semiconductor losses besides the losses in the inductor itself. At this point of the design, the layout arrangement of the inverter components is considered and the RM12 core fits much better into the design than the RM14. As the difference in losses between the RM12 and RM14 cores is small (cf. **Fig. 9.2**) (14.1 W for RM12 at 80 μH and 13.5 W for RM14 at 100 μH), the RM12 inductor design is chosen. Detailed parameters of the design are given in **Tab. 9.2**.

Tab. 9.2: Inductor design details.

Parameter	Value
Core size	RM12
Core material	N87
Inductance	80 μ H
Number of turns	23 (= 8 + 7 + 8)
Strand diameter	71 μ m
Number of strands	300
Diameter of wire	1.8 mm

9.1.2 Filter Capacitor

Based on the capacitor evaluations in [120], the ceramic capacitor C5750X6S2W225KT with X6S temperature characteristic of the dielectric is chosen. A single discrete component provides a capacitance of 2.2 μ F, without any bias voltage. Unfortunately, the capacitance heavily depends on the bias voltage. For example, for 200 V bias voltage, the capacitance drops by 65 %, i.e. from 2.2 μ F to 0.77 μ F. To attenuate this effect, the capacitors are connected as shown in **Fig. 9.2**, i.e. to DC- and to DC+. Like this, always one of the capacitors will be biased with higher voltage while the other capacitor experiences a lower bias, resulting in a total capacitance, which is less dependent on the bias voltage, as shown in **Fig. 9.3**. Therefore, from the schematic, the filtering capacitance is C and its value may be chosen such that a certain desired cut off frequency of the filter ($1/(2\pi\sqrt{LC})$) is achieved. For example, if a THD of the voltage of around 1 % is desired at the filter output, a total filtering capacitance of $C = 4.8 \mu\text{F}$ should be chosen, assuming $L = 80 \mu\text{H}$. This would require 4 discrete capacitors as the total capacitance still drops to 1.54 μF at 200 V (cf. **Fig. 9.3**). Therefore, considering a safety margin, space for 3 capacitor connections to DC+ and 3 to DC- is considered for the PCB layout, such that finally the total number of discrete capacitors may be chosen to be either 2, 4 or 6 during testing of the inverter.

9.1.3 Filter Damping

The choice of the damping resistor and capacitor R_d and C_d in **Fig. 9.1** needs to provide a sufficient damping factor and as low as possible losses. According to the analysis performed in [122], the damping resistance value should be

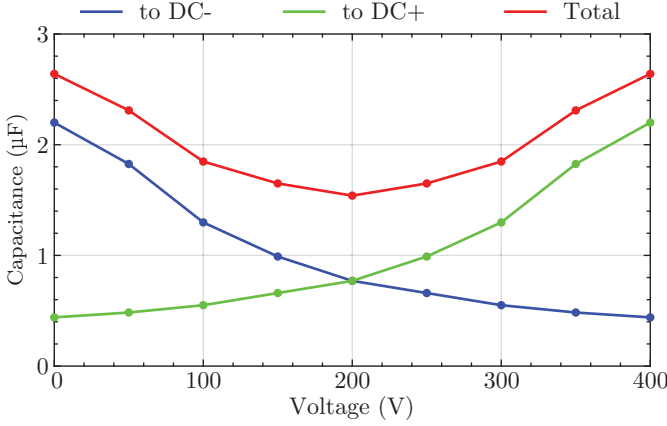


Fig. 9.3: Voltage dependent capacitance of a single discrete C5750X6S2W225KT capacitor shown over the bias voltage [121]. By connecting one filter capacitor to DC- and another one to DC+ (cf. Fig. 9.1), the total differential filtering capacitance increases and shows less dependence on the bias voltage.

equal to

$$R_d = R_{0d} \sqrt{\frac{(2+n)(4+3n)}{2n^2(4+n)}},$$

where $R_{0d} = \sqrt{L/C}$ and $n = 1$. The damping capacitance is determined as $C_d = nC$.

9.1.4 Heatsink Design

In order to dissipate the losses generated in the power semiconductors, typically a heatsink is used. To design a heatsink, a certain cooling system performance index (*CSPI*) should be assumed (cf. [123]), which represents a possible thermal conductance $C_{th,hs}$ per volume of the heatsink

$$CSPI = \frac{1}{R_{th,hs} \cdot V_{hs}} = 12 \frac{W}{K \text{ dm}^3},$$

where $R_{th,hs} = C_{th,hs}^{-1}$ is the thermal resistance of the heatsink and V_{hs} its volume. From the desired temperature difference between the power semiconductor junction and the ambient, the required $R_{th,hs}$ can be calculated and

therefore, the required volume of the heatsink. To do so, the first step is to calculate the losses of the half-bridge, which based on the current waveform and chosen filter inductance are $P_{v,hb} = 10.2$ W. The heatsink volume is determined for 9 half-bridges, since the inverter in total employs 18 half-bridges, which are equally partitioned and arranged at opposite sides of the PCB, such that 9 inverter phase outputs are available for connection on each side. The losses of 9 half-bridges result as $P_{v,9hb} = 9P_{v,hb} = 92$ W. The equivalent thermal resistance of the 9 half-bridges may be obtained as

$$R_{th,tot} = \frac{R_{th,jc} + R_{th,vias} + R_{th,tim}}{9} + R_{th,hs} = \frac{T_j - T_{amb}}{P_{v,9hb}},$$

where $R_{th,jc} = 0.55$ K/W denotes the thermal resistance from junction to case. The thermal resistance of 180 vias in the PCB is $R_{th,vias} = 1.23$ K/W and the thermal resistance of the thermal interface material is $R_{th,tim} = 0.5$ K/W. It should be mentioned that these thermal resistances are per half-bridge. If the temperature difference between the semiconductor junction and the ambient is assumed to be $T_j - T_{amb} = 70$ °C, then the required thermal resistance of the heatsink for the 9 half-bridges results as $R_{th,hs} = 0.5$ K/W. Therefore, the required heatsink volume is

$$V_{hs} = 0.17 \text{ dm}^3.$$

This value is used as a minimum value in the 3D-CAD design of the inverter's heatsink.

9.1.5 Inverter Prototype

In **Fig. 9.4** the inverter prototype is shown. The inverter features two PCB boards, a top one, with power and signal tracks and a bottom one where the inductors and the electrolytic DC-link capacitors are attached. The connector for the Xilinx ZYNQ 7000 control board to which all the measurement and the gate signals are connected is placed in the center of the top board. As it can be seen in the picture, the power semiconductor half-bridges are arranged close to the edges of the top board and have $2 \times 1 \mu\text{F}$, 500 V Cera Link commutation capacitors soldered close to them. From bottom, it can be seen that the heatsinks are directly attached beneath the power semiconductors and also have fans for forced air cooling.

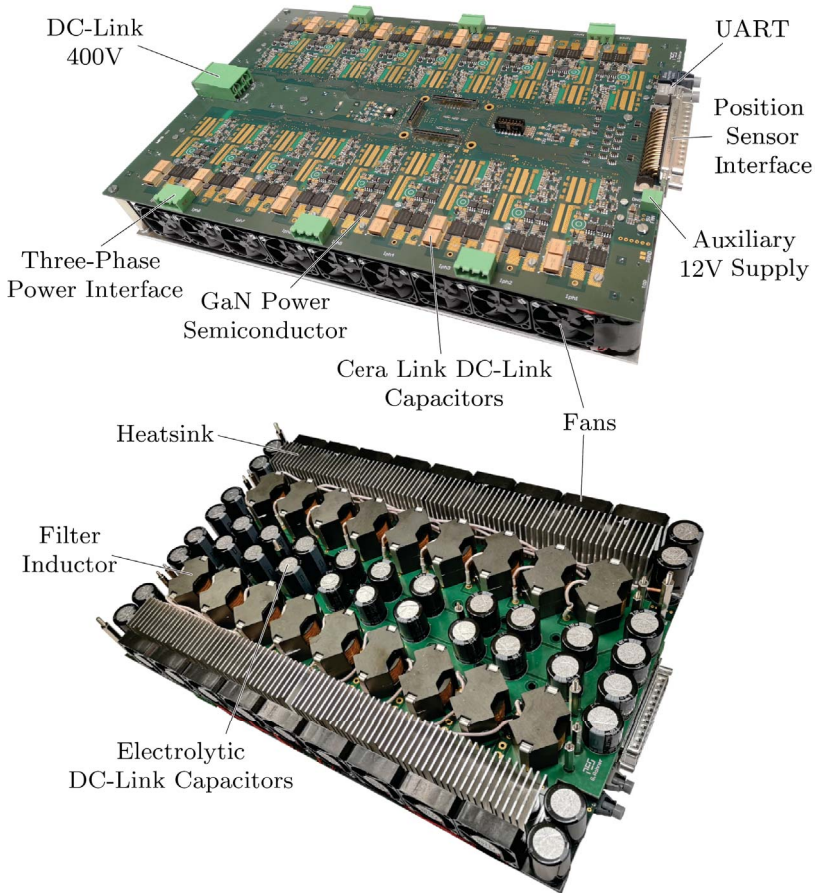


Fig. 9.4: Top and bottom view of the inverter prototype. The inverter has a single power input supplied from a 400 V DC source. There are 6×3 phase output power interfaces. The inverter also features a UART communication interface and a position sensor interface. The low voltage circuitry is supplied from a 12 V auxiliary supply.

9.2 Position Sensor Design

The position sensor system consists of:

- the radial position sensor (eddy-current based),
- the circumferential position sensor (Hall-effect) and
- the linear position sensor (Hall-effect).

All three sensors are arranged on PCBs which are placed inside the DS LiRA, cf. **Fig. 8.26**. The radial and the circumferential position sensors are arranged on the outer PCBs, while the linear position sensor is arranged on the inner sensor PCB.

9.3 Radial Position Sensor

The radial and the circumferential position sensors are arranged on the same PCBs, but feature very different operation principles and design methods.

The radial position sensors are working on the eddy-current principle. An illustration of its layout is shown in **Fig. 9.5**. In order to utilize the eddy-current effect, the surface of the mover must be conductive, e.g. made out of aluminum or stainless steel, such that an eddy-current i_{eddy} could be induced. For the following analysis, the mutual coupling between the pick-up coils (L_{x1} , L_{x2} , L_{y1} , L_{y2}) is neglected and only the couplings between the injection coil and the individual pick-up coils is considered, i.e. $M_{\text{inj}-x1}$, $M_{\text{inj}-x2}$, $M_{\text{inj}-y1}$ and $M_{\text{inj}-y2}$. For the typically small radial displacements Δx in the DS LiRA, which are not larger than 0.6 mm, the change of the mutual inductances may be assumed to be linear. Therefore, it can be written

$$\begin{aligned}
 M_{\text{inj}-x1} &= M_0 + \frac{\partial M_{\text{inj}-x1}}{\partial x} \Delta x \\
 M_{\text{inj}-x2} &= M_0 + \frac{\partial M_{\text{inj}-x2}}{\partial x} \Delta x \\
 M_{\text{inj}-y1} &= M_0 + \frac{\partial M_{\text{inj}-y1}}{\partial y} \Delta y \\
 M_{\text{inj}-y2} &= M_0 + \frac{\partial M_{\text{inj}-y2}}{\partial y} \Delta y
 \end{aligned} \tag{9.1}$$

where M_0 is the mutual inductance when the mover is placed in the center and Δx and Δy are displacements in x - and y -directions, respectively. The

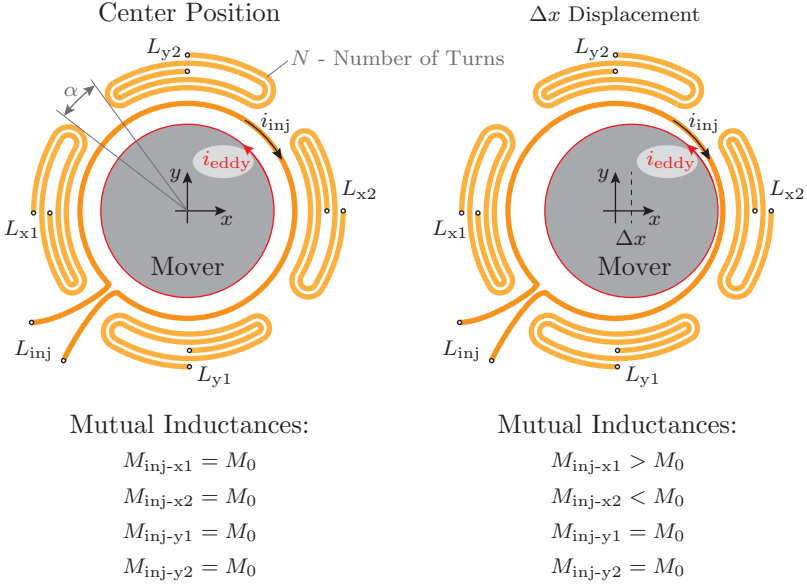


Fig. 9.5: Eddy-current sensor functioning principle. The sensor consists of an injection coil L_{inj} and the 4 pick-up coils (also called *sense coils*) L_{x1} , L_{x2} , L_{y1} , L_{y2} . The injection coil encircles the conductive mover surface with the HF current i_{inj} . In the mover surface an eddy-current i_{eddy} is induced with the tendency to compensate the field of the injection current. When the mover is located in the middle, all the mutual inductances between the injection coil and the pick-up coils are the same and equal to M_0 . Once the mover is displaced in positive x -direction, the eddy-current in the mover i_{eddy} increasingly compensates the field generated by i_{inj} in L_{x2} resulting in a reduced coupling M_{inj-x2} . In contrast M_{inj-x1} is increased. The angle α defines the empty space on the PCB between the pick-up coils. Each pick-up coil has the same number of turns equal to N .

partial derivatives of the mutual inductances per x or y are the sensitivities of the mutual inductance on the change of the mover's radial position. It should be noted that these sensitivities of the opposite coils of the same axis (L_{x1} and L_{x2} or L_{y1} and L_{y2}) have the same absolute value but the opposite sign, i.e.

$$\frac{\partial M_{\text{inj-x1}}}{\partial x} = -\frac{\partial M_{\text{inj-x2}}}{\partial x} \quad \text{and} \quad \frac{\partial M_{\text{inj-y1}}}{\partial y} = -\frac{\partial M_{\text{inj-y2}}}{\partial y}.$$

Additionally, due to symmetry, these sensitivities are the same in the x - and y -directions, and, therefore, it may be written

$$\frac{\partial M_{\text{inj-x1}}}{\partial x} = -\frac{\partial M_{\text{inj-x2}}}{\partial x} = \frac{\partial M_{\text{inj-y1}}}{\partial y} = -\frac{\partial M_{\text{inj-y2}}}{\partial y} = \frac{\partial M}{\partial r},$$

where $\partial M/\partial r$ is the mutual inductance radial sensitivity in either x - or y -direction.

The current in the injection coil is assumed to be sinusoidal with an amplitude \hat{I}_{inj} and an angular frequency ω_{osc} ,

$$i_{\text{inj}} = \hat{I}_{\text{inj}} \sin(\omega_{\text{osc}} t).$$

The induced voltages in the pick-up coils, in e.g. x -direction (similar applies for the y -direction), are equal to

$$\begin{aligned} e_{x1} &= M_{\text{inj-x1}} \frac{\partial i_{\text{inj}}}{\partial t} \\ e_{x2} &= M_{\text{inj-x2}} \frac{\partial i_{\text{inj}}}{\partial t} \end{aligned} \quad (9.2)$$

Subtracting these two equations results in

$$e_{x1} - e_{x2} = \omega_{\text{osc}} \hat{I}_{\text{inj}} (M_{\text{inj-x1}} - M_{\text{inj-x2}}) \cos(\omega_{\text{osc}} t).$$

Considering (9.1), we have

$$\Delta e_x = e_{x1} - e_{x2} = \omega_{\text{osc}} \hat{I}_{\text{inj}} 2 \frac{\partial M}{\partial r} \Delta x \cos(\omega_{\text{osc}} t). \quad (9.3)$$

The voltage Δe_x is measured over the anti-series connection the pick-up coils L_{x1} and L_{x2} . It should be noticed that Δe_x exists only if there is a non-zero Δx displacement of the mover. Consequently, Δe_x may be used for the position sensing of the mover.

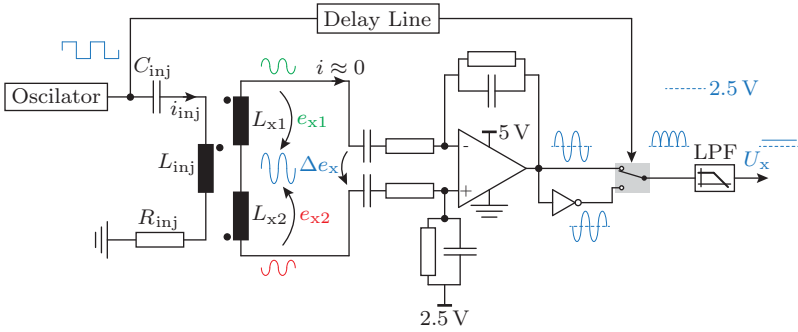


Fig. 9.6: Electrical circuit model of the radial eddy-current position sensor in x -direction. A circuit of same topology is used for y -direction measurement. The injection coil circuit consists of the oscillator that generates a HF voltage and excites the current i_{inj} in the injection coil L_{inj} . The induced voltage occurring over the anti-series connection of the pick-up coils is rectified around 2.5 V and low pass filtered, which finally provides a DC signal U_x proportional to the displacement Δx .

In **Fig. 9.6** an equivalent circuit for the sensor in x -direction is shown with additional electronic components that are needed to transform the induced voltage Δe_x at the anti-series connection of the pick-up coils into a DC voltage $U_x \in [0 \dots 5 \text{ V}]$ that can be digitized and used in the position controller software.

The sensor depicted **Fig. 9.5** is modeled with coupled inductors (cf. **Fig. 9.6**). The current i_{inj} in the injection coil L_{inj} is excited with a HF voltage signal supplied from an oscillator. At the utilized frequency the impedance $\omega_{osc} L_{inj}$ of the inductor would be too large and therefore the current i_{inj} would be too small to induce any voltage at the output. Therefore, typically a series resonance is created by adding an external capacitor C_{inj} , which should have the value

$$C_{inj} = \frac{1}{\omega_{osc}^2 L_{inj}}. \quad (9.4)$$

In such circuit, the current i_{inj} is only limited by the injection coil resistance R_{inj} , which is influenced by the skin and proximity effects and typically shows a value of $\approx 20 \, \Omega$.

From (9.3) it can be seen that the sensor DC voltage U_x is proportional to

$$U_x \sim 2\omega_{osc} \hat{I}_{inj} \frac{\partial M}{\partial r} \Delta x. \quad (9.5)$$

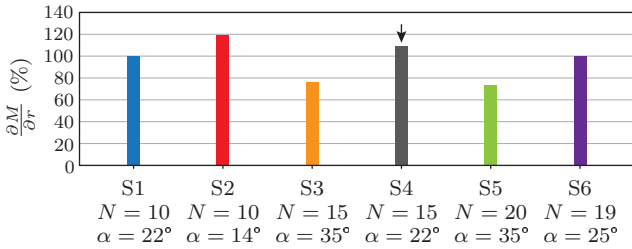


Fig. 9.7: Eddy-current sensor (cf. **Fig. 9.5**) geometry optimization. The radial mutual inductance sensitivities are compared, where the values with respect to the S1 are shown, i.e. for the S1 sensor geometry featuring $\partial M/\partial r = 100\%$. The sensor geometries S1,...,S6 are considered. Finally, S4 is the chosen for the sensor implementation.

Therefore, to increase the sensitivity of the sensor, i.e. $\partial U_x/\partial(\Delta x)$, the oscillation frequency ω_{inj} , the injection current amplitude \hat{I}_{inj} and the mutual inductance sensitivity $\partial M/\partial r$ should be as large as possible. The oscillation frequency ω_{osc} is limited by the sensor's geometry, i.e. after a certain frequency value (resonant frequency of the sensor), the sensor's inductive behavior turns to capacitive and therefore an operation as sensor is not any more possible. The injection current amplitude \hat{I}_{inj} is limited by R_{inj} . The radial sensitivity of the mutual inductance $\partial M/\partial r$ can be changed by changing the sensor geometry, i.e. by varying the parameters α and N , cf. **Fig. 9.5**. In **Fig. 9.7** the mutual inductance radial sensitivity is evaluated for various sensor geometries, which allows to choose the best performing sensor PCB layout. These results are obtained using Ansys Q3D software. It can be seen that by increasing the angle α the sensitivity $\partial M/\partial r$ reduces, since the area of the pick-up coils reduces, which may be seen by comparing S1 and S2, S3 and S4, S5 and S6 sensor designs. Increasing the number of turns N would not necessarily increase $\partial M/\partial r$, as with a larger number of turns, the pick-up coil grows in size and shows a larger distance to the injection coil and, therefore, experiences less magnetic flux. For example, by increasing the number of turns from $N = 10$ to $N = 15$, S1 and S4, $\partial M/\partial r$ increases, while by increasing the number of turns from $N = 15$ to $N = 20$, S3 and S5, $\partial M/\partial r$ does not change. The sensor designs with the largest $\partial M/\partial r$ are S2 and S4. Finally, the design S4 is chosen, even though it shows slightly lower $\partial M/\partial r$, but it features larger α , i.e. it leaves more PCB space between the pick-up coils that may be used for the components necessary for the sensor operation. This can be seen in **Fig. 9.8** where the sensor prototype is shown.

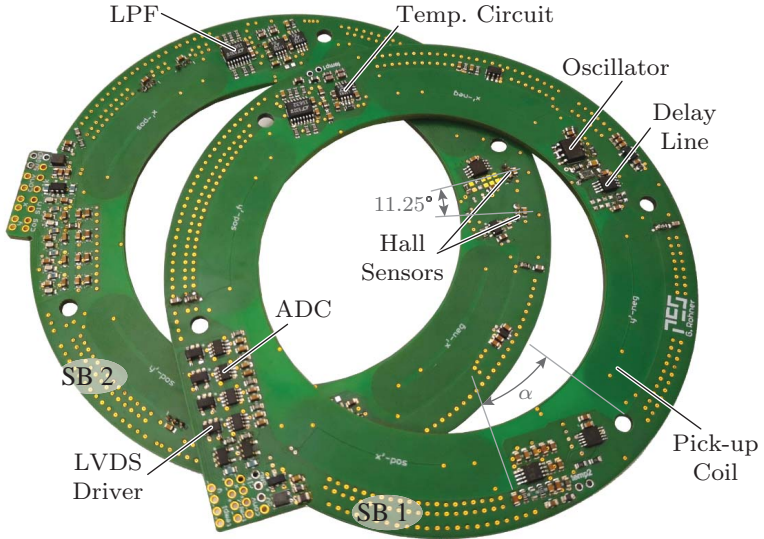


Fig. 9.8: DS LiRA outer position sensor PCBs with radial eddy-current sensors and circumferential Hall-effect based sensors. The boards also interface the 100 k Ω NTC resistors embedded into the outer stator winding for temperature measurement. The sensor PCBs feature on-board ADCs for signal digitization and interface the control board with SPI protocol. The radial eddy-current sensor pick-up coils are realized with $N = 15$ turns and $\alpha = 22^\circ$. Most of the electronic ICs is fitted between the pick-up coils, which confirms the S_4 choice for the sensor design, cf. **Fig. 9.7**.

Tab. 9.3: Eddy-current sensor parameters at 1 MHz.

Parameter	Simulation value	Measurement value
$L_{x1}, L_{x2}, L_{y1}, L_{y2}$	2.2 μH	2 μH
L_{inj}	97 μH	100 μH
$M_{\text{inj-x1}}, M_{\text{inj-x2}}, M_{\text{inj-y1}}, M_{\text{inj-y2}}$	0.72 – 1.42 μH	0.68 – 1.5 μH

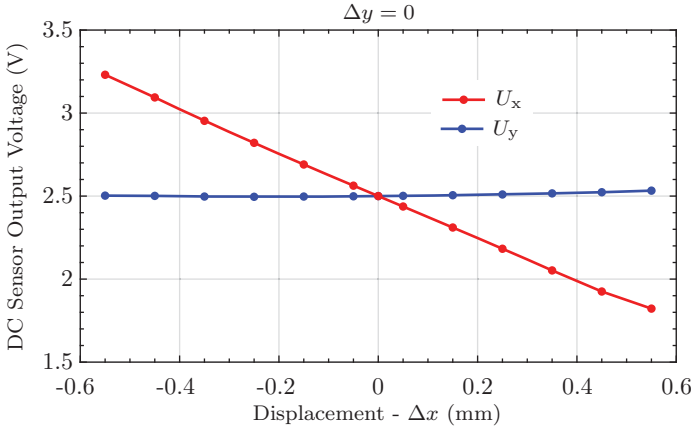


Fig. 9.9: The measured sensor sensitivity is 1.17 V/mm. The decoupling between the x- and y-axis is immediately visible.

In order to verify the Ansys Q3D design model, the parameters of the prototype are measured and compared with the simulations. The measurements are done with the impedance analyzer Agilent and shown in **Tab. 9.3**. The self-inductances do not depend on the radial displacement of the mover, while the mutual inductances are changing by a factor of ≈ 2 in the considered displacement range. Additionally, from the impedance measurements, it is seen that the sensor's resonant frequency is 4.2 MHz and therefore, the oscillation frequency is chosen as

$$\omega_{\text{osc}} = 2\pi \cdot 3.2 \text{ MHz}$$

resulting in $C_{\text{inj}} \approx 25 \text{ pF}$ (cf. (9.4)).

After the sensor design verification, its sensitivity is measured, and shown in **Fig. 9.9**.

9.4 Circumferential Position Sensor

In order to detect the circumferential position of the mover, the field of the mover PMs is measured with Hall-effect sensors. This is a very well known method where signals from the two sensors displaced by 90° electrical are used. As the DS LiRA mover has 8 pole pairs, the Hall-effect elements are displaced by $90^\circ/8 = 11.25^\circ$, as shown in **Fig. 9.8**. The used Hall-effect sensors detect the radial field component. The electrical angle is then detected as

$$\varphi_{el} = \text{atan2} \left(\frac{U_{\sin, \text{rot}}}{U_{\cos, \text{rot}}} \right),$$

where

$$U_{\sin, \text{rot}} = A \sin(\varphi_{el}) \quad \text{and} \quad U_{\cos, \text{rot}} = A \cos(\varphi_{el})$$

are the voltage signals measured by the Hall-effect sensors. The function atan2 returns a correct and unambiguous value for the angle φ_{el} between $-\pi$ and π [65]. The calculated value should be scaled and shifted, such that the mechanical mover angle is estimated as

$$\varphi_{\text{mech}} = \frac{\varphi_{el} + k 2\pi}{8},$$

where 8 is the number of pole pairs and k counts the PM pole pair segments of the mover and it can take integer values between 0 and 7. It should be noted that the electrical angle values are $\varphi_{el} \in [0, 2\pi]$ and with the integer number k , the same range for the mechanical angle φ_{mech} is obtained, i.e. $\varphi_{\text{mech}} \in [0, 2\pi]$.

The used Hall-effect sensors can sense moderate fields up to ± 42 mT.

9.5 Linear Position Sensor

The inner linear sensor works on the same Hall-effect principle as the one for the circumferential position sensing, discussed in **Section 9.4**. The linear position sensor implementation is shown in **Fig. 9.10**. It should be noted that the 90° electrical degrees shift is achieved by displacing the Hall-effect sensors axially. The PM pole size is 6.25 mm, therefore, the Hall-effect elements should be displaced by $6.25 \text{ mm}/2 = 3.125 \text{ mm}$. This displacement cannot be controlled exactly, since it also depends on the PCB and the soldering thickness. Consequently, with the measurements on the prototype it is found

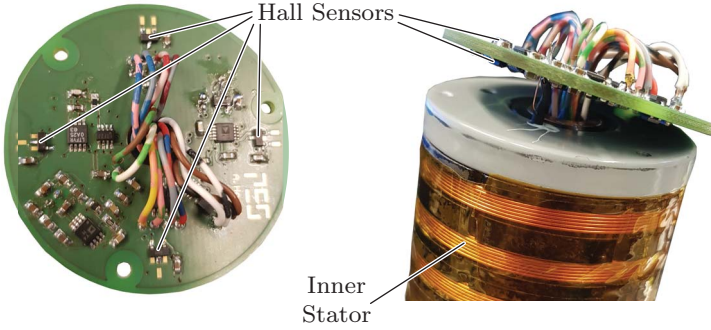


Fig. 9.10: Hall-effect based inner linear position sensor implemented on a PCB and mounted at the inner stator's axial end. As it can be seen, the sensor interface cables pass through the inner stator copper pipe. The sensor has 4 Hall-effect sensor elements distributed circumferentially, such that mover radial displacements do not distort the linear position measurement.

that the actual electrical angle between the Hall-effect sensor signals is 85° , i.e. there is an error of 5° . Therefore, the electrical angle of the linear stator is estimated as

$$\theta_{el} = \text{atan2} \left(\frac{\frac{U_{\sin, \text{lin}}}{U_{\cos, \text{lin}}} - \sin(5^\circ)}{\cos(5^\circ)} \right), \quad (9.6)$$

where the measured signals are equal to

$$U_{\sin, \text{lin}} = A \sin(\theta_{el} + 5^\circ) \quad U_{\cos, \text{lin}} = A \cos(\theta_{el}).$$

The expression (9.6) compensates for the 5° angle deviation, which can be proven if the trigonometric identity $\sin(\alpha + \beta) = \sin(\alpha) \cos(\beta) + \cos(\alpha) \sin(\beta)$ is used

$$\frac{1}{\cos(5^\circ)} \left(\frac{\sin(\theta_{el}) \cos(5^\circ) + \cos(\theta_{el}) \sin(5^\circ)}{\cos(\theta_{el})} - \sin(5^\circ) \right) = \frac{\sin(\theta_{el})}{\cos(\theta_{el})}. \quad (9.7)$$

Finally, the linear position is calculated from the electrical angle as

$$z = \frac{\tau_p}{\pi} (\theta_{el} + k 2\pi),$$

where k is similar as for the rotational angle φ_{mech} . The PM pole size is equal to

$$\tau_p = \frac{L}{N_{p,\text{lin}}} = 6.25 \text{ mm.}$$

9.6 Summary

In this chapter, a design of the DS LiRA 18 phase inverter supply and the design of the position sensors are discussed. The inverter is built with 600 V, 70 mΩ GaN power semiconductors from Infineon and is supplied from a 400 V DC-link. Each inverter phase includes an LC output filter, which provides smooth voltages to the corresponding DS LiRA winding. The filter inductor is built with a RM12 ferrite core and litz wire winding. The heatsink for the power semiconductors is designed with $CSPI = 12 \text{ W}/(\text{Kdm}^3)$.

The position sensors are realized on three separate PCBs, two integrated into the outer rotary stator and one into the inner linear stator. The outer rotary stator sensors are used for the radial and the circumferential position sensing. The radial position sensors are eddy-current based with a measured sensitivity of 1.17 V/mm. The circumferential and the linear position sensors are Hall-effect based and are verified with prototypes.

At this point, all hardware parts of the DS LiRA are designed and manufactured (cf. **Chapter 8** and this **Chapter 9**). Therefore, in a next step (**Chapter 10**) the control system design and implementation is considered.

10

Controller Design of the Double Stator Machine

To verify the operation of the DS LiRA, its inverter, and position sensor, a control system for the DS LiRA is designed, which is shown in this chapter.

10.1 Overview of the DS LiRA Winding Systems

The DS LiRA has two outer rotary stators and a single inner linear stator. The rotary stator has 6 tooth windings (cf. **Fig. 10.1**) with the currents that control the torque and the bearing forces on the mover. Therefore, in the rotary stator two three-phase systems are superimposed, the three-phase system that controls the torque $\{i_{r,a}, i_{r,b}, i_{r,c}\}$ and the three-phase system that controls the bearing forces on the mover $\{i_{b,a}, i_{b,b}, i_{b,c}\}$. Therefore, the currents in the DS LiRA rotary stators are sum of the two components

$$\begin{bmatrix} i_1 \\ i_2 \\ i_3 \\ i_4 \\ i_5 \\ i_6 \end{bmatrix} = \begin{bmatrix} i_{r,a} + i_{b,a} \\ i_{r,b} - i_{b,c} \\ i_{r,c} + i_{b,b} \\ i_{r,a} - i_{b,a} \\ i_{r,b} + i_{b,c} \\ i_{r,c} - i_{b,b} \end{bmatrix} = \mathbf{W} \begin{bmatrix} i_{r,a} \\ i_{r,b} \\ i_{r,c} \\ i_{b,a} \\ i_{b,b} \\ i_{b,c} \end{bmatrix} \quad (10.1)$$

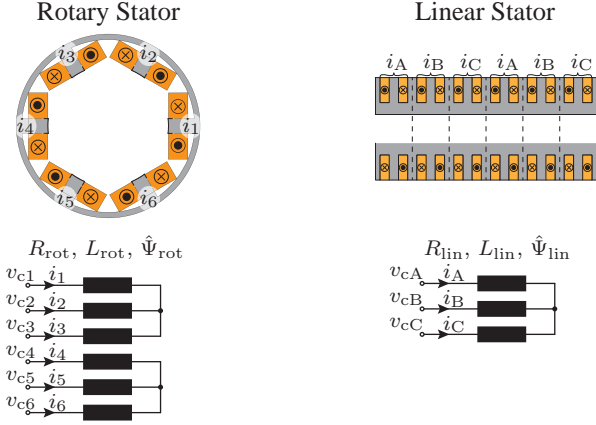


Fig. 10.1: DS LiRA rotary stator with the 6 tooth windings that superimpose two three-phase systems, therefore, resulting in 6 different currents in the stator i_1, \dots, i_6 . The linear stator is three-phase with the currents i_A, i_B and i_C . The DS LiRA machine parameters are summarized in **Tab. 10.1**. The rotary and linear currents are controlled with the supply inverter, operated with constant 140 kHz switching frequency PWM.

where the matrix \mathbf{W} is used to decouple the 'rotary' and the 'bearing' currents and it is equal to

$$\mathbf{W} = \begin{bmatrix} 1 & 0 & 0 & 1 & 0 & 0 \\ 0 & 1 & 0 & 0 & 0 & -1 \\ 0 & 0 & 1 & 0 & 1 & 0 \\ 1 & 0 & 0 & -1 & 0 & 0 \\ 0 & 1 & 0 & 1 & 0 & 1 \\ 0 & 0 & 1 & 1 & -1 & 0 \end{bmatrix}. \quad (10.2)$$

The matrix \mathbf{W} is invertible. The phase currents of the two three-phase systems are such that the rotary component couples with the 16 pole PM field and is able to generate torque with a winding factor of 0.866, while the bearing component is such that it can couple with $16 - 2 = 14$ poles to generate torque, which will allow to control the bearing force on the 16 pole mover. This is known as $2P - 2$ self-bearing method, cf. [22].

The linear stator winding is a conventional three-phase winding that couples with 16 PM poles on the mover and generates the drive force with a winding factor of 0.866.

Tab. 10.1: DS LiRA machine parameters.

Symbol	Description	Value
Rotary stator		
R_{rot}	Phase resistance	1.8 Ω
L_{rot}	Phase inductance	2.4 mH
Ψ_{rot}	Flux linkage	20.7 mWb
K_{R}	Torque constant (per rotary stator)	0.21 Nm/A
K_{B}	Bearing constant (per rotary stator)	3.7 N/A
Linear stator		
R_{lin}	Phase resistance	6.3 Ω
L_{lin}	Phase inductance	31 mH
Ψ_{lin}	Flux linkage	110 mWb
K_{L}	Force constant	83.5 N/A
Mover		
m	Mass	1.24 kg
J	Moment of inertia	0.001 45 kgm
K_{A}	Attraction constant (per rotary stator)	45.8 N/mm

10.2 Current Controller of the Rotary Stator

As shown in **Fig. 9.1** the DS LiRA inverter employs an LC output filter. Beside controlling the DS LiRA phase currents (i_1, \dots, i_6), this involves additional controller loops that control the voltages at the filter capacitors (v_{c1}, \dots, v_{c6}) and the currents through the filter inductors (i_{L1}, \dots, i_{L6}). Similar as the DS LiRA rotary stator currents, the capacitor voltages and the filter inductor currents will have rotary and bearing components, i.e. we have

$$\begin{bmatrix} v_{c1} \\ v_{c2} \\ v_{c3} \\ v_{c4} \\ v_{c5} \\ v_{c6} \end{bmatrix} = \begin{bmatrix} v_{\text{cr,a}} + v_{\text{cb,a}} \\ v_{\text{cr,b}} - v_{\text{cb,c}} \\ v_{\text{cr,c}} + v_{\text{cb,b}} \\ v_{\text{cr,a}} - v_{\text{cb,a}} \\ v_{\text{cr,b}} + v_{\text{cb,c}} \\ v_{\text{cr,c}} - v_{\text{cb,b}} \end{bmatrix}, \quad \begin{bmatrix} i_{L1} \\ i_{L2} \\ i_{L3} \\ i_{L4} \\ i_{L5} \\ i_{L6} \end{bmatrix} = \begin{bmatrix} i_{\text{Lr,a}} + i_{\text{Lb,a}} \\ i_{\text{Lr,b}} - i_{\text{Lb,c}} \\ i_{\text{Lr,c}} + i_{\text{Lb,b}} \\ i_{\text{Lr,a}} - i_{\text{Lb,a}} \\ i_{\text{Lr,b}} + i_{\text{Lb,c}} \\ i_{\text{Lr,c}} - i_{\text{Lb,b}} \end{bmatrix}.$$

For decoupling the rotary and the bearing components of the capacitor voltages and the inductor currents, the same matrix \mathbf{W} may be used.

In order to control the voltages and currents, they should be first transformed into the dq -coordinates. The scheme of the measurement and dq -transformations for the rotary stator of the DS LiRA are shown in **Fig. 10.2**. Since the rotary and the bearing current components coexist in the same winding, after measurement these components should be decoupled, which is achieved by multiplying the measurements with \mathbf{W}^{-1} . This is done for the

Tab. 10.2: DS LiRA rotary current controller gains.

Symbol	Name	Unit	Value
PI-1, phase current controllers - i			
K_p	Proportional gain	V/A	20
K_i	Integral gain	V/(As)	10000
PI-2, capacitor voltage controllers - v_c			
K_p	Proportional gain	A/V	0.405
K_i	Integral gain	A/(Vs)	3553
P-3, inductor current controllers - i_L			
K_p	Proportional gain	V/A	10.23
K_i	Integral gain	V/(As)	0

inductor currents, capacitor voltages (output voltages) and the DS LiRA rotary stator currents. Next, the three-phase rotary and the bearing voltages/currents are transformed into the dq -coordinates by T_{dq} matrix transformation, where

$$\mathbf{T}_{dq} = \begin{bmatrix} \cos(\varphi) & \cos(\varphi - \frac{2\pi}{3}) & \cos(\varphi + \frac{2\pi}{3}) \\ -\sin(\varphi) & -\sin(\varphi - \frac{2\pi}{3}) & -\sin(\varphi + \frac{2\pi}{3}) \end{bmatrix}. \quad (10.3)$$

The electrical angle φ used in the transformation is $\varphi = \varphi_r$ for the rotary three-phase systems and $\varphi = \varphi_b$ for the bearing three-phase systems.

The DS LiRA current controller structure is shown in **Fig. 10.3**. The references come from the position controller, that demands certain force or torque to act on the mover. It can be seen that the controller includes feedback as well as feed-forward components that enhance the controller operation. The controller uses measurements shown in **Fig. 10.2** and gives outputs that are algebraically transformed into the duty cycles. The current controller gains are given in **Tab. 10.2**. To implement these gains, the current controller execution frequency should be high. Therefore, it is implemented on ZYNQ's 7000 FPGA fabric and executed with 280 kHz. As the switching frequency of the converter is 140 kHz, so called 'double update' of the duty cycle is implemented.

10.3 Current Controller of the Linear Stator

The current control of the DS LiRA linear stator is a conventional three-phase control in the dq -coordinates. The structure of the current measurement and the controller action are shown in **Fig. 10.2**, whereas the structure of the controller itself is given in **Fig. 10.3**. The controller gains are given in **Tab. 10.3**.

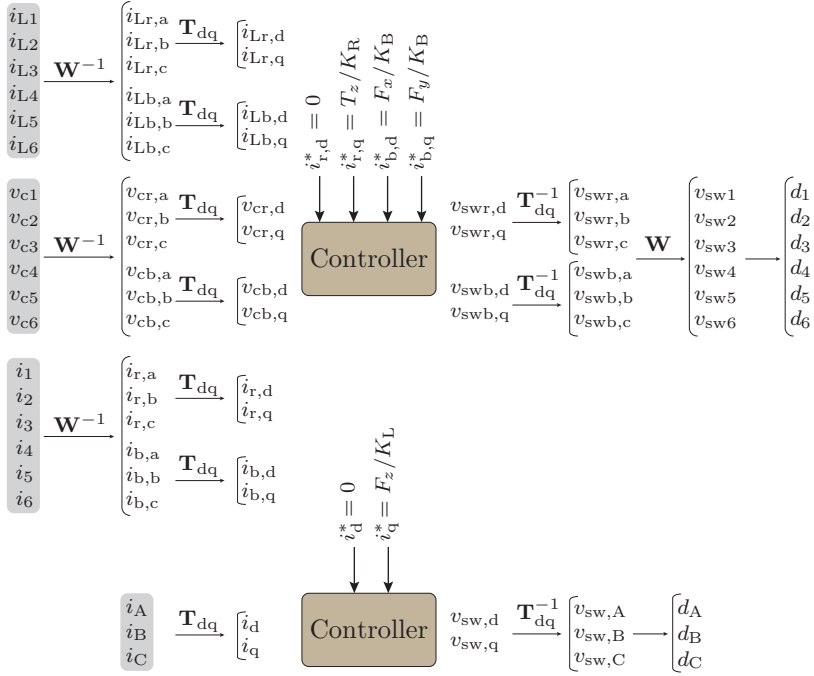


Fig. 10.2: Structure of the measurement and decoupling for the current control in the DS LiRa. The measured quantities are shaded in gray. Finally, the output of the rotary stator current control are the duty cycles (d_1, \dots, d_6) that are directly applied for the control of the half-bridges. For the linear stator current control, the measured three-phase currents are directly transformed into the dq -coordinates and supplied to the controller.

Tab. 10.3: DS LiRA linear current controller gains.

Symbol	Name	Unit	Value
PI-1, phase current controllers - i			
K_p	Proportional gain	V/A	60
K_i	Integral gain	V/(As)	30000
PI-2, capacitor voltage controllers - v_c			
K_p	Proportional gain	A/V	0.405
K_i	Integral gain	A/(Vs)	3553
P-3, inductor current controllers - i_L			
K_p	Proportional gain	V/A	10.23
K_i	Integral gain	V/(As)	0

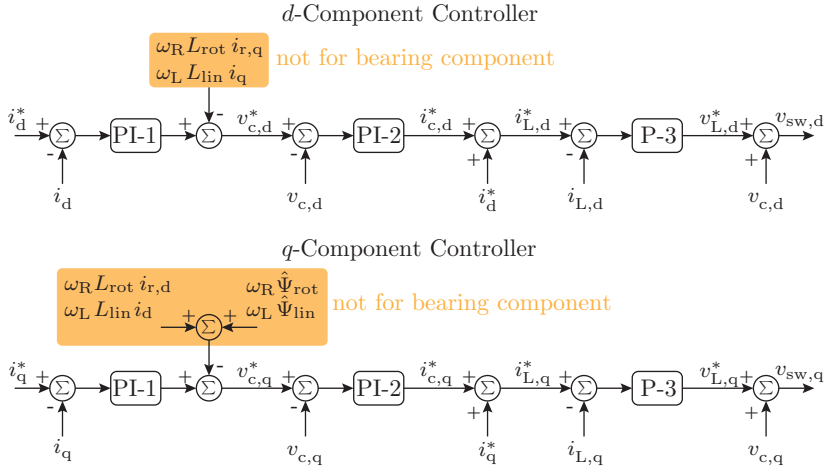


Fig. 10.3: DS LiRA current controller structure for *d*- and *q*-components. The same controller is used for the rotary and the bearing *dq* quantities, where the components denoted in orange are used only for the rotary and linear stator quantities. The most inner controller (P-3) is implemented in the FPGA and executed with 280 kHz (double update PWM with 140 kHz switching frequency). Therefore, there is no need to compensate for execution delays in current control loops.

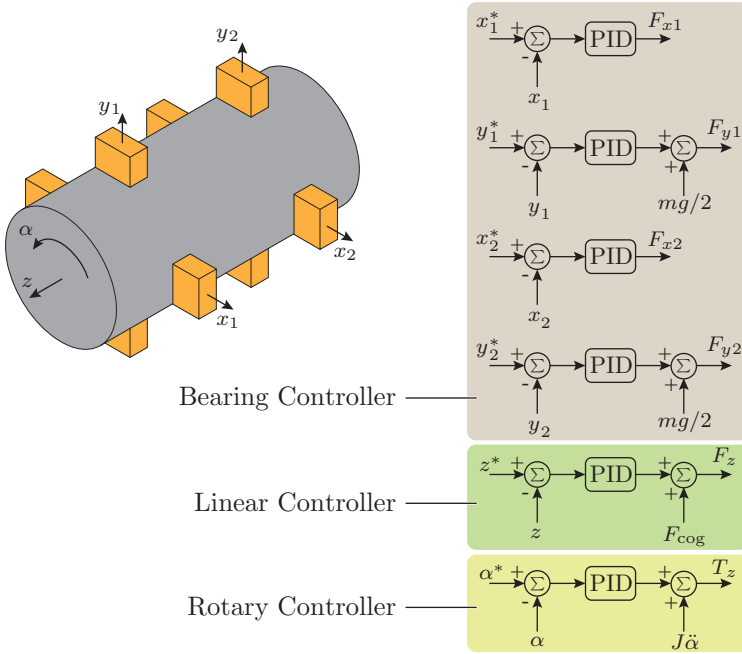


Fig. 10.4: Structure of the decentralized DS LiRA position control consisting of 6 individual PID controllers, 4 of which control the radial positions, while the other 2 control circumferential and linear positions. The feedback control action is enhanced with feed-forward components added at the output of the controllers.

10.4 Position Controller

The implemented position control is decentralized consisting of multiple SISO controllers that control positions in different directions, as shown in **Fig. 10.4**. Similar as for the MALTA, a MIMO realization of the position controller would be possible. Speed controller loops can be omitted since the position controllers include a derivative 'D' gain of the position errors. The outputs of the position controllers are the force references that are used to calculate the current references for the current controllers in **Fig. 10.2**. The gains used for the position controllers are given in **Tab. 10.4**.

The position control gains are possible in connection with an observer of the respective positions (modes), otherwise, the control is unstable. The Luenberger observer assumes a second order differential equation of the

Tab. 10.4: DS LiRA position control gains.

Symbol	Name	Unit	Value
Bearing Controllers			
K_p	Proportional gain	N/m	680
K_i	Integral gain	N/(ms)	10200
K_d	Differential gain	Ns/(m)	2.55
	Saturation limit	N	26.2
Rotational Controller			
K_p	Proportional gain	N/rad	25
K_i	Integral gain	N/(rads)	99
K_d	Differential gain	Ns/(rad)	0.8
	Saturation limit	Nm	0.839
Linear Controller			
K_p	Proportional gain	N/m	125
K_i	Integral gain	N/(ms)	5862
K_d	Differential gain	Ns/(m)	1
	Saturation limit	N	166

positions

$$m_0 \ddot{q} = c_0 \dot{q} + k_0 q + h(t) \quad (10.4)$$

where q represents a general coordinate. For translation, $q = \{x_1, y_1, x_2, y_2, z\}$, while for rotation $q = \alpha$. Similarly, for translation m_0 is the mass, while for rotation it is moment of inertia. The drive input to the system is $h(t)$, which represents either force or torque. To realize the position observer, a state-space equation is formed by introducing a new vector variable

$$\vec{p} = \begin{bmatrix} q \\ \dot{q} \end{bmatrix}.$$

The state-space equation of the observer in discretized form (Forward Euler) is

$$\hat{\vec{p}}_{n+1} = \mathbf{A} \hat{\vec{p}}_n + \mathbf{B} h_n + \mathbf{L} (q_n - \mathbf{C} \hat{\vec{p}}_n), \quad (10.5)$$

where the measurement matrix is equal to

$$\mathbf{C} = \begin{bmatrix} 1 & 0 \end{bmatrix}.$$

The other matrices \mathbf{A} , \mathbf{B} and \mathbf{L} are given in **Tab. 10.5** for different observer modes such as bearing x_1, y_1, x_2, y_2 , rotational α and linear z , which are denoted in **Fig. 10.4**. The time step Δt is the position controller execution period that is equal to

$$\Delta t = 1/35 \text{ kHz} = 28.57 \mu\text{s}. \quad (10.6)$$

Tab. 10.5: DS LiRA position controller gains.

Matrix	Bearing Observer	Rotational Observer	Linear Observer
$\mathbf{A} =$	$\begin{bmatrix} 1 & \Delta t \\ \frac{2K_A\Delta t}{m} & 1 \end{bmatrix}$	$\begin{bmatrix} 1 & \Delta t \\ 0 & 1 \end{bmatrix}$	$\begin{bmatrix} 1 & \Delta t \\ 0 & 1 \end{bmatrix}$
$\mathbf{B} =$	$\begin{bmatrix} 0 \\ \frac{2\Delta t}{m} \end{bmatrix}$	$\begin{bmatrix} 0 \\ \frac{\Delta t}{J} \end{bmatrix}$	$\begin{bmatrix} 0 \\ \frac{2\Delta t}{m} \end{bmatrix}$
$\mathbf{L} =$	$\begin{bmatrix} 0.06 & 0 \\ 0 & 0.04 \end{bmatrix}$	$\begin{bmatrix} 1 & 0 \\ 0 & 0.005 \end{bmatrix}$	$\begin{bmatrix} 0.02 & 0 \\ 0 & 0.09 \end{bmatrix}$

Further relevant parameters are the attraction constant K_A , the mass m and the moment of inertia J of the mover, which are given in **Tab. 10.1**. It should be noted that from the assumed dynamics in (10.4), $c_0 = 0$ for all the three modes, while for the bearing observer $k_0 = K_A$. The parameters $m_0 = m/2$ in case of the bearing and linear observer, but $m_0 = J$ for the rotational observer.

10.5 Summary

In this chapter designs of the current and position controllers for the DS LiRA are explained. As the DS LiRA inverter stage employs an output LC filters, a control of internal states, such as inductor currents and capacitor voltages is necessary. Therefore, a cascaded controller structure is established, where a separation in loop bandwidths must be guaranteed.

For the position control, DS LiRA has 6 degrees of freedom that should be controlled, therefore, 6 independent SISO PID position controllers are established for this purpose. Also, for each of the controlled position modes, there is a dedicated observer that provides a respective position and its derivative.

In the following **Chapter 11** measurement results of an experimental analysis of the DS LiRA are shown.

11

Experimental Analysis of the Double Stator Machine

To verify the DS LiRA design and its controller design implementation, an experimental analysis on the prototype is conducted and measurement results are shown in this chapter.

11.1 Introduction

The experimental analysis of the DS LiRA with MBs is still ongoing at the time of writing this thesis. Therefore, the shown measurements are conducted for the linear motion and rotation separately, i.e. the linear stator and the rotary stator are tested on separate test-benches. For the linear motion and testing of the linear stator, the mover is held by dedicated mechanical bearings, while for the rotation, the MBs are used, i.e. the self-bearing feature of the DS LiRA is verified.

11.2 Current Control

The switching node voltages of the DS LiRA inverter stages are filtered before being connected to the DS LiRA phase windings. The *LC* filter scheme is shown in **Fig. 9.1** and the design and the structure of the current controller of an inverter output are given in **Chapter 10**. The controller is realized with three cascaded loops, cf. **Fig. 10.3**, where the most inner one controls the filter inductor current i_L , the next outer one (the middle one) controls the filter capacitor voltage v_c and, finally, the most outer one controls the corresponding DS LiRA phase current.

As for the magnetic levitation, i.e. the MBs, an as high as possible current control bandwidth is important, only the current controller design for the rotary stator is shown here. The controllers are tuned according to **Tab. 10.3**, which gains are derived using iterative approach, i.e. each time the gain was increased, it was implemented and tested in hardware. Therefore, the gains given in **Tab. 10.3** yield the maximum possible bandwidth while keeping the step response stable, which is shown in **Fig. 11.1**. The step response of the DS LiRA phase currents was tested in simulation and measurement. The control is implemented in stationary dq -coordinates and tested on the current component that generates torque, cf. **Fig. 10.2**. It should be noted that only the d -components are shown, while the reference for the q -components is kept to zero, $i_q^* = 0$. Due to coupling of the d - and the q -components, during the transients minor effects are noticed on the q -components, but are successfully controlled to zero by the controllers.

From the controller response in **Fig. 11.1** for $i_{r,d}$, the DS LiRA current control bandwidth may be deduced by using the information about the rise time. The rise time is the time between 10 % and 90 % of the step response, and is equal to 0.12 ms for $i_{r,d}$. By using a simple formula [124] that relates the bandwidth of the closed-loop system and the rise time, the closed-loop bandwidth may be estimated as

$$f_{BW,i} = \frac{1}{3 \cdot 0.12 \text{ ms}} = 2.78 \text{ kHz}. \quad (11.1)$$

The filter capacitor voltage $v_{cr,d}$ and the filter inductor current $i_{Lr,d}$ controls are stable as indicated by the step transient waveforms, cf. **Fig. 11.1**. Additionally, the simulated waveforms match quite well with the measured ones, which verifies the current controller models used for the design.

It should be mentioned that typically the inverter stages driving an electric machine do not employ an output filter, but use the machine inductance for filtering the current ripple. In that case, the current control is way simpler and consists of a single control loop and it is not a challenge to implement the controller to achieve high current control bandwidths. Nevertheless, in high precision applications, actuator drives typically employ an output filter.

At this stage, once the current control of the DS LiRA is properly tuned, the position controllers may be analyzed, as done in the following sections.

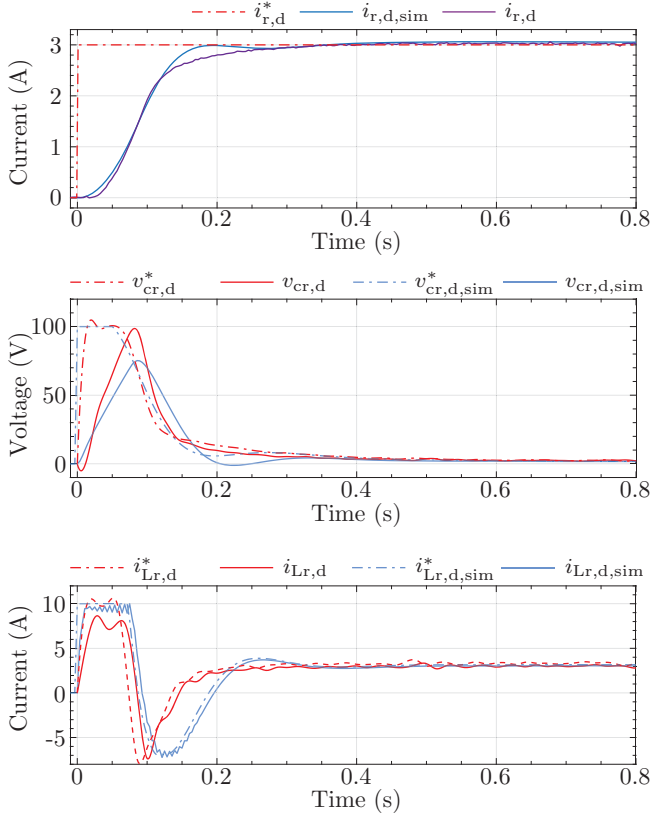


Fig. 11.1: Measurement and simulation of the d -current $i_{r,d}$ rotary stator step response (cf. Fig. 10.2). Only d -components are shown. The q -current reference is kept to zero, $i_{r,q}^* = 0$. From the i_d current step response, the rise time of 0.12 ms may be deduced (the time between 10 % and 90 % of the reference value), which gives a closed loop current control bandwidth of around 2.78 kHz. The waveforms of the capacitor voltage $v_{cr,d}$ and the filter inductor current $i_{Lr,d}$ are shown below. For the performed step response, the inverter was attached to the DS LiRA rotary stator and tested separately from the position controller. During the position controller testing, due to separation in frequency, the current controllers are assumed to ideally impress the desired output current references.

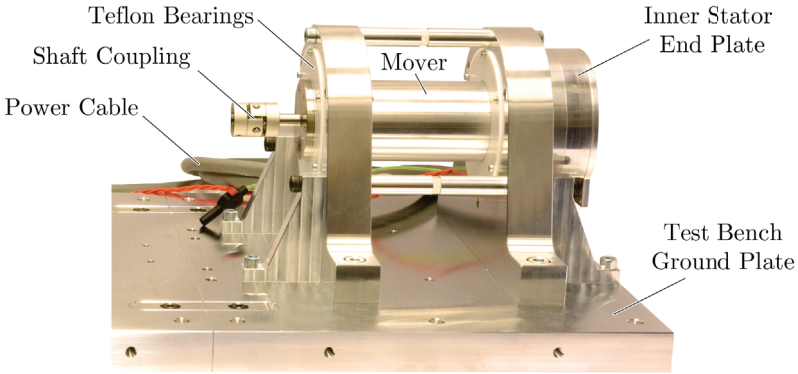


Fig. 11.2: Test bench setup for testing the linear inner stator of the DS LiRA. Teflon bearings support the mover.

11.3 Linear Position Controller

At this moment, the measurements for the linear and rotary stators are performed separately, i.e. the inner linear stator is tested without the outer rotary one. In order to support the mover, auxiliary mechanical bearings are manufactured out of teflon (PTFE) and used in a customized test bench as shown in **Fig. 11.2**.

The linear position controller structure is given in **Fig. 10.4** and the controller gains in **Tab. 10.4**. In order to verify the operation of the inner linear stator, two measurement experiments are conducted, linear reference tracking and oscillatory operation.

In **Fig. 11.3** the linear position reference tracking is shown. The reference z^* is changed from $z_0 = -6$ mm to $z_1 = 6$ mm using a sigmoid function for reference generation

$$z^*(t) = z_0 + \frac{1}{2} (z_1 - z_0) \left(1 + \operatorname{erf} \left(\frac{5}{t_r} (t - t_r/2) \right) \right), \quad (11.2)$$

where t is the time and the rise time t_r is obtained as

$$t_r = |z_1 - z_0| \cdot 0.01 + 0.027 \text{ s}. \quad (11.3)$$

In this example $t_r = 147$ ms. The pure feedback control has good reference tracking with the position error z_{error} not exceeding 0.2 mm, which is 1.7 %

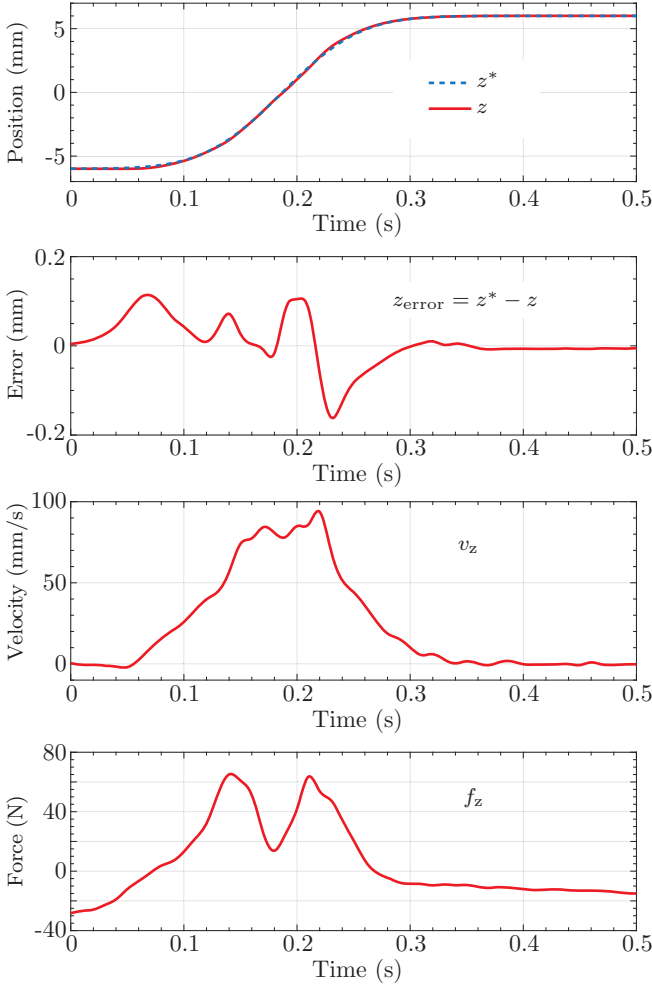


Fig. 11.3: Step response measurement results of the inner linear stator with a stroke of 12 mm and sigmoid reference. The controller has good trajectory tracking with a tracking error that stays below $z_{\text{error}} < 0.2$ mm. The maximum speed achieved is very low and stays below $v_z = 0.1$ m/s, which suits to the electrical frequency of $v_z/\tau_{\text{pp}} = 8$ Hz. The linear force f_z has non-zero steady-state values due to cogging force compensation. The cogging force has a fundamental harmonic peak of ~ 29 N with a period of 6.25 mm.

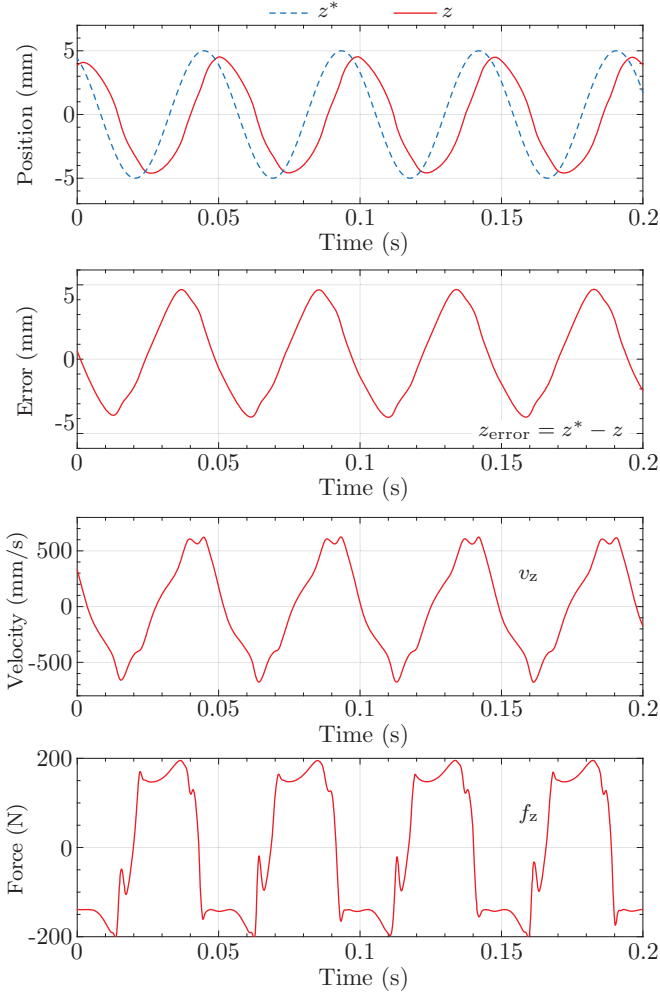


Fig. 11.4: Measurement of the linear position on the test bench shown in **Fig. 11.2**. The linear position reference z^* oscillates with 20 Hz and an amplitude of 5 mm. The maximum achieved linear speed during this motion is in the range of 500 mm/s, which results in the electrical frequency of $(500 \text{ mm/s})/\tau_{\text{pp}} = 40 \text{ Hz}$, where $\tau_{\text{pp}} = L/(2N_{\text{p,lin}}) = 100 \text{ mm}/8 = 12.5 \text{ mm}$. The linear force reaches maximum values of 200 N.

compared to the performed linear stroke. The linear drive force f_z has peculiar shape due to large cogging force that the linear actuator exhibits.

The oscillatory operation of the inner linear stator is shown in **Fig. 11.4**. For the selected operating frequency (20 Hz), an amplitude attenuation is expected and it is equal to 0.9; furthermore, a quite large phase shift of 52.6° occurs. It should be mentioned that this is only the action of the feedback controller and only the cogging force mapped is added to the drive current reference (cf. **Fig. 10.4**). Also, the friction from the teflon mechanical bearings contributes to the increase of the phase shift. In a next step, for the oscillatory operation, a feed-forward term to the position controller will be added.

11.4 Rotation and Magnetic Bearing Controller

In this section, the experiments with rotation and MBs are conducted without inner stator. The mover is levitated by the outer rotary stators and circumferential positioning tasks and continuous rotation are performed.

In **Fig. 11.5** and **Fig. 11.6** the experimental results for a mover angle step response are shown. The rotation characteristic quantities are shown in **Fig. 11.5**, while the MBs characteristic quantities which occur simultaneously in the same experiment are shown in **Fig. 11.6**. The angle step reference α^* from $\alpha_0 = 15^\circ$ to $\alpha_1 = 180^\circ$ results in a circumferential stroke of 165° , where the step function is used for the reference generation. The current controller limit is set to 3 A. This results in the torque saturation at $2 K_R \cdot 3 \text{ A} = 1.26 \text{ Nm}$, where the factor 2 accounts for the 2 rotary stators. During this step response, the self-bearing operation of the rotary stators held the mover hovering in the outer DS LiRAs air gap, which is shown by the measurements in **Fig. 11.6**, where the radial positions and the respective radial forces are shown. When performing the circumferential step response, the radial positions are disturbed, but the radial position controller damps the oscillations rather fast. The amplitude of the radial position deviation from the center position, for this extreme positioning task, does not exceed $60 \mu\text{m}$.

Another experiment performed with MBs is the constant rotation of the DS LiRA mover, while levitating it. As it can be seen in **Fig. 11.7**, the mover starts from rest and reaches the reference speed of $n_\alpha^* = 60 \text{ rpm}$. It can be seen that at start the mover is attracted to the bottom of rotary stator 1, while it is attracted to the top of rotary stator 2. After the start transient has passed, the mover's radial position is kept within $20 \mu\text{m}$. This is shown in **Fig. 11.8** where the radial coordinates of the rotary stators 1 and 2 are plotted. Also,

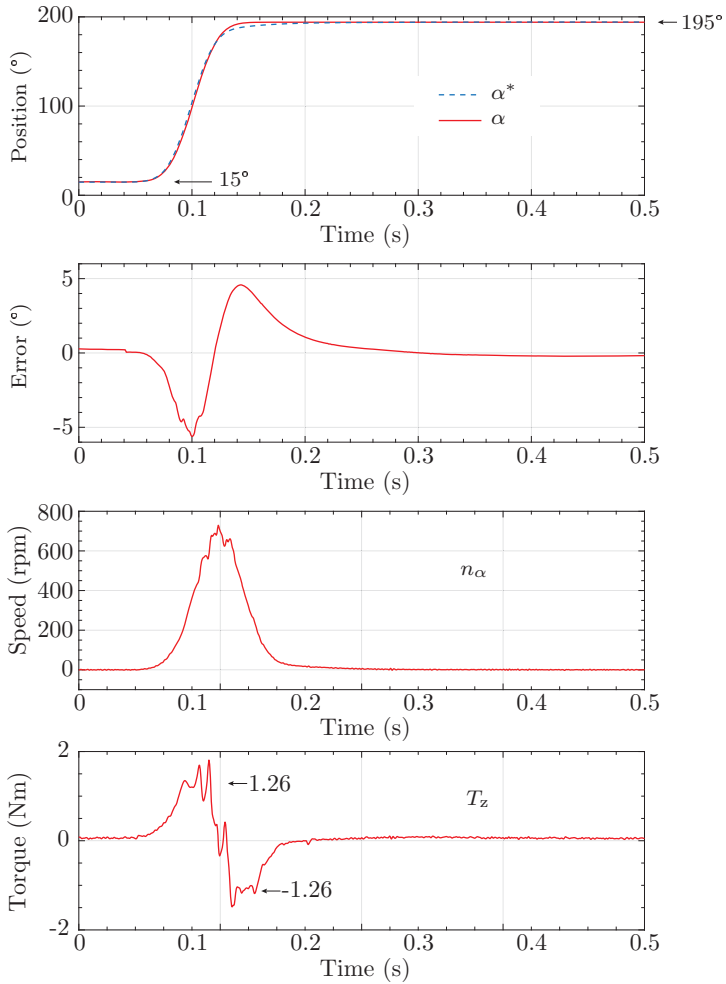


Fig. 11.5: Step response measurement results (sigmoid reference) of the rotary outer stators without inner stator and MBs supporting the mover. The angle stroke reference step is 180° . The maximum achieved speed is around 700 rpm, which corresponds to the electrical frequency of 93.33 Hz. The maximum torque is determined by the current limit of $1.26 \text{ Nm}/(2K_R) = 3 \text{ A}$. The response of the MBs, i.e. the radial positions and forces, are given in Fig. 11.6.

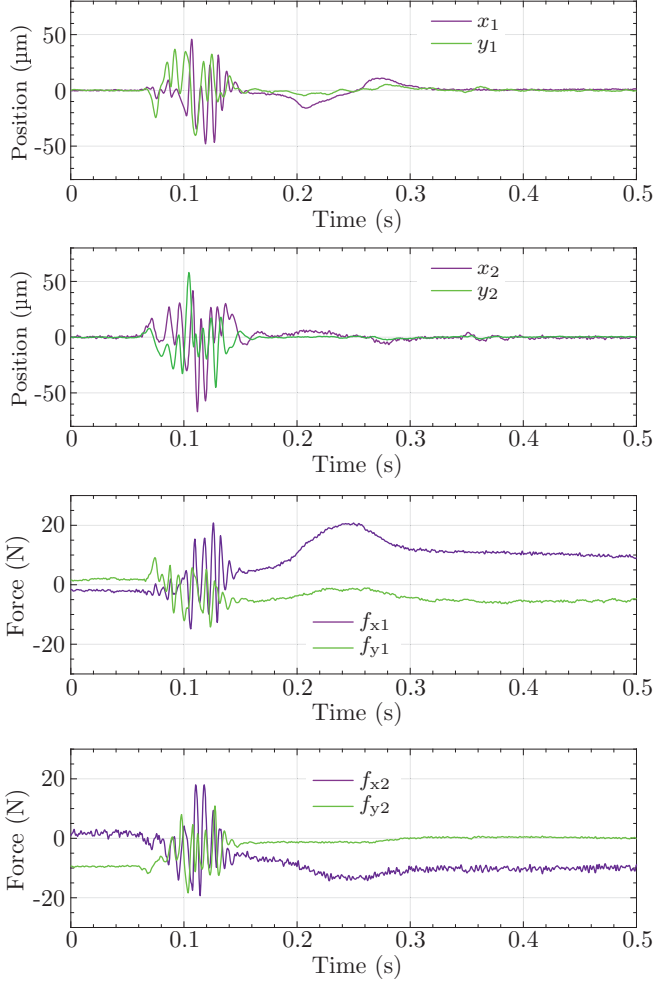


Fig. 11.6: The radial positions of the DS LiRA that correspond to the circumferential step response shown in Fig. 11.5. The radial position oscillations stay below 60 μm .

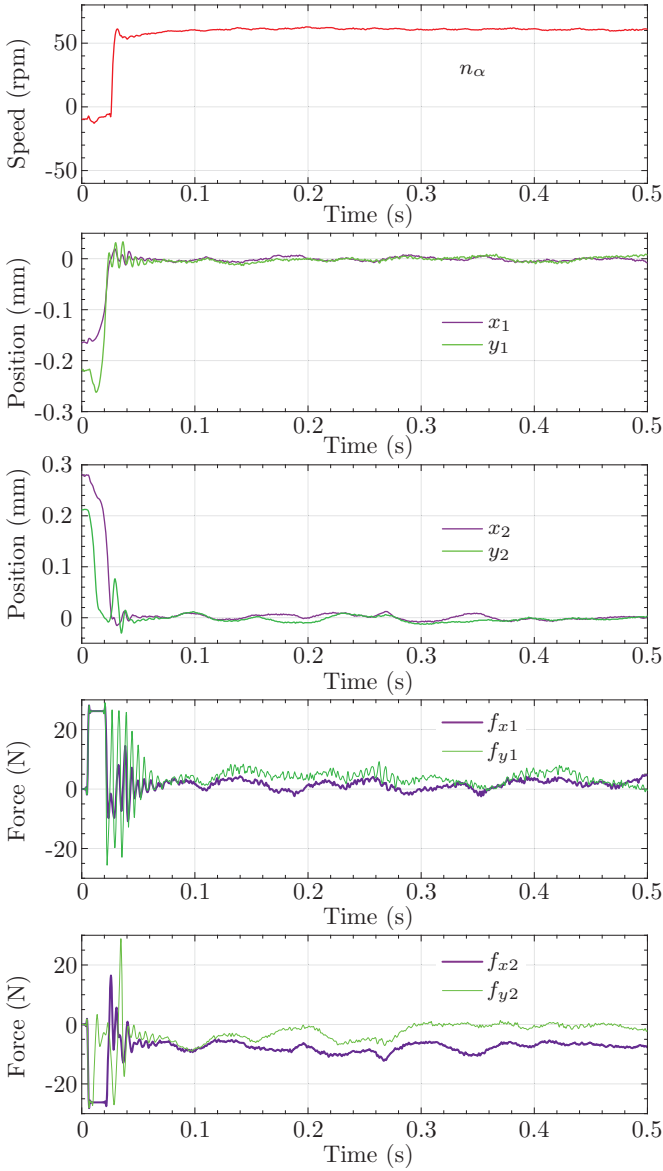


Fig. 11.7: Measurement results of the MBs start-up and speed control response of the DS LiRA without the inner stator. The speed reference is $n_\alpha^* = 60$ rpm.

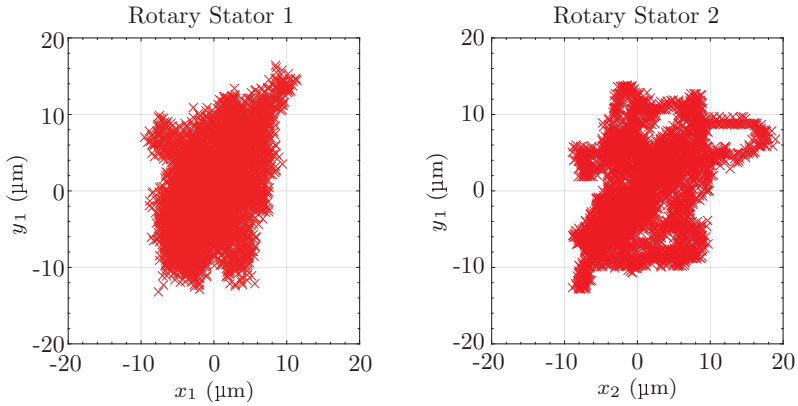


Fig. 11.8: Radial x- and y-coordinate distribution of the DS LiRA rotary stators during a steady-state rotation at $n_\alpha = 60$ rpm. The plotted data is taken from **Fig. 11.7** in the time interval $0.05 \text{ s} \leq t \leq 0.5 \text{ s}$. It can be seen that the radial position deviation stays below $20 \mu\text{m}$.

Tab. 11.1: Radial position statistical parameters at $n_\alpha = 60$ rpm from 9000 samples.

Symbol	Mean (μm)	Standard Deviation (μm)	Motion Range (μm)
x_1	$-0.41 \mu\text{m}$	$3.74 \mu\text{m}$	$\pm 700 \mu\text{m}$
y_1	$-0.21 \mu\text{m}$	$5.41 \mu\text{m}$	$\pm 700 \mu\text{m}$
x_2	$0.15 \mu\text{m}$	$5.01 \mu\text{m}$	$\pm 700 \mu\text{m}$
y_2	$-0.26 \mu\text{m}$	$5.87 \mu\text{m}$	$\pm 700 \mu\text{m}$

the radial positions show quite low standard deviation during the rotation, cf. **Tab. 11.1**.

11.5 Summary

This section verifies the operation of the DS LiRAs inverter and the inner and outer stators.

The current control of the DS LiRA inverter employs three cascaded control loops due to filter stages at each output, which makes its implementation challenging. The taken measurement results show the successful operation of the current control with a close loop control bandwidth of the actual DS LiRAs current of 2.78 kHz .

The position measurements for the rotary and linear stators are conducted on separate test benches, i.e. the mover is either moved linearly or rotated. The linear motion of the mover shows successful operation of the inner stator where a linear trajectory with 12 mm stroke and 147 ms rise time is tracked with a position error staying below 0.2 mm. The linear oscillatory motion is performed with 20 Hz and an amplitude of 5 mm.

Simultaneous rotation and levitation of the mover with the MBs is verified with measurements taken without the inner stator. For this purpose, two experiments are conducted: (1) rotary step response and (2) continuous rotation, where in both cases the mover is hovered with the MBs. In the first experiment, when performing the rotary step, the radial position is disturbed and an oscillation of the radial position is observed. The amplitude of this radial position oscillations stays below 60 μm . In the second experiment, the mover is rotated with 60 rpm, where the mover is started from resting on the touchdown bearing. During the rotation, the radial position of the mover stays within $\pm 20 \mu\text{m}$ from the center with a maximum standard deviation of 5.9 μm .

A further experimental analysis should focus on the simultaneous operation of the rotary and the linear stator of the DS LiRA, where the mover performs coupled rotary and linear motion.

12

Conclusion and Outlook

12.1 Summary

Linear or linear-rotary actuators¹ (LiRAs) are used in applications that require linear or coupled linear and rotary motion, such as pick-and-place robots in electronics or semiconductor industry, packaging or sorting in food or pharmaceutical industry, to mention a few. During their operation, they may be attached to a fixed assembly or to a moving robot arm, parallel kinematics or gantry system and moved in space to perform certain tasks. The rotor of the LiRAs is typically called *mover* and ideally it can simultaneously move linearly and rotate. More often, in price constrained applications LiRAs are built with mechanical bearings (steel ball bearings or plastic slider ring bearings), while in high end applications air bearings may be used.

Depending on the application requirements, the performance of the LiRA is limited by the mechanical or the air bearings. More specifically, in pick-and-place applications where the SMD components are getting smaller due to smaller PCB track distances and footprints, its placements becomes more challenging since these components are more brittle as a result of the size reduction. The only way to successfully mount such components is to control the tilting of the mover and therefore the placing nozzle, which is not possible with the conventional LiRA. Another example of limited performance is the limited precision of the conventional LiRA due to eventual thermal expansions that may occur in the overall mechanical assembly that holds the LiRA. For example, if the temperature of the parallel kinematics that hold and move the LiRA increases, the positioning precision is compromised. A radial control of the LiRA mover position would solve this issue, but this is not possible with

¹machines, motors

either mechanical or air bearings. Finally, not just the performance of the LiRA is limited by the conventional bearings, but also its usage in application areas that require extremely high purity or operation in vacuum.

Having in mind the limitations of LiRAs caused by conventional bearings, this thesis focuses on studying possibilities to integrate magnetic bearings (MBs) into LiRAs. Two different actuator topologies that feature MBs are studied in this work: (1) *a Linear Actuator with Magnetic Bearings* and (2) *a Double Stator Linear-Rotary Actuator*.

Linear Actuator with Magnetic Bearings

As a first step of an integration of MBs into the actuators, a coupling of the linear actuator and the MB is performed, resulting in a so called *magnetically levitated tubular actuator (MALTA)*. Since the MALTA originates from the conventional tubular linear actuator (TLA), its topology derivation is explained step-by-step, explaining the stator teeth arrangement from the flux density distribution requirement in the air gap. An extensive comparison of the winding realizations is conducted, where both combined and separated winding types are considered. The chosen winding realization results in a minimum number of individual phases and the maximum force-per-copper loss. Immediately after, the geometry of a MALTA prototype is optimized for the maximum possible drive and bearing force and linear (axial) acceleration, using a 3D-FEM model. The manufactured MALTA prototype is embedded into a customized test-bench where flux linkage and force measurements are performed. The measurement results are matching well with results obtained with the 3D-FEM models. Moreover, the measurement results verify the decoupling of the bearing and the drive force, necessary to control the MALTA.

Once the MALTA prototype is established, the inverter power supply and the position sensors are built. The inverter is suitable for supplying the 18 phases of the MALTA, since it has 24 individually controlled half-bridges. The inverter integrates a large DC-link capacitor (88 mF), such that it can stabilize the DC-link voltage during the braking of the MALTA mover (acceleration and deceleration of the mover results in motor and generator mode). Due to the high number of phase currents that need to be controlled, a large number of current measurements needs to be taken (18), resulting in a correspondingly high number of digital pins required from the control board ($18 \times 3 = 54$ pins assuming 3 pin single sided ADCs). Therefore, the Xilinx ZYNQ Z-7020 SoC is used, with 152 available digital pins. A position sensor

that provides the linear and the radial position information of the MALTA mover is built. The linear sensor is Hall-effect based and the influence of the mover's radial motion onto the sensor output due to PM field change is resolved by placing 4 Hall-effect elements distributed along the circumference. The radial position sensor is eddy-current based, where the achieved radial position resolution is $0.75 \mu\text{m}/\text{bit}$, out of 1600 bits that quantize the mover's radial play within the touchdown bearing limits.

Once all the hardware pieces are built, i.e. the MALTA electromechanical part, its position sensor and the inverter supply, a control system is developed and implemented. In the first attempt, the control system is developed based on the full MIMO dynamic model of the MALTA's mover, that assumes couplings between certain axes. The derivation of the model starts from the first principles, by writing the *Newton-Euler equations* of motion, which results in a nonlinear model that is in the next step linearized. The requirement for the position controller bandwidth is derived based on the position of the farthest unstable pole. The designed position controller is LQR type.

The experimental analysis of the MALTA shows successful levitation and linear position control. In an axial reference tracking experiment with a stroke of 10 mm, the axial force reaches a positive peak of 15 N during the acceleration and a negative peak of $\approx -14 \text{ N}$ during the deceleration of the mover. In this positioning maneuver the radial positions of the mover, supported by the integrated MBs, are staying within $\pm 20 \mu\text{m}$. To assess the quality of the MALTA's positioning, the standard deviation of a steady-state position is calculated based on 2000 measured position samples, which results in $\approx 0.5 \mu\text{m}$ for the radial positions and $15.4 \mu\text{m}$ for the linear (axial) position. This difference in positioning quality of the radial and linear directions originates from the position sensor noise and range (in general Hall-effect sensors are noisier than eddy-current ones). As a last experiment, a very important measurement that verifies the tilting capability of the MALTA mover is performed. Namely, a sinusoidal radial position reference with an amplitude of $200 \mu\text{m}$ is applied on one axial end, while the other axial end of the mover is kept in the center. This measurement proves mover tilting control in any circumferential angle possible.

Double Stator Linear-Rotary Actuator with Magnetic Bearings

The *double stator linear-rotary actuator (DS LiRA)* with MBs is built with outer rotary stators and an inner linear stator. The challenge of cooling the inner

stator by promoting axial heat flow is addressed. A solution where a copper pipe is integrated into the inner stator geometry is proposed. In order to build a DS LiRA prototype, its geometry is optimized first. Since the magnetic and the thermal aspects play an important role in this case (the inserted copper pipe reduces the iron volume, while increasing the thermal conductivity of the inner stator), an optimization procedure that couples magnetic 2D FEM models and analytic thermal models is performed. It is based on a grid search method, where 24 192 designs are evaluated. The grid search method does not require any cost function definition and it can calculate the performance over a wide range of the design space, i.e. it will not converge to the local performance maximum. The only drawback is increased computational effort, i.e. each point of the design space is evaluated. The final design is chosen based on the Pareto plots, generated from the optimization results. The 3D-CAD model of the DS LiRA and its parts is developed and the prototype manufactured. The outer stator windings are potted.

The inverter supply of the DS LiRA has 18 half-bridges with *LC* output filters. The inverter is supplied from 400 Vdc and should provide 10 A peak output current with the fundamental frequency in the range of 0 – 400 Hz. A reduced optimization of the filter inductor is performed and a design with 80 μ H and RM12 ferrite core is chosen, as it results in a minimum of the total (semiconductor + inductor) losses. The switching frequency is 140 kHz. The heatsink is designed based on a cooling system performance index of $CSPI = 12 \text{ W}/(\text{Kdm}^3)$.

The operation of the DS LiRA eddy-current position sensor is explained in detail. It consists of a HF injection coil and four pick-up coils, two per *x*, *y* axes. To maximize the sensitivity, the sensor geometry is optimized using Ansys Q3D software. The chosen sensor design operates at 3.2 MHz injection frequency and features a sensitivity of around 1.17 V/mm. The circumferential and linear position sensors are based on Hall-effect elements.

The control of the torque and the bearing forces is performed by the outer rotary stators, while the linear (axial) drive force is established by the inner linear stator. As the same windings in the rotary stator generate the torque and the bearing force, the phase currents contain two components, which are deduced from the measured phase currents by algebraic additions and subtractions, formally expressed with the matrix **W**. Because of the output filter, the current controller is designed with three cascaded control loops, with the most inner one controlling the filter inductor current, the middle one controlling the filter output capacitor voltage and the outer one controlling the actual DS LiRAs phase current. Each of the rotary stators

has two dedicated PID position controllers that control the DS LiRA's mover radial position in x - and y -direction. Therefore, in total the DS LiRA employs $4\times$ PID controllers for the radial position control and, $1\times$ PID controller for the torque control and $1\times$ PID controller for the linear force control.

The measurement result conducted on the DS LiRA inverter prototype show a current controller bandwidth of ~ 2.78 kHz. The commissioning and experimental analysis of the DS LiRA is conducted separately for the linear and rotary stators. The measurement results taken with the inner linear stator show successful linear reference tracking with a stroke of 12 mm and a rise time of 147 ms, where the tracking error stays below 0.2 mm. An oscillatory motion of the linear stator with 20 Hz and an amplitude of 5 mm is also successfully performed. The most important experiment is the operation of the MBs with the rotary stators. In this regard, two experiments are conducted, rotary position step response and continuous rotation, while hovering the mover with the MBs. During step response, a somewhat higher oscillation of the mover's radial position of $60\text{ }\mu\text{m}$ is observed. During the continuous rotation, the radial position of the mover stays within $20\text{ }\mu\text{m}$. Future work on the prototype should focus on the simultaneous operation of the inner linear and the outer rotary stators.

12.2 Outlook

In this thesis possible options for the realization of a linear and a linear-rotary actuator (LiRA) with magnetic bearings (MBs) are studied. Two of them are realized and verified in hardware. In order to bring the LiRA concept with MBs closer to a practical application and finally make it a successful product, the following aspects should be considered in further research:

- *Linear and circumferential position sensors:* The implemented sensors for the linear and the circumferential position measurement are Hall-effect based, where the field from the mover's PMs is measured and its position deduced. At the moment the sensors are placed at the axial end of the machine, where the field is distorted due to end effects. For future designs, it is suggested to test and place the Hall-effect elements "inside" the machine, where the end effects are not pronounced (especially in the case of the linear position sensing).

As shown in measurements where the standard deviation of the Hall-effect sensors is $\approx 15\text{ }\mu\text{m}$, high precision (e.g. around or below μm) cannot be achieved. Therefore, position encoders should be tested as

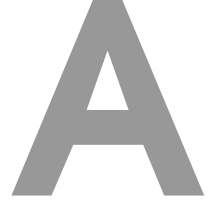
alternative. It should be noted that the encoders are very sensitive to radial displacements, which are allowed with MBs. Additional issues with encoders are their sensor grids that are always manufactured flat and not in tubular shape, which does not allow their placing onto the mover. For future high precision LiRAs with MBs, it is suggested to develop sensor grids that could be used for tubular shaped surfaces and potentially feature higher tolerance on radial position displacements. In this regard, engraving of the encoder grid directly onto the MB LiRAs mover could be an interesting solution.

- ▶ *Radial position sensing through a conductive surface:* In high purity applications, typically the stator and the mover of the LiRA are encapsulated in a stainless steel enclosure, to allow high purity hygienic designs. Consequently, the radial eddy-current sensor must be capable of sensing the movers position through a conductive stainless steel wall of the stator. For these applications, such sensor should be developed.
- ▶ *Sustainability of severe radial accelerations:* In pick-and-place application, MBs of the LiRA would be exposed to very high radial accelerations (up to $30g$), that may disturb its operation. The consequences could be instability of the MBs and increased losses due to high currents needed to compensate for the radial inertial forces. These aspects should be analyzed and the LiRA with MBs should be tested in parallel kinematics. The following measures could help to increase the robustness and reduce eventual high losses: (1) As the trajectory of the parallel kinematics is known, the resulting radial inertial force can be estimated and provided as a feed-forwarded signal to the position controller, which should increase the control robustness; (2) When exposed to high radial accelerations, in order to reduce the required MB forces, the mover could be displaced from its center position such that the passive radial pull force opposes the inertial force and compensates it, partially or entirely. Eventually, in such cases resting of the mover on the touchdown bearings could be allowed.
- ▶ *Gravity compensation:* In applications where the LiRA operates in vertical position, it is important to provide “gravity compensation” and to ensure that the mover does not fall out in case power supply interruptions. This caution measure is necessary to avoid eventual injury and/or damage of surrounding equipment. In case of the LiRA with MBs, this measure could eventually be realized by having the touchdown bearing surface made out of a material with higher friction, where the radial

pull force of the mover would be able to hold it, i.e. prevents it from falling out. Such approach is not possible with conventional LiRAs.

- *Cost analysis*: Finally, the LiRA with MBs will become a successful product in some applications once it is cost competitive with conventional solutions. Therefore, for a desired application, a cost analysis should be performed to predict when in the future the MB LiRA might become cheaper than a conventional system. For the analyzed applications, the LiRA with MBs has a good chance to be cost competitive, as it allows savings in the design of parallel kinematics, lower maintenance and longer lifetime.

Appendices



MALTA SISO Position Controller

The MALTA radial and axial positions of the mover are controlled by the magnetic forces. In order to actively control these magnetic forces, understanding of the MALTA mover dynamics is necessary, which is why in **Chapter 6** a mechanical dynamic model is derived that finally resulted in a coupled MIMO system. Therefore, in the same chapter, an LQG MIMO controller is designed, which is a straightforward task if a linearized state-space model is provided. In a later **Chapter 7** the controller is implemented and its operation is verified with measurements.

In this Appendix, a rather simplified approach for controller design is taken, where each direction (e.g. for radial x or y) is treated as independent, i.e. mechanically decoupled, and a dedicated SISO PID controller is designed for it. This approach is verified by implementing the controller and providing measurement results.

A.1 MALTA Control Algorithm

The MALTA control block diagram is shown in **Fig. A.1**. A cascaded control structure can be recognized, with inner (faster) current control loop and outer (slower) position control loop. For each control variable, an individual single-input single-output (SISO) controller is used. Therefore, in total 8 current controllers (4 per module) and 5 position controllers (4 for radial positions and 1 for the axial position) are needed.

The outer position controllers are realized as Proportional-Integral-Derivative (PID) controllers which translate the position error $\vec{r}^* - \vec{r}$ at the controller input into a corresponding force \vec{F}_c at the controller output. In particular, the radial positions $x^{(1,2)}, y^{(1,2)}$ sensed at each module are con-

trolled with the corresponding bearing forces $F_x^{(1,2)}, F_y^{(1,2)}$ generated by the same module. It should be pointed out that a derivative component is needed in order to stabilize the mechanical system, as it shows second order double integrator dynamics. Furthermore, this is implemented with a relocation on the feedback path, i.e. it is computed directly from the output \vec{r} rather than the control error $\vec{r}^* - \vec{r}$. This allows suppressing a zero in the resulting closed loop transfer function, as can be verified analytically, with the advantage of reducing overshoot and ringing in the response.

Based on the bearing and thrust force constants (cf. **Chapter 3**)

$$K_B = \frac{9}{4} \chi_{pm,M}, \quad K_L = \frac{9\pi}{\tau_{pp}} \hat{\Psi}_M, \quad (\text{A.1})$$

the force commands are then converted into the corresponding desired dq -current commands $\mathbf{I}_{dq}^{*(1,2)}$, which are the setpoints for the inner current controllers. The advantage of the complex space vector model of the MALTA is now apparent, as it allows controlling a highly sophisticated multi-phase machine with established control techniques. In fact, each transformed dq -current component evolves then like a first order RL network, which can be regulated with a simple Proportional-Integral (PI) control. Moreover, with a minimal number of only four controlled quantities, it is possible at any point in time to assign all of the nine phase voltages.

The measured axial position z is used to compute the linear electrical angle for the dq -transformation. Additionally, it is used for the feed-forward action $\vec{F}_{ff}(z)$ by the position controller, which compensates for the gravity and other detent forces such as cogging force and the radial pull force. The function $\vec{F}_{ff}(z)$ is experimentally recorded using the position controller reference signal in steady-state.

Due to the cascaded control structure, the bandwidth specification for the current controllers can be directly derived from the desired performances of the outer position control loop. The requirements for radial and axial position control are slightly different and are discussed separately in the following.

The needed dynamics of the radial position are determined for the $x^{(1,2)}$ - and $y^{(1,2)}$ -directions and are the same for both modules (*Module 1* and *Module 2*). Therefore, in the following the module notation is omitted and only x and y are used.

Furthermore, it is assumed that the radial subsystems of *Module 1* and *Module 2* are totally independent and each module is suspending one half of the rotor mass. If it is further assumed that the x - and y -direction are

completely decoupled, the accelerations are obtained as

$$a_x = \frac{2}{m} F_x, \quad a_y = \frac{2}{m} F_y, \quad (\text{A.2})$$

where $a_x = d^2x/dt^2$ and $a_y = d^2y/dt^2$ are the radial accelerations and m is the rotor mass. In (A.2) half the mass is accelerated as each of the modules lifts only a half of the rotor. In the Laplace domain, the open loop transfer function of the plant representing the radial positions is equal to

$$G_{OL}(s) = \frac{\{x(s), y(s)\}}{F_{\{x,y\}}(s)} = \frac{2}{m s^2}, \quad (\text{A.3})$$

where $s = \mathcal{L}(d/dt)$ is the Laplace transform of the time derivative. The desired radial position is zero at all times, i.e. the rotor is located in the center of the stator. Hence, the main specification for x and y can be expressed in terms of rejection of the external mechanical disturbing forces (gravity force and the radial pull force) that deviate the rotor from its center position. The most relevant are the radial pull forces $F_{x,pull}$, $F_{y,pull}$ between the rotor PMs and the stator. These destabilizing radial pull forces are measured to be linearly proportional within the possible mechanical air gap to the radial displacement (small signal) according to the radial pull constant K_{pull}

$$F_{pull,x} = x K_{pull}, \quad F_{pull,y} = y K_{pull}, \quad (\text{A.4})$$

and represent an input disturbance for the radial subsystems (A.2). The value of the radial pull constant for the MALTA is measured to be $K_{pull} = 8330 \text{ N/m}$ [35].

In a classic feedback control, the closed loop bandwidth requirement of the control system may be imposed by the disturbances as [125]

$$\omega_{BW} > \omega_D, \quad \omega_D \text{ such that } \|G_D^{pu}(j\omega_D)\| = 1 \quad (\text{A.5})$$

where ω_{BW} is the required closed loop bandwidth and G_D^{pu} is the open loop disturbance transfer function in per unit (unit-magnitude scaled). Since the disturbance is the radial pull force, the open loop disturbance transfer function is equal to the radial position plant (A.3), i.e. $G_D = G_{OL}$. As the requirement (A.5) is applied in a per unit system, the transfer function G_D should be normalized. For example, for the radial x -direction the G_D is normalized using the maximum expected displacements \hat{x} and the pull force $\hat{F}_{pull,x}$ as

$$G_D^{pu}(s) = \frac{x(s)/\hat{x}}{F_x(s)/\hat{F}_x} = \frac{2K_{pull}}{m s^2}, \quad (\text{A.6})$$

Tab. A.1: MALTA motor parameters.

Symbol	Quantity	Value
Electrical		
R	Phase winding resistance	2.2 Ω
L	Phase winding inductance	2.0 mH
Mechanical		
m	Mover mass	0.360 kg
Force Constants		
K_L	Drive constant per module	5.2 N/A
K_B	Bearing constant per module	5.2 N/A
K_{pull}	Radial pull constant per module	8330 N/m

where $\hat{F}_x = \hat{x} K_{\text{pull}}$. Using (A.5), the angular frequency ω_D is calculated as $\omega_D = \sqrt{2K_{\text{pull}}/m}$. Therefore, the closed loop bandwidth of the radial position controller should be larger than

$$\omega_{\text{BW}} > \sqrt{\frac{2 K_{\text{pull}}}{m}} \approx 220 \text{ rad/s}, \quad (\text{A.7})$$

where the values for K_{pull} and m are given in **Tab. A.1**. The same applies analogously for the radial subsystem in y -direction.

In order to guarantee the appropriate dynamic decoupling between the inner and outer control loops, the current control bandwidth has to be at least 5 times higher than the outer position controller bandwidth ω_{BW} , i.e. at least 1100 rad/s.

The axial position z evolves similarly according to the axial subsystem dynamics $a_z = F_z/m$, where $a_z = d^2z/dt^2$ is the axial acceleration and m is the mass of the MALTA rotor. The specifications for z depend on the desired dynamics and are usually specified in the time domain for a step response, mainly in terms of the desired rise time t_r . In order to tune the inner current control loop, the closed loop bandwidth should be given, which can be related to the rise time as $f_{\text{BW}} t_r = 1/3$ [124], where $f_{\text{BW}} = \omega_{\text{BW}}/2\pi$. Typical rise times of tubular linear motors with similar size are in the range of $t_r = 20$ ms [126]. Therefore, to achieve this rise time, the closed loop bandwidth of the axial position controller should be larger than ≈ 110 rad/s, which is half of the requirement for the radial position controller that has to suppress the radial pull disturbances (cf. (A.7)).

Finally, in order to achieve a proper dynamic decoupling from the position controller, the current controllers are tuned to a bandwidth of 3000 rad/s, which gives some margin to allow for faster position controller designs and

is useful to suppress radial and axial deviations even under stronger external disturbances. In fact, for this purpose, the final bandwidth of the radial position controllers is chosen to be around two times larger than the minimum required bandwidth ω_{BW} in (A.7), i.e. $\omega_{BW} \approx 400$ rad/s.

The corresponding position and current control PID gains are listed in **Tab. A.2**.

Tab. A.2: Position and current controller gains.

Variable	K_P	K_I	K_D
i_{0q}, i_{bd}	8.01 V/A	8.45 kV/(A s)	-
i_{0d}, i_{bq}	8.01 V/A	8.45 kV/(A s)	-
$x^{(1)}, x^{(2)}$	39 kN/m	1.8 MN/(m s)	150 N s/m
$y^{(1)}, y^{(2)}$	39 kN/m	1.8 MN/(m s)	150 N s/m
z	2.44 kN/m	42.87 kN/(m s)	35.07 N s/m

A.2 Measurements and Results

In this section the implemented control algorithm is verified with experimental measurements. All the signals are measured with internal sensors, collected by the firmware and transmitted to a user interface after the experiment is concluded. The following experiments are performed: (1) the system is started and stable levitation of the rotor is achieved (cf. **Fig. A.2**); (2) linear motor operation is performed by giving a sinusoidal reference along the axial direction (cf. **Fig. A.4**). The measurements show stable levitation and successful decoupling of the bearing and thrust force control.

A.3 Soft Start-Up

Initially, the MALTA rotor is located in its rest position on the touch-down bearing ($x_0^{(1)} = 0.1$ mm, $y_0^{(1)} = -0.7$ mm, $z_0 = -1$ mm). In order to avoid abrupt controller responses and provide a smooth lift up instead, the reference is shaped to guide the rotor from its start position to the center of the machine ($x^{(1)*} = 0$, $y^{(1)*} = 0$) as shown in **Fig. A.2(c)**. The selected reference is a filtered step with a cutoff frequency of ≈ 67 rad/s, i.e. the step response of the first order system

$$R(s) = \frac{1}{0.015s + 1} \quad (\text{A.8})$$

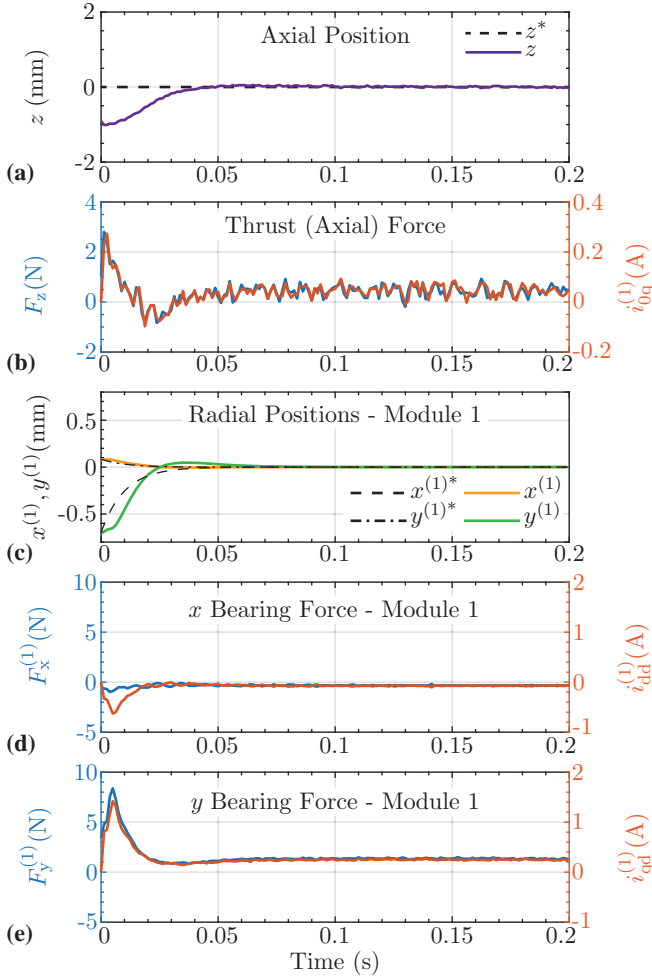


Fig. A.2: Measurements of the MALTA start-up experiment where the rotor in its initial position touches the touch down bearing ($x_0^{(1)} = 0.1$ mm, $y_0^{(1)} = -0.7$ mm and $z_0 = -1$ mm) and lifts up to the reference value ($x^{(1)*} = 0$, $y^{(1)*} = 0$ and $z^* = 0$). Radial positions of the first module ($x^{(1)}$, $y^{(1)}$) and the axial position (z) are shown. The shown force components are denoted in the control block diagram shown in **Fig. A.1**. The current $dq0$ -components responsible for the respective force components are labeled on the right side of the plots.

discretized at the sampling time $T_s = 50 \mu\text{s}$, which reaches the final value in 0.1 s. This is then appropriately scaled to reach the zero position starting from the initial $x_0^{(1)}$ and $y_0^{(1)}$ positions as

$$x^{(1)*} = x_0^{(1)} (1 - r(t)), \quad (\text{A.9})$$

$$y^{(1)*} = y_0^{(1)} (1 - r(t)), \quad (\text{A.10})$$

where $r(t) = \mathcal{L}^{-1}(R(s)/s)$ is the step response of (A.8) and \mathcal{L}^{-1} the inverse Laplace transform operator. The positions $x_0^{(1)}$ and $y_0^{(1)}$ are measured during an offset calibration routine executed once before the regular machine operation is started.

In order to overcome pull and gravity forces $F_{\text{pull},y}^{(1)}$ and $F_g = g m/2 = 3.53 \text{ N}$, with $g = 9.8 \text{ m/s}^2$ as acceleration of gravity, the integral part of the controller starts increasing the commanded $F_y^{(1)}$ (cf. **Fig. A.2(e)**). As soon as the balance condition

$$F_y^{(1)} = F_{\text{pull},y}^{(1)} + F_g \approx 8.3 \text{ N} \quad (\text{A.11})$$

is reached, the rotor lifts up. This happens at 0.005 s, when the current component $i_{\text{qd}}^{(1)}$ reaches the value 1.42 A, producing the bearing force $F_y^{(1)} = K_B i_{\text{qd}}^{(1)} \approx 8.3 \text{ N}$, which verifies the derived bearing constant.

The rotor then approaches the center of the machine with small overshoots (below 10 %) both in x - and y -directions and finally reaches the steady state at around 0.06 s, with an error which remains confined within $\pm 1 \mu\text{m}$.

Simultaneously, also the axial position z reaches the zero setpoint, with a steady state error of $\pm 20 \mu\text{m}$. The larger deviation in axial direction comes from the higher amount of axial sensor noise, which is due to the chosen Hall-effect sensing method.

Moreover, in **Fig. A.2(b)** one can observe that F_z and the corresponding current component $i_{0q}^{(1)}$ show a non-zero average value of $\approx 0.5 \text{ N}$ and $\approx 0.05 \text{ A}$ respectively, which are needed in order to compensate the cogging force and to maintain the rotor in the desired axial position. It should be noted that the plotted F_z is the overall thrust force, i.e. the sum of the individual forces produced by the two modules, whereas $i_{0q}^{(1)}$ is the corresponding current component only of the first module.

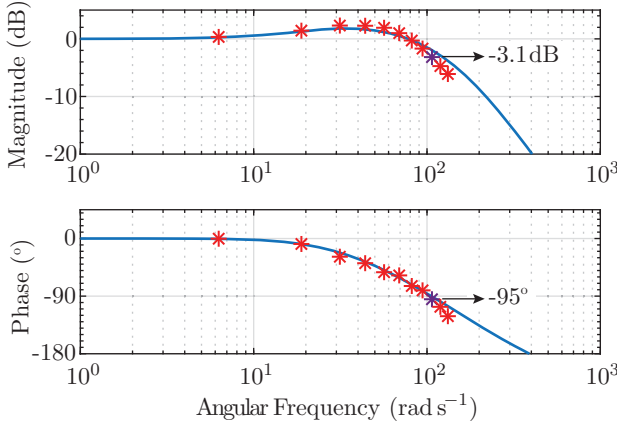


Fig. A.3: Experimental verification of the Bode magnitude and phase diagrams for the closed loop axial sub-plant of MALTA. The solid blue line corresponds to the predicted, analytically derived closed loop transfer function, whereas the red stars represent experimental measurements at the corresponding frequencies $f_z = \{1, 3, 5, \dots, 19, 21\}$ Hz, i.e. regular intervals of 2 Hz from 1 up to 21 Hz. The 17 Hz experiment is shown in the time domain in **Fig. A.4** (the measurement highlighted in violet).

A.4 Linear Motor Operation

The linear motor operation is tested and verified with a periodic sinusoidal axial movement, where the mass of the mover serves as a load. This kind of experiment is well justified for applications such as pick-and-place robots in semiconductor/electronics industry. In such cases, the mass of the moved and placed components is much smaller than the mass of the mover. In **Fig. A.3**, the Bode magnitude and phase diagrams for the closed loop axial sub-plant are shown. These are derived analytically from the simplified axial model and by using the PID gains of **Tab. A.2**. Furthermore, they are experimentally validated with axial position measurements for different frequencies of the sinusoidal reference, and the computed magnitudes and phases are reported in the diagram. In particular, f_z is chosen at regular intervals of 2 Hz from 1 up to 21 Hz. As can be observed, the predicted and measured frequency responses are in good agreement and the mismatches appearing after 100 rad/s can be justified with the neglected eddy-current braking effects and other nonlinearities.

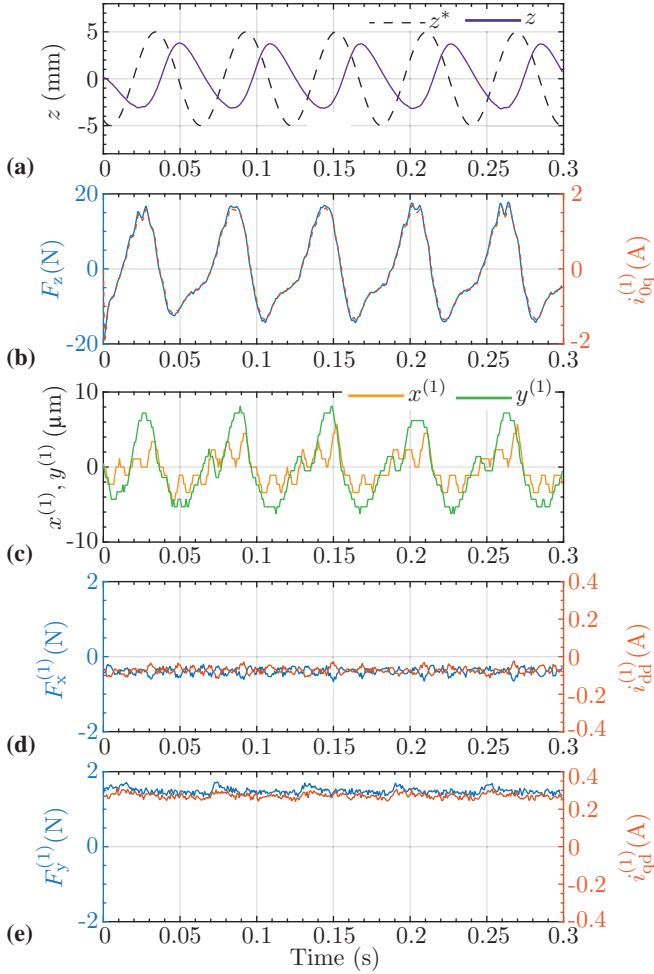


Fig. A.4: Measurements of the MALTA linear motor operation, where a sinusoidal reference for the axial position is given, $z^* = 5 \text{ mm} \cos(2\pi 17 \text{ Hz})$. The response is attenuated by a factor of 0.707 (-3 dB) as the closed loop axial position controller bandwidth is tuned to 17 Hz. The radial position is slightly disturbed during the axial movements of the rotor and stays between $\pm 8 \mu\text{m}$. The radial forces are nonzero such that radial pull onto the rotor is compensated during the linear motor operation.

The controlled axial system is capable of tracking sinusoidal references up to 10 rad/s, whereas faster signals would experience some amplification, which is however below 2 dB. After around 100 rad/s, the gain of the system starts rolling off with a -40 dB/dec slope. The phase shift between reference and measured signals reaches -90° for frequencies at around 100 rad/s and keeps decreasing towards -180° .

Therefore, the frequency of $f_z = 17$ Hz (≈ 107 rad/s) for motor operation is chosen to verify the bandwidth of the axial control system. In fact, in **Fig. A.4(a)** it can be observed that the amplitude of the measured axial position signal is reduced by -3 dB with respect to the original $\Delta z_{pp}^* = 10$ mm peak-to-peak amplitude, resulting in $\Delta z_{pp} = 7$ mm. Additionally, as also expected a phase shift of $\phi \approx 95^\circ$ is observed (cf. **Fig. A.4(a)**).

The commanded F_z in **Fig. A.4(b)** oscillates accordingly with $\Delta F_{z,pp} = 29.26$ N to provide the required acceleration.

Meanwhile, the radial positions oscillate slightly around their steady state position, but remain limited within $\pm 8 \mu\text{m}$ error thanks to the fast radial control tuning.

The corresponding bearing forces keep the rotor levitated while reacting against the disturbances from the fast axial motion. In particular, the average value of $F_y^{(1)}$ is 1.6 N, which corresponds to the force required to balance the gravity force F_g . Concerning $F_x^{(1)}$, an average value of -0.37 N instead of the ideal value 0 can be observed. This is due to the radial pull force created by manufacturing tolerances of the real prototype.

A.5 Summary

Two different measurement experiments that verify the SISO position controller are shown, start-up and linear motor operation. In the start-up experiment, the rotor of the MALTA is successfully lifted from rest to its center position. In the linear motor operation, the MALTA axial position is varied with a sinusoidal reference with a stroke of 10 mm and a mechanical frequency of 17 Hz. During this operation mode, the radial position deviation stayed below $\pm 8 \mu\text{m}$. These results verify the proposed models and the position controller design.

B

Double Stator Machine with a Single Set of PMs

The double stator linear-rotary actuator (DS LiRA) considered and built-in this thesis is shown in **Chapter 8**. Its mover consists of the back iron and the PMs that interact with the linear stator from the inner side of the back iron and the PMs that interact with the rotary stator from the outer side of the back iron. Therefore, the back iron of the DS LiRA is sandwiched between the two sets of the PMs, linear and rotary.

In this Appendix, a DS LiRA with a single set of PMs, that can suffice the operation of the linear and the rotary stator, without back iron, is considered.

B.1 Introduction

The advantage of the LiRA with radially stacked stators over that with axially displaced stators is its lower axial length. However, the requirement of a back iron results in a high mass and moment of inertia (MoM) of the conventional mover (CM). As a result, the dynamics (linear and circumferential accelerations) of the DS LiRA with CM are limited, which restricts its usage to applications with high force and torque demands rather than those requiring high dynamics.

The DS LiRA with CM designed in [14], which is similar to the one shown in **Fig. B.1**, is used as an example in the following considerations. Based on the mass densities of the employed steel and rare earth PMs, an average mass density of the CM of $7 \times 10^3 \text{ kg/m}^3$ is assumed, resulting in an overall CM mass of $\approx 11.7 \text{ kg}$. Given the rated force of the actuator of 650 N , the achievable axial acceleration is estimated to be $\approx 55 \text{ m/s}^2$, where bearing friction has

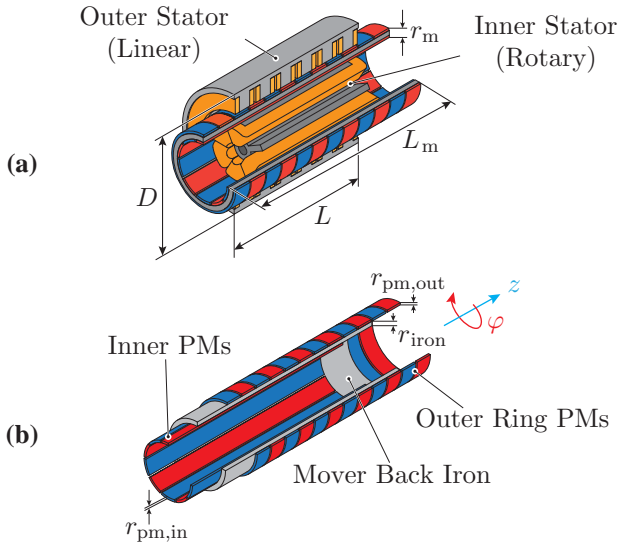


Fig. B.1: (a) DS LiRA with inner rotary and outer linear actuators, where r_m denotes the mover thickness. (b) CM of the DS LiRA with two sets of PMs. The radial thickness of the mover is $r_m = r_{pm,in} + r_{iron} + r_{pm,out}$.

been neglected. This acceleration is about one third of that achieved by LiRAs used in applications requiring high dynamics. A LiRA which achieves a maximum linear acceleration of 150 m/s^2 is presented in [39]. Aside from this, manufacturing of a DS LiRA with CM is challenging, as PMs have to be placed and fixed on both sides of the CM back iron.

In order to increase the dynamics and resolve the issues related to manufacturing of the DS LiRA with CM, two ironless mover layouts with a single set of PMs are proposed in this chapter.

B.2 Proposed Double Stator Actuator

In this section, a DS LiRA with two different ironless mover layouts incorporating only a single set of PMs is proposed to overcome the drawbacks of the DS LiRA with CM (see **Section B.1**). The arrangement of PMs in the proposed mover is chosen such that North and South poles alternate in the axial and circumferential direction. Two possible layouts that fulfill this requirement are shown in **Fig. B.2**. Based on an unfolded view of the mover, the PM pole sizes in axial and circumferential direction can be identified and are denoted by τ_z and τ_ϕ , respectively. Subsequently, the proposed layouts are referred to as DM and SM, for the arrangements featuring diamond-shaped PMs (see **Fig. B.2(a)**) and square-shaped PMs (see **Fig. B.2(b)**), respectively.

Figure B.3 shows the radial component of the PM flux density B_r at the inner and outer side of the mover. The alternation of the PM poles in the axial and circumferential direction is clearly visible for the CM (see **Fig. B.3(a)**). For the DM and SM, the PM pole alternation is interrupted compared to the CM. Nevertheless, a higher magnitude of the PM flux density is possible for the DM and SM for the given mover thickness because of thicker PMs. While the magnitude of B_r for the CM is $\approx 0.38 \text{ T}$, $\hat{B}_r \approx 0.52 \text{ T}$ is reached for the DM and SM.

The unfolded version of the PM arrangement shown in **Fig. B.2** is used in planar actuator systems. For example, a synchronous PM planar motor with a similar PM arrangement is shown in [127]. A magnetically levitated moving-magnet planar actuator with single layer windings in the stator is proposed in [87]. A planar actuator with multilayer windings in the stator and a PM arrangement in the mover that is similar to the unfolded DM (see **Fig. B.2(b)**) is analyzed and optimized in [128].

A LiRA with a PM arrangement as shown in **Fig. B.2(b)** and a single stator is proposed in [129]. The stator of this LiRA is slotted with double layer windings, i.e. linear and rotary windings, that are radially displaced.

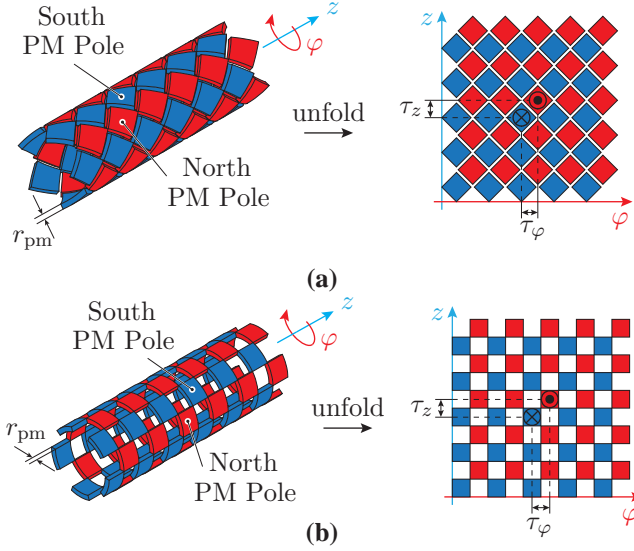


Fig. B.2: Proposed ironless mover layouts for the DS LiRA with a single set of PMs. Mover layout with (a) diamond-shaped PMs referred to as DM, and (b) square-shaped PMs referred to as SM. The sizes of the axial and circumferential poles are denoted by τ_z and τ_ϕ , respectively. The mover thickness is equal to the PM thickness, $r_m = r_{pm}$.

Tab. B.1: Parameters of the simulated actuators shown in Fig. B.3.

Parameter (Symbol)	Values		
PM remanent flux density	1.3 T		
Iron relative permeability	500		
	CM	DM	SM
Inner PM thickness ($r_{pm,in}$)	1 mm	-	-
Outer PM thickness ($r_{pm,out}$)	1 mm	-	-
Back iron thickness (r_{iron})	2 mm	-	-
PM thickness (r_{pm})	-	4 mm	4 mm
Mover thickness (r_m)	4 mm	4 mm	4 mm
Inner mover radius	11.5 mm	11.5 mm	11.5 mm
Outer mover radius	15.5 mm	15.5 mm	15.5 mm
Circumferential pole size (τ_ϕ)	36°	36°	36°
Axial pole size (τ_z)	7.5 mm	7.5 mm	7.5 mm

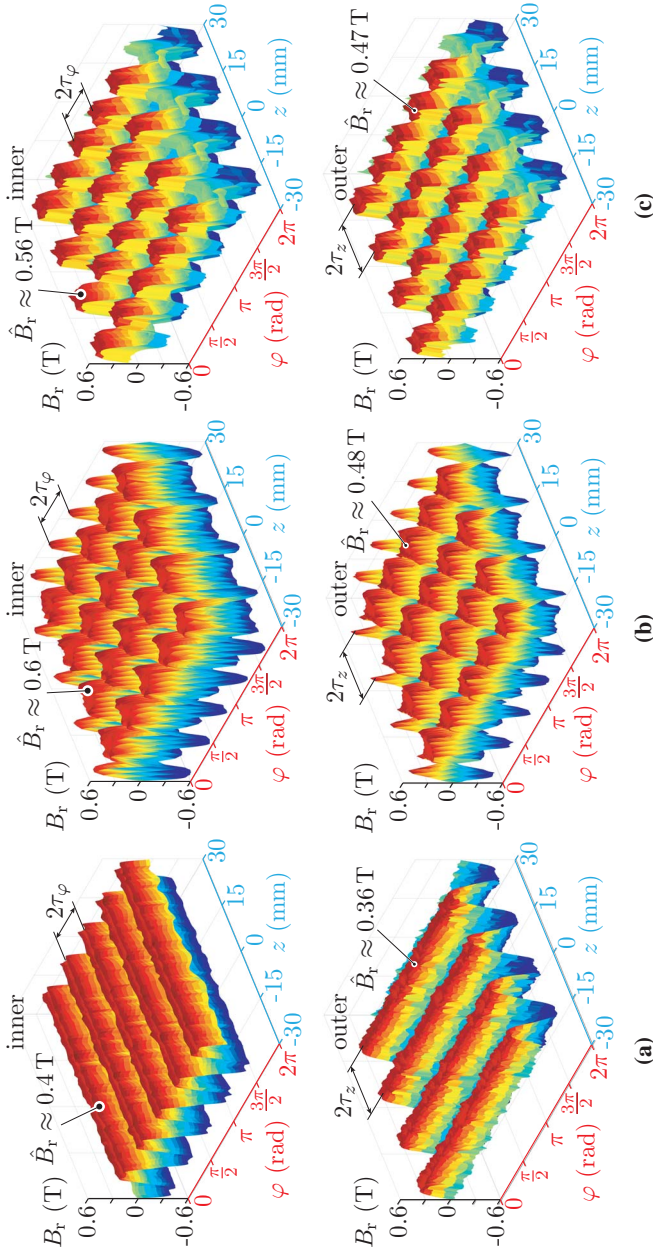


Fig. B.3: FEM simulation of the radial flux density component B_r at the inner and outer side of the mover: **(a)** CM, **(b)** DM, and **(c)** SM. The inner and outer radii for all movers are 11.5 mm and 15.5 mm, respectively. The radial positions for which B_r is shown are 11.15 mm for the inner side and 15.85 mm for the outer side. The rest of the parameters are given in **Tab. B.1**. Pole pair sizes in axial and circumferential directions are denoted by τ_z and τ_φ , respectively.

The manufacturing effort of such a stator is high as the stator core is slotted both in circumferential and axial direction. Another LiRA, again with PM arrangements as shown in **Fig. B.2**, is proposed in [130]. Linear and rotary actuation in this LiRA are achieved by two separated stators, which are dislocated circumferentially. This results in several drawbacks of the system, such as the requirement for a back iron in the mover and the existence of a radial magnetic pull originating from the asymmetrical LiRA geometry in the circumferential direction. In the proposed DS LiRA, no radial magnetic pull exists, since the radial dislocation of the stators results in a symmetrical geometry.

B.3 Basic Characteristics of the Conventional and Proposed Double Stator Actuators

In this section, a comparative analysis of the DS LiRA with CM and the proposed DS LiRAs with a DM and SM is provided. The back iron in the CM accounts for about half of the mover thickness (see the proposed designs in [16]). If the mover contains only PMs, $r_m = r_{pm,in} + r_{pm,out}$ holds. In order to obtain a fair comparison, only PM material is assumed in the movers. Therefore, the back iron of the CM is replaced by PM material and the mover thickness is shared equally between the inner and outer PMs, $r_{pm,in} = r_{pm,out}$ (see **Fig. B.4**), resulting in a *theoretical* idealized CM (iCM). In the DM and the SM, no mechanical support is assumed, which also results in *theoretical* idealized DM and SM (iDM and iSM). It should be noted that such movers cannot be manufactured and therefore are used only for first step comparative purposes in this section.

The comparison is carried out considering rare-earth PMs. The parameters of the compared LiRAs are provided in **Tab. B.2**. The available space in radial direction is shared equally between the inner (rotary) and outer (linear) actuator windings. The force and torque of each analyzed LiRA are determined using magnetostatic FEM models. The electrical loading is chosen such that 15 W of copper losses are dissipated in each of the actuators. This assumed value for the electrical loading stems from the simplified lumped-parameter thermal model that was established for tubular actuators of similar size in [16]. While the actual admissible electrical loading depends on the application and available cooling of the LiRA, the assumed constant electric loading provides a good basis for relative comparison.

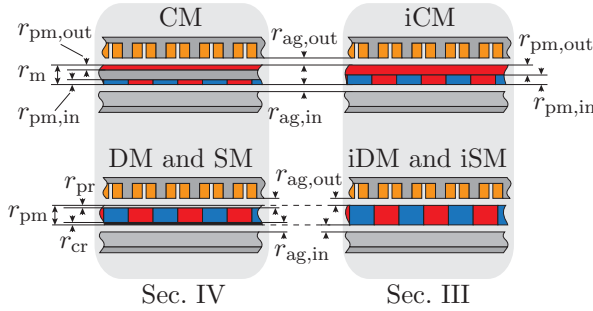


Fig. B.4: Summary of the analysis scenarios. Initial analysis is conducted in **Section B.3**, in which the movers are solely made of PM material. Therefore, for CM there is no back-iron and for DM and SM there is no mechanical support. In **Section B.4**, DS LiRAs with physically manufacturable movers are further analyzed and compared. Inner and outer magnetic air gaps are denoted as $r_{ag,in}$ and $r_{ag,out}$, respectively. Inner and outer mechanical air gaps are equal to $r_{ag,in} - r_{cr}$ and $r_{ag,out} - r_{pr}$, respectively, where r_{cr} and r_{pr} are carbon rod and PM protection thicknesses (see **Section B.4**).

Tab. B.2: Parameters of the DS LiRAs for which the performance is shown in **Fig. B.5**.

Parameter (Symbol)	Values		
PM remanent flux density	1.3 T		
Iron relative permeability	500		
PM mass density	7550 kg/m ³		
Iron mass density	7870 kg/m ³		
Stator length (L)	60 mm		
Outer stator diameter (D)	50 mm		
Number of poles (N_ϕ)	10		
Number of poles (N_z)	8		
Pole size (τ_ϕ)	36°		
Pole size (τ_z)	7.5 mm		
Inner and outer air gaps	0.7 mm		
Stator back iron thickness	2 mm		
	iCM	iDM	iSM
Inner PM thickness ($r_{pm,in}$)	1-2 mm	-	-
Outer PM thickness ($r_{pm,out}$)	1-2 mm	-	-
Mover back iron (r_{iron})	o	-	-
PM thickness (r_{pm})	-	1-4 mm	1-4 mm
Mover thickness (r_m)	2-4 mm	1-4 mm	1-4 mm

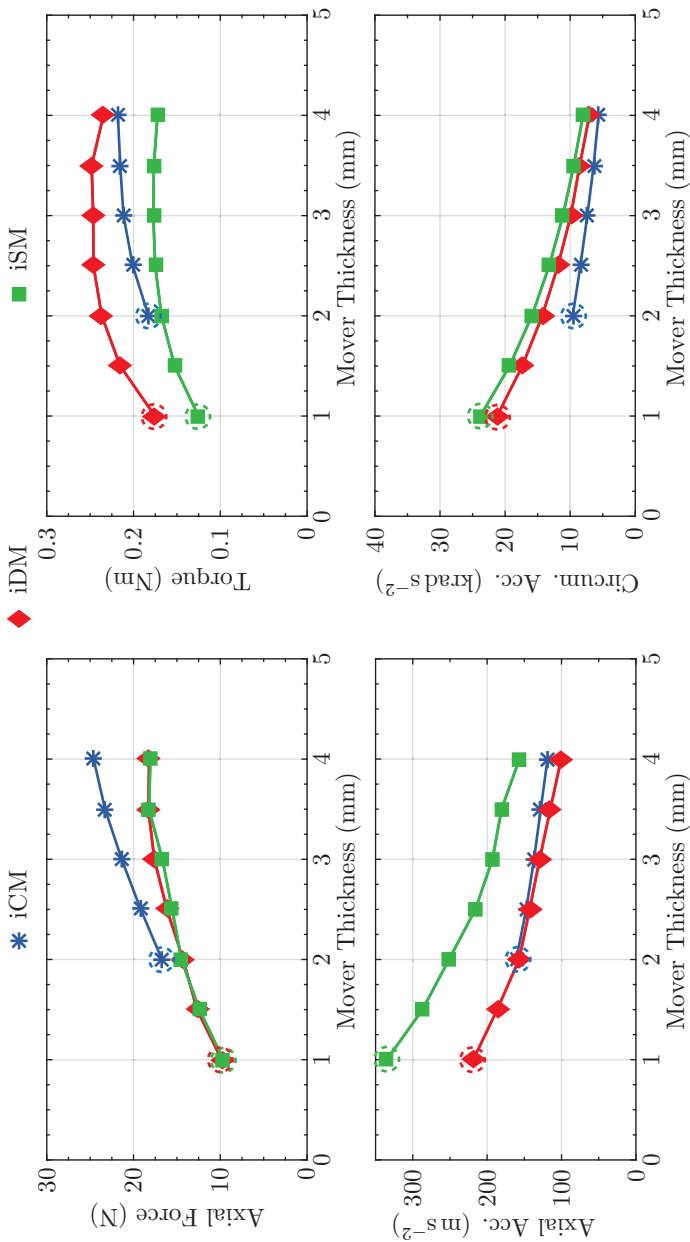


Fig. B.5: Comparison of the DS LiRAs with three different mover layouts: iCM (blue), iDM (red) and iSM (green). Axial and circumferential accelerations are calculated using only the mass and moment of inertia of the mover. Material and geometry properties are given in **Tab. B.2**. The results are obtained using FEM models in which winding copper losses are fixed to 15 W for all designs. Circled simulation points are relatively compared in **Fig. B.6**.

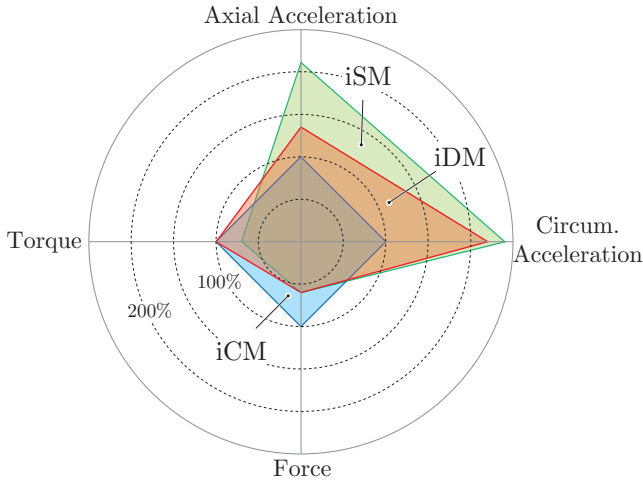


Fig. B.6: Relative comparison of the designs from **Fig. B.5** with a PM thickness of 1 mm. The mover thickness is 2 mm for the iCM and 1 mm for the iDM and iSM. Compared designs are encircled in **Fig. B.5**.

A comparison of the axial force and acceleration is shown in **Fig. B.5** on the left hand side, while a comparison of the torque and circumferential accelerations is shown in **Fig. B.5** on the right hand side. The analysis has been carried out for different mover thicknesses, where the FEM simulation points are marked by blue asterisks (*) for the DS LiRA with iCM, red rhomboids (◆) for the DS LiRA with iDM and green squares (■) for the DS LiRA with iSM. The minimum PM thickness has been set to 1 mm, which results in a minimum mover thickness of the iCM of 2 mm, since it has two sets of PMs displaced radially. Contrarily, the minimum thickness of the iDM and iSM is 1 mm.

Even though the axial force of the DS LiRA with iCM is the highest, the iSM reaches the highest axial acceleration. This is due to the PM volume in the iSM being almost cut in half compared to the iCM or iDM. A similar trend can be observed for the circumferential LiRA properties. The circumferential acceleration of the LiRAs with the iDM and iSM is similar, while the iDM features a higher torque.

A relative comparison of the achievable torque, force, and accelerations, for the same copper losses in the actuator windings, is shown in **Fig. B.6**. Compared to the iCM, the proposed mover layouts (see **Fig. B.2**) can achieve

higher axial and circumferential accelerations for the same amount of copper losses.

B.4 Manufacturing of the Proposed Double Stator Actuator

Manufacturing constraints and their influence on the design and the performance of the actuator are studied in detail in this section. The proposed mover concepts were shown in **Fig. B.2** without any mechanical support. The suggested manufacturing steps for the DM are outlined in **Fig. B.7**. The complete mover consists of three parts: a carbon rod, a 3D-printed fixture for the PMs, and the PMs. The ease of manufacturing of such an arrangement, compared to the CM with two sets of PMs, has several advantages. The PMs for the CM have to be fixed to both sides of the back iron (see **Fig. B.1(b)**), which is a challenging task considering the forces between the PMs. Moreover, the PMs are prone to breaking due to their small thickness to length ratio

$$\frac{r_{\text{pm}}}{L_{\text{m}}} \approx \frac{1}{90}, \quad (\text{B.1})$$

when optimized for high dynamics [16], see **Fig. B.1(b)**. Contrarily, all PMs feature the same shape (e.g. North and South poles for the DM shown in **Fig. B.7**) in the proposed manufacturing scenario, which simplifies fabrication. The PM pieces are mounted from only one side of the mover and the risk of breaking is low, as the thickness to length ratio is higher. The proposed mechanical support for the SM is conceptually the same, with the 3D-printed fixture (see **Fig. B.7**) having a shape that suits the respective PM arrangement (see **Fig. B.2(b)**).

Another important manufacturing aspect of the DS LiRA is the radial support of the mover. The conventional approach is to use mechanical bearings or air bearings. Such bearings require an additional mechanical assembly, which increases the mass and moment of inertia of the mover. To overcome this disadvantage, the proposed concept is planned to employ magnetic bearings (MBs) [22] in the final realization.

B.4.1 Performance Comparison

The introduction of the mechanical support for the DM (see **Fig. B.7**) and SM influences the DS LiRA design and performance, i.e. it increases the size of

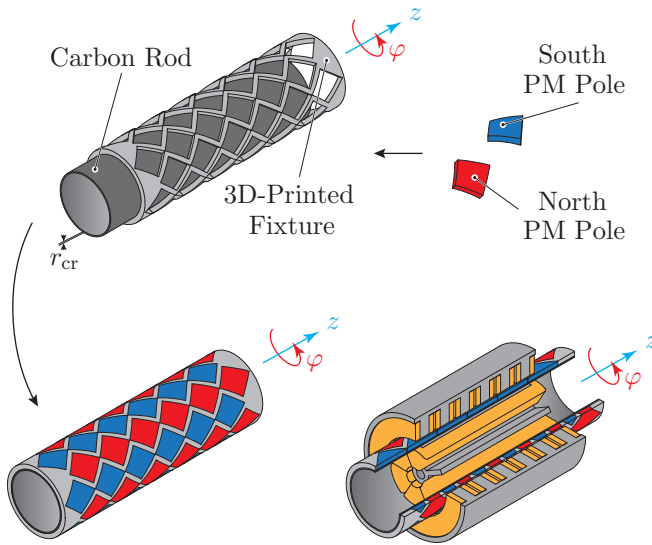


Fig. B.7: Manufacturing concept for the proposed double stator actuator. The thickness of the carbon rod is $r_{cr} = 0.5$ mm.

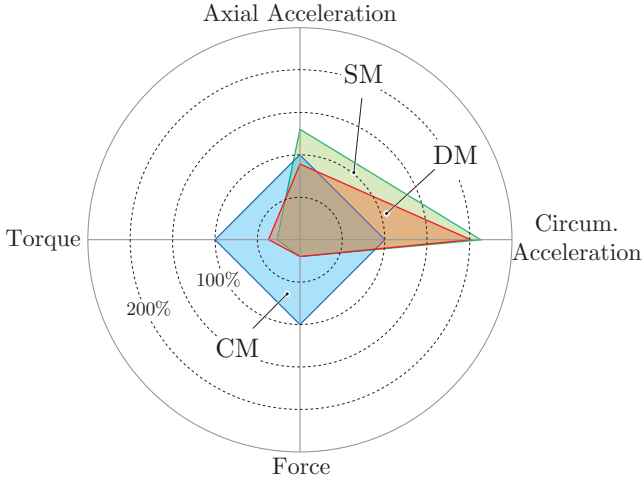


Fig. B.8: Relative comparison of the designs from **Fig. B.6** with manufacturing limitations being considered.

the mover and the magnetic air gap (see **Fig. B.4**). The related effects on the performance are shown in **Fig. B.8**. An electrical loading resulting in 15 W of copper losses is chosen, which is identical to that used above. The geometrical parameters, physical properties, and absolute values of the performance with included manufacturing limitations are given in **Tab. B.3**. In order to consider a lightweight carbon rod with a wall thickness of $r_{cr} = 0.5$ mm for the mechanical support of the proposed DM and SM, the inner magnetic air gap is enlarged to 1.2 mm. The outer air gap is also enlarged to 1.2 mm, providing increased space for additional mechanical protection of the PMs. These manufacturing constraints degrade the performance of the proposed DS LiRAs, which is seen from the comparison of **Fig. B.6** and **Fig. B.8**. The accelerations for the DS LiRA with DM and SM are calculated including the mass and moment of inertia of the carbon rod and 3D-printed fixture. Even with the included manufacturing constraints, the proposed DS LiRAs achieve higher accelerations than a DS LiRA with CM.

B.4.2 Cogging Torque and Force

Due to the interaction of the mover PMs with the inner and outer stator iron, a cogging torque T_{cog} and a cogging force F_{cog} act on the mover. The

Tab. B.3: DS LiRAs with included manufacturing constraints.

Parameter	Values		
Number of poles in RA	10		
Number of poles in LA	8		
Number of slots in RA	6		
Number of poles in LA	6		
Geometrical parameters	CM	DM	SM
Inner PM thickness ($r_{\text{pm,in}}$)	1 mm	-	-
Outer PM thickness ($r_{\text{pm,out}}$)	1 mm	-	-
Mover back iron (r_{iron})	2 mm	-	-
PM thickness (r_{pm})	-	1 mm	1 mm
Carbon rod thickness (r_{cr})	-	0.5 mm	0.5 mm
PM mechanical protection (r_{pr})	-	0.5 mm	0.5 mm
Mover thickness (r_{m})	4 mm	1 mm	1 mm
Magnetic air gaps	0.7 mm	1.2 mm	1.2 mm
Mechanical air gaps	0.7 mm	0.7 mm	0.7 mm
Physical properties (Unit)			
Mover mass (g)	240	52	36
Mover MoM ($\times 10^{-6} \text{kg m}^2$)	51.5	9.35	6.54
Performance (Unit)			
Axial force (N)	35.9	7.1	7.0
Torque (Nm)	0.3	0.11	0.081
Axial acc. (m/s^2)	150	134	194
Circumferential acc. (rad/s^2)	5825	11 764	12 393

amplitude of the cogging torque/force can be estimated by [131]

$$\{T_{\text{cog}}, F_{\text{cog}}\} \sim \phi^2 \frac{dR}{d\{\varphi, z\}}, \quad (\text{B.2})$$

where ϕ denotes the PM flux crossing the air gap and R is the total reluctance through which the flux passes. The waveform of the cogging torque/force can be described by means of a Fourier series expansion [132], [133]. The fundamental period of the cogging torque/force can be determined as [131], [134]

$$\tau_{\text{cog}}^{\{\text{T}, \text{F}\}} = \frac{\{360^\circ, L\}}{\text{LCM}(N_s, N_p)}, \quad (\text{B.3})$$

where L is the stator length of the linear actuator, N_s is the total number of slots in the stator (either linear or rotary), N_p is the number of poles (for the linear actuator N_p is the number of poles covered by the stator, while in the rotary actuator N_p is the total number of poles), and $\text{LCM}()$ denotes the least common multiple function. The fundamental cogging torque period for the rotary actuator is

$$\tau_{\text{cog}}^{\text{T}} = \frac{360^\circ}{\text{LCM}(6, 10)} = 12^\circ, \quad (\text{B.4})$$

while the period of the fundamental component of the cogging force for the linear actuator is

$$\tau_{\text{cog}}^{\text{F}} = \frac{60 \text{ mm}}{\text{LCM}(6, 8)} = 2.5 \text{ mm}. \quad (\text{B.5})$$

Cogging torque waveforms of the DS LiRA designs from **Tab. B.3** are shown in **Fig. B.9**. The period of the fundamental component of the cogging torque is estimated by curve fitting of the waveforms. As a cogging torque (or force) is undesired (especially in high-precision positioning systems), it is usually compensated for by feed-forward control of a current reference that depends on the circumferential and axial position φ and z , respectively. The current component that compensates for the cogging torque increases the copper losses in the rotary actuator windings of the DS LiRA with CM by about 0.4 W, which is very low due to low cogging torque. Hence, the increase of copper losses in the DM and SM LiRAs for this compensation is negligible.

Cogging force waveforms of the DS LiRA designs given in **Tab. B.3** are shown in **Fig. B.10** for an axial stroke of the mover from -7.5 mm to 7.5 mm . The period of the fundamental component of the cogging force is estimated by curve fitting of the waveforms from **Fig. B.10**. This obtained value agrees

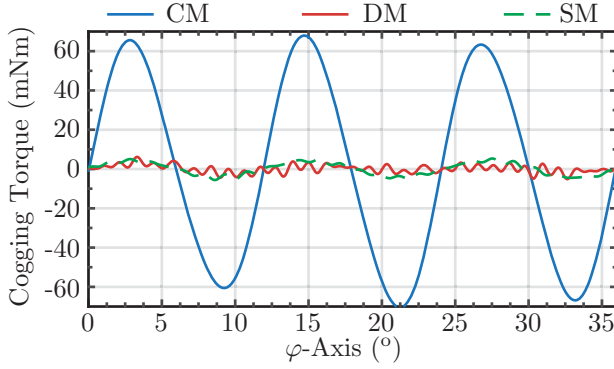


Fig. B.9: Cogging torque of the DS LiRA designs given in **Tab. B.3**.

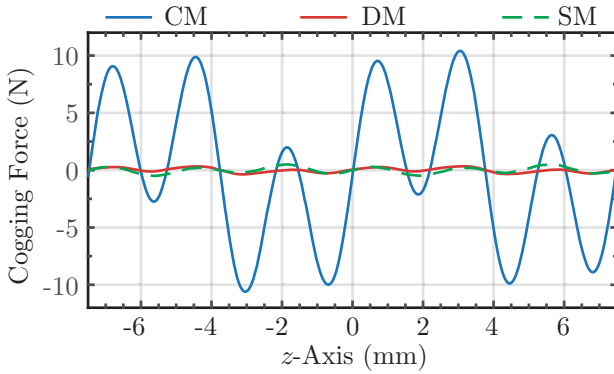


Fig. B.10: Cogging force of the DS LiRA designs given in **Tab. B.3**.

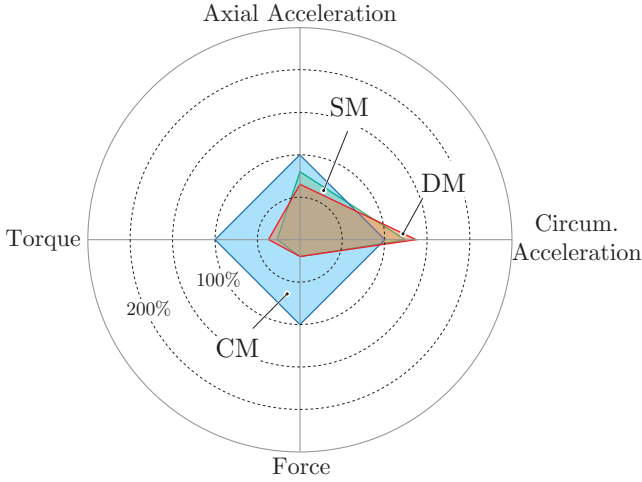


Fig. B.11: Relative comparison of the performance with a load.

with τ_{cog}^F calculated in (B.5). Compensation of the cogging force waveform by a feed-forward current increases the copper losses of the DS LiRA with CM by 0.5 W. Again, the increase of copper losses for this compensation in the DM and SM LiRA is negligible.

B.4.3 Influence of Mechanical Load

In manufacturing applications, a DS LiRA can be used to pick and place different objects, e.g. electronic components that are placed on a printed circuit board. The mass and inertia of such components are negligibly low. However, in order to carry these components, a nozzle needs to be mounted to the end of the mover. Considering the dimensions of the mover, a nozzle with $m_{\text{load}} = 30 \text{ g}$ and $I_{\text{load}} = 6 \times 10^{-6} \text{ kg m}^2$ is assumed to be attached to the mover. Consequently, the DS LiRA designs from **Tab. B.3** have a modified mass and moment of inertia of the movers, resulting in the updated performance characteristics provided in **Tab. B.4**. The relative reduction of the performance is shown in **Fig. B.11**. Therefore, special care should be taken when designing a DS LiRA with a DM or SM, as its performance (acceleration) strongly depends on the additional mechanical load. The latter depends on the application of the DS LiRA, for which a further application-specific optimization is possible.

Tab. B.4: Performance of DS LiRAs with a mechanical load attached to the mover.

Parameter	Values		
Physical properties (Unit)	CM	DM	SM
Mover mass (g)	270	82	66
Mover MoM ($\times 10^{-6} \text{kg m}^2$)	57.5	15.35	12.54
Performance (Unit)			
Axial force (N)	35.9	7.1	7.0
Torque (N m)	0.3	0.11	0.081
Axial acc. (m/s^2)	133	86.6	106.1
Circumferential acc. (rad/s^2)	5217	7166	6459

B.4.4 Summary of the Conducted Comparison

Double stator LiRAs with CM, DM and SM are compared in this section in terms of actuation properties (achievable torque and force), dynamics (circumferential and axial accelerations), cogging torque and cogging force. DS LiRA with CM achieves higher torque and force, which in some applications is not needed (e.g. high speed pick-and-place packaging robots) as throughput is determined by accelerations. Proposed DS LiRAs with DM or SM have double circumferential acceleration and about 30 % higher axial acceleration in case there is no load at the mover, see **Fig. B.8**. The additional load can deteriorate the dynamics, which is shown in **Fig. B.11** where an additional load with $m_{\text{load}} = 30 \text{ g}$ and $I_{\text{load}} = 6 \times 10^{-6} \text{ kg m}^2$ is assumed. Nevertheless, it should be kept in mind that manufacturing of DS LiRAs with DM and SM is simpler. Cogging torque and force of the proposed DS LiRAs with DM and SM are much lower, see **Fig. B.9** and **Fig. B.10**, which is an important aspect as they cause disturbances in positioning systems.

B.5 Simplified Planar Hardware Setup

In order to verify the FEM models used in the analysis, a simplified planar actuator is implemented. The hardware setup of the actuator is shown in **Fig. B.12**. It consists of a planar mover and two planar stators, which are placed above and below the mover. Each of the stators features three concentrated coils with 100 turns of insulated copper wire with a diameter of 0.4 mm. The implemented mover resembles the SM type analyzed in this chapter. During the manufacturing procedure of the mover, the PMs are initially arranged in a 3D printed fixture (see **Fig. B.12**), before 1 mm thick

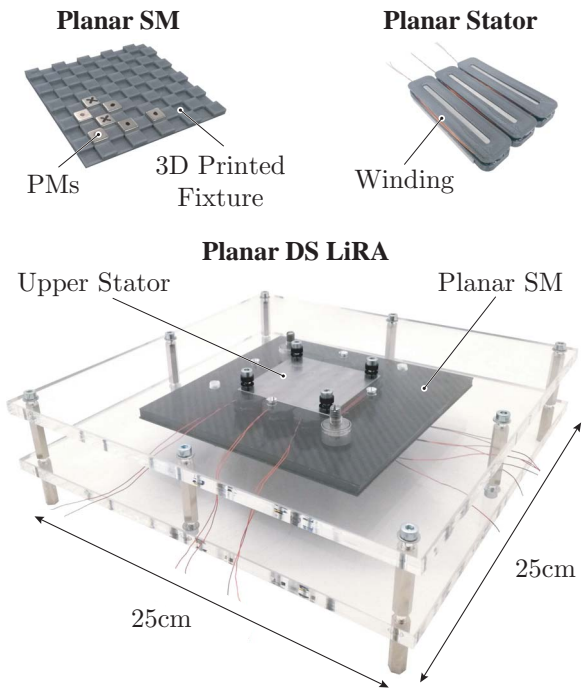


Fig. B.12: Simplified planar hardware setup. Not all PMs are mounted in the photo of the planar SM.

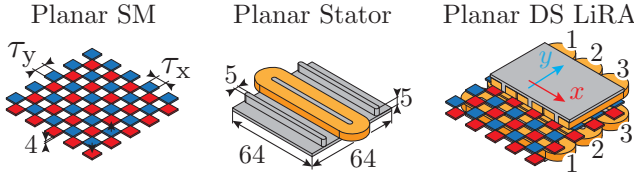


Fig. B.13: Geometry and coordinate system of the simplified planar hardware setup. All dimensions are in mm. The upper and lower air gaps are 2.2 mm. Pole sizes are $\tau_x = \tau_y = 8$ mm.

Tab. B.5: Comparison of simulated and measured results for the flux linkage.

Lower Stator		
Flux linkage	FEM simulation	3.4 mWb
Flux linkage	Measurement	3.3 mWb

carbon fiber plates are glued from both sides for mechanical stability. The dimensions of the stator and the mover geometry are provided in **Fig. B.13**.

The comparison of the FEM simulation results with measurements is carried out for the flux linkage. The measurement results for the flux linkage are obtained by integrating the induced back-EMF in the windings of the lower and upper stators. To induce the back-EMF, the mover is driven in the y -axis direction (see **Fig. B.13** for the orientation of the coordinate system).

Further, the flux linkage is studied for different mover positions in the y -axis by using a FEM model of the planar setup. In **Fig. B.14**, the flux linkage waveforms are shown for a single winding turn of the lower and upper stator coils. The flux linkage for the turns in the lower stator is $\approx 34 \mu\text{Wb}$. This value is multiplied by the number of turns of the manufactured coils (100) and compared to the measured flux linkage in **Tab. B.5**. The results show a good agreement of the measurement and FEM simulation results, which verifies the correctness of the employed FEM models.

The waveform of the flux linkage in the lower stator can be modeled as

$$\psi_L(y(t)) = N \hat{\Psi}_{L,y} \cos\left(\frac{\pi}{\tau_y} y(t)\right), \quad (\text{B.6})$$

where N represents the number of turns in the coil, $\hat{\Psi}_{L,y} = 34 \mu\text{Wb}$ from **Fig. B.14**, and $\tau_y = 8$ mm is the pole size in the y -direction. The flux linkage in the upper stator due to the same movement in the y -direction is modeled

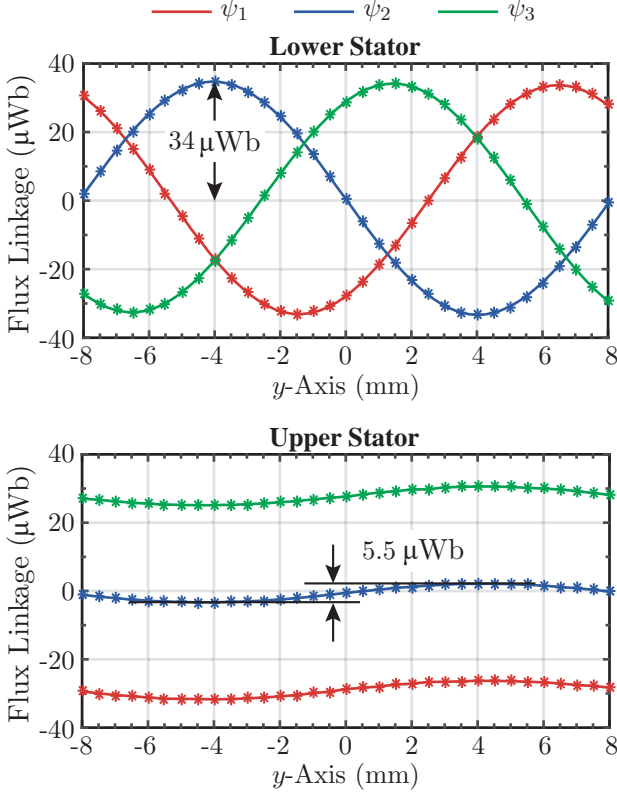


Fig. B.14: FEM simulation results for the flux linkage per turn of the lower and upper stators of the planar setup shown in **Fig. B.13**. Flux linkages ψ_1 , ψ_2 and ψ_3 are flux linkages of the coils 1, 2 and 3 of the lower and upper stator, respectively. Asterisks represent FEM simulation points. The coil numbers are denoted in **Fig. B.13** (right).

as

$$\psi_U(y(t)) = N\hat{\Psi}_{U,y} \cos\left(\frac{\pi}{\tau_y} y(t)\right) + \psi_{U,\text{offset}}(x(t)), \quad (\text{B.7})$$

where $\hat{\Psi}_{U,y} = 2.75 \mu\text{Wb}$ from **Fig. B.14** and $\psi_{U,\text{offset}}(x(t))$ is the offset that depends on the x position of the mover. $\hat{\Psi}_{U,y}$ represents an undesired coupling, since ideally no change of the flux linkage in the upper stator is expected for a movement in the y -direction. The ratio of the induced back-EMF amplitudes in the upper and lower stator windings due to a movement in the y -direction is $E_U/E_L = \hat{\Psi}_{U,y}/\hat{\Psi}_{L,y} \approx 8.1\%$. Therefore, for the planar actuator shown in **Fig. B.13**, the undesired back-EMF is about 8.1 % of the expected back-EMF. Coupling effects between the stators in the LiRA, with a DM or SM, will be studied in future work.

B.6 Summary

State-of-the-art double stator (DS) linear-rotary actuators (LiRAs) are mainly used in high force/torque applications, such as tooling machines. Their usage in highly dynamic applications is limited by the bulky mover design, referred here as conventional mover (CM). CMs employ two sets of permanent magnets (PMs) and a back iron. In order to increase the dynamics of the DS LiRA, two different ironless mover concepts with a single set of PMs (DM and SM) are proposed in this chapter. Moreover, manufacturing steps for the proposed mover layouts are provided. After accounting for manufacturing constraints, an axial acceleration of the proposed DS LiRA with SM is around 30 % higher than that of a DS LiRA with CM, while the circumferential acceleration nearly doubles. Additionally, the cogging torque and the cogging force of the proposed DS LiRAs are negligible compared to those of the DS LiRA with CM. Manufacturing of the proposed movers (DM and SM) is simpler. On the other hand, due to lower torque and force of the DS LiRAs with DM and SM, accelerations decrease faster in case an additional load is attached to the mover compared to the DS LiRA with CM. The advantage of a CM having two sets of magnets is that the mover can be optimized either for high circumferential or high axial acceleration, which is not possible with the proposed DM and SM as they feature only a single set of magnets.

Bibliography

- [1] JUSTEK, Linear Motion Technology, <http://www.justek.com/english/index.php>, accessed: 30/11/2020 .
- [2] ETEL, <https://www.etel.ch/>, accessed: 30/11/2020 .
- [3] LinMot, <https://linmot.com/>, accessed: 30/11/2020 .
- [4] Mirae, <http://www.mirae.com/en/index.asp>, accessed: 30/11/2020 .
- [5] Nippon Pulse Motor, <https://www.pulsemotor.com/global/>, accessed: 30/11/2020 .
- [6] SWIS, SEWOO INDUSTRIAL SYSTEM CO. LTD, <http://www.sewoomotor.com/>, accessed: 30/11/2020 .
- [7] SINADRIVERS, Direct Drive Experts, <https://sinadrives.com/en/products/>, accessed: 30/11/2020 .
- [8] SINFONIA, https://www.sinfo-t.jp/eng/servo_act.html, accessed: 30/11/2020 .
- [9] Sodick, <https://www.sodick.co.jp/en/product/motion/>, accessed: 30/11/2020 .
- [10] TECHNOTION, the Linear Motion Company, <https://www.tecnotion.com/>, accessed: 30/11/2020 .
- [11] TCP Mechatronics Corp., <https://www.tpcpage.com/>, accessed: 30/11/2020 .
- [12] Akribis, where precision matters, <http://www.akribis-sys.com/>, accessed: 30/11/2020 .
- [13] LinMot, Linear Rotary Motors, <https://linmot.com/products/linear-rotary-motors/>, accessed: 30/11/2020 .
- [14] L. Xu, M. Lin, X. Fu, and N. Li, "Design and Analysis of a Double-Stator Linear-Rotary Permanent-Magnet Motor," *IEEE Transactions on Applied Superconductivity*, vol. 26, no. 4, pp. 1–4, 2016, DOI: 10.1109/TASC.2016.2517018.

- [15] S. Mirić, M. Schuck, A. Tüysüz, and J. W. Kolar, “Double Stator Linear-Rotary Actuator with a Single Set of Mover Magnets,” in *Proc. of IEEE Energy Conversion Congress and Exposition (ECCE USA)*, Portland, OR, USA, 2018, DOI: 10.1109/ECCE.2018.8557575.
- [16] S. Mirić, A. Tüysüz, and J. W. Kolar, “Comparative Evaluation of Linear-Rotary Actuator Topologies for Highly Dynamic Applications,” in *Proc. of IEEE International Electric Machines and Drives Conference (IEMDC)*, Miami, FL, USA, 2017, DOI: 10.1109/IEMDC.2017.8002236.
- [17] K. Meessen, J. Paulides, and E. Lomonova, “Analysis of a Novel Magnetization Pattern for 2-DoF Rotary-Linear Actuators,” *IEEE Transactions on Magnetics*, vol. 48, no. 11, pp. 3867–3870, 2012, DOI: 10.1109/TMAG.2012.2199094.
- [18] S. Mirić, R. Giuffrida, D. Bortis, and J. W. Kolar, “Enhanced Complex Space Vector Modeling and Control System Design of Multiphase Magnetically Levitated Rotary-Linear Machines,” *IEEE Journal of Emerging and Selected Topics in Power Electronics*, vol. 8, no. 2, pp. 1833–1849, 2019, DOI: 10.1109/JESTPE.2019.2945625.
- [19] P. Jin, H. Lin, S. Fang, and S. Ho, “Decoupling Control of Linear and Rotary Permanent Magnet Actuator Using Two-Directional $d-q$ Transformation,” *IEEE Transactions on Magnetics*, vol. 48, no. 10, pp. 2585–2591, 2012, DOI: 10.1109/TMAG.2012.2202321.
- [20] J. Schmied, “Experience with Magnetic Bearings Supporting a Pipeline Compressor,” in *Proc. of International Symposium on Magnetic Bearings (ISMB)*, Tokyo, Japan, 1990.
- [21] P. McMullen, V. Vuong, and L. Hawkins, “Flywheel Energy Storage System with AMBs and Hybrid Backup Bearings,” in *Proc. of International Symposium on Magnetic Bearings (ISMB)*, Martigny, Switzerland, 2006.
- [22] H. Bleuler, M. Cole, P. Keogh, R. Larssonneur, E. Maslen, Y. Okada, G. Schweitzer, A. Traxler *et al.*, *Magnetic Bearings: Theory, Design, and Application to Rotating Machinery*. Springer Science & Business Media, 2009.
- [23] S. Mirić, D. Bortis, and J. W. Kolar, “Design and Comparison of Permanent Magnet Self-Bearing Linear-Rotary Actuators,” in *Proc. of 12th*

- IEEE International Symposium on Linear Drives for Industry Applications (LDIA)*, Neuchatel, Switzerland, 2019, DOI: 10.1109/LDIA.2019.8770986.
- [24] K. J. Meessen, J. J. Paulides, and E. A. Lomonova, "Modeling and Experimental Verification of a Tubular Actuator for 20-g Acceleration in a Pick-and-Place Application," *IEEE Transactions on Industry Applications*, vol. 46, no. 5, pp. 1891–1898, 2010, DOI: 10.1109/TIA.2010.2057392.
- [25] L. Xie, J. Si, Y. Hu, and Z. Wang, "Overview of 2-Degree-of-Freedom Rotary-Linear Motors Focusing on Coupling Effect," *IEEE Transactions on Magnetics*, vol. 55, no. 4, 2019, DOI: 10.1109/TMAG.2019.2898609.
- [26] K. Guo and Y. Guo, "Key Parameter Design and Analysis of Flux Reversal Linear Rotary Permanent Magnet Actuator," *IEEE Transactions on Applied Superconductivity*, vol. 29, no. 2, 2019, DOI: 10.1109/TASC.2018.2889625.
- [27] T. Yamasaki, "Electric Linear Motion Actuator and Electric Brake System," Patent US9 970 499B2, 2013.
- [28] W. Lee, S. Li, D. Han, B. Sarlioglu, T. A. Minav, and M. Pietola, "A Review of Integrated Motor Drive and Wide-Bandgap Power Electronics for High-Performance Electro-Hydrostatic Actuators," *IEEE Transactions on Transportation Electrification*, vol. 4, no. 3, pp. 684–693, 2018, DOI: 10.1109/TTE.2018.2853994.
- [29] T. Reichert, T. Nussbaumer, and J. W. Kolar, "Torque Scaling Laws for Interior and Exterior Rotor Permanent Magnet Machines," in *Proc. of the IEEE International Magnetics Conference (INTERMAG)*, Shanghai, China, 2009, pp. 1–4.
- [30] K. Meessen, J. Paulides, and E. Lomonova, "Analysis and Design Considerations of a 2-DoF Rotary-Linear Actuator," in *Proc. of IEEE International Electric Machines and Drives Conference (IEMDC)*, Niagara Falls, ON, Canada, 2011, DOI: 10.1109/IEMDC.2011.5994616.
- [31] P. Jin, H. Lin, S. Fang, Y. Yuan, Y. Guo, and Z. Jia, "3-D Analytical Linear Force and Rotary Torque Analysis of Linear and Rotary Permanent Magnet Actuator," *IEEE Transactions on Magnetics*, vol. 49, no. 7, pp. 3989–3992, 2013, DOI: 10.1109/TMAG.2013.2238897.
- [32] G. Krebs, A. Tounzi, B. Pauwels, D. Willemot, and M. Piriou, "Design of a Permanent Magnet Actuator for Linear and Rotary Movements,"

- The European Physical Journal-Applied Physics*, vol. 44, no. 1, pp. 77–85, 2008, DOI: 10.1051/epjap:2008105.
- [33] A. Schleicher and R. Werner, “Theoretical and Experimental Analysis of Controllability of a Novel Bearingless Rotary-Linear Reluctance Motor with Optimal Chessboard Tothing,” in *Proc. of IEEE International Conference on Industrial Technology (ICIT)*, Lyon, France, 2018, DOI: 10.1109/ICIT.2018.8352234.
 - [34] N.-C. Tsai and C.-W. Chiang, “Design and Analysis of Magnetically-Drive Actuator Applied for Linear Compressor,” *Elsevier Mechatronics*, vol. 20, no. 5, pp. 596–603, 2010, DOI: 10.1016/j.mechatronics.2010.06.001.
 - [35] S. Mirić, P. Küttel, A. Tüysüz, and J. W. Kolar, “Design and Experimental Analysis of a New Magnetically Levitated Tubular Linear Actuator,” *IEEE Transactions on Industrial Electronics*, vol. 66, no. 6, pp. 4816–4825, 2019, DOI: 10.1109/TIE.2018.2868286.
 - [36] T. Baumgartner and J. W. Kolar, “Multivariable State Feedback Control of a 500 000-r/min Self-Bearing Permanent-Magnet Motor,” *IEEE/ASME Transactions on Mechatronics*, vol. 20, no. 3, pp. 1149–1159, 2015, DOI: 10.1109/TMECH.2014.2323944.
 - [37] N. Simpson, R. Wrobel, and P. H. Mellor, “Estimation of Equivalent Thermal Parameters of Impregnated Electrical Windings,” *IEEE Transactions on Industry Applications*, vol. 49, no. 6, pp. 2505–2515, 2013, DOI: 10.1109/TIA.2013.2263271.
 - [38] E. Lomonova, “Advanced Actuation Systems - State of the Art: Fundamental and Applied Research,” in *Proc. of International Conference on Electrical Machines and Systems (ICEMS)*, Incheon, South Korea, 2010.
 - [39] T. Overboom, J. Jansen, E. Lomonova, and F. Tacken, “Design and Optimization of a Rotary Actuator for a Two-Degree-of-Freedom $z - \varphi$ Module,” *IEEE Transactions on Industry Applications*, vol. 46, no. 6, pp. 2401–2409, 2010, DOI: 10.1109/TIA.2010.2073430.
 - [40] P. R. Eckert, A. F. Flores Filho, E. Perondi, and D. G. Dorrell, “Dual Quasi-Halbach Linear Tubular Actuator with Coreless Moving-Coil for Semi-Active and Active Suspension,” *IEEE Transactions on Industrial Electronics*, vol. 65, no. 12, pp. 9873–9883, 2018, DOI: 10.1109/TIE.2018.2818656.

-
- [41] X. Xue, K. W. E. E. Cheng, and Z. Zhang, "Model, Analysis and Application of Tubular Linear Switched Reluctance Actuator for Linear Compressors," *IEEE Transactions on Industrial Electronics*, vol. 65, no. 12, pp. 9863–9872, 2018, DOI: 10.1109/TIE.2018.2818638.
- [42] V. DelliColli, P. Cancelliere, F. Marignetti, R. DiStefano, and M. Scarano, "A Tubular-Generator Drive for Wave Energy Conversion," *IEEE Transactions on Industrial Electronics*, vol. 53, no. 4, pp. 1152–1159, 2006, DOI: 10.1109/TIE.2006.878318.
- [43] J. J. Paulides, J. L. Janssen, and E. A. Lomonova, "Bearing Lifetime of Linear PM Machines," in *Proc. of IEEE Energy Conversion Congress and Exposition (ECCE USA)*, San Jose, CA, USA, 2009, DOI: 10.1109/ECCE.2009.5316359.
- [44] K. J. Meessen, "Electromagnetic Fields and Interactions in 3D Cylindrical Structures: Modeling and Application," Ph.D. dissertation, Eindhoven University of Technology, Eindhoven, Netherlands, 2012.
- [45] D. Steinert, T. Nussbaumer, and J. W. Kolar, "Slotless Bearingless Disk Drive for High-Speed and High-Purity Applications," *IEEE Transactions on Industrial Electronics*, vol. 61, no. 11, pp. 5974–5986, 2014, DOI: 10.1109/TIE.2014.2311379.
- [46] P. Puentener, M. Schuck, D. Steinert, T. Nussbaumer, and J. W. Kolar, "A 150 000-r/min Bearingless Slice Motor," *IEEE/ASME Transactions on Mechatronics*, vol. 23, no. 6, pp. 2963–2967, 2018, DOI: 10.1109/TMECH.2018.2873894.
- [47] M. Schuck, D. Steinert, T. Nussbaumer, and J. W. Kolar, "Ultrafast Rotation of Magnetically Levitated Macroscopic Steel Spheres," *American Association for the Advancement of Science, Science Advances*, vol. 4, no. 1, p. e1701519, 2018, DOI: 10.1126/sciadv.1701519.
- [48] A. G. Rainer Gloess, "Nanometer Resolution of Magnetic Levitation Stages for Planar and Linear Scan Application," in *Proc. of International Symposium on Magnetic Bearings (ISMB)*, Beijing, China, 2018.
- [49] H. B. Ertan, M. Y. Üçtug, R. Colyer, and A. Consoli, *Modern Electrical Drives*. Springer Science & Business Media, 2013, vol. 369.
- [50] E. Levi, M. Jones, S. N. Vukosavic, and H. A. Toliyat, "A Novel Concept of a Multiphase, Multimotor Vector Controlled Drive System Supplied

- from a Single Voltage Source Inverter,” *IEEE Transactions on Power Electronics*, vol. 19, no. 2, pp. 320–335, 2004, DOI: 10.1109/TPEL.2003.823241.
- [51] A. Iqbal and E. Levi, “Space Vector Modulation Schemes for a Five-Phase Voltage Source Inverter,” in *Proc. of European Conference on Power Electronics and Applications (EPE)*, Dresden, Germany, 2005, DOI: 10.1109/EPE.2005.219194.
- [52] J. A. Riveros, F. Barrero, E. Levi, M. J. Durán, S. Toral, and M. Jones, “Variable-Speed Five-Phase Induction Motor Drive Based on Predictive Torque Control,” *IEEE Transactions on Industrial Electronics*, vol. 60, no. 8, pp. 2957–2968, 2012, DOI: 10.1109/TIE.2012.2198034.
- [53] E. Levi, M. Jones, and S. Vukosavic, “Even-Phase Multi-Motor Vector Controlled Drive with Single Inverter Supply and Series Connection of Stator Windings,” *IET IEE Proceedings - Electric Power Applications*, vol. 150, no. 5, pp. 580–590, 2003, DOI: 10.1049/ip-epa:20030424.
- [54] D. Dujic, G. Grandi, M. Jones, and E. Levi, “A Space Vector PWM Scheme for Multifrequency Output Voltage Generation with Multi-Phase Voltage-Source Inverters,” *IEEE Transactions on Industrial Electronics*, vol. 55, no. 5, pp. 1943–1955, 2008, DOI: 10.1109/TIE.2008.918468.
- [55] E. Levi, “A Unified Approach to Main Flux Saturation Modelling in DQ Axis Models of Induction Machines,” *IEEE Transactions on Energy Conversion*, vol. 10, no. 3, pp. 455–461, 1995, DOI: 10.1109/60.464868.
- [56] J. Pyrhonen, V. Hrabovcova, and R. S. Semken, *Electrical Machine Drives Control: An Introduction*. John Wiley & Sons, 2016.
- [57] K. P. Kovács and I. Rácz, *Transiente Vorgänge in Wechselstrommaschinen (in German)*. Verlag der ungarischen Akademie der Wissenschaften, 1959, vol. 1.
- [58] A. Mora, R. Cárdenas, M. Espinoza, and M. Díaz, “Active Power Oscillation Elimination in 4-Leg Grid-Connected Converters Under Unbalanced Network Conditions,” in *Proc. of Annual Conference of the IEEE Industrial Electronics Society (IECON)*, Florence, Italy, 2016, DOI: 10.1109/IECON.2016.7792960.
- [59] G. Sala, G. Valente, A. Formentini, L. Papini, D. Gerada, P. Zanchetta, A. Tani, and C. Gerada, “Space Vectors and Pseudoinverse Matrix Methods for the Radial Force Control in Bearingless Multisector Permanent

- Magnet Machines,” *IEEE Transactions on Industrial Electronics*, vol. 65, no. 9, pp. 6912–6922, 2018, DOI: 10.1109/TIE.2018.2795590.
- [60] G. Valente, L. Papini, A. Formentini, C. Gerada, and P. Zanchetta, “Radial Force Control of Multisector Permanent-Magnet Machines for Vibration Suppression,” *IEEE Transactions on Industrial Electronics*, vol. 65, no. 7, pp. 5395–5405, 2017, DOI: 10.1109/TIE.2017.2780039.
- [61] J. Chen, Y. Qin, A. M. Bozorgi, and M. Farasat, “Low Complexity Dual-Vector Model Predictive Current Control for Surface-Mounted Permanent Magnet Synchronous Motor Drives,” *IEEE Journal of Emerging and Selected Topics in Power Electronics*, vol. 8, no. 3, pp. 2655–2663, 2019, DOI: 10.1109/JESTPE.2019.2917865.
- [62] M. Khalilzadeh and S. Vaez-Zadeh, “Computation Efficiency and Robustness Improvement of Predictive Control for PMS Motors,” *IEEE Journal of Emerging and Selected Topics in Power Electronics*, vol. 8, no. 3, pp. 2645–2654, 2019, DOI: 10.1109/JESTPE.2019.2916926.
- [63] B. Hu, L. Kang, J. Cheng, X. Luo, and Z. Zhang, “Model Predictive Power Control with Dual Vectors for Three-Level Inverter,” *IEEE Journal of Emerging and Selected Topics in Power Electronics*, vol. 7, no. 4, pp. 2204–2212, 2019, DOI: 10.1109/JESTPE.2019.2910588.
- [64] L. Serrano-Iribarnegaray, “Space Phasor Theory and Control of Multiphase Machines Through Their Decoupling Into Equivalent Three-Phase Machines,” *Springer, Electrical Engineering*, vol. 96, no. 1, pp. 79–94, 2014, DOI: 10.1007/s00202-013-0278-6.
- [65] Atan2, <https://en.wikipedia.org/wiki/Atan2>, accessed: 12/06/2019 .
- [66] F. Meier, “Permanent-Magnet Synchronous Machines with Non-Overlapping Concentrated Windings for Low-Speed Direct-Drive Applications,” Ph.D. dissertation, KTH Stockholm, Stockholm, Sweden, 2008.
- [67] EMETOR, <https://www.emetor.com>, accessed: 12/06/2019 .
- [68] E. Severson, S. Gandikota, and N. Mohan, “Practical Implementation of Dual-Purpose No-Voltage Drives for Bearingless Motors,” in *Proc. of IEEE Applied Power Electronics Conference and Exposition (APEC)*, Charlotte, NC, USA, 2015, DOI: 10.1109/APEC.2015.7104444.

- [69] T. I. Baumgartner, “A Magnetically Levitated 500 000 rpm Electrical Drive System,” Ph.D. dissertation, ETH Zurich, Zurich, Switzerland, 2013.
- [70] K. Raggl, T. Nussbaumer, and J. W. Kolar, “A Comparison of Separated and Combined Winding Concepts for Bearingless Centrifugal Pumps,” in *Proc. of IEEE International Conference on Power Electronics*, Daegu, South Korea, 2007, DOI: 10.1109/ICPE.2007.4692535.
- [71] I. Boldea, *Linear Electric Machines, Drives, and MAGLEVs Handbook*. CRC Press, 2013.
- [72] J. Paulides, L. Encica, K. Meessen, and E. Lomonova, “Fast Component Placement with Optimized Long-Stroke Passive Gravity Compensation Integrated in a Cylindrical/Tubular PM Actuator,” in *Proc. of International Conference on Electrical Machines and Systems (ICEMS)*, Busan, Korea (South), 2013, DOI: 10.11142/jicems.2013.2.3.275.
- [73] E. A. Baran, T. E. Kurt, and A. Sabanovic, “Lightweight Design and Encoderless Control of a Miniature Direct Drive Linear Delta Robot,” in *Proc. of 8th International Conference on Electrical and Electronics Engineering (ELECO)*, Bursa, Turkey, 2013, DOI: 10.1109/ELECO.2013.6713893.
- [74] F. Bechet, K. Ogawa, E. Sariyildiz, and K. Ohnishi, “Electrohydraulic Transmission System for Minimally Invasive Robotics,” *IEEE Transactions on Industrial Electronics*, vol. 62, no. 12, pp. 7643–7654, 2015, DOI: 10.1109/TIE.2015.2453930.
- [75] Y. Nakajima, T. Nozaki, and K. Ohnishi, “Heartbeat Synchronization with Haptic Feedback for Telesurgical Robot,” *IEEE Transactions on Industrial Electronics*, vol. 61, no. 7, pp. 3753–3764, 2013, DOI: 10.1109/TIE.2013.2287258.
- [76] J. Wang, W. Wang, and K. Atallah, “A Linear Permanent-Magnet Motor for Active Vehicle Suspension,” *IEEE Transactions on Vehicular Technology*, vol. 60, no. 1, pp. 55–63, 2010, DOI: 10.1109/TVT.2010.2089546.
- [77] J. Wang, W. Wang, G. W. Jewell, and D. Howe, “A Low-Power, Linear, Permanent-Magnet Generator/Energy Storage System,” *IEEE Transactions on Industrial Electronics*, vol. 49, no. 3, pp. 640–648, 2002, DOI: 10.1109/TIE.2002.1005391.

-
- [78] J. Wang, M. West, D. Howe, H. Zelaya-De La Parra, and W. M. Arshad, "Design and Experimental Verification of a Linear Permanent Magnet Generator for a Free-Piston Energy Converter," *IEEE Transactions on Industrial Electronics*, vol. 22, no. 2, pp. 299–306, 2017, DOI: 10.1109/TEC.2006.875434.
- [79] I. Boldea, L. Tutelea, W. Xu, and M. Pucci, "Linear Electric Machines, Drives and MAGLEVs: An Overview," *IEEE Transactions on Industrial Electronics*, vol. 65, no. 9, pp. 7504–7515, 2017, DOI: 10.1109/TIE.2017.2733492.
- [80] J. Latham, M. L. McIntyre, and M. Mohebbi, "Parameter Estimation and a Series of Nonlinear Observers for the System Dynamics of a Linear Vapor Compressor," *IEEE Transactions on Industrial Electronics*, vol. 63, no. 11, pp. 6736–6744, 2016, DOI: 10.1109/TIE.2016.2582728.
- [81] J. Wang, D. Howe, and Z. Lin, "Design Optimization of Short-Stroke Single-Phase Tubular Permanent-Magnet Motor for Refrigeration Applications," *IEEE Transactions on Industrial Electronics*, vol. 57, no. 1, pp. 327–334, 2009, DOI: 10.1109/TIE.2009.2025710.
- [82] G. Zhong, H. Deng, G. Xin, and H. Wang, "Dynamic Hybrid Control of a Hexapod Walking Robot: Experimental Verification," *IEEE Transactions on Industrial Electronics*, vol. 63, no. 8, pp. 5001–5011, 2016, DOI: 10.1109/TIE.2016.2551679.
- [83] J. Zhang, W. Li, J. Yu, Q. Zhang, S. Cui, Y. Li, S. Li, and G. Chen, "Development of a Virtual Platform for Telepresence Control of an Underwater Manipulator Mounted on a Submersible Vehicle," *IEEE Transactions on Industrial Electronics*, vol. 64, no. 2, pp. 1716–1727, 2016, DOI: 10.1109/TIE.2016.2557309.
- [84] LinMot, Stainless Steel Motors, <http://www.linmot.com/products/stainless-steel-motors/>, accessed: 12/06/2019 .
- [85] S. Silber, W. Amrhein, P. Bosch, R. Schob, and N. Barletta, "Design Aspects of Bearingless Slice Motors," *IEEE/ASME Transactions on Mechatronics*, vol. 10, no. 6, pp. 611–617, 2005, DOI: 10.1109/TMECH.2005.859813.
- [86] J. W. Jansen, C. M. M. van Lierop, E. A. Lomonova, and A. J. A. Vandenput, "Modeling of Magnetically Levitated Planar Actuators with

- Moving Magnets,” *IEEE Transactions on Magnetics*, vol. 43, no. 1, pp. 15–25, 2007, DOI: 10.1109/TMAG.2006.886051.
- [87] J. W. Jansen, C. M. M. van Lierop, E. A. Lomonova, and A. J. A. Vandenput, “Magnetically Levitated Planar Actuator with Moving Magnets,” *IEEE Transactions on Industry Applications*, vol. 44, no. 4, pp. 1108–1115, 2008, DOI: 10.1109/TIA.2008.926065.
- [88] M. Flankl, A. Tüysüz, and J. W. Kolar, “Impact of Iron Dust on Electromechanical Systems: A Case Study,” in *Proc. of IEEE Southern Power Electronics Conference (SPEC)*, Auckland, New Zealand, 2016, DOI: 10.1109/SPEC.2016.7846069.
- [89] C. M. Zingerli, P. Imoberdorf, J. W. Kolar, and T. Nussbaumer, “Rotor Position Measurement for a Magnetically Levitated 500’000 rpm Permanent Magnet Machine,” in *Proc. of IEEE Energy Conversion Congress and Exposition (ECCE USA)*, Phoenix, AZ, USA, 2011, DOI: 10.1109/ECCE.2011.6063999.
- [90] EPCOS - TDK, *NTC Thermistors for Temperature Measurement, B57550G1 Datasheet*, 2016.
- [91] Messtechnik Schaffhausen GmbH, *LFP-19-10kg Datasheet*, 2017.
- [92] TE Connectivity Measurement Specialties, *FX1901 Compression Load Cell Datasheet*, 2017.
- [93] S. Miric, R. Giuffrida, D. Bortis, and J. Kolar, “Dynamic Electromechanical Model and Position Controller Design of a New High-Precision Self-Bearing Linear Actuator,” *IEEE Transactions on Industrial Electronics*, vol. 68, no. 1, pp. 744–755, 2020, DOI: 10.1109/TIE.2020.2992943.
- [94] Texas Instruments - TI, *LMG5200 80V, 10A GaN Half-Bridge Power Stage*, 2018.
- [95] Analog Devices, *High Voltage, Bidirectional Current Sense Amplifier*, 2019.
- [96] Linear Technology, *12-Bit, 2.5Msps Serial Sampling ADC in TSOT*, 2013.
- [97] Xilinx, *Zynq-7000 SoC Data Sheet: Overview*, 2018.

-
- [98] S. Pan, P. A. Commings, and H. Du, "Tubular Linear Motor Position Detection by Hall-Effect Sensors," in *Proc. of IEEE Australasian Universities Power Engineering Conference (AUPEC)*, Wollongong, NSW, Australia, 2015, DOI: 10.1109/AUPEC.2015.7324830.
- [99] A. Muesing, C. Zingerli, P. Imoberdorf, and J. W. Kolar, "PEEC-Based Numerical Optimization of Compact Radial Position Sensors for Active Magnetic Bearings," in *Proc. of VDE 5th International Conference on Integrated Power Electronics Systems*, Nuremberg, Germany, 2008.
- [100] Rohde & Schwarz Co., *UPV Audio Analyzer, Manual and Specification*, 2015.
- [101] B. Kou, J. Luo, X. Yang, and L. Zhang, "Modeling and Analysis of a Novel Transverse-Flux Flux-Reversal Linear Motor for Long-Stroke Application," *IEEE Transactions on Industrial Electronics*, vol. 63, no. 10, pp. 6238–6248, 2016, DOI: 10.1109/TIE.2016.2581142.
- [102] X. Zhen Huang, J. Li, Q. Tan, Z. Y. Qian, C. Zhang, and L. Li, "Sectional Combinations of the Modular Tubular Permanent Magnet Linear Motor and the Optimization Design," *IEEE Transactions on Industrial Electronics*, vol. 65, no. 12, pp. 9658–9667, 2018, DOI: 10.1109/TIE.2018.2826465.
- [103] T. J. Teo, H. Zhu, S.-L. Chen, G. Yang, and C. K. Pang, "Principle and Modelling of a Novel Moving Coil Linear-Rotary Electromagnetic Actuator," *IEEE Transactions on Industrial Electronics*, vol. 63, no. 11, pp. 6930–6940, 2016, DOI: 10.1109/TIE.2016.2585540.
- [104] C.-T. Liu, C.-C. Hwang, and Y.-W. Chiu, "Design of a Coaxially Magnetic-Geared Linear Actuator for Electric Power Steering System Applications," *IEEE Transactions on Industry Applications*, vol. 53, no. 3, pp. 2401–2408, 2017, DOI: 10.1109/TIA.2017.2672665.
- [105] I. A. Smadi, H. Omori, and Y. Fujimoto, "Development, Analysis, and Experimental Realization of a Direct-Drive Helical Motor," *IEEE Transactions on Industrial Electronics*, vol. 59, no. 5, pp. 2208–2216, 2011, DOI: 10.1109/TIE.2011.2148687.
- [106] S.-L. Chen, T. Teo, and G. Yang, "Control of a Novel Linear-Rotary Actuator for High-Speed Pick-and-Place Application," *Australian Journal of Electric. and Electron. Eng.*, vol. 11, no. 3, pp. 289–296, 2014, DOI: 10.7158/1448837X.2014.11464430.

- [107] R. H. Bishop, *Mechatronic Systems, Sensors, and Actuators: Fundamentals and Modeling*. CRC Press Boca Raton, FL, ISBN 0-8493-9258-6, 2008.
- [108] J. Awrejcewicz and Z. Koruba, *Classical Mechanics: Applied Mechanics and Mechatronics*. Springer Science & Business Media, 2012, vol. 30.
- [109] Frobenius Inner Product, https://en.wikipedia.org/wiki/Frobenius_inner_product, accessed: 12/06/2019 .
- [110] L. Guzzella, *Analysis and Synthesis of Single-Input Single-Output Control Systems*. VDF Hochschulverlag AG, 2011.
- [111] K. J. Astrom and R. M. Murray, *Feedback Systems: An Introduction for Scientists and Engineers*. Princeton University Press, USA, 2008.
- [112] R. Bojoi, E. Levi, F. Farina, A. Tenconi, and F. Profumo, “Dual Three-Phase Induction Motor Drive with Digital Current Control in the Stationary Reference Frame,” *IET IEE Proceedings-Electric Power Applications*, vol. 153, no. 1, pp. 129–139, 2006, DOI: 10.1049/ip-epa:20050215.
- [113] A. Turner, K. Ramsay, R. Clark, and D. Howe, “Direct-Drive Rotary-Linear Electromechanical Actuation System for Control of Gearshifts in Automated Transmissions,” in *Proc. of IEEE Vehicle Power and Propulsion Conference*, Arlington, TX, USA, 2007, DOI: 10.1109/VPPC.2007.4544136.
- [114] J. Pan, Y. Zou, and N. C. Cheung, “Performance Analysis and Decoupling Control of an Integrated Rotary-Linear Machine with Coupled Magnetic Paths,” *IEEE Transactions on Magnetics*, vol. 50, no. 2, 2014, DOI: 10.1109/TMAG.2013.2281477.
- [115] S. Tanaka, T. Shimono, and Y. Fujimoto, “Optimal Design of Length Factor for Cross-Coupled 2-DOF Motor with Halbach Magnet Array,” in *Proc. of IEEE International Conference on Mechatronics (ICM)*, Nagoya, Japan, 2015, DOI: 10.1109/ICMECH.2015.7084032.
- [116] S.-M. Jang, S.-H. Lee, H. W. Cho, and S. K. Cho, “Design and Analysis of Helical Motion Permanent Magnet Motor with Cylindrical Halbach Array,” *IEEE Transactions on Magnetics*, vol. 39, no. 5, pp. 3007–3009, 2003, DOI: 10.1109/TMAG.2003.816724.
- [117] O. Dordevic, M. Jones, and E. Levi, “A Comparison of Carrier-Based and Space Vector PWM Techniques for Three-Level Five-Phase Voltage Source Inverters,” *IEEE Transactions on Industrial Informatics*, vol. 9, no. 2, pp. 609–619, 2012, DOI: 10.1109/TII.2012.2220553.

-
- [118] E. Levi, "Advances in Converter Control and Innovative Exploitation of Additional Degrees of Freedom for Multiphase Machines," *IEEE Transactions on Industrial Electronics*, vol. 63, no. 1, pp. 433–448, 2016, DOI: 10.1109/TIE.2015.2434999.
- [119] Infineon, *IGLD60Ro70D1 - 600V CoolGaN Enhancement Mode Power Transistor*, 2016.
- [120] C. B. Barth, T. Foulkes, I. Moon, Y. Lei, S. Qin, and R. C. Pilawa-Podgurski, "Experimental Evaluation of Capacitors for Power Buffering in Single-Phase Power Converters," *IEEE Transactions on Power Electronics*, vol. 34, no. 8, pp. 7887–7899, 2018, DOI: 10.1109/TPEL.2018.2878825.
- [121] TDK, *Ceramic Capacitor C5750X6S2W225K250KA*, 2016.
- [122] R. W. Erickson, "Optimal Single Resistors Damping of Input Filters," in *Proc. of IEEE Applied Power Electronics Conference and Exposition (APEC)*, Dallas, TX, USA, 1999, DOI: 10.1109/LDIA.2019.8770986.
- [123] U. Drofenik, G. Laimer, and J. W. Kolar, "Theoretical Converter Power Density Limits for Forced Convection Cooling," in *Proc. of the International Conference on Power Electronics and Intelligent Motion (PCIM)*, Nuremberg, Germany, 2005.
- [124] S. N. Vukosavic, *Digital Control of Electrical Drives*. Springer Science & Business Media, 2007.
- [125] S. Skogestad and I. Postlethwaite, *Multivariable Feedback Control: Analysis and Design*. Wiley New York, 2007.
- [126] K. Meessen, J. Paulides, and E. Lomonova, "Force Calculations in 3-D Cylindrical Structures using Fourier Analysis and the Maxwell Stress Tensor," *IEEE Transactions on Magnetics*, vol. 49, no. 1, pp. 536–545, 2012, DOI: 10.1109/TMAG.2012.2206821.
- [127] H.-S. Cho and H.-K. Jung, "Analysis and Design of Synchronous Permanent-Magnet Planar Motors," *IEEE Transactions on Energy Conversion*, vol. 17, no. 4, pp. 492–499, 2002, DOI: 10.1109/TEC.2002.805295.
- [128] L. Guo, H. Zhang, M. Galea, J. Li, and C. Gerada, "Multiobjective Optimization of a Magnetically Levitated Planar Motor with Multilayer Windings," *IEEE Transactions on Industrial Electronics*, vol. 63, no. 6, pp. 3522–3532, 2016, DOI: 10.1109/TIE.2016.2522389.

- [129] L. Chen and W. Hofmann, "Design of One Rotary-Linear Permanent Magnet Motor with Two Independently Energized Three Phase Windings," in *Proc. of IEEE International Conference on Power Electronics and Drive Systems*, Bangkok, Thailand, 2007, DOI: 10.1109/PEDS.2007.4487883.
- [130] A. Chitayat and M. Faizullahoy, "System and Method to Control a Rotary-Linear Actuator," Patent US7 218 017B1, 2007.
- [131] D. C. Hanselman, *Brushless Permanent Magnet Motor Design*. The Writers' Collective, 2003.
- [132] L. Zhu, S. Jiang, Z. Zhu, and C. Chan, "Analytical Methods for Minimizing Cogging Torque in Permanent-Magnet Machines," *IEEE Transactions on Magnetics*, vol. 45, no. 4, pp. 2023–2031, 2009, DOI: 10.1109/TMAG.2008.2011363.
- [133] P. Hor, Z. Zhu, D. Howe, and J. Rees-Jones, "Minimization of Cogging Force in a Linear Permanent Magnet Motor," *IEEE Transactions on Magnetics*, vol. 34, no. 5, pp. 3544–3547, 1998, DOI: 10.1109/20.717836.
- [134] N. Bianchi, S. Bolognani, and A. Cappello, "Reduction of Cogging Force in PM Linear Motors by Pole-Shifting," *IEE Proceedings-Electric Power Applications*, vol. 152, no. 3, pp. 703–709, 2005, DOI: 10.1049/ip-epa:20045082.

Curriculum Vitae

Personal Information



Name	Spasoje Mirić
Date of Birth	September 29, 1989
Place of Birth	Belgrade, Serbia
Citizen of	Serbia
Contact	spasojemiric@gmail.com +41 44 632 61 23

Education

2016 – 2021	Doctorate - Power Electronic Systems Laboratory (PES) Swiss Federal Institute of Technology - ETH Zurich Zurich, Switzerland
2013 – 2018	Doctoral Studies in Electrical Engineering University of Belgrade Belgrade, Serbia
2012 – 2013	Master Studies in Electrical Engineering (GPA 10/10) University of Belgrade Belgrade, Serbia
2008 – 2012	Bachelor Studies in Electrical Engineering (GPA 9.62/10) University of Belgrade Belgrade, Serbia
2004 – 2008	Technical High School - Kolubara Lazarevac, Serbia

Work Experience

2016 – 2021	Scientific Assistant - PES Swiss Federal Institute of Technology - ETH Zurich Zurich, Switzerland
2013–2016	Laboratory Teaching Assistant University of Belgrade Belgrade, Serbia
2013	ABB Sales Engineer Belgrade, Serbia